



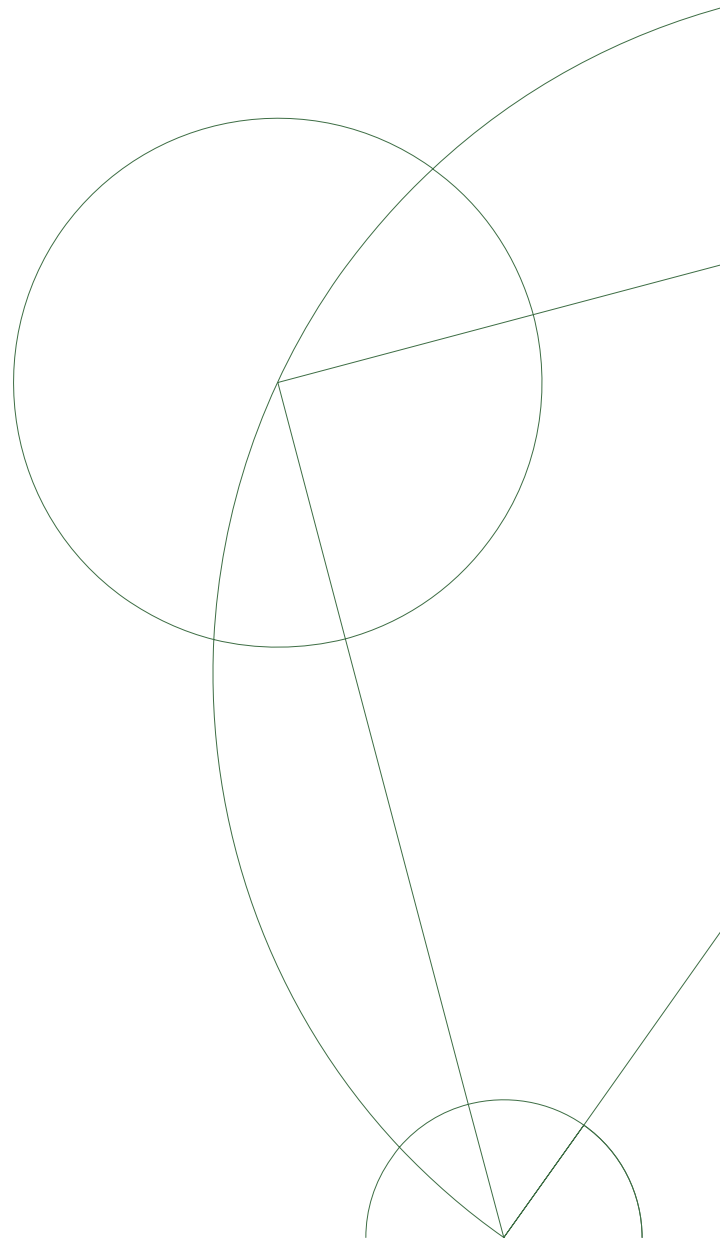
Master's thesis

Pseudorapidity Dependence of Elliptic Flow in Pb+Pb Collisions at $\sqrt{s_{NN}} = 2.76$ TeV with ALICE

Alexander Colliander Hansen

Academic Advisor:
Jens Jørgen Gaardhøje
Niels Bohr Institute
University of Copenhagen

August 2011



English Summary

This thesis presents an analysis of data from Pb+Pb collisions at a centre of mass energy of 2.76 TeV per nucleon, with ALICE at the LHC. I utilize for Forward Multiplicity Detector (FMD) and the Silicon Pixel Detector (SPD). Together they provide a pseudorapidity, η , coverage from -3.75 to 5.

An analysis of the elliptic flow coefficient, v_2 , is presented. At earlier experiments v_2 has been measured and found to be significant. It is interpreted as one of the most important signs of a Quark-Gluon plasma having formed in the collisions. Typically elliptic flow measurements are done as a function of the transverse momentum or centrality. Here the wide pseudorapidity coverage of the two detectors is utilized to study flow as a function of pseudorapidity.

In the thesis the basic theory of high energy heavy ion physics is touched upon, with a particular focus on flow and fluctuations. The experimental apparatus is described. And a more technical description on how the detectors measure particles is presented. It is shown that most of the particles traversing the FMD are secondary particles, created in interactions with detector material. It turns out that the secondaries bias the measurements, and that a Monte Carlo correction is needed.

To measure v_2 a new method developed by people in the ALICE FLOW group is used. It turns out this method is biased under certain fluctuations, which means a study of how this affects the measurement is needed. This study is done, and the optimal measuring region is found, such that unnecessary bias from fluctuations is avoided. It turns out the analysis has some problems, in particular in the FMD. A measurement is still possible, and even though it has some relatively large systematic errors, it yields a good indication on how the elliptic flow behaves as a function of η at LHC energy. The result is compared to earlier experiments at lower energies, and it is found that the shape of $v_2(\eta)$ has changed significantly.

Resume på dansk - Pseudorapiditets afhængighed af elliptisk flow i bly-bly kollisioner ved 2.76 TeV med ALICE

I dette speciale præsenterer jeg en analyse af data fra bly kollisioner ved en energi på 2.76 TeV per nukleon, taget med ALICE experimentet ved LHC. Jeg benytter mig af de to detektorer, Forward Multiplicity Detector (FMD) og Silicon Pixel Detector (SPD). Tilsammen dækker de et pseudorapiditets interval fra -3.75 til 5.

Jeg præsenterer en analyse af den elliptiske flow koefficient, v_2 . Ved tidligere eksperimenter er v_2 blevet målt til at have en betydelig størrelse, og det anses for at være en af de vigtige tegn på at en kvark gluon plasma er dannet i kollisionerne. Typisk måles det elliptiske flow som en funktion af den transverse impuls, eller centralitet. I denne analyse udnyttes den brede pseudorapiditets, η dækning af FMD'en og SPD'en til at kigge på elliptisk flow som funktion af pseudorapiditet.

Undervejs præsenteres de grundliggende antagelser i den moderne høj energi tung-ions fysik, med et specielt fokus på flow og fluktuationer. Det eksperimentelle apparatur beskrives og en teknisk beskrivelse af hvordan detektorerne måler partiklerne gives. Det bliver vist at størstedelen af de partikler, som rammer FMD'en er blevet skabt efter kollisionen, ved interaktioner med forskelligt materiale i experimentet. Det viser sig at disse partikler er med til at forstyrre flow målingen, og en korrektion baseret på Monte Carlo studier er nødvendig.

Til at måle v_2 koefficienten benyttes en ny metode udviklet af medlemmer af ALICE FLOW gruppen. Det bliver vist at denne metode reagerer specielt på fluktuationer, hvilket betyder at en kort undersøgelse af fluktuationerne indflydelse er nødvendig. Denne udføres, og det optimale måle interval bestemmes, hvormed man undgår unødige bias fra fluktuationer. Det viser sig at analysen har nogle problemer. En foreløbig måling er dog mulig, og selvom relativt store usikkerheder præger resultaterne giver de en god indikation af hvordan det elliptiske flow som funktion af η ser ud ved LHC energier. Dette resultat sammenlignes med tidligere eksperimenter ved lavere energier, og det viser sig at formen af $v_2(\eta)$ her ændret sig markant.

Preface

In November 2009 the Large Hadron Collider at CERN collided two proton beams for the first time. Since then machine development and understanding has progressed fast, and in November 2010 the accelerator provided the LHC experiments with the first data from Pb+Pb collisions, at a centre of mass energy of $\sqrt{s_{NN}} = 2.76$ TeV. The four experiments (ALICE, ATLAS, CMS and LHCb) have already published a number of exciting new results. With more than 2.5 fb^{-1} of pp data at $\sqrt{s} = 7$ TeV delivered for both ATLAS and CMS, the two experiments are closer than ever to either finding or excluding the elusive Higgs particle. Meanwhile the heavy ion data is being analysed and, in particular in ALICE, new heavy ion publications are coming out fast.

This thesis summarises my work over the past year as a Master's student in the High Energy Heavy Ion (HEHI) group at the Niels Bohr Institute (NBI). The work presented here is an analysis of the 2010 Pb+Pb data taken with the Forward Multiplicity Detector (FMD), which is built by the HEHI group, and the Silicon Pixel Detector (SPD) in ALICE. Using these two detectors, it is possible to measure the elliptic flow coefficient, v_2 , over a wide pseudorapidity¹ range, η . Flow coefficients are a Fourier expansion of the azimuthal particle yield, and the elliptic flow coefficient is the second order term ($\cos 2\phi$). This term gives information on the elliptic eccentricity of the initial fireball, created in the heavy ion collision. The observation of a large elliptic flow component at earlier heavy ion experiments has been one of the strongest signals of a Quark-Gluon Plasma having formed[1]. Preliminary results from ATLAS and CMS shows $v_2(\eta)$ in the region $-2.5 < \eta < 2.5$, the analysis presented here expands the region to $-3.75 < \eta < 5$.

The thesis is organised in the following way: Chapters 1 and 2 touches on the theoretical foundation of heavy ion physics, where Chapter 2 focus on flow and fluctuations. It is the purpose of these chapters to motivate the measurement presented in later chapters. Chapter 3 and 4 describes the experimental setup, the basics on how the detectors work and how the data is read out and processed from the detector electronics. Chapter 5 describes the method used for the flow measurement. Chapter 6 describes the analysis, and the studies carried out in order to understand the method and detectors involved. Finally in Chapter 7 the systematic errors are discussed, and in Chapter 8 it all comes together and the results are presented.

Please note that the results presented here are a work in progress. They have not been approved by the ALICE collaboration yet, and should not be cited.

Acknowledgements

I would like to thank the High Energy Heavy Ion group at the Niels Bohr Institute (NBI), and in particular my supervisor Professor Jens Jørgen Gaardhøje for introducing me to the field of heavy ion physics, and giving me the opportunity to do this project for my Master's thesis. Special thanks goes to Professor Jamie Nagle, who was a visiting fellow at the Discovery Center at NBI for six months, for his impressive insight in all aspects of heavy ion physics. Without his assistance and ideas I seriously doubt the analysis would have been in the almost finished state presented here, at this time.

¹The pseudorapidity is a measure of the polar angle in the experiment.

I would like to thank the three PhD students in HEHI, Hans Hjersing Dalsgaard, Casper Nygaard and Carsten Sogaard for many discussions and much help over the past year. I would like to thank Christian Holm Christensen and Hans Hjersing Dalsgaard for the FMD and SPD code used to get the data from ESD files to AOD files. And special to Christian Holm Christensen and Børge Svane Niels for proof reading this thesis and giving lots of constructive criticism. Special thanks also goes to Ante Bilandzic, whose many emails about using flow cumulants helped me understand what I was doing, and helped solve many problems encountered during the past year.

I would also like to thank the FLOW group in ALICE for valuable input, the ALICE Collaboration for providing the data, and the LHC accelerator for many days of stable beam time. Users of the coffee machine in the Q-building kitchen and Ian Gardner Bearden also deserves thanks for many encouraging words and fun breaks from the everyday thesis work.

Finally, I would like to thank my family and friends; especially Ida Margrethe Ringgaard, for their love, understanding and support during the past year.

With the startup of the LHC it is an exciting time to be a young student in the world of physics, and I have thoroughly enjoyed the last year at NBI and CERN.

Alexander Colliander Hansen
Copenhagen, August 2011

Contents

1	Heavy Ion Physics	1
1.1	The Standard Model of Particle Physics	1
1.1.1	Quantum Chromodynamics	2
1.1.2	Quark-Gluon Plasma	4
1.2	Heavy Ion Collisions	4
1.2.1	The Geometry of a Collision	5
1.2.2	Kinematics	5
1.3	Multiplicity	8
1.4	Transverse Momentum	11
1.4.1	Spectra	11
1.4.2	High p_t	12
1.5	Jet Quenching	13
2	Flow	15
2.1	Fourier Series Expansion	15
2.2	Anisotropic Azimuthal Flow	16
2.3	Azimuthal Correlations	17
2.4	Higher Order Flow	18
2.5	Elliptic Flow	19
2.5.1	p_t Dependence	19
2.5.2	η Dependence	23
2.5.3	Model Predictions	27
2.6	Flow Fluctuations and Non-flow	28
3	Experiment	31
3.1	The Large Hadron Collider	31
3.1.1	The Four Experiments	31
3.2	ALICE	32
3.3	The V0 Detector	34
3.4	The Forward Multiplicity Detector and the Silicon Pixel Detector	35
3.4.1	Energy Loss of Particles Traversing a Material	35
3.4.2	Silicon Detectors	36
3.4.3	The Forward Multiplicity Detector	37
3.4.4	The Silicon Pixel Detector	38
4	Data	39
4.1	FMD Electronics	40
4.2	SPD Electronics	41
4.3	Monte Carlo Tools	42
4.3.1	HIJING	42
4.3.2	AMPT	42

4.3.3	GEANT3	43
4.3.4	Digitization	44
4.4	Reconstruction	44
4.4.1	Reconstructing Bare Multiplicity with the FMD	44
4.4.2	Cluster Finding and Tracking with the SPD	45
4.5	The Grid	45
5	Method	47
5.1	The Event Plane Method	47
5.2	Particle Cumulants	48
5.2.1	Reference Flow	49
5.2.2	Differential flow	52
5.2.3	Discussion On Statistical Uncertainties	54
5.2.4	Discussion On Fluctuations and Non-flow	55
5.3	Other methods	56
6	Analysis	57
6.1	Resolution effects	57
6.2	Toy Monte Carlo Studies	58
6.2.1	No Flow Fluctuations or Non-flow	58
6.2.2	With Flow Fluctuations	60
6.2.3	With Non-flow	61
6.2.4	With Non-uniform Azimuthal Acceptance	65
6.3	Discussion On Statistical Uncertainty Calculations	65
6.4	Analysis Object Data	68
6.4.1	The SPD: From Event Summary Data to Analysis Object Data	68
6.4.2	The FMD: Sharing Correction With Hit Merging	68
6.4.3	The FMD: Particle Counting With Energy Distributions	71
6.4.4	The FMD and SPD: Secondary Particles	76
6.4.5	The FMD and SPD: Acceptance Issues	80
6.5	Full Monte Carlo Simulations	81
6.5.1	Flow with an Afterburner	81
6.5.2	Flow with AMPT	81
6.5.3	No Flow	84
6.6	Track Reference Analysis	84
6.7	Analysis of Real Data	86
7	Systematic Error Estimates	93
7.1	Error Contribution From Hit Merging and Particle Counting	93
7.2	Errors from the MC Correction	93
7.2.1	p_t Contribution	94
7.2.2	η Contribution	94
7.2.3	Centrality Contribution	96
7.2.4	Particle ID Contribution	96
7.2.5	Material Budget	99
7.3	Final Error Estimate	99
8	Results	101
8.1	Applying the Monte Carlo Correction	101
8.2	Comparing to Published LHC Data	102
8.3	Comparing to Previous Experiments	110

9 Conclusion	115
Bibliography	117
Appendices	
A Statistical Uncertainties	123
A.1 Two-particle Reference Flow	123
A.2 Four-particle Reference Flow	123
A.3 Two-particle Differential Flow	124
A.4 Four-particle Differential Flow	124
B Flow Fluctuations	127
B.1 $v\{2\}$	127
B.2 $v\{4\}$	128
C Differential Flow Fluctuations	129
C.1 v' and v are independent	129
C.2 v' and v are identical	130
C.3 v' and v are dependent	130
D Azimuthal Coverage for Different Vertex Bins	133
E Run Number List	137

List of Figures

1.1	Quark-quark potential	3
1.2	Schematic QCD phase diagram	4
1.3	A heavy ion collision	5
1.4	ALICE centrality determination with V0 amplitude	7
1.5	Centrality and impact parameter	8
1.6	$N_{ch}(\sqrt{s_{NN}})$	9
1.7	$dN_{ch}/d\eta$ at $\sqrt{s_{NN}} = 2.76$ TeV	9
1.8	Integrated charged particle multiplicity	10
1.9	$dN_{ch}/d\eta$ at $\sqrt{s_{NN}} = 200$ GeV	10
1.10	Particle production per number of participant pairs	11
1.11	$1/(2\pi p_t)(d^2N_{ch})/(d\eta dp_t)$ at $\sqrt{s_{NN}} = 2.76$ TeV	12
1.12	p_t spectra at RHIC and LHC	13
1.13	Nuclear modification factor at $\sqrt{s_{NN}} = 2.76$ TeV.	14
1.14	Jet quenching	14
2.1	A+A collision in the transverse plane	16
2.2	The ridge and Mach cone	17
2.3	Two-particle azimuthal correlations	18
2.4	Global fit at different p_t	20
2.5	Glauber fluctuations	20
2.6	Centrality dependence of $v_2 - v_6$	21
2.7	Transverse momentum dependence of $v_2 - v_5$	21
2.8	Elliptic flow over a wide $\sqrt{s_{NN}}$ range	22
2.9	Elliptic flow vs. centrality at $\sqrt{s_{NN}} = 2.76$ TeV	22
2.10	Elliptic flow vs. p_t at $\sqrt{s_{NN}} = 2.76$ TeV	23
2.11	Elliptic flow for identified particles at RHIC	24
2.12	Elliptic flow vs. η at $\sqrt{s_{NN}} = 200$ GeV with PHOBOS	25
2.13	Elliptic flow vs. η at $\sqrt{s_{NN}} = 200$ GeV with STAR	26
2.14	Elliptic flow vs. η in the rest frame of a nuclei	26
2.15	Elliptic flow vs. η at $\sqrt{s_{NN}} = 2.76$ TeV with ATLAS	27
2.16	Stopping in a heavy ion collision.	28
2.17	Transparency in a heavy ion collision.	28
2.18	Fits to PHOBOS v_2 data from the Hydrodynamical Buda-Lund model	29
2.19	Extrapolation from RHIC data to LHC design energy	29
2.20	Non-flow and fluctuations in elliptic flow	30
3.1	The CERN accelerator complex	32
3.2	The ALICE detectors	33
3.3	Centrality resolution	34
3.4	The Bethe-Bloch curve	35
3.5	Band-gaps in insulator, semi-conductors and metals	36

3.6	The Forward Multiplicity Detector	37
3.7	The Silicon Pixel Detector	38
4.1	Data flow through AliRoot	39
4.2	Schematic of the FMD Front-End electronics	40
4.3	FMD calibration plots	41
4.4	Block diagram of the electronics of an SPD pixel cell	41
4.5	Elliptic flow in the AMPT model	43
4.6	SPD cluster types in experimental and MC data	45
6.1	Flow with different ϕ -segmentations	58
6.2	Q-Cumulants with different ϕ -segmentations - flat distribution	59
6.3	Q-Cumulants with different ϕ -segmentations - Gaussian distribution	60
6.4	Elliptic flow with multiplicity fluctuations	61
6.5	Simple elliptic flow fluctuations - flat distribution	62
6.6	Simple elliptic flow fluctuations - Gaussian distribution	62
6.7	Independent elliptic flow fluctuations - flat distribution	63
6.8	Independent elliptic flow fluctuations - Gaussian distribution	63
6.9	Elliptic flow with non-flow	64
6.10	Q-Cumulants with non-uniform azimuthal coverage	66
6.11	Toy MC with fluctuations, non-flow and non-uniform azimuthal coverage	67
6.12	Statistical uncertainty method comparison	68
6.13	Signal sharing	69
6.14	Flow chart of the sharing algorithm.	70
6.15	E_{hit} cut determination with MC data	70
6.16	Different cases of sharing over three strips and how the algorithm handles it.	72
6.17	FMD noise	73
6.18	Energy distributions before and after hit merging	73
6.19	Energy distribution fitting	75
6.20	Poisson method correction	76
6.21	Secondary particles in FMD and SPD	77
6.22	ϕ -blurring in the FMD	78
6.23	The effect of ϕ -blurring on elliptic flow	79
6.24	Azimuthal coverage in the SPD and FMD	80
6.25	HIJING MC of Pb+Pb collisions at $\sqrt{s_{NN}} = 2.76$ TeV with a flow afterburner	82
6.26	AMPT MC of Pb+Pb collisions at $\sqrt{s_{NN}} = 2.76$ TeV	83
6.27	$v_2(cent)$ for a HIJING Pb+Pb simulation at $\sqrt{s_{NN}} = 2.76$ TeV	85
6.28	$v_2(\eta)$ for a HIJING Pb+Pb simulation at $\sqrt{s_{NN}} = 2.76$ TeV	85
6.29	MC correction	87
6.30	Vertex distribution in analysed events	88
6.31	Centrality distribution in analysed events	89
6.32	Analysis with wide reference binning	89
6.33	Analysis with smaller reference binning	90
6.34	Uncorrected $v_2\{2\}$ results	91
6.35	Uncorrected $v_2\{4\}$ results	91
7.1	Systematic errors from detector measurements	94
7.2	$v_2\{2\}$ systematic errors from p_t dependence	95
7.3	$v_2\{4\}$ systematic errors from p_t dependence	95
7.4	$v_2\{2\}$ systematic errors from η dependence	96
7.5	$v_2\{4\}$ systematic errors from η dependence	97
7.6	$v_2\{2\}$ systematic errors from centrality determination	97

7.7	$v_2\{4\}$ systematic errors from centrality determination	98
7.8	Systematic errors from $v_2(PID)$	98
7.9	Systematic error from the material description	99
8.1	$v_2\{2\}(\eta)$ at $\sqrt{s_{NN}} = 2.76$ TeV.	102
8.2	$v_2\{4\}(\eta)$ at $\sqrt{s_{NN}} = 2.76$ TeV.	103
8.3	Forward-backward symmetry in corrected v_2 measurement	104
8.4	Comparison to RHIC top energy	105
8.5	Centrality dependence with systematic error bars	106
8.6	$v_2\{2\}$ centrality dependence in η -intervals	106
8.7	$v_2\{4\}$ centrality dependence in η -intervals	107
8.8	$v_2\{2\}$ comparison to CMS results	107
8.9	$v_2\{4\}$ comparison to CMS results	108
8.10	$v_2\{2\}$ comparison to ATLAS results	108
8.11	Comparison to ALICE results	109
8.12	Elliptic flow vs. $\sqrt{s_{NN}}$	110
8.13	Elliptic flow vs. pseudorapidity over a wide energy range.	111
8.14	Elliptic flow vs. $\sqrt{s_{NN}}$ in different $ \eta $ -ranges	112
8.15	Elliptic flow vs. $\eta - y_{beam}$	113
D.1	Azimuthal acceptance for $-6 \text{ cm} < v_z < -4 \text{ cm}$	133
D.2	Azimuthal acceptance for $-4 \text{ cm} < v_z < -2 \text{ cm}$	134
D.3	Azimuthal acceptance for $-2 \text{ cm} < v_z < 0 \text{ cm}$	134
D.4	Azimuthal acceptance for $0 \text{ cm} < v_z < 2 \text{ cm}$	135
D.5	Azimuthal acceptance for $2 \text{ cm} < v_z < 4 \text{ cm}$	135
D.6	Azimuthal acceptance for $4 \text{ cm} < v_z < 6 \text{ cm}$	136

List of Tables

1.1	The Standard Model bosons	2
1.2	The Standard Model fermions	2
1.3	The Standard Model Quarks	2
3.1	Overview of parameters for the FMD rings	37
7.1	Systematic errors for $v_2\{2\}$	100
7.2	Systematic errors for $v_2\{4\}$	100

Chapter 1

Heavy Ion Physics

The focus of this chapter is on the physics motivation behind this thesis. First the framework of high energy physics is touched upon. This begins with the Standard Model of Particle Physics. The first part of this chapter also contains a section about Quantum Chromodynamics (QCD) used to motivate the concept of Quark-Gluon Plasma (QGP). After this a more practical experimental viewpoint is established: The geometry of a heavy ion collision is described and an overview of the most important observables presented. One of these observables, namely flow is of particular interest to this work. It will get its own chapter, following this one.

1.1 The Standard Model of Particle Physics

Particle physics is the study of the fundamental constituents of matter and their interactions. The Standard Model (SM) attempts to explain these in terms of a small number of particles. The particles are divided into three types: quarks, leptons and gauge bosons. The gauge bosons are the mediators of the interactions between the quarks and leptons. They represent three of the four fundamental forces of nature; the electromagnetic force, the weak force and the strong force. In the SM the strong force is described by QCD. The weak force and electromagnetism is described by a unification of Quantum Weak Dynamics and Quantum Electro Dynamics, so-called Electroweak Dynamics. The SM contains six different gauge bosons: The massless photons and gluons, the massive W^+ , W^- and Z bosons and finally the Higgs particle. The Higgs particle is the only particle of the SM that has not yet been discovered. To discover the Higgs is the main goal of modern high energy experiments, such as the Large Hadron Collider (LHC) and Tevatron. In the SM the Higgs particle is what gives the particles mass, it does not mediate a force like the other gauge bosons. The photon and the three massive bosons are the carriers of the electroweak force, and the gluons are the carriers of the strong force. Table 1.1 shows the basic properties of the gauge bosons. A description of gravity is not part of the Standard Model. There are plenty of theories going beyond the Standard Model, which contain a quantum description of gravity, but none of these have any experimental evidence yet.

There are six leptons divided into three generations in the SM: The electron and electron neutrino, the muon and muon neutrino and the tau and tau neutrino. The leptons interact with each other via the electromagnetic force and the weak force. They are not affected by the strong force. Table 1.2 shows some of the basic properties of leptons. The SM also contains six quarks, also divided into three generations: The up and down quarks, the charm and strange quarks and the top and bottom quarks. The quarks are affected by all three forces of the SM. The strong force is responsible for binding quarks together in hadrons, such as the protons and neutrons.[3] Quarks, gluons and the strong interaction are of particular interest in heavy ion physics, and are described in more detail in the next section. Table 1.3 shows the basic properties of the SM quarks.

Name	Symbol	Charge	Mass
Photon	γ	0	$< 10^{-18} \text{ eV}/c^2$
W boson	W^\pm	± 1	80.399 ± 0.023
Z bosons	Z	0	91.1876 ± 0.0021
Gluon	g	0	0
Higgs	H	0	unknown

Table 1.1: The six bosons of the Standard Model. Charge is electromagnetic charge in units of e . Mass is in units of GeV/c^2 unless otherwise noted. The mass of the gluon is a theoretical value.[2]

The gauge bosons, leptons and quarks all have anti-particles. For the leptons and quarks there is simply one anti-particle for each particle, which has mostly the same properties as the particle but opposite sign on the charges. For the gauge bosons it is more complicated. The photon, gluon, Z boson and Higgs particles all have an anti-particle, but it is indistinguishable from the normal particle. The W^+ and W^- are each other's anti-particle.[3]

Name	Symbol	Charge	Mass
Electron	e	-1	0.510999
Electron neutrino	ν_e	0	$< 2 \text{ eV}/c^2$
Muon	μ	-1	105.658
Muon neutrino	ν_μ	0	< 0.19
Tau	τ	-1	1776.82 ± 0.16
Tau neutrino	ν_τ	0	< 18.2

Table 1.2: The six leptons of the Standard Model. Charge is electromagnetic charge in units of e , mass is in units of MeV/c^2 unless otherwise noted.[2]

Name	Symbol	Charge	Mass
Up	u	$+2/3$	$1.7 - 3.3$
Down	d	$-1/3$	$3.0 - 4.8$
Charm	c	$+2/3$	$1.27^{+0.07}_{-0.09}$
Strange	s	$-1/3$	101^{+29}_{-21}
Top	t	$+2/3$	$172.0 \pm 0.9 \pm 1.3 \text{ GeV}/c^2$
Bottom	b	$-1/3$	$4.19^{+0.18}_{-0.06} \text{ GeV}/c^2$

Table 1.3: The six quarks of the Standard Model. Charge is electromagnetic charge in units of e , mass is in units of MeV/c^2 unless otherwise noted.[2]

1.1.1 Quantum Chromodynamics

Quantum Chromodynamics (QCD) is the quantum theory describing the strong interaction. As discussed in the previous section only quarks and gluons (or particles composed of these) are affected by the strong interaction. Much like the well known electrical charge used in electrodynamics, quarks and gluons are said to have a colour charge. The charge of the strong interaction is a bit more complicated than the electromagnetic charge. Where the electromagnetic charge only has positive and negative value, the strong interaction has red (r), green (g) and blue (b) and anti-red (\bar{r}), anti-green (\bar{g}) and anti-blue (\bar{b}) charges. Much like a positively charged particle and a negatively charged particle can form an electromagnetically neutral object, so can a coloured and an anti-coloured object combine into a colour neutral object e.g., a green and

an anti-green quark can combine to form a colour neutral meson¹. But there is an extra combination of colour charges that gives a colour neutral object, namely combining an (anti-)red, (anti-)green and an (anti-)blue quark to give a colour neutral (anti-)baryon².

In fact all known hadrons are colour neutral, and it seems that nature avoids free colour charge. Where gravity and the electroweak force gets weaker at long distances, the strong force becomes much stronger, this is known as colour confinement. Figure 1.1 shows the potential between two quarks as a function of distance, the approximately linear rise with distance above 0.5 fm is clearly seen. This means that two quarks moving away from each other will increase the energy in the colour field between them, until at some point the stored energy is converted into a new quark-anti-quark pair. Thus confining the original quarks in two new hadrons, each with one of the newly created quarks. Much like stretching a rubber band initially increases the tension in the band, until at some point it snaps and becomes two (smaller) rubber bands.

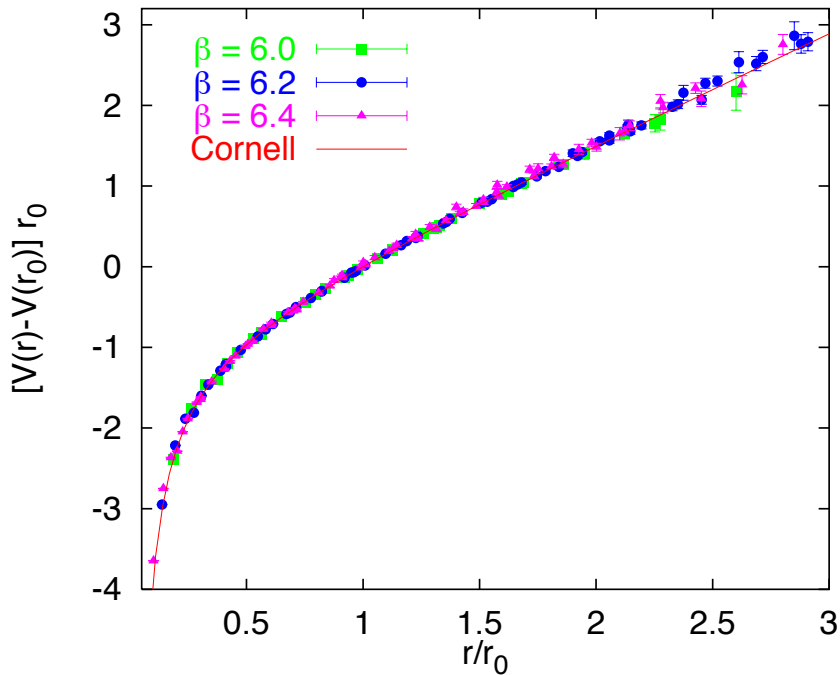


Figure 1.1: A plot of the quark-quark potential, calculated from lattice QCD (lQCD). In the plot $r_0 = 0.5$ fm ($1/3$ the proton radius). The β factor in the legend is from lQCD and can be ignored. The important thing is the shape of the potential.[4]

In the opposite limit, where two quarks are moved closer to each other, at one point the force becomes zero. In effect this means that at some distance, where two quarks are very close to each other, they will not interact via the strong force at all. This is known as asymptotic freedom, and is of great importance in the field of heavy ion physics.[3]

If the force between two quarks is close to zero and the quarks stop interacting, they are, in a sense, free quarks. So forcing quarks close together makes it possible to observe how free coloured particles behaves. Something that is otherwise impossible due to colour confinement. Designing an experiment where there is a high density of quarks is a good way to study QCD at short distances. An idea on how to set up such an experiment came in 1974 at a workshop in Bear Mountain, New York, where T.D. Lee suggested that by distributing high energy density or high nucleon density over a relatively large volume, it might be possible to create abnormal dense states of nuclear matter. The dense nuclear matter would contain asymptotically free quarks.

¹A meson is a hadron consisting of two quarks.

²A baryon is a hadron consisting of three quarks, an anti-baryon consists of 3 anti-quarks.

First the dense state was referred to as a quark soup - today it is known as the Quark-Gluon Plasma (QGP) [5]. Creating and studying such a plasma is exactly what heavy ion physics is all about.

1.1.2 Quark-Gluon Plasma

The Quark-Gluon Plasma is a very dense state of matter where quarks and gluons are deconfined. QCD is non-perturbative in the asymptotically free region due to the non-linearity of the strong interaction. Because of that analytical results are not possible. In order to do QCD calculations in the asymptotically free limit theorists have invented Lattice QCD (lQCD for short). lQCD is a gauge theory formulated on a lattice in space and time. Mathematically it is a well defined theory, and it is a powerful tool in the investigation of non-perturbative phenomena, such as the QGP phase [6].

It is believed that the energy densities needed to create a QGP was available in the universe at about $1 \mu\text{s}$ after the big bang, and that the entire universe was in a QGP state at that time. While experimental results from heavy ion collisions suggest the QGP to be very strongly interacting, it is believed that the QGP of the early universe was weakly interacting. Another place in the universe where QGP is believed to exist is inside neutron stars, in this case it is a very high baryon chemical potential which is the cause of the phase transition. A schematic of the QCD phase vs. baryon chemical potential and temperature is shown in figure 1.2. [6]

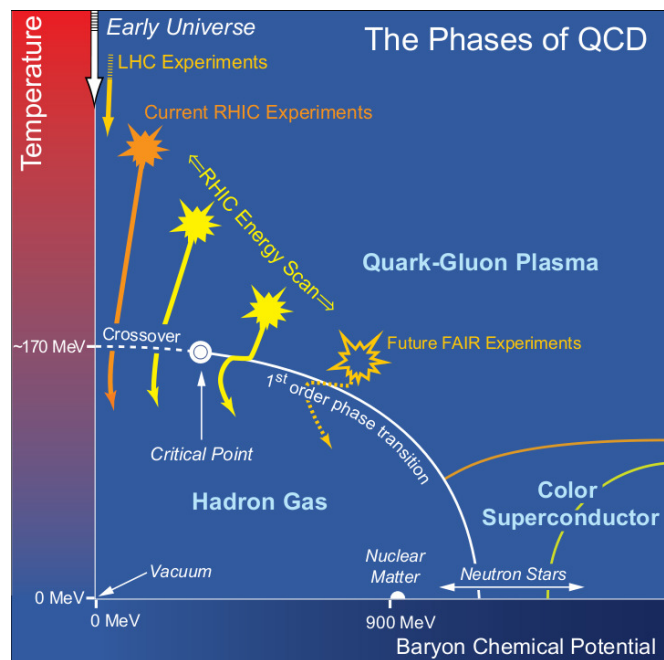


Figure 1.2: Schematic QCD phase diagram for nuclear matter. The solid lines show the phase boundaries for the indicated phases. The solid circle depicts the critical point. Possible trajectories for systems created in the QGP phase at different accelerator facilities are also shown. Adapted from [7]

1.2 Heavy Ion Collisions

In the previous section the state of matter called the Quark-Gluon Plasma was introduced. The field of relativistic heavy ion physics has evolved around the notion that new knowledge could be gained by creating and studying this state of matter. At the Relativistic Heavy Ion Collider

(RHIC) and now at the LHC it is believed that creating a QGP has been accomplished. In the next section results indicating a creation of QGP and some of its properties are presented. But first, a look into the geometry of a collisions and an introduction to the important variables is necessary.

1.2.1 The Geometry of a Collision

When observed from the centre of mass (CM) frame, two nuclei accelerated to highly relativistic speeds will appear as two flat pancakes due to Lorentz contraction. A schematic view of this is presented in figure 1.3. The radius of a nuclei is $R \approx 1.2A^{1/3}$, where A is the atomic mass number. For Pb ions this gives approximately 7 fm ($1 \text{ fm} = 10^{-15} \text{ m}$). It is not possible to make a collider where such precision is obtained, so it is completely random how much overlap there is between two colliding nuclei. This makes it convenient to have a measure of the overlap; the vector \mathbf{b} , shown in figure 1.3(a), going from the centre of one nucleus to the centre of the other, is a measurement of the overlap between the two nuclei.

Figure 1.3(b) shows the system after a collision, the particles inside the overlap region create a fireball, expanding in all directions. They are known as participant particles. The particles outside of the overlap continues along their original trajectories, and are known as spectators. At lower energies the spectators has a shadowing effect on particles in the fireball [8], but at the energies of RHIC and LHC they carry so much momentum they do not have time to interact with the other particles.

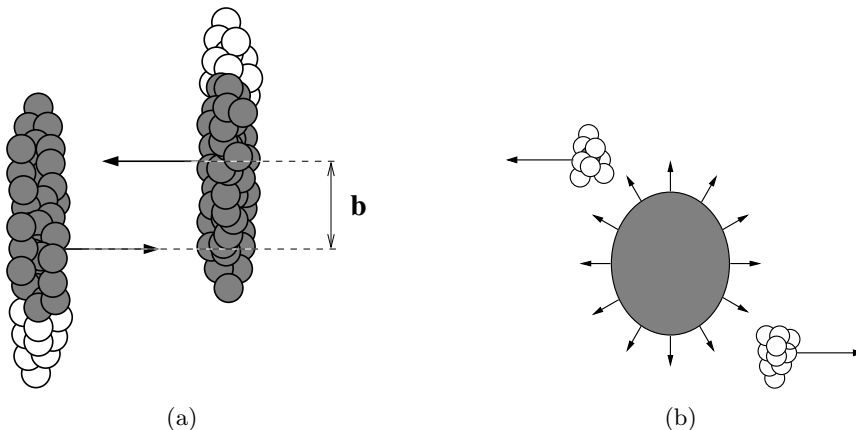


Figure 1.3: A heavy ion collision seen from the CM frame. (a): Impact parameter and (b): Spectators and participants.

1.2.2 Kinematics

At the LHC, the coordinate system is such that the z -axis is parallel to the collision axis, the x -axis is horizontal, pointing into the centre of the accelerator. The y -axis is vertical, pointing up. The nominal interaction point (IP) is at the $(0, 0, 0)$ -coordinate, the beams are aimed such that collisions take place around this point. Collisions do not always happen exactly at the IP. In the x and y direction they are rarely displaced from the IP by more than 0.1 mm, but on the z -axis displacements of more than 10 cm are not uncommon. Thus the collision point also has to be measured, this is called the *primary vertex* or sometimes just *vertex*.

Collision Energies

The energy in the CM frame can be calculated using the 4-vectors of the beams $\mathbf{E}(E, 0, 0, p_z)$. It is simply:

$$E_{CM} = \sqrt{(E^\mu + E^\nu)^2} = \sqrt{(2E)^2} = 2E \quad (1.1)$$

I.e. twice the beam energy. Usually the CM energy is denoted as \sqrt{s} . For heavy ion collision $\sqrt{s_{NN}}$ is often used instead, the 'NN' implies the energy per nucleon pair. Using the available energy per nucleon pair makes it easier to compare heavy ion experiments with different kinds of nuclei. So for the LHC the notation is $\sqrt{s_{NN}} = 2.76$ TeV (5.5 TeV) for the current (design) energy, while the total CM energy is really $208 \cdot \sqrt{s_{NN}} = 574.08$ TeV (1.144 PeV).

Transverse momentum

Often the momentum is divided into two terms. A transverse momentum, and a p_z momentum. The transverse momentum has the advantage of being Lorentz invariant. It is defined as:

$$p_t = \sqrt{p_x^2 + p_y^2} \quad (1.2)$$

It is Lorentz invariant, as the x and y components of the 4-momentum transforms as $p_x = p'_x$ and $p_y = p'_y$.

Rapidity

Actually p_z is rarely used by itself, rather it goes into defining the rapidity, y , of a particle:

$$y = \ln \frac{1}{2} \left(\frac{E + p_z}{E - p_z} \right) \quad (1.3)$$

Rapidity has the advantage of being additively invariant under Lorentz transformations, while p_z is not. This also means that dy is Lorentz invariant.

Pseudorapidity

It requires knowledge about the mass of a particle in order to calculate its rapidity. Experimentally the mass is not necessarily known, so experimentalists often use pseudorapidity, η , for unidentified particles:

$$\eta = -\ln[\tan(\theta/2)] \quad (1.4)$$

where $\tan(\theta) = \sqrt{x^2 + y^2}/z$. Since this reduces the variables to (x, y, z) -coordinates knowledge about the momentum of a particle is not necessary either to calculate the pseudorapidity. For particles with $m \ll p$ the energy $E = \sqrt{m^2 + p^2} \rightarrow p$ and $y \rightarrow \eta$.

Multiplicity

The multiplicity is defined as the number of particles coming from the collision. Often the multiplicity will refer only to the number of charged particles (as it will in this thesis), and should really be called charged particle multiplicity. The multiplicity is often measured differentially as a function of pseudorapidity, $dN/d\eta$.

Centrality

In section 1.2.1 the impact parameter was briefly discussed. It is impossible to measure the impact parameter directly. But since the observables in a very peripheral collision is different from the observables in a very central one, it is crucial to have a measure on the overlap of the two nuclei. Using the argument that if a larger number of particles participate in the collision

the total multiplicity is also larger, one can construct a measurement on how central a collision is. An example of this is seen in figure 1.4. The red line is a "Glauber fit". A Glauber model is a tool to help relate the measured quantities with initial state geometric quantities such as impact parameter and the shape of the collisions region. It was originally developed to model high energy scattering with composite particles. There are several approaches to this (see [9] for an extensive review), the one used in the figure takes the Monte Carlo approach, where the individual nucleons are stochastically distributed event-by-event [10]. This is used to find the number of participating nucleons, N_{part} , and the number of spectator nucleons, N_{spec} . From there a negative binomial distribution is assumed for the particle production [11]. This gives a reasonable fit to the data, as is seen in the figure.

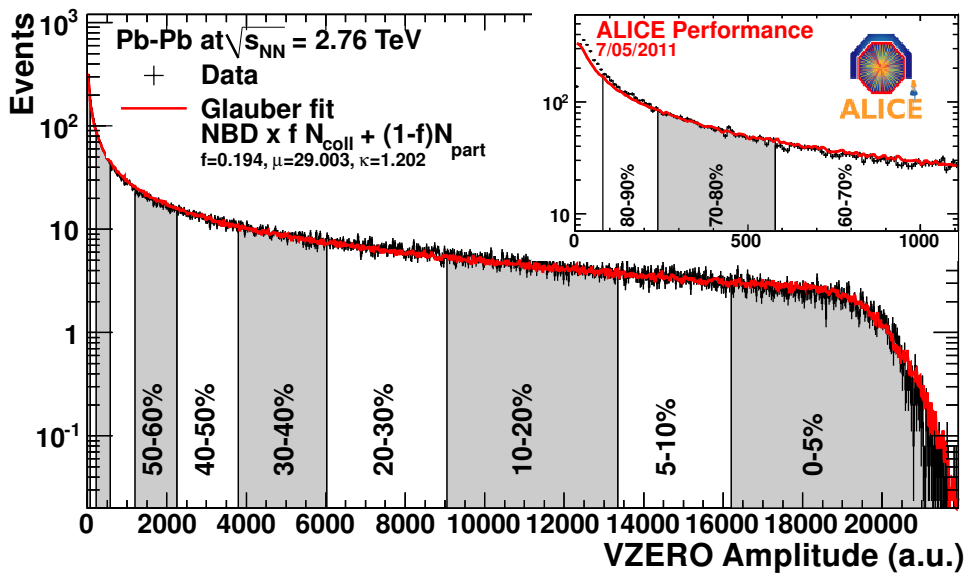


Figure 1.4: Centrality determination in ALICE. The V0 amplitude is proportional to the number of charged particles produced in the collision. A fit to a distribution from a Monte Carlo Glauber model and a negative binomial distribution for the particle production is seen as the red line. The parameters under the Glauber fit in the legend is from the fitting procedure. A description of these is beyond the scope of this thesis. [11]

The centrality is defined as a number from 0% to 100%, such that a 0% central event has $b = 0$ and is thus the most central event possible. Whereas an event with centrality 100% is the most peripheral possible. The slicing in centrality is such that if you choose events with centrality 0 – 10% you will get the top 10% most central events.

But determining the centrality from a probability distribution in multiplicity makes the connection to impact parameter non-trivial. In principle it should follow the relation: [12]

$$c = \frac{\int_0^{b_c} \frac{d\sigma_{inel}(b)}{db} db}{\sigma_{inel}} \quad (1.5)$$

where σ_{inel} is the total inelastic nuclear cross section and $\frac{d\sigma_{inel}(b)}{db}$ is the differential cross section at impact parameter b . For two identical nuclei the differential cross section becomes $\frac{d\sigma_{inel}(b)}{db} = 2\pi b db$ using this and that the maximum impact parameter $b_{max} = 2R$, the total cross section becomes $\sigma_{inel} = 4\pi R^2$. And finally the centrality is:

$$c = \frac{b^2}{4R^2} \quad (1.6)$$

which for PbPb means that 10% centrality is equal to $b \approx 4.5$ fm. Unfortunately this does not correspond completely to the centrality measured. This is seen in figure 1.5. One other important point is observed in the figure: The 5% most central events correspond to almost 20% of the total impact parameter range (the 0-5% bin goes up to about 3.5 fm). This is important to keep in mind when looking at plots from the LHC; even though an event has a low centrality, it may not be completely central in terms of impact parameter.

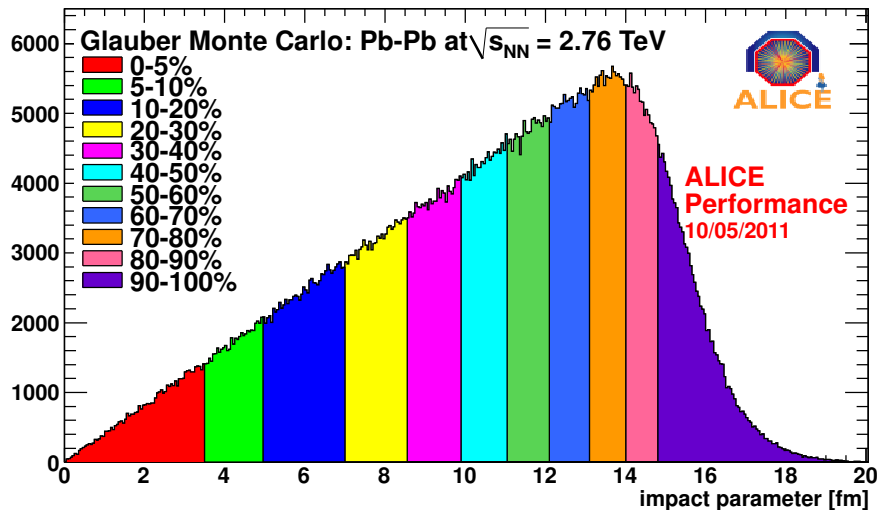


Figure 1.5: Centrality determination in ALICE. A Glauber Monte Carlo has been used to visualise impact parameter in centrality slices. [13]

1.3 Multiplicity

The first step in characterizing the system produced in heavy ion collisions is measuring the charged particle pseudorapidity density. This is used to constrain the dominant particle production mechanisms using models and to help determine the initial energy density. Models that successfully describe RHIC data vary by a factor of two in predicting $dN_{ch}/d\eta|_{\eta=0}$ at the LHC energy [11]. Figure 1.6 shows the charged particle multiplicity at mid-rapidity as a function of energy for pp and A+A collisions. For A+A systems it is scaled to the number of participant pairs in order to be able to compare between different collisions systems including pp. The observed trend from lower energies fits with the LHC data, and in general there is higher multiplicity in A+A collisions than in pp. Specifically the charged particle multiplicity per participant pair has doubled in going from RHIC to LHC.

The charged particle pseudorapidity density as a function of η has been measured with the Forward Multiplicity Detector (FMD) and Silicon Pixel Detector (SPD) in ALICE and is presented in figures 1.7-1.8. In figure 1.7 $dN_{ch}/d\eta$ is shown for different centrality classes. For all centrality classes the multiplicity is largest at $|\eta| = 2$. This was also observed at RHIC, but was less pronounced as is apparent in figure 1.9, and the $dN/d\eta$ at the LHC is more similar to pp spectra than lower energy heavy ion spectra are.

The total charged particle multiplicity integrated from $-y_{beam}$ to y_{beam} is seen in figure 1.8 for different centrality bins, here shown by the number of participants. For the most central collision (0 – 5%) an average of 17200 charged particles are produced.

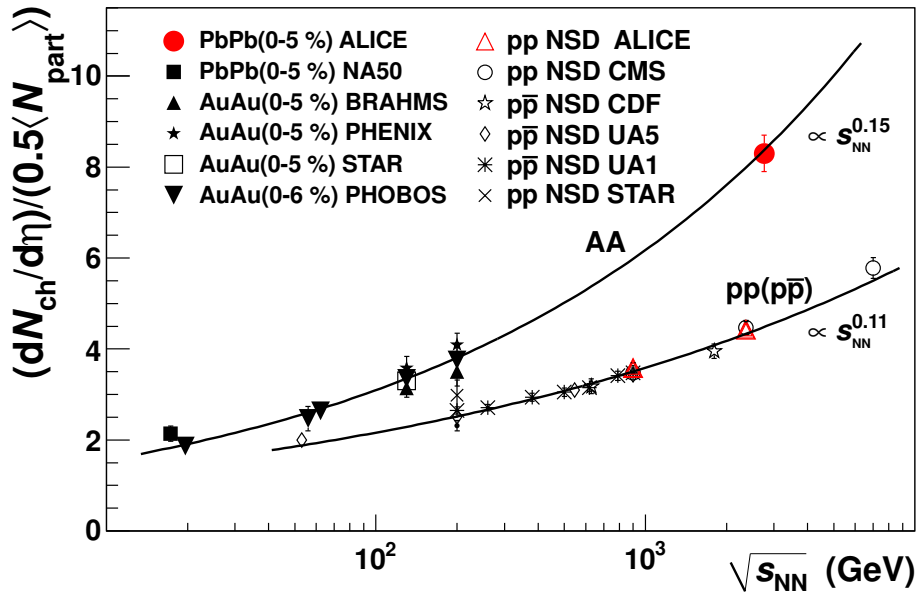


Figure 1.6: Charged particle multiplicity at mid-rapidity scaled to the number of participant pairs at different energies and for different collision system. The LHC data fits the trend from lower energies well. [11]

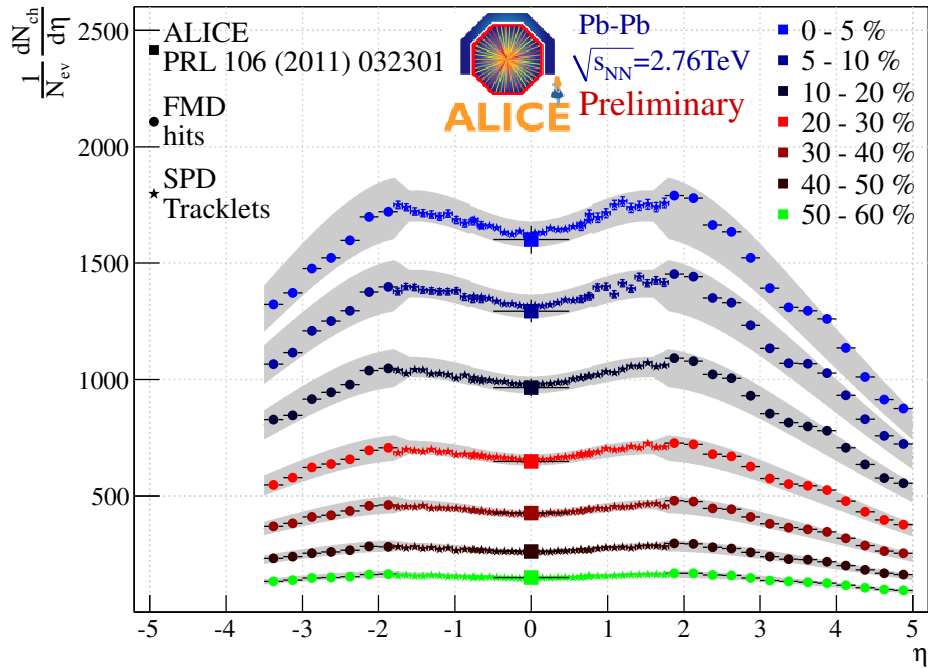


Figure 1.7: $dN/d\eta$ for different centrality classes, as measured with the ALICE Forward Multiplicity Detector and Silicon Pixel Detector. [14]

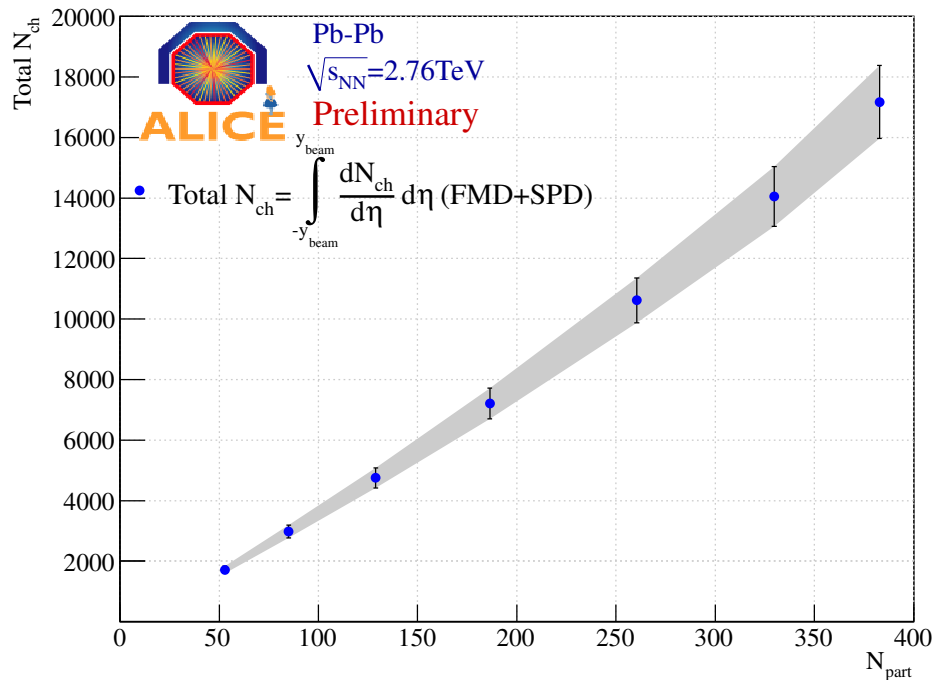


Figure 1.8: Integrated charged particle multiplicity for different numbers of participants for Pb+Pb collisions at 2.76 TeV measured with the ALICE Forward Multiplicity Detector and Silicon Pixel Detector. In the most central collisions 17200 particles are produced. [15]

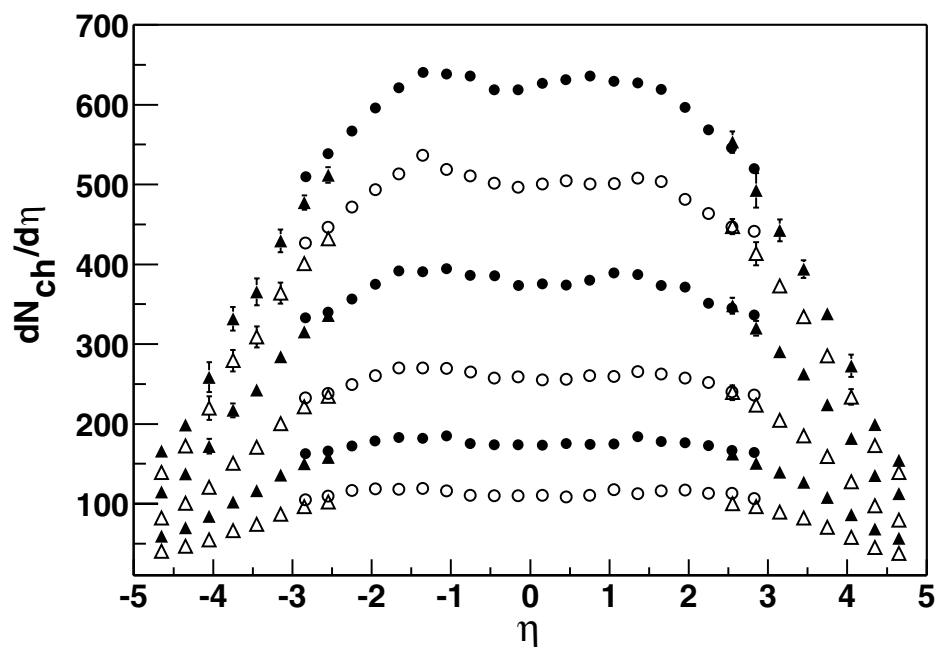


Figure 1.9: Pseudorapidity density in Au+Au collisions at $\sqrt{s_{NN}} = 200$ GeV for different centrality bins. From top to bottom 0-5%, 5-10%, 10-20%, 20-30%, 30-40% and 40-50%. By BRAHMS [16].

It is also interesting to study how the particle production mechanism depends on the centrality. Figure 1.10 shows how many particles are produced per participant pair for different N_{part} . And indeed for a larger system there is a larger particle production per participant pair. However, the trend is the same both in the central and forward regions, which means that the particle production mechanism is likely to be the same at all rapidities, but may change with centrality. [14]

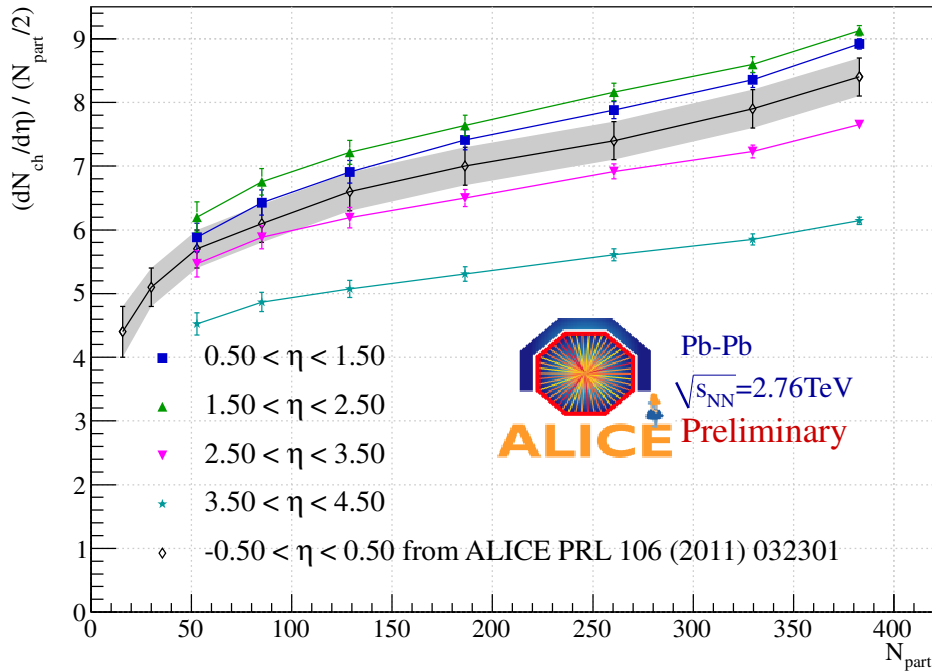


Figure 1.10: Particle production per number of participant pairs vs. N_{part} . The particle production seems to have a small dependence on the centrality, maybe a bit stronger for the most peripheral events. The scaling is the same in all η regions, meaning the particle production mechanism is likely the same for forward and central rapidities. [14]

1.4 Transverse Momentum

This section on transverse momentum is divided into two parts. The first part is about the p_t spectrum, and is closely related to the previous section on multiplicity. The second part is about hard processes and high p_t , and is closely related to the last section of this chapter, which is about jet quenching.

1.4.1 Spectra

Another way to observe if there is a change in production mechanism is to look at the p_t spectrum for different centralities. This is done in figure 1.11. This plot shows $1/(2\pi p_t)(d^2 N_{ch})/(d\eta dp_t)$ vs. p_t for different centralities in Pb+Pb collisions and for pp collisions. The shape of the curve is the same for all centralities and again this points to a similar production mechanism.

For dN/dp_t a change is seen in going from RHIC to LHC. Figure 1.12 shows a comparison between the p_t spectra for different negatively charged identified particles at LHC and RHIC. The p_t spectra are shifted towards a higher p_t at the LHC, which is due to a much stronger

radial flow at 2.76 TeV than at 200 GeV [17]. This is very important to keep in mind when comparing flow results between RHIC and LHC (see chapter 2).

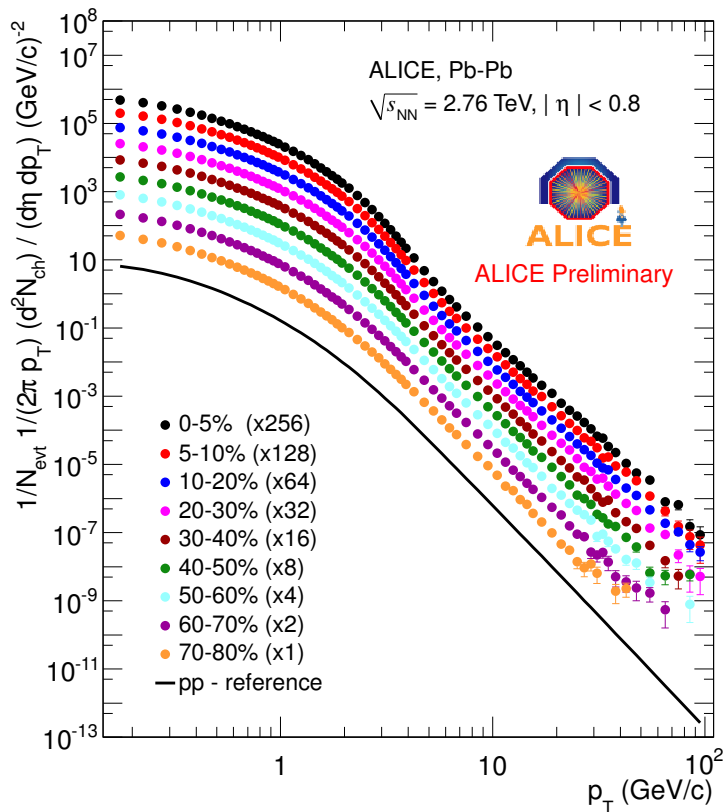


Figure 1.11: $1/(2\pi p_t)(d^2N_{ch})/(d\eta dp_t)$ for unidentified particles in different centrality bins. A comparison to pp is also seen. All the curves have the same shape, pointing to a similar underlying particle production mechanism.[18]

1.4.2 High p_t

At RHIC one of the first signals of a QGP was the discovery of the suppression of high p_t particles in Au+Au collisions at $\sqrt{s_{NN}} = 200$ GeV [20], in comparison with pp collisions at the same energy. The measured quantity is known as the nuclear modification factor, and is defined as:

$$R_{AA} \equiv \frac{d^2N/dp_t d\eta_{AA}}{N_{bin} d^2N/dp_t d\eta_{pp}} \quad (1.7)$$

R_{AA} then is the transverse particle production in A+A collisions relative to pp collisions scaled by the number of binary collisions, N_{bin} . The first results from the LHC shows an even stronger suppression than at RHIC [21]. The suppression scales with centrality, (see figure 1.13), such that the most central events show the strongest suppression. This is in agreement with the theory, that suppression is due to strong colour interactions in the medium where a traversing coloured object with high momentum will emit gluon brehmsstrahlung. Further signs of this is seen in d+Au data where there is no suppression [22]. In direct photons there is no suppression observed, indicating that it is in fact a QCD phenomenon, and not electromagnetic in origin [23].

The rise at very high p_t is not fully understood, but there are models which predict such a behaviour e.g., the Gyulassy-Levai-Vitev energy loss models [24].

The suppression happens at the quark level before hadronization. Once they are hadronized they will no longer be affected by the suppression. Often R_{AA} analysis is done for identified

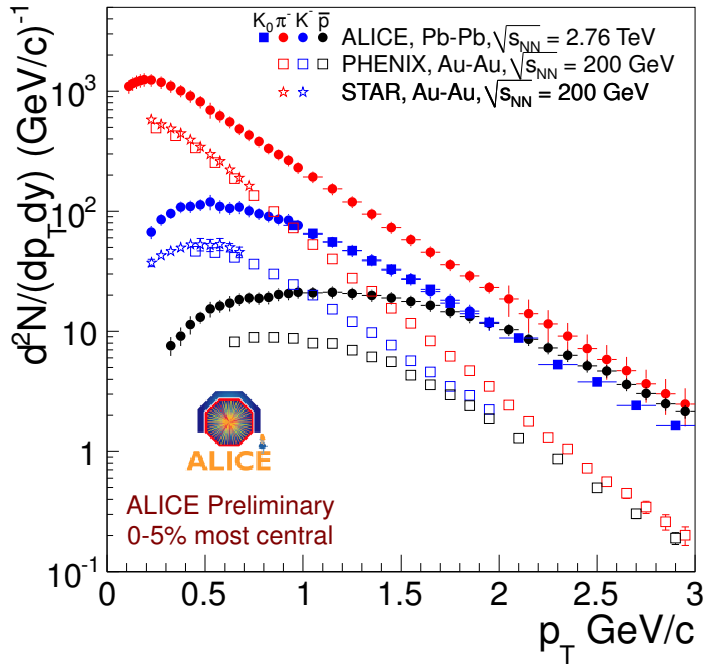


Figure 1.12: A comparison between $1/(2\pi p_t)(d^2 N_{ch})/(dy dp_t)$ for identified negatively charged particles as seen in ALICE LHC data and PHENIX and STAR RHIC data. ALICE observes a higher particle yield at higher p_t , particularly for protons. This is due to a strong radial flow at 2.76 TeV as compared to 200 GeV.[19]

particles. As different hadrons hadronize at different times, a difference in R_{AA} for identified particles can give important information about the evolution of the system. An example of this is J/Ψ suppression. Since the J/Ψ is composed of two charm quarks it is created at the very early times after the collisions[25]. However, further discussion about R_{AA} of the J/Ψ and other identified particles is beyond the scope of this thesis.

1.5 Jet Quenching

An extreme example of the suppression mentioned above is seen in the analysis of jets. A jet is a high p_t quark or gluon, which fragments into a number of highly correlated hadrons. Dihadron azimuthal correlations can be used to observe jets. The idea is that if two jets are created near the fireball edge, one is emitted away from the fireball, while the other traverses the medium and appear on the other side. This is true in both pp and d+Au collisions, but not in Au+Au collisions at RHIC. An example of a dihadron azimuthal correlation analysis is shown in figure 1.14. The red points from d+Au collisions, the black line from pp collisions and the blue points from Au+Au collisions show a peak at $\Delta\phi = 0$, this is the near side jet³, which is emitted away from the fireball. At $\Delta\phi = \pi$ only d+Au and pp data shows a peak. This means the away side jet does not appear in Au+Au collisions [27]. The theory is that the jet is completely 'quenched', i.e. it loses all its energy while traversing the medium. The same effect has recently been seen at the LHC in Pb+Pb collisions [28].

³In pp and d+A collisions where there are two jets either one of them can be called the near side jet. In A+A collisions where only one jet is found it is then dubbed the near side jet.

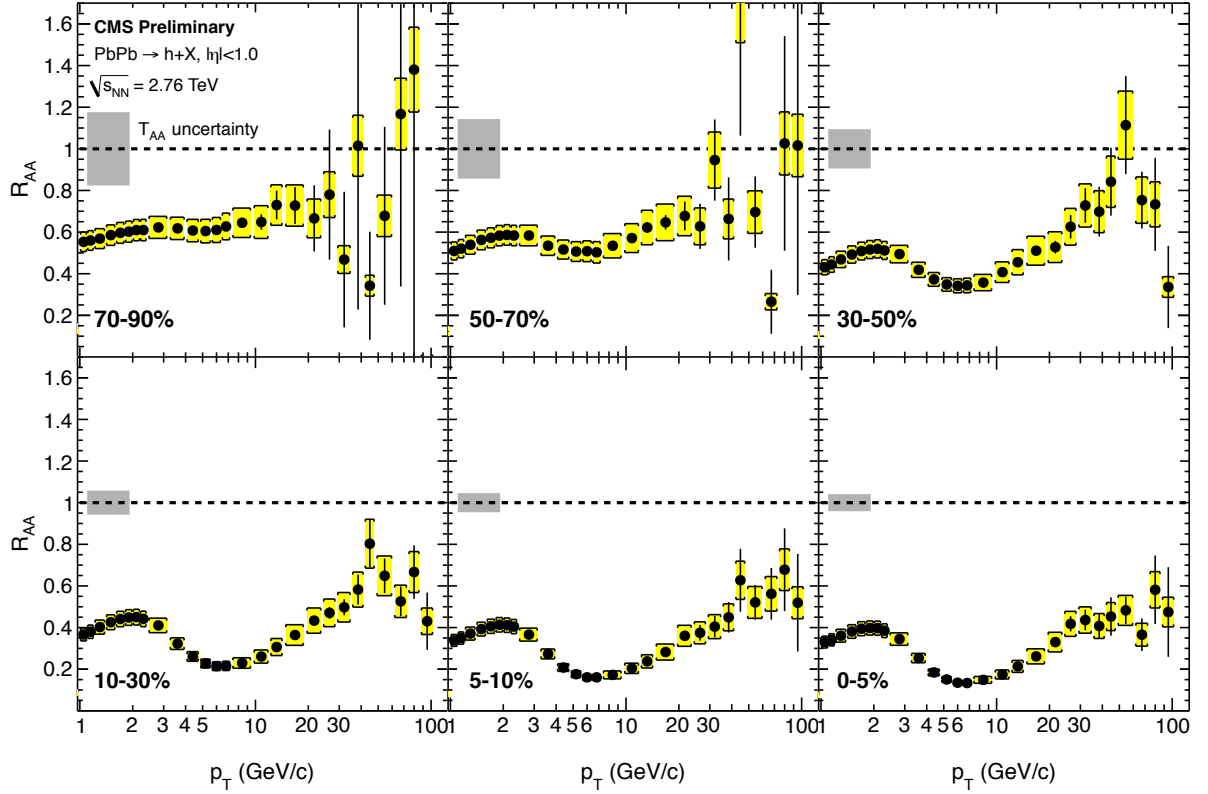


Figure 1.13: The nuclear modification factor (defined in equation 1.7) as a function of p_t at different centralities. A clear suppression in the high p_t transverse particle production is seen with a higher suppression for more central events. The effect is understood as high p_t particles having a strong interaction with the coloured medium. [26]

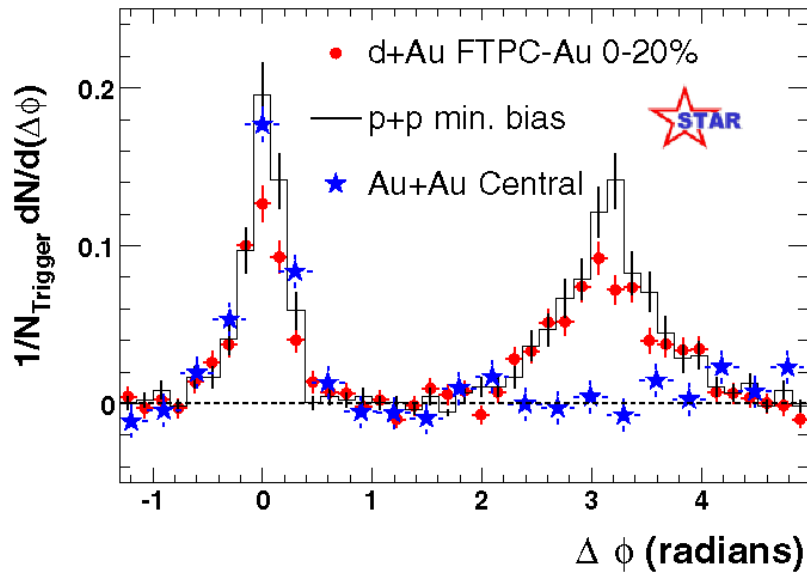


Figure 1.14: Jet quenching observed in dihadron azimuthal correlations. Only the near side peak (jet) is observed in Au+Au collisions, while an away side peak (jet) is observed in d+Au and pp collisions [27].

Chapter 2

Flow

This chapter covers the main topic of this thesis, which is flow. First flow in the context of heavy ion collisions is defined. This gives a motivation for measuring the elliptic flow component, v_2 . Then a section is devoted to azimuthal correlation analysis and in particular "the ridge and the Mach cone" is explained. Recently this phenomenon has been linked to higher order flow components [29]. This is used as a motivation for measuring higher order flow, and recent results of such measurements are presented. Finally the last part of the chapter is devoted to elliptic flow, as it is the main focus of this work. Results are shown for v_2 vs. a number of observables and relevant models are presented. This chapter concludes the physics motivation of this work, and the coming chapters are concerned with the experimental setup and data analysis.

Since the beginning of high energy heavy ion physics, hydrodynamics has been used as an important tool in the description of collective phenomena in the collision [30]. One of the experimental signals of the hydrodynamic behaviour of a quark-gluon liquid is azimuthal anisotropies [31]. The reason for this is found by looking at the geometry of a heavy ion collision. This has already been done in Section 1.2.1. However, in order to understand why an anisotropy in the particle yield develops, it is necessary to look at it again, but from a different perspective. This is done in figure 2.1, where a collision is shown in the transverse plane. It is seen that the participant particles are initially confined to an almond shaped region, tilted with respect to the horizontal plane by the reaction plane angle, Ψ_R . This initial spatial anisotropy leads to a pressure gradient, and the outward pressure along the minor axis becomes larger than the outward pressure along the major axis. This leads to an anisotropy in the particle yield i.e., there is a higher particle yield in the direction of the minor axis of the almond.

2.1 Fourier Series Expansion

Originally azimuthal anisotropy analysis was done using directivity and sphericity tensor analysis, but in 1994 it was suggested by Voloshin and Zhang to use a Fourier series expansion instead [32]. Fourier series are series of cosine and sine terms, and are very useful when describing periodic functions. They also constitute a very important tool when solving problems that involve ordinary or partial differential equations. A function, f , is said to be periodic, if there is any positive p such that [33]:

$$f(x) = f(x + p) \quad (2.1)$$

The number p is then said to be the period of f . Practically any periodic function can be described by a trigonometric series of the form [33]:

$$a_0 + \sum_{n=1}^{\infty} (a_n \cos nx + b_n \sin nx) \quad (2.2)$$

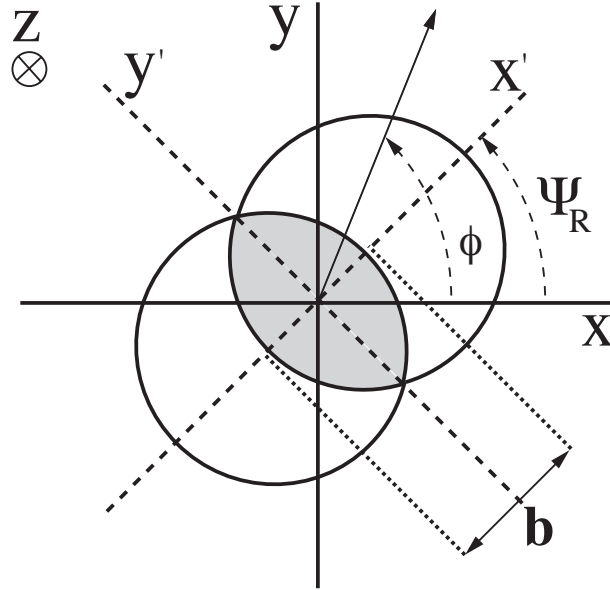


Figure 2.1: Schematic view of a non-central nucleus-nucleus collision in the transverse plane. Ψ_R denotes the reaction plane angle.

It can be shown that the coefficients of such as series can be found with the so-called Euler formulas:

$$\begin{aligned}
 a_0 &= \frac{1}{2\pi} \int_{-\infty}^{\infty} f(x) dx \\
 a_n &= \frac{1}{\pi} \int_{-\infty}^{\infty} f(x) \cos nx dx \\
 b_n &= \frac{1}{\pi} \int_{-\infty}^{\infty} f(x) \sin nx dx
 \end{aligned} \tag{2.3}$$

The results of these formulas are called Fourier coefficients. And the trigonometric series with these numbers as coefficients are called the Fourier series of $f(x)$ [33].

2.2 Anisotropic Azimuthal Flow

The different orders of anisotropic flow are characterized by coefficients in the Fourier expansion of the azimuthal dependence of the invariant yield of particles, relative to the reaction plane [32]:

$$\begin{aligned}
 \frac{d^3N}{dp_t^2 d\phi dy} &= \frac{1}{2\pi} \frac{d^2N}{p_t dp_t dy} \left(1 + \sum_{n=1}^{\infty} 2v_n \cos[n(\phi - \Psi_R)] \right) \\
 &= \frac{1}{2\pi} \frac{d^2N}{p_t dp_t dy} (1 + 2v_1 \cos(\phi - \Psi_R) + 2v_2 \cos 2(\phi - \Psi_R) + \dots)
 \end{aligned} \tag{2.4}$$

where ϕ is the azimuthal angle. v_1 is called directed flow, v_2 is called elliptic flow, v_3 is called triangular flow and so on. Until recently only directed and elliptic flow had been analysed in detail, and some analysis had been done on v_4 [34]. But now all moments up to v_6 are considered to be important [35]. More on this in Section 2.4.

At the LHC v_1 is essentially 0, while at RHIC it was shown to have an odd dependence on rapidity. Recently Teaney and Yan has suggested that v_1 may have an even rapidity part also

STAR Au+Au 0-10%

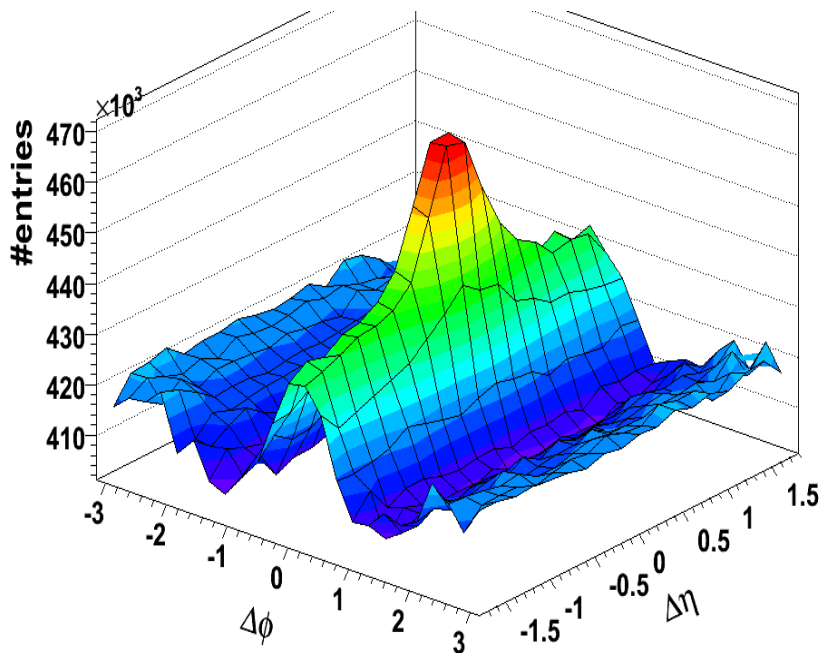


Figure 2.2: The ridge and Mach cone. [41]

[36], and this is currently a topic of great interest in the flow community [37]. However, the focus in the rest of the chapter is on the higher orders.

2.3 Azimuthal Correlations

Azimuthal correlations have already been described in jet quenching in section 1.5. The two-particle azimuthal correlations are measured by calculating:

$$C(\Delta\phi, \Delta\eta) \equiv \frac{N_{mixed}}{N_{same}} \cdot \frac{N_{same}(\Delta\phi, \Delta\eta)}{N_{mixed}(\Delta\phi, \Delta\eta)} \quad (2.5)$$

where $N_{same}(\Delta\phi, \Delta\eta)$ and $N_{mixed}(\Delta\phi, \Delta\eta)$ are pair distributions from the same and mixed events, respectively and $\Delta\phi = \phi_{trig} - \phi_{assoc}$ [38],[39]. Where ϕ_{trig} is the azimuthal angle of the jet trigger particle, and ϕ_{assoc} is the azimuthal angle of the particles associated with the trigger particle. The RHIC experiments found the structure shown in figure 2.2. Most noticeable is the peak around $\Delta\phi = 0$ and $\Delta\eta = 0$. This is consistent with jet fragmentation. But there is also a rise for all values of $\Delta\eta$ along $\Delta\phi = 0$, this is known as the ridge. Around $\Delta\phi \approx \pi$ two bumps are seen, until recently they were interpreted as various jet-medium modifications e.g., Mach cones [39]. Now they are understood to be manifestations of triangular flow, which is discussed in the next section.

Interestingly CMS has seen the same features in high multiplicity ($M > 110$) pp collisions at $\sqrt{s} = 7$ TeV for particles with $1 \text{ GeV} < p_t < 3 \text{ GeV}$ [40]. There are no conclusions on this yet, but it suggests that either there is a relatively large, strongly interacting medium in these pp collisions, or maybe the underlying physics is different than from A+A collisions, even if the correlations look similar.

2.4 Higher Order Flow

By looking at a $\Delta\eta$ slice away from the jet peak, or by only looking at low p_t particles inside it, the away side peaks become more pronounced. This is clearly seen with the blue data points in figure 2.3. Also in the figure is a red line, representing the sum of the measured moments from two to five. Decomposing the ridge and Mach cone in flow moments was first suggested by Alver and Roland [29], and has since been done by PHENIX[42], ATLAS[43], ALICE[44] and CMS[35]. This means the ridge and cone are not artifacts of jet-medium interaction, but is a signature of the underlying geometry and fluctuations of the medium.

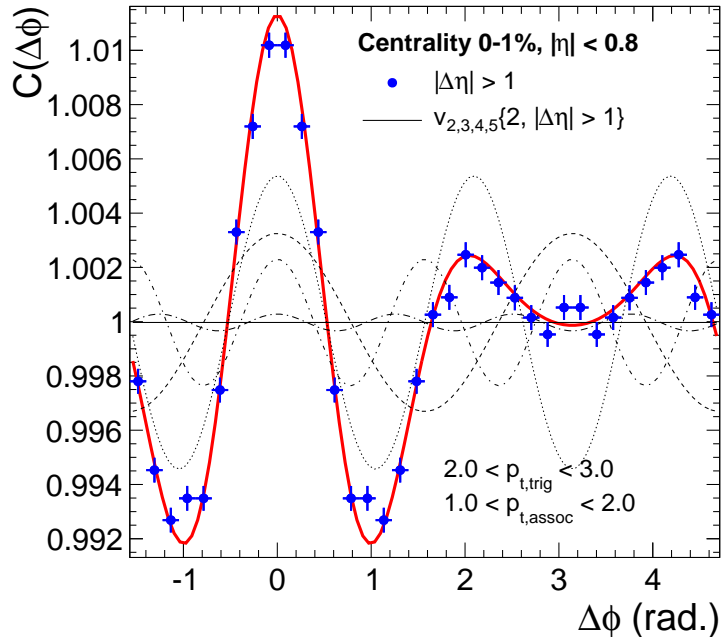


Figure 2.3: Blue data points are from two-particle azimuthal correlations with trigger particle with $2 \text{ GeV} < p_t < 3 \text{ GeV}$, and an associated particle with $1 \text{ GeV} < p_t < 2 \text{ GeV}$ for the 0 – 1% centrality class. The red line is the sum of the flow coefficients v_2 , v_3 , v_4 and v_5 . [44]

High p_t particles in jets still exhibit the same structure as in pp and d+A collisions, with the addition of jet quenching. This suggests that the above factorization does not hold for high p_t particles [38]. It is therefore necessary to look at the global fit (red line in figure 2.3) more closely. This is done in figure 2.4. The figure shows how well the azimuthal correlations are described by the flow moments for different trigger particle p_t and associate particle p_t . Figure 2.4(a) is for v_2 and figure 2.4(b) is for v_3 . Not shown here are the global fits for v_4 and v_5 , but they show the same structure as that of v_3 . The plots can be difficult to understand at first, so a little explanation is needed; the x -axis is divided into trigger p_t bins (blue), while each trigger p_t bin is divided into associate particle p_t bins (black). The trigger particle bins are responsible for the large structures in the top plots. The associate particle bins are responsible for the smaller substructures, which is mostly a rise towards the next large structure. The bottom plots shows the value of the azimuthal correlation divided by the combined v_n of the trigger and associate particles. As long as the data points are on the horizontal line crossing the y -axis at 1, the azimuthal correlations are well described by flow moments, and thus the flow moments give a good global fit. So $v_3 - v_5$ give good global fits for trigger and associate p_t all the way up for about 6 GeV. v_2 starts having problems a bit earlier at p_t around 4 GeV. Here the azimuthal correlations are much larger than the flow components. This can be understood as back-to-back jets, which the $n = 2$ correlations are particularly sensitive to.

It was made clear in the previous section why there is a v_2 moment; it followed directly from the almond shaped collision zone, which created a pressure gradient, which in turn created the azimuthal anisotropy in the particle yield. But what about the higher orders? It seems that the collisions is not as simple as the schematic in figure 2.1 suggests. The left panel in figure 2.5 shows a simulation of the nucleons in a $\sqrt{s_{NN}} = 2.76$ TeV Pb+Pb collision with the PHOBOS Glauber Monte Carlo. The right panel shows the same plot, but with shapes corresponding to flow moments laid on top. It is clear that the initial geometrical shape is not just elliptical. For the even moments v_2 and v_4 the direction is dictated by the participants plane, which is in essence still the almond. The odd moments v_3 and v_5 have directions uncorrelated with the participants plane. These moments are sensitive to initial state fluctuations i.e., "hot spots" in the overlap zone.

As mentioned above, most heavy ion experiments have now published results on higher order harmonics. All of the measured harmonics dependence on centrality is shown in figure 2.6 as measured by ATLAS. The elliptic flow is the largest, except for the most central events, where the triangular is a bit larger. In general $v_3 - v_6$ show a weak dependence on centrality, which is also what is expected, as they are not correlated with the eccentricity of the almond. The hexagonal flow is seen to be vanishingly small ($< 1\%$). The p_t dependence of v_2 to v_5 as measured by ALICE is shown in figure 2.7. All the moments rise with p_t .

2.5 Elliptic Flow

It is the goal of this thesis to present a measurement of the elliptic flow, v_2 , as a function of pseudorapidity. In the previous sections it was mentioned that elliptic flow has been measured in heavy ion collisions for a long time. This is perhaps best illustrated by figure 2.8, which shows elliptic flow measurements from almost every heavy ion experiment in the last 25 years. Most notably E877 and E895 from the BNL Alternating Gradient Synchrotron (AGS). NA49 from the CERN SPS. And PHENIX, STAR and PHOBOS from RHIC, and ALICE from LHC. The v_2 shown is integrated over all p_t and measured in the 20 – 30% centrality bin. Notice the negative values around $\sqrt{s_{NN}} = 2$ GeV, these are due to shadowing effects[8] from the spectator nucleons on the produced particles. At higher energies the spectators are gone before they can have any shadowing effect, and v_2 becomes positive again. A flattening of the energy dependence happens around 20 GeV, and at the LHC the integrated v_2 is only about 30% higher than at RHIC, even though the $\sqrt{s_{NN}}$ energy is 14 times higher.

The centrality dependence of v_2 was already shown in figure 2.6. In figure 2.9 it is compared with RHIC results. The legend in the figure marks four different flow methods applied to the ALICE data. A discussion on methods for flow measurement is found in Chapter 5. In general the LHC points are 30% above the corresponding RHIC lines. The attentive reader will note that none of the ALICE points in the 20 – 30% centrality bin corresponds to the value seen in figure 2.8, this is because the points in figure 2.9 are only integrated over the $0.2 \text{ GeV} < p_t < 5 \text{ GeV}$ range, while they are integrated over all p_t in the previous plot [17]. For the most central events, where the almond shape is more of a circle shape, the elliptic flow is small. For more peripheral ones it becomes increasingly larger. For the most peripheral ($> 70\%$) the elliptic flow becomes slightly lower, this is likely caused by the energy density of the medium being smaller. [17]

2.5.1 p_t Dependence

The transverse momentum dependence of v_2 at the LHC is compared to RHIC results in figure 2.10. The ALICE points are almost identical to the STAR data, this suggests that a saturation has taken place, where the maximum elliptic flow has been achieved [17]. The reason

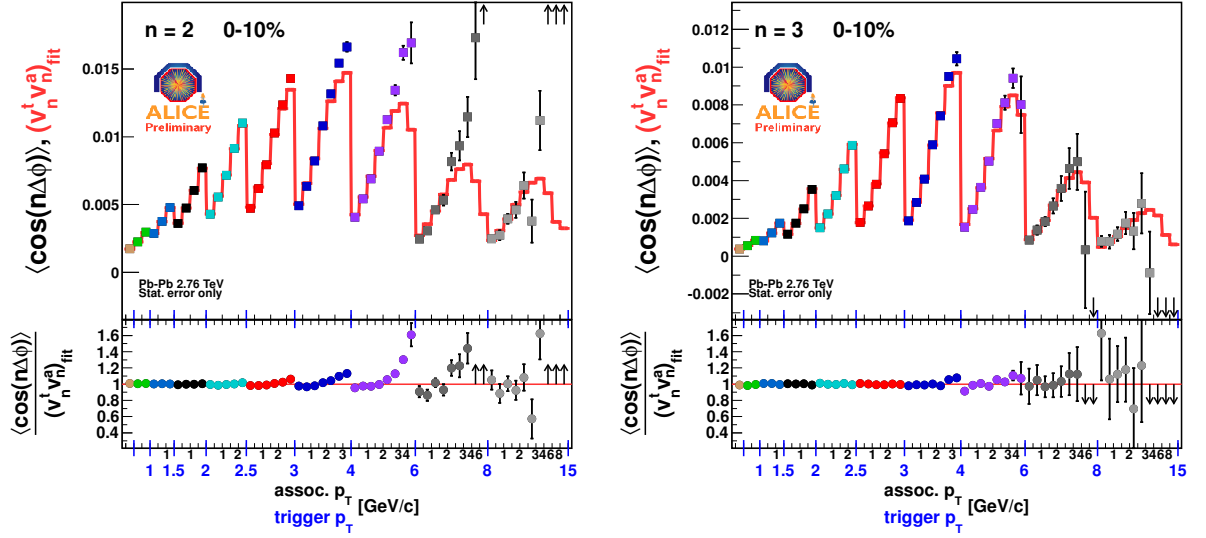
(a) Global fit for v_2 for different $p_{t,trig}$ and $p_{t,assoc}$.(b) Global fit for v_3 for different $p_{t,trig}$ and $p_{t,assoc}$.

Figure 2.4: These plots show how well the azimuthal correlations are decomposed into flow moments for different trigger and associate particle p_t . As long as the points are on the horizontal line in the bottom plots it is a good fit. v_3 is representative for v_4 and v_5 and they all start giving bad global fits around a trigger and associate p_t of 6 GeV. v_2 is showing problems already at $p_t = 4$ GeV. This can be attributed to back-to-back jets. Both plots are for the 0 – 10% centrality bin. [38]

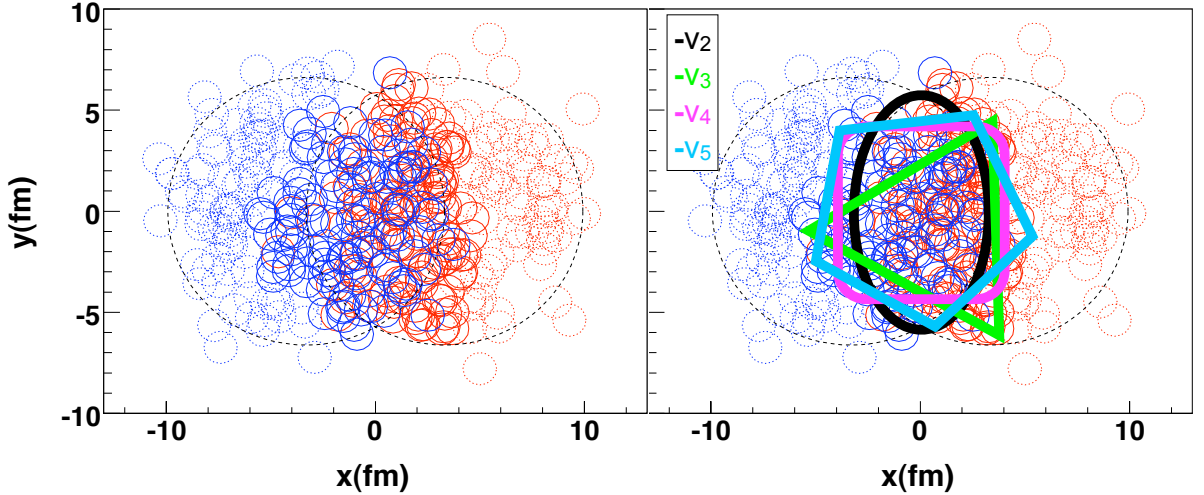


Figure 2.5: Left and right panel are plots from a simulated Pb+Pb collision at $\sqrt{s_{NN}} = 2.76$ TeV with the PHOBOS Monte Carlo Glauber [10]. Full circles are participating nucleons, dotted circles are spectator nucleons. In the right panel is the same plot, with shapes laid on top to visualize flow moments. It is shown that the fluctuations in the initial state give rise to more than elliptic shapes.

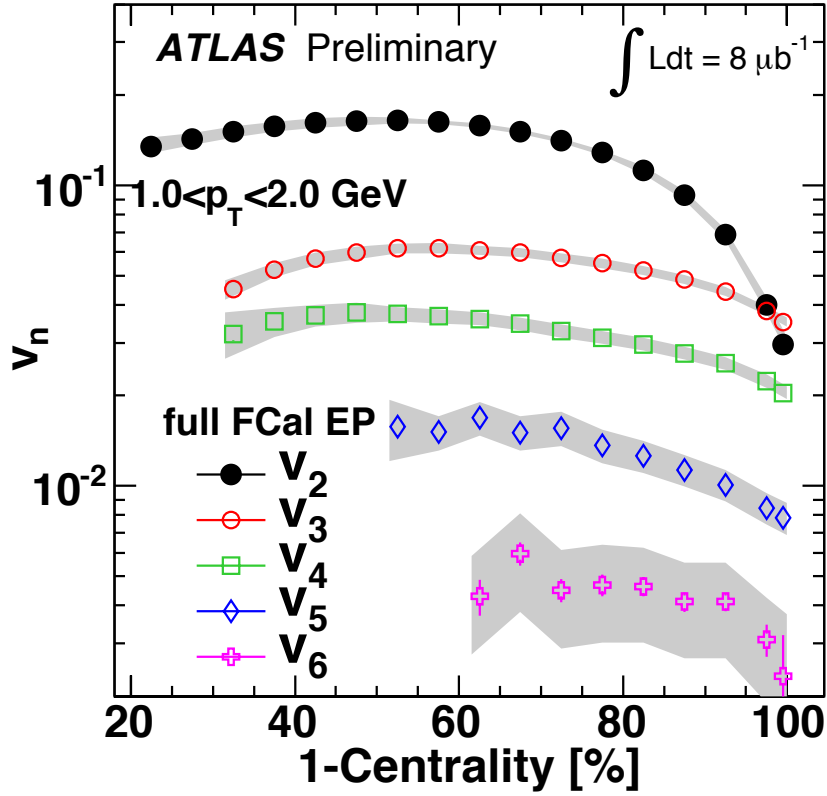


Figure 2.6: Centrality dependence of the second to sixth Fourier moment. A weak centrality dependence is observed for moments other than v_2 . [43]

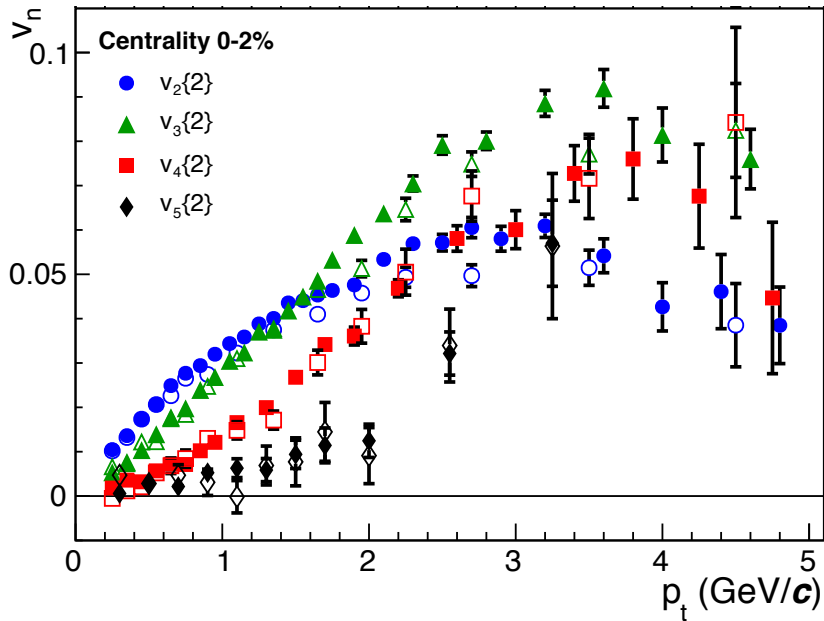


Figure 2.7: The p_t dependence of the second to fifth flow moment. The full (open) symbols are for $\Delta\eta > 0.2$ ($\Delta\eta > 1.0$). [44]

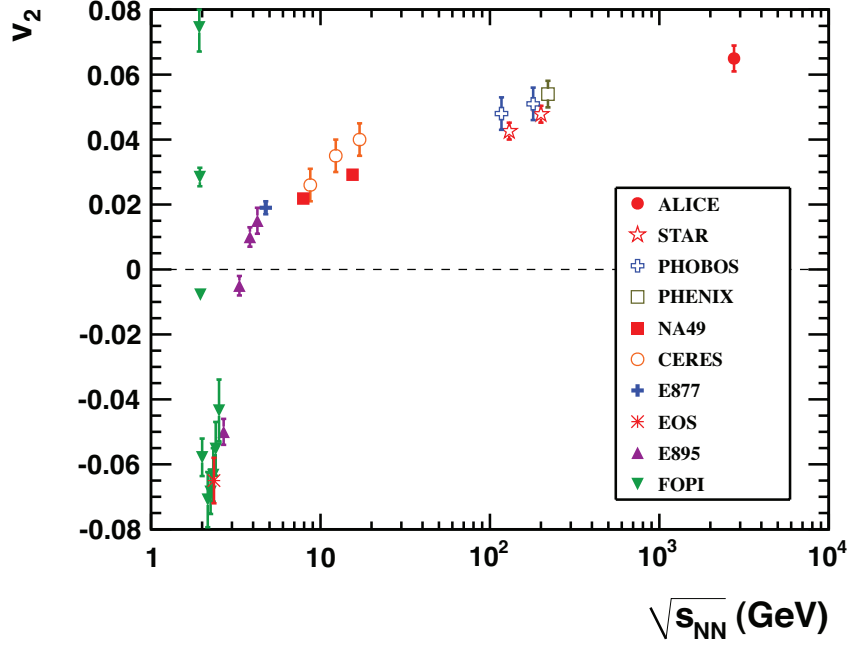


Figure 2.8: Elliptic flow for the 20 – 30% centrality class over a very wide center-of-mass range. The flow is integrated over all p_t . [17]

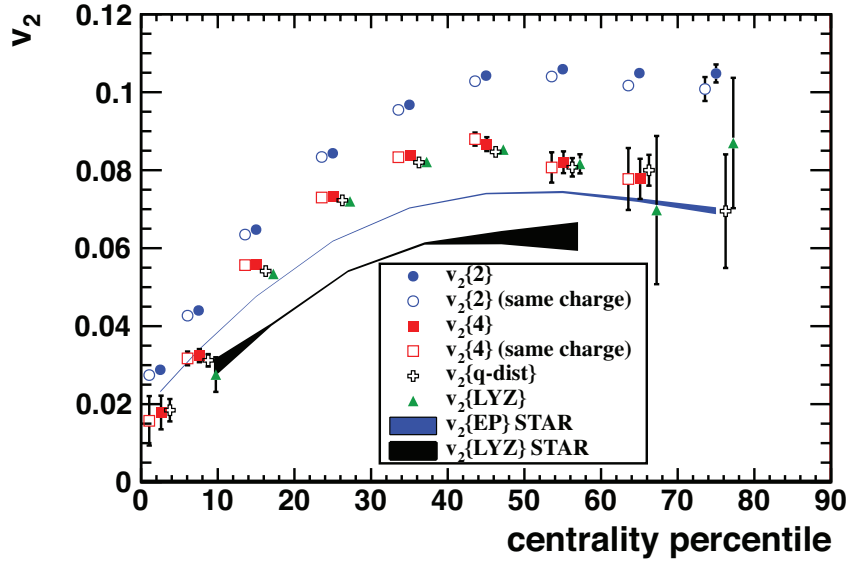


Figure 2.9: Elliptic flow as a function of centrality with ALICE (points), integrated over $0.2 \text{ GeV} < p_t < 5 \text{ GeV}$. A comparison with STAR is shown (lines). Different methods for flow analysis are shown, in general they can be divided into two groups; one is those that get higher when there are fluctuations and the other, those that get lower when there are fluctuations (for a more detailed discussion on flow methods see Chapter 5). In general the LHC points are about 30% higher than the corresponding RHIC lines. [17]

for why v_2 vs. centrality is almost 30% larger at LHC, when v_2 vs. p_t is almost identical is found in figure 1.11. At LHC the p_t spectrum is shifted towards higher p_t , than the corresponding spectrum at RHIC. So when the v_2 is integrated with respect to p_t , the higher p_t particles contribute more, and since they have higher v_2 , the integrated v_2 becomes larger [17].

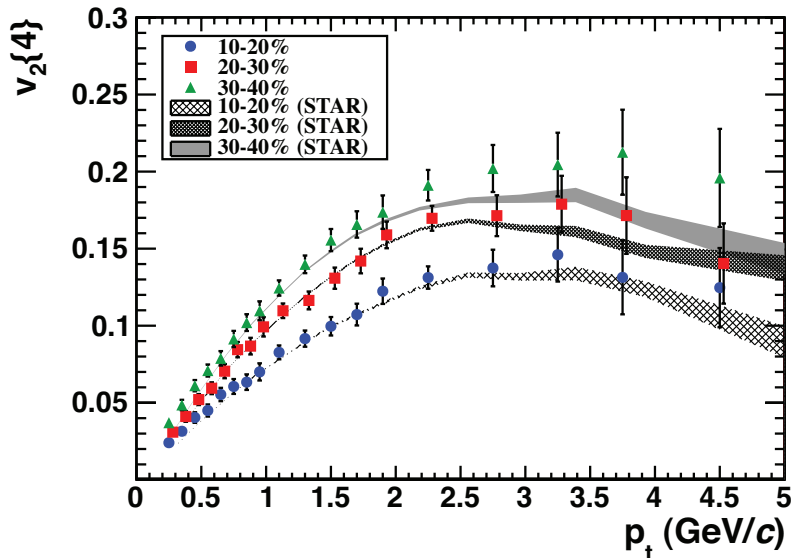


Figure 2.10: Elliptic flow as a function of p_t at the LHC and at RHIC. The dependence is almost the same, and it would seem that a saturation has taken place, where the maximum elliptic flow has been reached.[17]

The p_t dependence becomes even more interesting when looking at identified particles. One of the assumptions in all of this chapter has been that the flow develops before the quarks hadronise. The most convincing evidence of this is shown in figure 2.11. The top plot shows a number of identified particle v_2 vs. p_t data for different centralities. In the bottom plot the x -axis has been changed to show the kinetic transverse energy divided by the number of valence quarks, and the y -axis has been rescaled to show v_2 divided by the number of quarks times a geometrical factor ϵ . ϵ is used as a scale between the different system sizes obtained in different centralities. The convincing part is that while all the particles v_2 vs. p_t are different, they all fall into perfect agreement with these simple scalings. This strongly suggests that flow develops at the quark level, not at the hadron level.

2.5.2 η Dependence

In Chapter 8 $v_2(\eta)$ results are presented in a wide η -range for the first time at the LHC. This section covers previous wide η -range analyses at lower energies and the small η -range analyses done by ATLAS and CMS at LHC. The η dependence of the elliptic flow gives important information about the longitudinal expansion of the created medium. If the elliptic flow drops off quickly with η i.e., it is peaked around $\eta = 0$, it is a sign of the QGP having a very limited longitudinal expanse, and being mostly limited to the two-dimensional (x, y) -plane. Likewise a flat v_2 vs. η is a sign of the QGP extending along the beam direction, i.e. it is large enough to affect particles in both the x -, y - and z -direction. More on this in the next section, where various models are presented.

In figure 2.12(a) the pseudorapidity dependence of the elliptic flow is shown for Au+Au collisions at four different energies for the 0 – 40% centrality bin averaged over all p_t . All the distributions show a similar peak at mid-rapidity and then a linear drop in both the forward and backward directions. Figure 2.12(c) shows the same plots for Cu+Cu collisions at two different

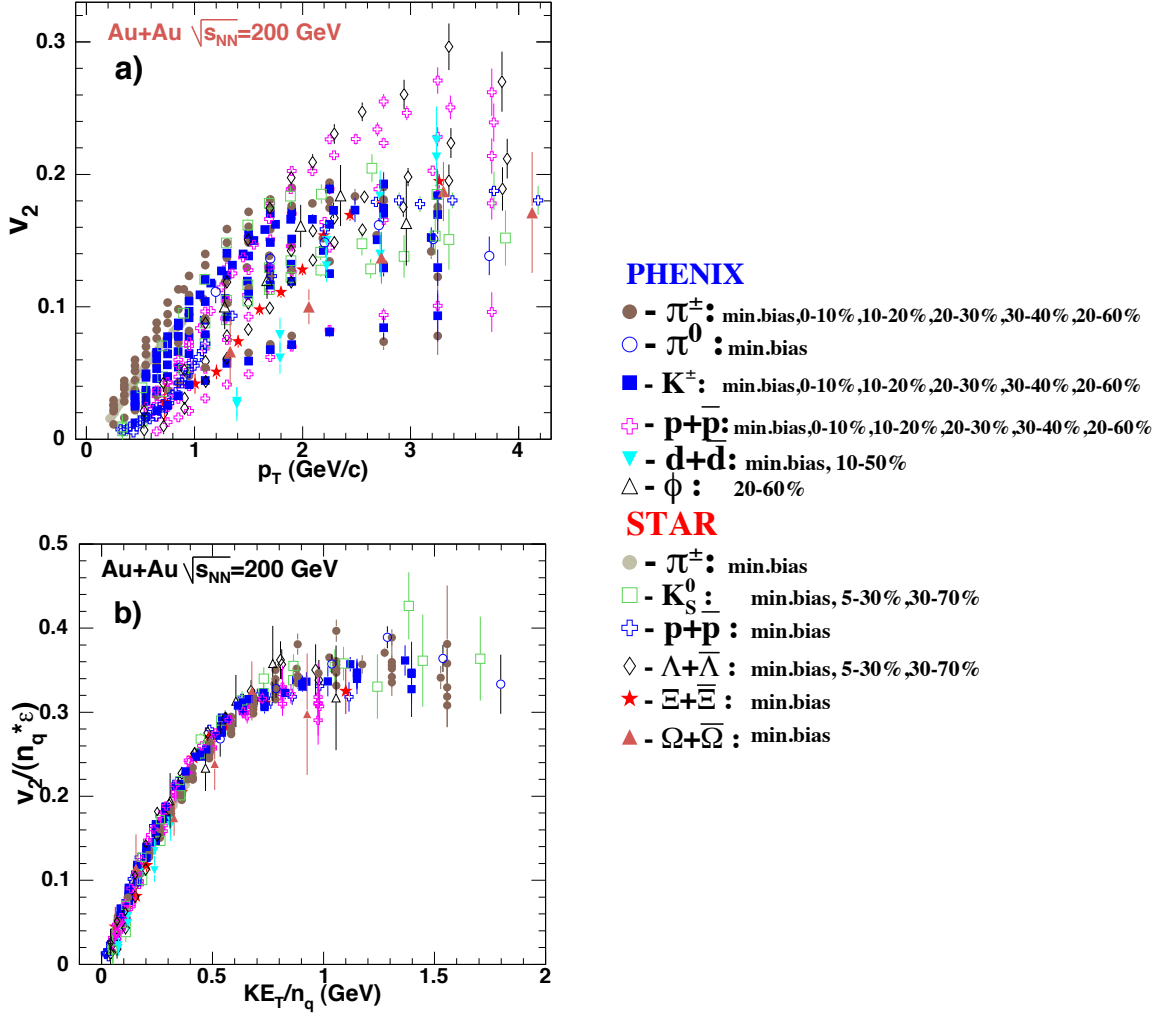
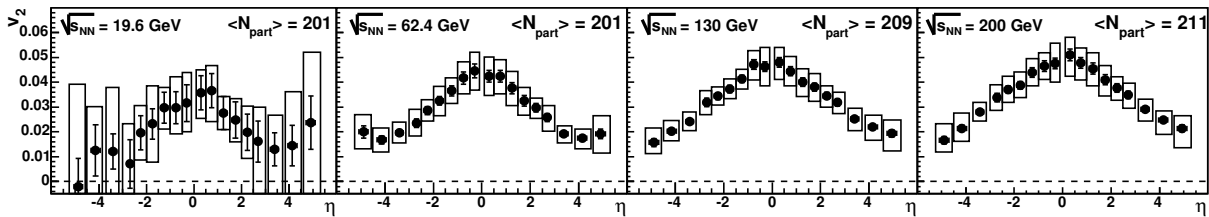


Figure 2.11: Top left: Elliptic flow as a function of p_t for a number of different identified particles and centralities. Bottom left: Same as above, but with a rescaling of the axes. The x -axis has been changed to kinetic transverse energy, KE_T , and divided by the number of valence quarks, n_q . The y -axis has been divided by the number of valence quarks and a geometrical factor, ϵ , which comes from the difference in eccentricity at different centralities. This causes all the data points to align nicely. [45]

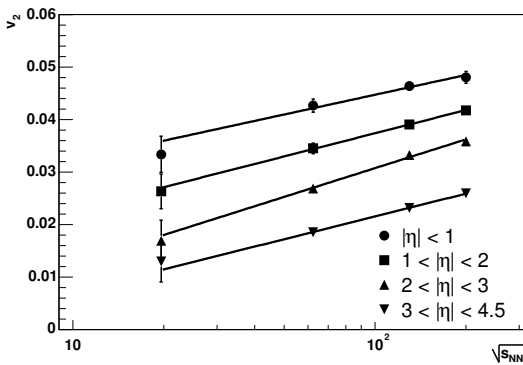
2.5 Elliptic Flow

energies, and compares them to the 200 GeV Au+Au collision in figure (a). The same shape is seen, but the Cu+Cu data is a bit lower. This suggests that v_2 scales with system size.

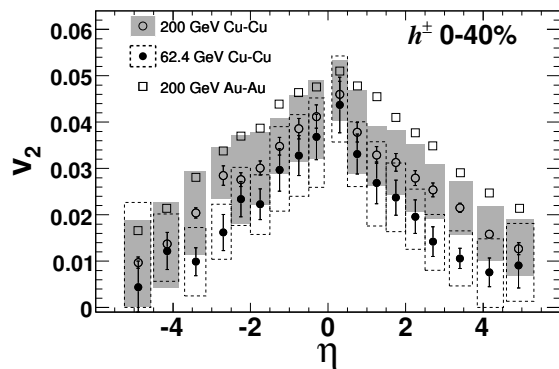
The logarithmic dependence of v_2 on energy was already shown in figure 2.8, in figure 2.12(c) it is shown to also be present for particles not at mid-rapidity.



(a) Pseudorapidity dependence of v_2 in Au+Au collisions at four different energies. Data points are averaged over the 0 – 40% most central events. By PHOBOS [46].



(b) Same data as above, this time presented as a function of $\sqrt{s_{NN}}$ for different η -bins [46].



(c) Pseudorapidity dependence of v_2 in Cu+Cu at two different energies, compared with the 200 GeV Au+Au data also seen above. Also average over the 0 – 40% most central events. By PHOBOS [47].

Figure 2.12: Different representations of elliptic flow as a function of pseudorapidity at various energies and system sizes. All plots are for the 0 – 40% centrality bin and integrated over all p_t . All distributions have a peak at mid-rapidity. The magnitude of the flow scales with energy and system size in a similar manner at all pseudorapidities.

Interestingly STAR data does not seem to agree with the PHOBOS data presented above. In figure 2.13 two STAR measurements for Au+Au collisions at $\sqrt{s_{NN}} = 200$ GeV show a flat pseudorapidity dependence at mid-rapidity. The centrality bin is the same as in the PHOBOS plots, but the integrated p_t range is only 0.15 to 2.0 GeV. But this should not have such a large effect, as by far most of the particles are covered in this interval. It is difficult to draw any conclusions when the only two measurements available do not agree, but it is worth noting that within the systematic error bars, the PHOBOS data could be flat too. In another paper PHOBOS does see a flat dependence at mid-rapidity for the 3 – 15% most central events [48]. So while there is a clear peak for $\sqrt{s_{NN}} = 19.6$ GeV to 130 GeV, there may be a small flat area at mid-rapidity for 200 GeV.

PHOBOS has looked at v_2 vs. η in the rest frame of one of the colliding nuclei, as seen in figure 2.14. It is observed that in this case the elliptic flow is independent of energy over the entire rapidity range.

ATLAS and CMS have also measured the elliptic flow coefficient as a function of pseudorapidity. Both experiments have reported a flat elliptic flow in the pseudorapidity range -2.5 to 2.5 for the 50% most central events, as can be seen in figure 2.15. Beyond 50% there is

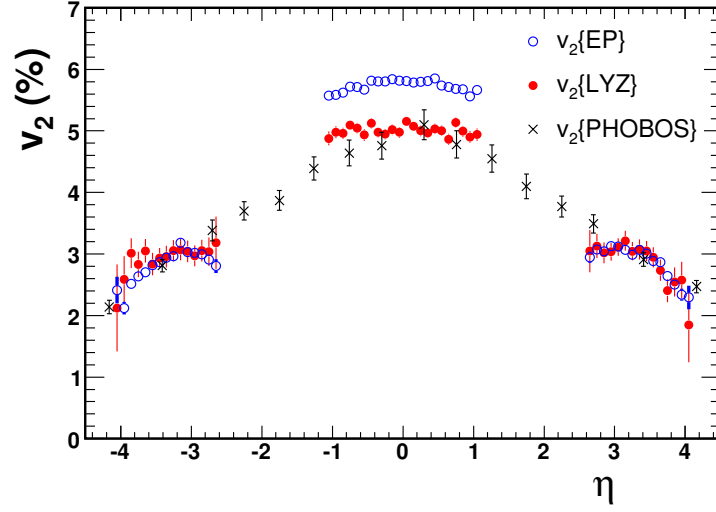


Figure 2.13: Elliptic flow as a function of pseudorapidity as measured by the STAR and PHOBOS experiments in Au+Au collisions at $\sqrt{s_{NN}} = 200$ GeV for the 40% most central events. The data points are integrated over p_t from 0.15 to 2.0 GeV [49]

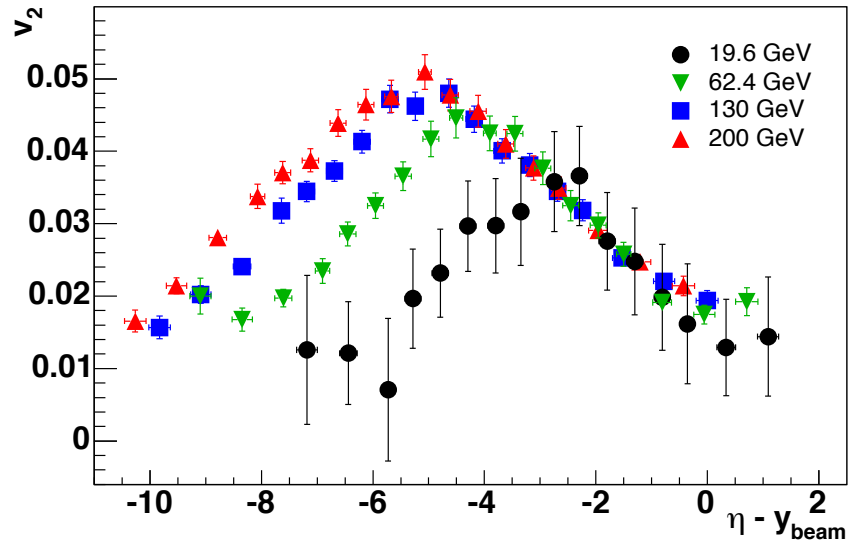


Figure 2.14: Pseudorapidity dependence of elliptic flow seen in the rest frame of one of the colliding nuclei. By PHOBOS [46].

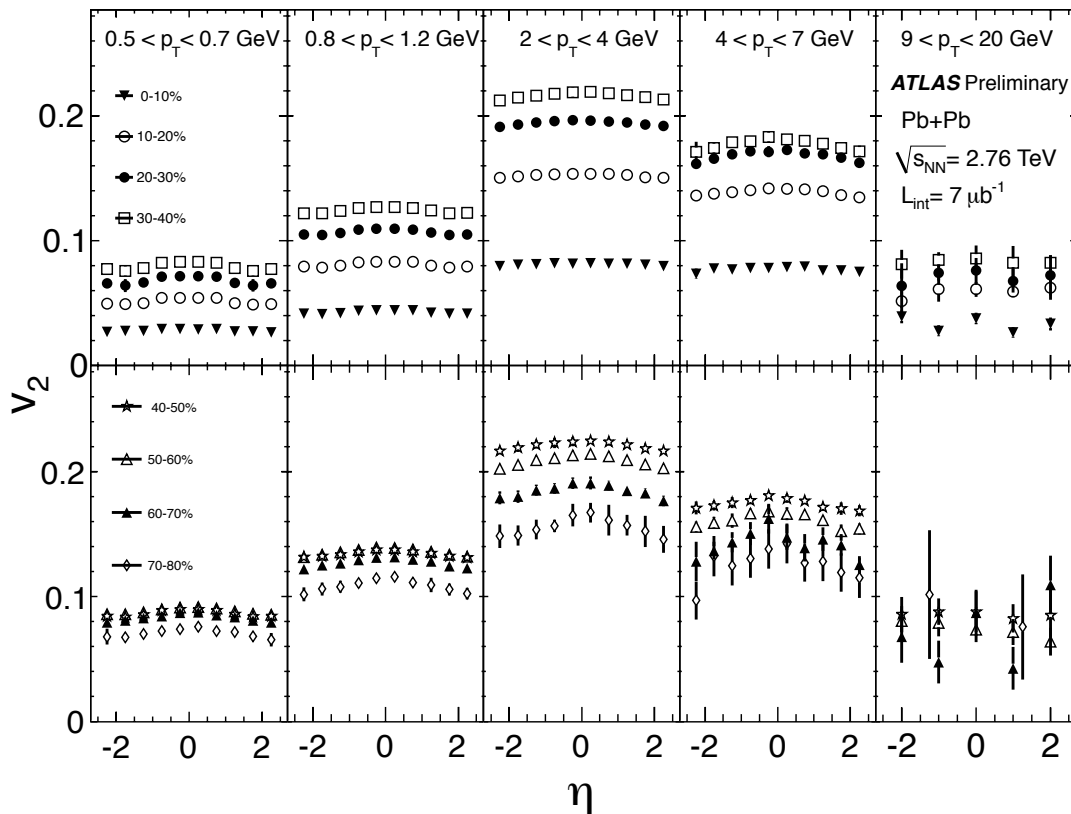


Figure 2.15: Elliptic flow as a function of pseudorapidity in Pb+Pb collisions at $\sqrt{s_{NN}} = 2.76$ TeV. [43]

an η dependence, which is similar to the one seen at RHIC. These are the first plots of the pseudorapidity dependence of elliptic flow at $\sqrt{s_{NN}} = 2.76$ TeV in Pb+Pb collisions. That the elliptic flow has a small pseudorapidity dependence at LHC energies suggests that the flat shape observed by STAR at $\sqrt{s_{NN}} = 200$ GeV is likely more true than the peak in the PHOBOS data. The results from this thesis will almost double this coverage, and show a v_2 measurement down to $\eta = -3.75$ and up to $\eta = 5$. With this measurement it is possible to make a plot similar to figure 2.14 and see if indeed it still holds at forward rapidities at the LHC.

2.5.3 Model Predictions

There are two views on how an A+A collision can take place. One takes the approach of "stopping", this is illustrated in figure 2.16. In this case the participants of the two nuclei stop at the collision point, and the longitudinal expansion happens via the fireball from this point. In this case elliptic flow has a limited longitudinal expansion, and this could be what is observed in RHIC data.

The other approach is transparency, which is shown in figure 2.17. In this case the participants in the nuclei will continue through the oncoming nucleus, creating a strong colour field between the two. In this case the fireball has an initial longitudinal component, and the elliptic flow has less pseudorapidity dependence. This is more consistent with the recent results from ATLAS and CMS.

Of course both of the above approaches are crude simplifications of what might be going on. Most of the results from RHIC can also be described by relativistic hydrodynamical calculations. Many of the models that gave a good description of the first measurements at mid-rapidity failed

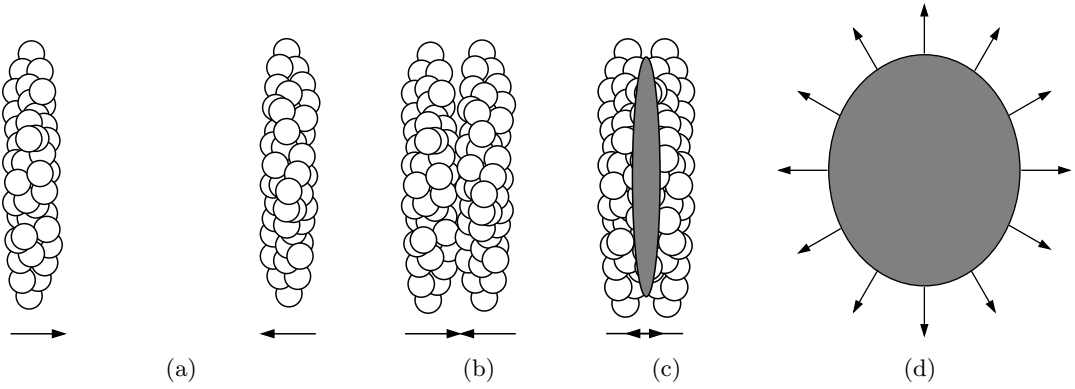


Figure 2.16: Stopping in a heavy ion collision.

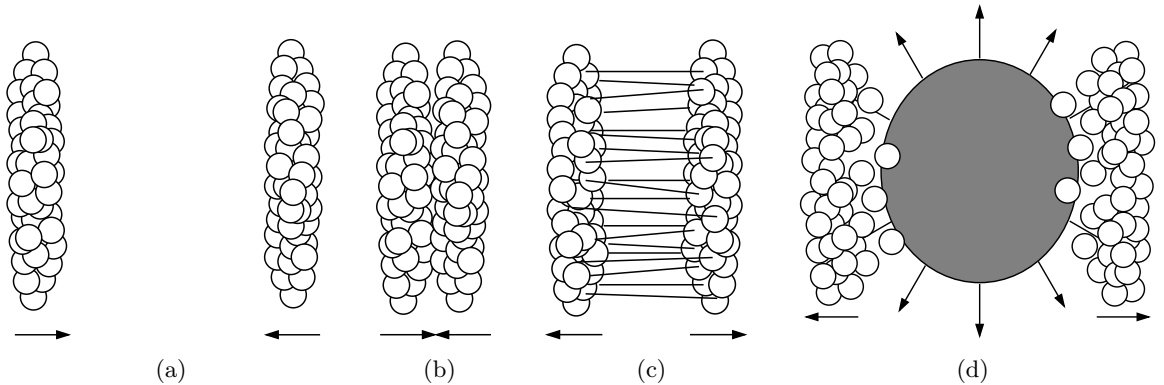


Figure 2.17: Transparency in a heavy ion collision.

to describe the observed pseudorapidity dependence, although some models did claim to succeed by using ideal hydrodynamics [50], [51]. An example of this is the Buda-Lund model, which has been used to describe the data from PHOBOS (see figure 2.18). According to the authors of the paper, this model provides good fits to the data. The model appears to have a flattening of the dependence around mid-rapidity, which becomes wider at higher energies. This seems to be consistent with the experimental data. It could be interesting to see what the model predicts for LHC energies.

The next prediction is not a model, but an extrapolation from lower energies to LHC design energy. The extrapolation is done by using the $\ln(\sqrt{s_{NN}})$ dependence from RHIC to extrapolate out to $\sqrt{s_{NN}} = 5.5$ TeV for the pseudorapidity dependence observed by PHOBOS [52]. This is done by shifting the data in η according to how y_{beam} scales with energy. The result is shown in figure 2.19. The plot suggests that at forward rapidities there should be a pseudorapidity dependence similar to the one seen at RHIC. The extrapolation is done to $\sqrt{s_{NN}} = 5.5$, if it was done to 2.76 TeV instead the points would not be shifted as much in η , and the rapidity dependence would start at smaller η . This means that with the coverage of the analysis presented here, it should be possible to observe.

2.6 Flow Fluctuations and Non-flow

This section is about flow fluctuations and non-flow. Both are effects that bias the measured flow values, if not taken into account. Elliptic flow in particular is sensitive to non-flow.

There are several sources of flow fluctuations. One is if the centrality binning is too coarse. In this case events with different flow are analysed together, and when averaged over to extract

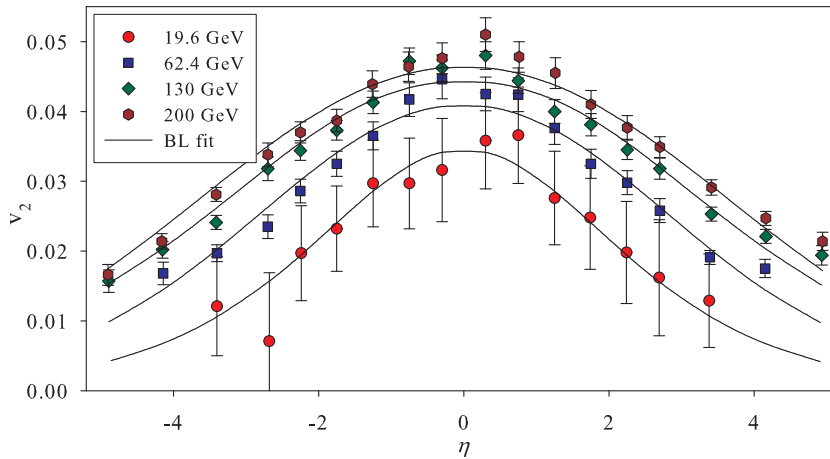


Figure 2.18: Fits to PHOBOS v_2 data from the Hydrodynamical Buda-Lund model [50].

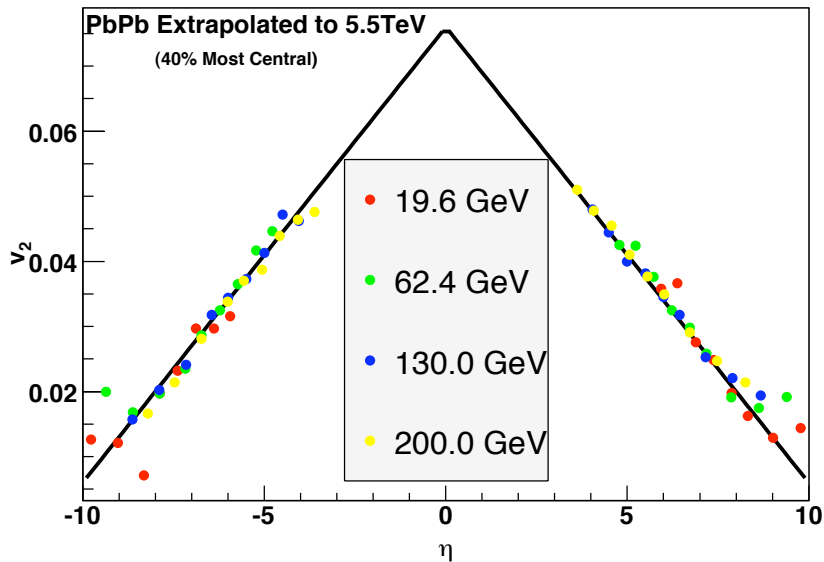


Figure 2.19: Extrapolation from RHIC data to LHC design energy [52].

the actual value there may be a bias due to the centrality dependence of flow. Another cause is actual fluctuations in the initial geometry, such as those that create the odd flow harmonics [53]. Different flow methods respond differently to fluctuations. In general two particle correlation measurements overestimate the flow when there are fluctuations present. While multi-particle correlations underestimate the flow when there are fluctuations. [54]

Non-flow is a term used to describe azimuthal correlations that look like flow, but are in fact something else. There are several sources of non-flow. Most of these are related to elliptic flow, as they exhibit back-to-back behaviour, which is easily mistaken as elliptic flow. For a discussion on which methods are sensitive to non-flow see Chapter 5. One source of non-flow is resonance decays such as $\Delta \rightarrow p\pi$ or $\rho \rightarrow \pi\pi$. In these cases the decay products are highly correlated due to momentum conservation. The Hounsfield-Brown-Twiss effect is also known to cause quantum correlations, which may contribute to elliptic flow measurements. Finally, jet fragmentation creates many particles that are highly correlated in a back-to-back structure. The

non-flow contribution scales as $1/N$, where N is the multiplicity. This means it is negligible in the most central events, but quite important for the most peripheral [55].

In figure 2.9 two different measurements of v_2 are presented. One uses two-particle correlations, the other uses four-particle correlations. The reason these do not overlap is due to flow fluctuations and non-flow. In general the four-particle correlations are not affected by non-flow, but as mentioned above it is lowered when there are fluctuations. The two-particle correlation method on the other hand is generally higher than the actual v_2 due to both non-flow and flow fluctuations (mathematical proof is given in appendix B). This is of course a problem when comparing to different models. A model may be developed to describe some collective behaviour, but not take into account resonance decays and fluctuations, in this case comparing to data is difficult. It is possible to estimate the contributions of fluctuations and non-flow [56]. And when the flow measurements are corrected for these, the different methods agree very nicely (see figure 2.20).

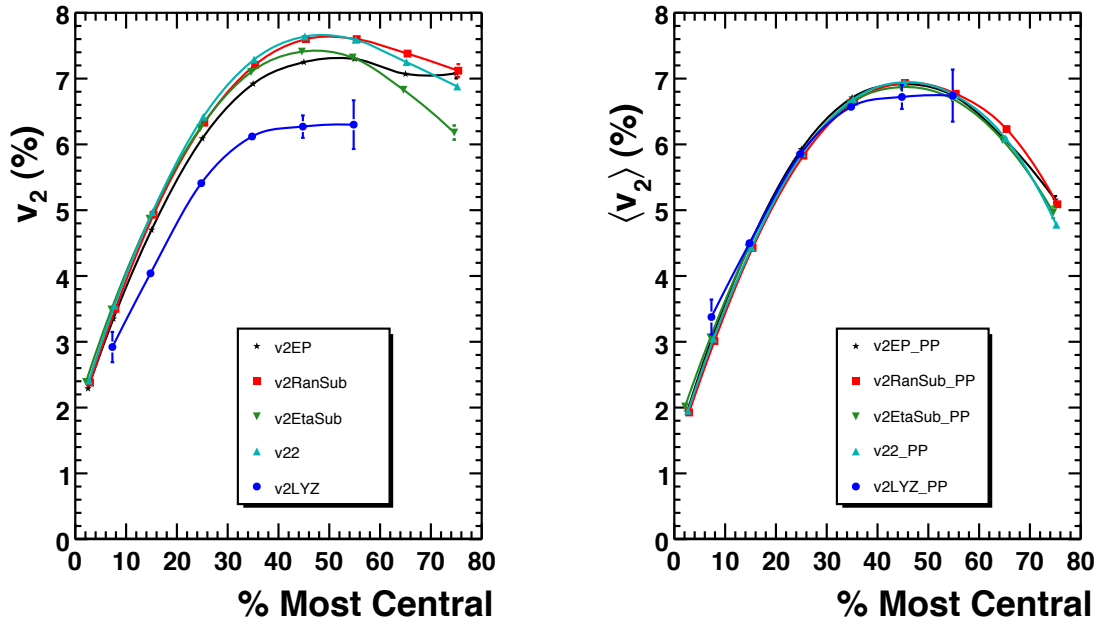


Figure 2.20: Left plot: Elliptic flow measurements in STAR using various methods. Each method has its own bias from fluctuations and non-flow. Right plot: The data is corrected for fluctuations and non-flow, and all the methods agree reasonably well. [56]

Chapter 3

Experiment

This chapter contains an overview of the experimental apparatus used for the analysis presented in this thesis. First facts about the LHC and CERN are presented to give an overview of the experimental facilities used. The particle beams' journey from laboratory to collision is described, leading to first a presentation of the four large LHC experiments and then a more detailed description of ALICE. Finally a more technical description of the three detectors of choice for this work is presented. The reconstruction of the data, from raw detector output to analysis ready data is left to the next chapter.

3.1 The Large Hadron Collider

The LHC is located at the European Organization for Nuclear Research (CERN). The LHC is the worlds largest and most powerful particle accelerator. Located on average 100 m below the surface, on the border between France and Switzerland. It is a circular accelerator with a circumference of 27 km. Currently the LHC has accelerated both protons and lead ions to collisions, though only with collisions between two proton beams or two ion beams. In late 2011 tests will be made to find out if it will be possible to collide a proton beam with an ion beam. Currently the LHC runs with proton beams nine months of the year and lead ion beams one month followed by two months of winter shut down.

Proton collisions has been carried out at centre of mass energies of $\sqrt{s} = 900$ GeV, 2.34 TeV, 2.76 TeV and 7 TeV. Lead collisions have been carried out at $\sqrt{s_{NN}} = 2.76$ TeV only. The accelerator is designed to do proton collisions at 14 TeV and lead collisions at 5.5 TeV.

Many of the old accelerators are still functioning and today they serve as helpers for the LHC. The impressive accelerator complex is shown in figure 3.1. This way the LHC receives the beams from the Super Proton Synchrotron (SPS) at an injection energy of 450 GeV per beam for protons.

Both protons and ions go through 4 steps before being injected into the LHC ring. They both start at a linear accelerator facility, LINAC 2 for protons and LINAC 3 for ions. From the linear accelerator they are injected into a circular accelerator, BOOSTER for protons and Leir (Low energy ion ring) for ions. The rest of the journey is the same for protons and ions. They are injected into the Proton Synchrotron (PS), from which they are injected to the SPS.

3.1.1 The Four Experiments

The beams collide on four points along the ring. On each of these point a major experiment is set up. There are two general purpose experiments, ATLAS (A Toroidal Lhc ApparatuS) and CMS (Compact Muon Solenoid). They are the largest of the four. Their main purpose is to find new particles, mainly the elusive Higgs particle, but also other heavy particles such as

those predicted by supersymmetry and other models describing new physics beyond the Standard Model. The LHCb experiment is designed to look at CP-violation in bottom quark decays, since most bottom quarks are produced at large rapidity it only covers a small area along the beam pipe, and only on one direction from the interaction point. Finally there is ALICE (A Large Ion Collider Experiment) which is designed specifically to look at heavy ion collisions. ALICE is described in detail in the next section.

Although ATLAS and CMS are designed for discovering new particles, they also have a heavy ion programme. Likewise ALICE also takes data and publishes proton physics analysis results, although ALICE will never be able to do the detailed analysis required to find a Higgs or any other elusive new particle. Only LHCb is limited to proton physics, and is thus turned off during the one month of each year where the proton beams are replaced with lead ion beams.

The reason for having several experiments that measure the same thing is one of the basic requirements for good science: Reproducibility. If the ATLAS collaboration finds a Higgs particle at some mass, then CMS better be able to see it too. Otherwise chances are that it is not really a Higgs ATLAS sees, but an artefact of poor understanding of their detector. The LHC experiments are very complex detectors and it is only too easy to make a mistake and see something that is not really there.

3.2 ALICE

As mentioned above, ALICE is the only experiment dedicated to heavy ion physics at the LHC. It is designed to address the physics of the strong interaction and the quark-gluon plasma. There are two important differences between proton and ion collisions at the LHC. An ion collisions will produce many more particles than a proton collision, but they happen at a much lower interaction rate; 10 kHz for Pb+Pb collisions compared to more than 40 MHz for pp collisions. The large number of particles means that ALICE must have very good particle tracking. Also, the study of QGP requires good particle identification (PID) which is a major design criteria for ALICE. The lower interaction rate enables the use of slower, but more precise detectors. The use of slower detector types has an implication on the proton physics programme, as ALICE is not able to take data at the high interaction rates that CMS and ATLAS do. In order to lower the

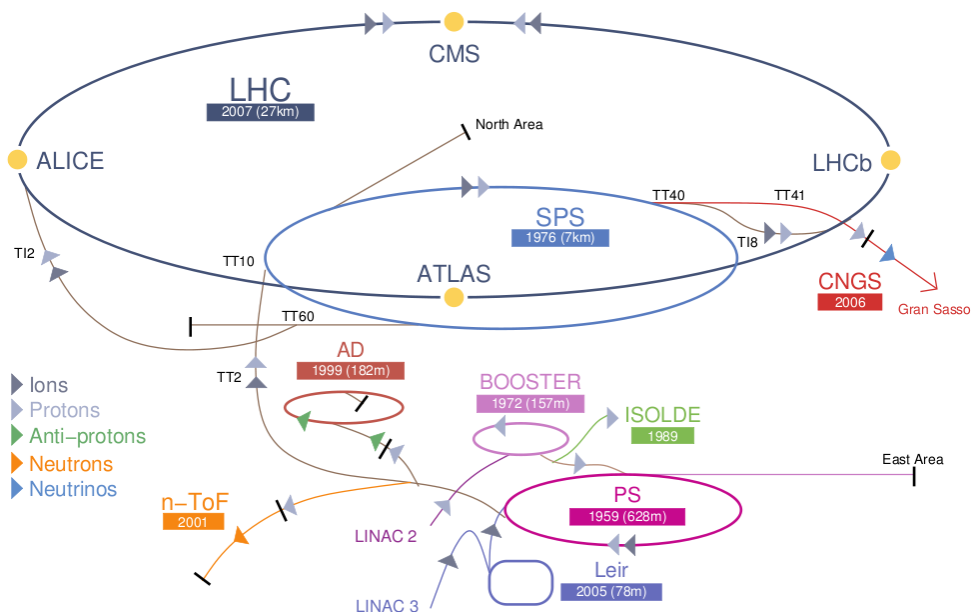


Figure 3.1: The CERN accelerator complex. Courtesy of CERN.

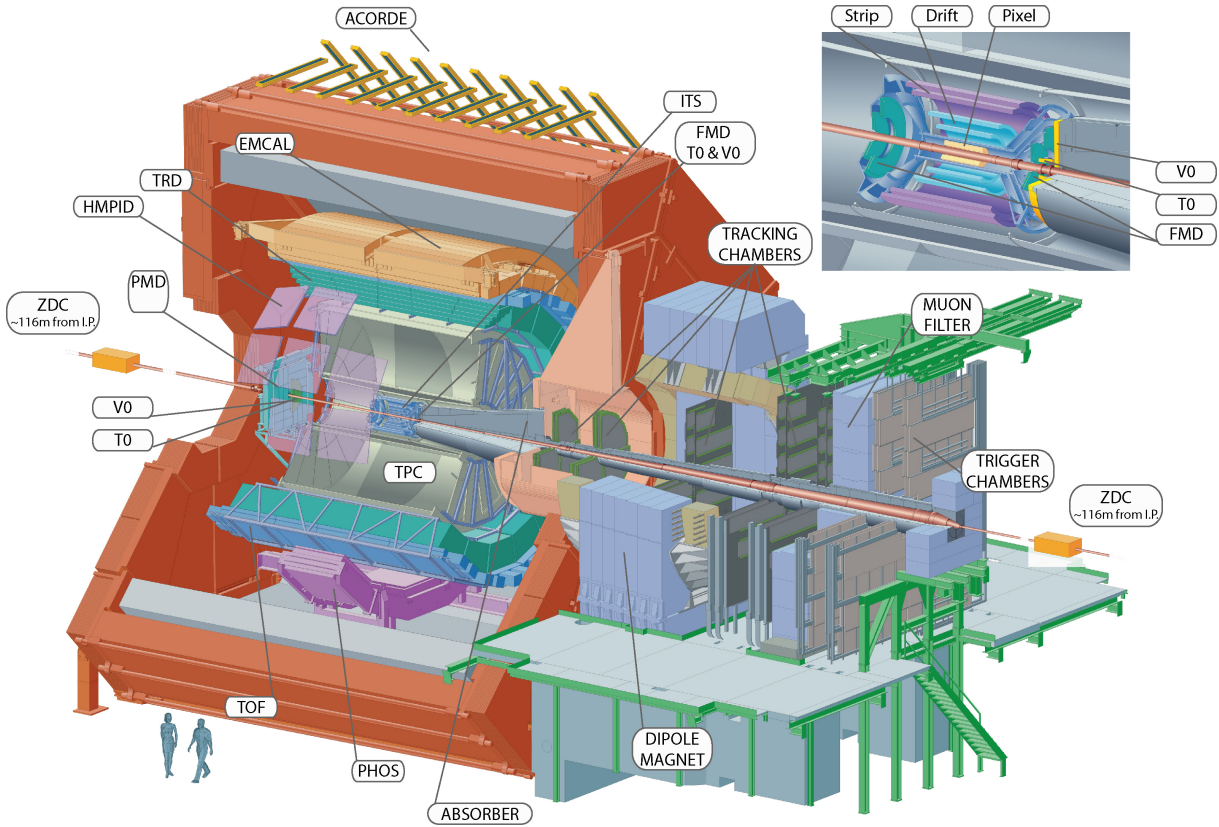


Figure 3.2: ALICE with the position of the sub-detectors shown. The top right corner shows the inner detectors.

interaction rate in ALICE the beams are slightly displaced while going through the collision zone.

Figure 3.2 shows ALICE with the different sub-detectors marked, two persons are also shown to get an idea of the dimensions. ALICE measures $16 \times 16 \times 26 \text{ m}^3$ and weighs approximately 10000 t.

ALICE can be divided into two large parts. One is the L3 magnet and the detectors within. The magnet is reused from the L3 experiment at LEP. It is the large red object on the left of figure 3.2. The other is the forward muon spectrometer shown as the large construction on the right of the figure. The muon spectrometer contains a muon tracker and a muon trigger.

Inside L3 are the detectors for measuring hadrons, electrons and photons. Closest to the interaction point is the Inner Tracking System (ITS). The ITS consist of three silicon detector systems, the Silicon Pixel Detector (SPD), the Silicon Drift Detector (SDD) and the Silicon Strip Detector (SSD). The SPD is used for the analysis presented in this thesis, and is described in more detail in the next section. The ITS detector provide vertex information, tracking and is used for triggering. Immediately outside the ITS is the Time Projection Chamber (TPC). The TPC consists of a large gas chamber with a volume of 90 m^3 , this provides very precise tracking and momentum information, but has the disadvantage of being relatively slow. Together with the ITS it provides a measurement of both primary and secondary vertices¹. The TPC is followed by three particle identification arrays of the Transition Radiation Detector (TRD), the Time-of-Flight (TOF) detector and the High-Momentum Particle Identification Detector (HMPID). The HMPID is a ring imaging Cherenkov radiation detector. Between TOF and the L3 magnet are the two electromagnetic calorimeters PHOS and EMCAL. To summarize ALICE utilizes the following techniques for PID: energy loss dE/dx (TPC), time-of-flight, transition radiation ,

¹Secondary vertices are from resonance decays.

Cherenkov radiation, electromagnetic calorimetry, muon filters (in the muon spectrometer) and topological decay reconstruction (ITS and TPC).

Finally there are five detectors placed at small angles along the beam pipe. The Zero Degree Calorimeter (ZDC), the Photon Multiplicity Detector (PMD), T0, V0 and the Forward Multiplicity Detector (FMD). The T0 is used for the timing of some of the other detectors like TOF and TRD and it is a trigger. V0 is used for triggering in conjunction with the SPD and for this thesis the V0 is also used for the centrality selection, it is described in more detail below. Finally the FMD is used for detecting charged particles at high $|\eta|$. It is the most important detector for this thesis and is described in much more detail on the following section [57].

3.3 The V0 Detector

The V0 detector is a scintillating counter detector. It consists of two sub-detectors V0A and V0C, placed on either side of the IP. It has a similar pseudorapidity coverage as the FMD, i.e. $-3.7 < \eta < -1.7$ and $2.8 < \eta < 5.1$. V0A is made of 32 elementary counters arranged in four rings each with eight counters of 45° in ϕ . V0C is made of 48 elementary counters distributed in two inner rings of eight counters and two outer rings of 16 counters. This means that the V0 does not have a very high resolution either in azimuth or η . But what it lacks in spatial resolution it makes up for in timing resolution; each counter has an individual time resolution that is better than 1 ns. This allows the V0 to serve as a good trigger detector. It can serve in either AND mode or OR mode i.e., trigger when there is a hit in V0A AND/OR V0C. It is used as part of the ALICE Minimum Bias (MB) trigger. It can also be used for luminosity measurements in pp collisions [57].

For this thesis the V0 is used as part of the MB trigger and the centrality determination. Currently the V0 provides the best centrality resolution in ALICE (see figure 3.3).

V0 has also been used for $dN/d\eta$ analysis and reaction plane determination for various flow measurements.

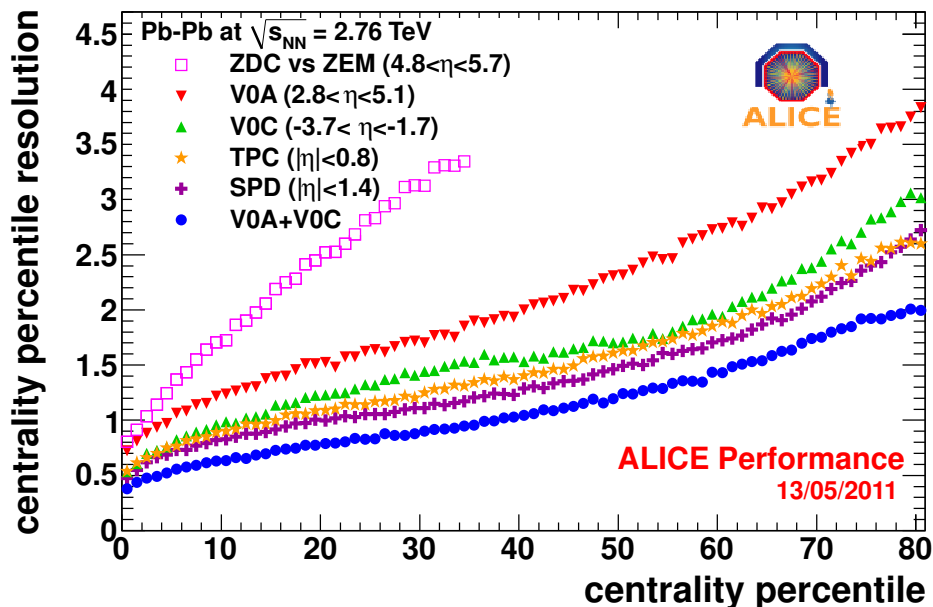


Figure 3.3: Centrality percentile resolution for the different detectors in ALICE.

3.4 The Forward Multiplicity Detector and the Silicon Pixel Detector

In order to understand the deeper workings of the FMD and SPD, the next two sections describes first what happens when a particle traverse material. Then some of the basic principles of silicon detectors is presented. As both the FMD and SPD are silicon detectors knowledge about these two subjects is crucial to understand how the particle detection works in these two detectors.

3.4.1 Energy Loss of Particles Traversing a Material

When a particle traverses a material it deposits energy in the material. An example of this is a charged particle traversing a silicon sensor. In general, the average energy loss per length (also known as the stopping power) is described by the Bethe-Bloch equation. It was derived by Bethe and Bloch from a quantum mechanical description of charged particles scattering softly with electrons. The equation is quite long and complicated, and it is unnecessary to spend time on its full form in this text, a visual representation is sufficient. It can be found in figure 3.4.

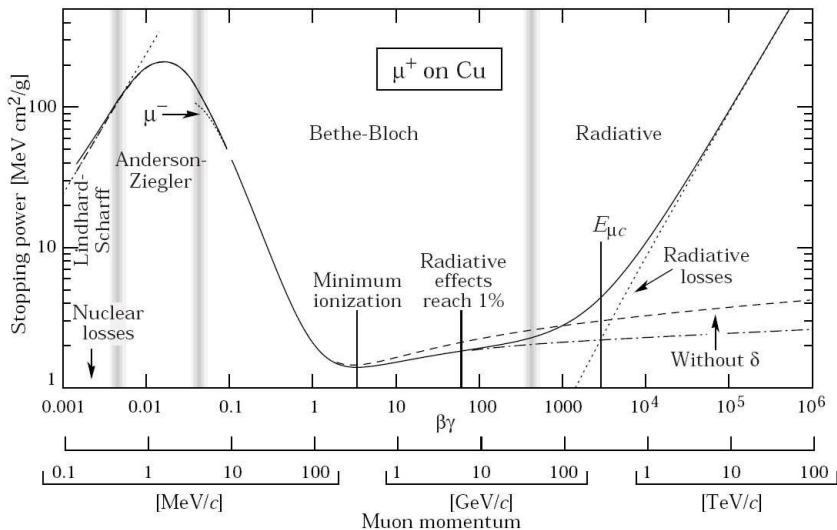


Figure 3.4: Stopping power for μ^+ in copper as a function of $\beta\gamma$ over 12 orders of magnitude in energy. The Bethe-Bloch region and above is the interesting area for the detectors used in this thesis.

In general the stopping power is a function of $\beta\gamma^2$ and the Bethe-Bloch equation only holds for $\beta\gamma > 0.1$. From the figure it is seen that a (relatively) slow particle deposits more energy than a faster particle, at least up to a certain point where radiative losses start to kick in. In the middle of the Bethe-Bloch region a minimum is observed, a particle incident with a $\beta\gamma$ of this value is said to be a minimum ionizing particle (MIP). [58]

Since energy loss is a quantum mechanical effect, it is a statistical process. Therefore it cannot be expected that a particle always deposits the amount of energy described by Bethe-Bloch. Rather there will be a probability distribution around the Bethe-Bloch value. This is known as energy loss straggling. For a thick absorber it is a Gaussian probability distribution. For thin absorbers, such as the ones in the FMD, it is complicated to calculate the energy loss due to the high probability of a single large energy transfer. Energy loss calculations in a thin sensor has been discovered by Landau, Symon and Valivov, the resulting probability distribution is known as a Landau distribution. It is characterized by having a peak around the

² $\beta\gamma = p/m$ and $\gamma = 1/\sqrt{1 - \beta^2}$.

minimum ionizing energy loss, and a long tail towards higher energies, due to the single high energy transfer probability mentioned above. [58]

3.4.2 Silicon Detectors

Silicon is a semi-conductor material. A material is said to be semi-conducting, when the band-gap between the valence and the conducting band is small compared to an insulator. This means that an electron requires a lot less energy to be excited from the valence band into the conducting band. In comparison it does not require any energy to do so in a metal, where the electron can roam the crystal freely. A schematic of the difference between an insulator, a semi-conductor and a metal is shown in figure 3.5

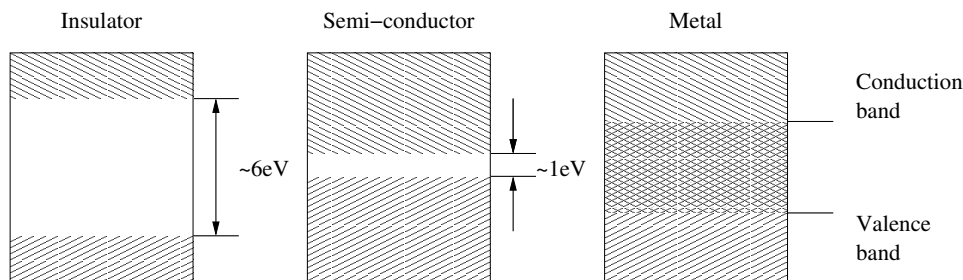


Figure 3.5: Band-gaps between valence and conducting band in insulators, semi-conductors and metals. [58]

Silicon is a tetravalent atom³. By replacing some of the silicon atoms with pentavalent atoms an extra energy state is introduced in the band-gap, which the extra electron is easily excited into, thereby increasing the conductivity. Such a crystal is called a doped n-type crystal. Similarly a trivalent atom can increase the conductivity as it introduces what is called an extra hole in the crystal. In semi-conductors holes behave as electrons with a positive charge. Such a crystal is called a doped p-type crystal. The concentration of either trivalent or pentavalent atoms will usually be very small ($\propto 10^{-9}$). [58]

A p-type crystal can be combined with a n-type crystal to form a pn-junction. The excess of electrons in the n side and the excess of holes on the p side cause a diffusion of charge between the two. Since both sides starts out neutral, the diffusion builds up charge on both sides, thus creating an electrical field across the junction. At some point this potential is strong enough to stop the diffusion. Any remaining charge carriers are left immobile in the region between the two sides, known as the depletion region. This greatly reduces the probability of thermal excitations. And thus in the context of detectors it can be used to reduce the noise of a sensor considerably. [58]

To further reduce the noise it is possible to apply a negative voltage to the p side of the junction, a so called reverse bias voltage. This voltage drags excess holes and electrons in the p and n side respectively further away from the junction, thus increasing the depletion region, or depletion depth as it is also known. [58]

All of the above combines to make silicon crystals excellent detectors. The small band-gap and low noise make them sensitive to ionizing radiation, and insensitive to thermal excitations. A charged particle traversing a silicon crystal will leave a trail of electron-hole pairs behind. By applying an external electrical field over the crystal, the electrons drift towards the anode, and the holes drift to the cathode, thereby setting up a current over the crystal. The current can be read out by the detector electronics. [58]

³Four electrons in the valence band.

3.4.3 The Forward Multiplicity Detector

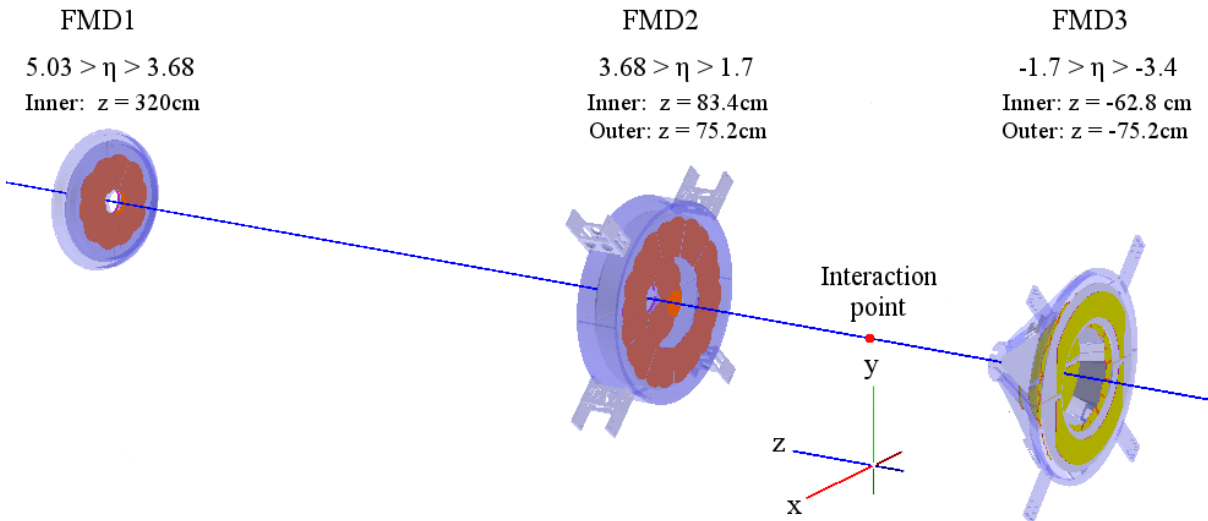


Figure 3.6: The 3 sub-detectors of the Forward Multiplicity Detector and the pseudorapidity coverage.

It is the purpose of the FMD to provide charged particle measurements over a wide pseudorapidity region both in the forward and backward directions where there are no tracking detectors. The FMD is a silicon strip detector and thus detects charged particles using the method described previously in this section. It consists of three sub-detectors, FMD1, FMD2 and FMD3. FMD2 and 3 each consists of two rings, an inner and an outer. FMD1 only consist of one ring, identical to the inner rings of FMD2 and 3. A drawing of the detector is seen in figure 3.6 along with the z -coordinates and pseudorapidity coverage of the sub-detectors. Each ring is divided into a number of sectors in azimuth, which in turn is divided into a number of arch-shaped strips in the radial direction. Each strip constitutes a sensor channel. Table 3.1 provides information on the segmentation and size of the sensors in the inner and outer rings.

	$N_{channels}$	$N_{sectors}$	r_{min}	r_{max}	$\Delta\phi_{sector}$	$N_{strips/sector}$	Strip pitch
Inner ring:	10240	20	4.2 cm	17.2 cm	18°	512	$250 \mu\text{m}$
Outer ring:	10240	40	15.4 cm	28.4 cm	9°	256	$500 \mu\text{m}$

Table 3.1: Overview of parameters for the FMD rings. In total the FMD has three inner rings and two outer rings adding up to 51200 channels.

The fine segmentation of the FMD means that even in the most central collisions there is on average only one charged particle per strip, while the design allows for the detection of up to 20 charged particles before the electronics saturates. This allows for precision measurements of event-by-event multiplicity fluctuations and event-plane determination along with flow measurements. At the time of design it was not considered necessary to measure flow order higher than two, thus the 20 azimuthal segments of the inner rings may turn out to be a limiting factor in the measurement of the highest moments of flow.

The system readout time larger than $88 \mu\text{s}$ and thus the FMD cannot be used as an online multiplicity trigger, though it can be used in the offline analysis [57]. For a detailed description of the data readout chain see chapter 4.

3.4.4 The Silicon Pixel Detector

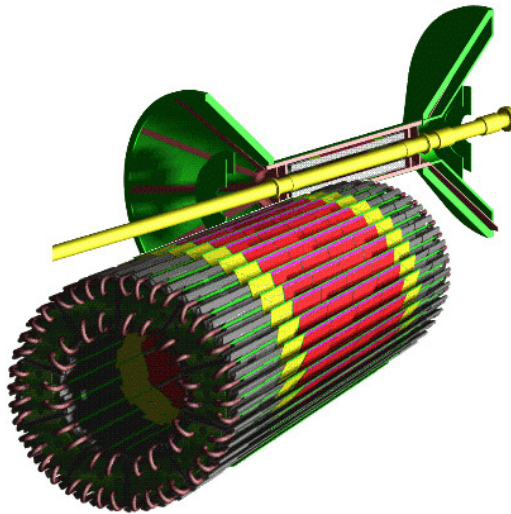


Figure 3.7: SPD barrel in front of its support. The two layers consisting of a total of 60 staves is seen.

The SPD is the innermost part of the ITS. It is based on hybrid silicon pixels, consisting of a two-dimensional matrix of reverse-biased silicon detector diodes. The readout is binary. Meaning that a threshold is set, if a signal is above that threshold the cell will read as being hit. This can be done due to the huge number of cells in the SPD, where the chance of two particles hitting the same cell is negligible, as opposed to the cells in the FMD, which must be able to readout how many particles have hit. Even for the most central Pb+Pb events a maximum occupancy of 2.1% (0.6%) is seen in the inner (outer) layer. [57]

The SPD consists of ten sectors, each sector supports two staves for the inner layer and four staves for the outer layer. Each stave is made up of four ladders, which in turn is made up of five chips. Each chip contains 256 cells in the $r\phi$ -direction times 32 in the z -direction. This adds up to a total of 60 staves, 240 ladders, 1200 chips and $9.8 \cdot 10^6$ cells. [57]

The inner layer is placed at an average distance of 3.9 cm from the beam axis, while the outer layer is placed at an average distance of 7.6 cm. It covers ± 14.1 cm along the z -axis, giving a pseudorapidity coverage of up to $|\eta| = 1.98$ for the inner layer. The size of a cell is $50 \mu\text{m}$ ($r\phi$) \times $425 \mu\text{m}$ (z). [57]

The SPD provides a Fast-OR trigger, which is read out every 100 ns. The pre-processed Fast-OR trigger can be used in the ALICE Central Trigger Processor (CTP) and contribute to the Level 0 trigger decision in ALICE. In order to do this the Fast-OR signal must reach the CTP within 800 ns. Together with the V0, the Fast-OR trigger of the SPD is used as the MB trigger in ALICE. It is triggered when one or more of the pixels in the SPD has a hit above threshold. [57]

Furthermore the SPD is used to determine the primary vertex position of the collision. It can also be used to determine secondary vertices from resonance decays, usually this is done in conjunction with the TPC and the other ITS detectors. Finally hits in the two layers can be combined to give tracklet information to be used either with tracks from the TPC, or by themselves to provide charged particle multiplicity information e.g., $dN/d\eta$ analysis or flow analysis, as it is done in this thesis. [57].

Chapter 4

Data

The physics observables and the experimental apparatus of interest in this thesis has now been presented. In the next chapters these are put together and the analysis is done. But first it is necessary to describe how data is processed. Modern particle detectors are complicated, and a lot of things has to be done before the data is ready for analysis. This chapter describes the path from detector calibration to raw data and finally to the Event Summary Data (ESD) format.

In high energy physics Monte Carlo (MC) tools are often used to understand the physics. For this thesis the MC tools can be divided into two categories; event generators and transport code. The event generators are used to simulate particle collisions. They contain different physics models describing the collision, and determine the outcome with MC methods. Transport code is used to propagate the particles created by the event generators through a virtual model of the experiment, and simulate the interactions between particles and detectors.

The initial processing of MC data is different from that of real data, but the path from the raw data format to the ESD data format is the same. The off-line toolkit in ALICE is AliRoot. The AliRoot framework is based on the ROOT toolkit. ROOT provides advanced data analysis and data representation tools. AliRoot adds libraries containing information about the detector geometry, tools for raw data reading and the physics analysis developed in the ALICE collaboration. Figure 4.1 shows the data flow in AliRoot.

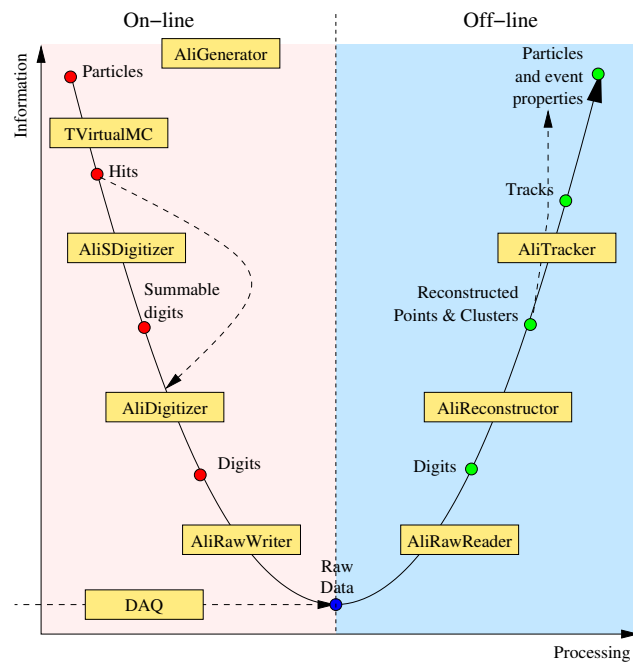


Figure 4.1: Data flow through AliRoot [58].

This chapter begins with a description of detector calibration for the FMD and SPD, and the path of real data up to the "Raw Data" point in the middle of figure 4.1. Then a description of simulated events up to the "Raw Data" point is presented, and finally the data flow in the right half of figure 4.1 is described. For the description of simulated events the different MC generators used in this thesis are also presented. For simulating collisions HIJING and AMPT are used. For particle transport GEANT3 is used, this is the generator that simulates the particle propagation and interactions out through the detector systems.

4.1 FMD Electronics

This section briefly describes the Front-End Electronics (FEE) of the FMD. The emphasis is on how the digital readout from the FMD is converted into an energy count. A schematic of the FMD FEE is shown in figure 4.2.

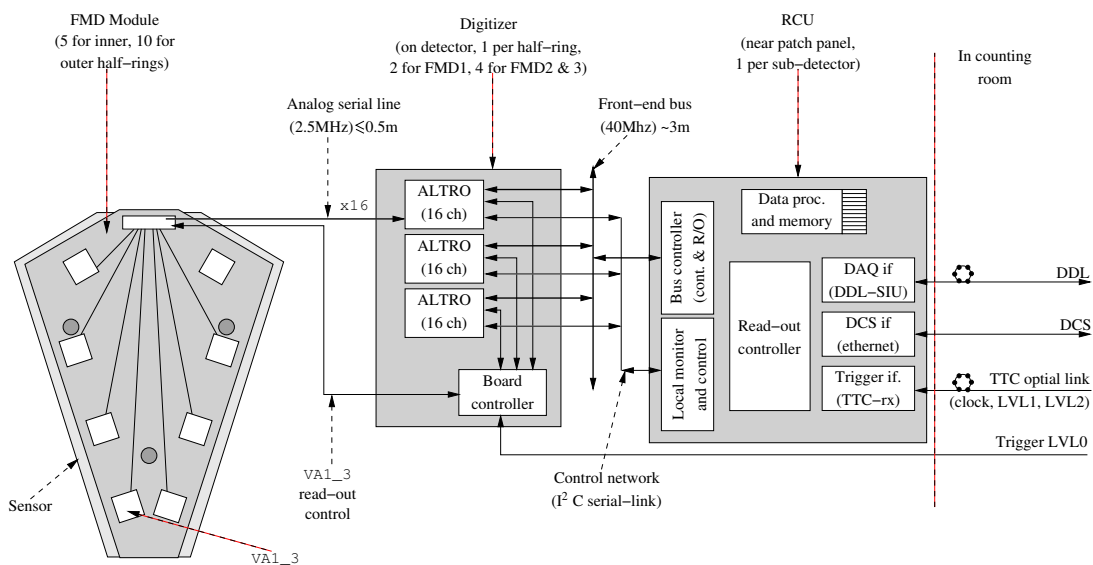


Figure 4.2: Schematic of the FMD Front-End electronics. The silicon modules are connected to the digitizer boards. From there data is sent to the Read-out Control Unit [58].

In section 3.4 it was described how a charged particle traversing a silicon detector will set up a current over the silicon crystal. This current is read out as an analogue signal, which is first amplified by the VA₁₃ pre-amplifier and then digitized by the ALTRO analogue-to-digital converter (ADC) chip. The output of the ADC is a value between 0 and 1023, this is known as the ADC count. Due to the external voltage kept over the FMD and noise from the electronics (cables, etc.) there is a signal from each FMD strip even in the absence of particles. This is called the pedestal. The pedestal is seen as a large structure in the low end of the ADC read-out spectrum [58]. By measuring the signal while there are no beams in the accelerator, it is possible to make a map of the pedestals for each strip. Pedestals can then be subtracted from the measured ADC signal.

There are two digitizer boards for each ring in the FMD (i.e. two for FMD1, four for FMD2 and 3 and ten in total). From these the signals are sent to the Read-out Control Unit (RCU) and on to the Data Acquisition System (DAQ) in ALICE. The different digitizer boards may have a different pre-amplification. This causes the distributions to shift on different digitizer boards, making an ADC count on one board correspond to a different energy than the same ADC count on a different board. The individual channels on a board do not have the same pre-amplification, so there is also a shift for each channel. By probing the FMD with a pulser

of known input voltage and comparing it to the output, it is possible to find the relative gain, which is a measure of this shift.[58]

Both the pedestal map and the relative gain is found by doing regular calibration runs of the FMD. This way any change in pedestal or gain over time does not introduce errors in the reconstruction process. Plots from a pedestal and a gain run is shown in figure 4.3.

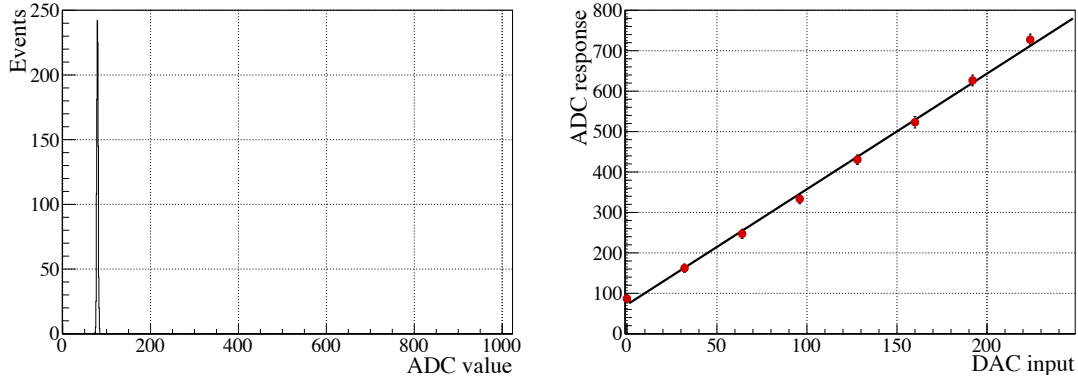


Figure 4.3: Left: The pedestal from FMD2I, sector 8, strip 3 taken in a calibration run. The pedestal is the mean of the distribution, and the noise is the standard deviation. Right: Response in a gain calibration run for the same strip as the left plot. The slope of the line is the gain calibration. [14]

From the DAQ system, the signal is propagated to the so-called Tier-0 computer centre at CERN, where an ADC value between 0 and 1023 is then saved for each strip in the FMD in a raw data file.

4.2 SPD Electronics

The front end electronics of the SPD has a very different setup from that of the FMD. This is partly because the read-out of a chip is binary (i.e. either there is a hit or there isn't) and because it is used as an online trigger detector. A block diagram of the front end electronics of the SPD is shown in figure 4.4.

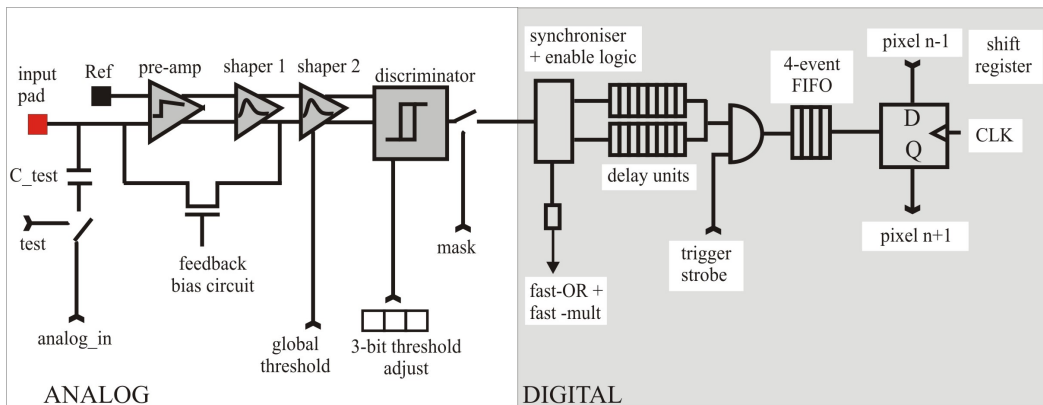


Figure 4.4: Block diagram of the electronics of an SPD pixel cell [59].

Like any other silicon cell, the initial signal is an analogue pulse. It is pre-amplified as in the case of the FMD and is then put through two shapers. The shapers have a detector signal and a clean signal, they are used to minimize the digital switching noise. It is then sent through

a discriminator which compares the signal to a chip global threshold. After the discriminator the signal is sent to the digital part of the chip and each cell is then counted as hit or not hit. As for the FMD, the SPD has the possibility to send test pulses into the pre-amplifier and in that way identify particularly noisy chips, which can then be thrown away by the discriminator. [59].

The latter part of the SPD read-out chain is much more complicated due to its role as an online trigger. Even though the SPD is used as a trigger detector for the data analysed in this thesis, the inner workings of the trigger system is not discussed further. The SPD's primary role in this thesis is for physics analysis. For further information on the SPD, including trigger information see [59].

4.3 Monte Carlo Tools

This section is on the Monte Carlo tools used. For this thesis two different event generators and one transport model are used. The event generators used are HIJING and AMPT, while the used transport code is GEANT3. HIJING is sometimes used in this thesis with a so-called afterburner. This particular afterburner adds flow to the particles, as HIJING does not contain this out of the box. Afterburners are often used to add extra physics the underlying event generator does not contain. The information from the event generators is often referred to as "Monte Carlo truth".

4.3.1 HIJING

HIJING (Heavy Ion Jet INteraction Generator) is the most commonly used event generator for heavy ion physics at the LHC. It is build on PYTHIA[60],[61] routines for hard interactions and JETSET[62] routines are used for string fragmentation¹. PYTHIA and JETSET has been used extensively in pp and p \bar{p} collisions². In HIJING they are used to describe the binary collisions of the nucleons. A Glauber model is used to determine the geometry of the collisions. Parton structure functions are included to study nuclear shadowing. Jet quenching is also part of HIJING, implemented as an effective energy loss parameter dE/dz . Finally multiple mini jet production is also included in the model. Usually these mini jets have too little energy to be seen experimentally, but they are still well described by perturbative QCD and play an important role in the particle production at high energies. HIJING is designed to simulate events with CM energies of $\sqrt{s_{NN}} = 4$ GeV and up for both pp, p+A and A+A collisions. [63].

Current versions of HIJING describe RHIC data well and were able to predict the mid-rapidity multiplicity at the LHC reasonably well [11]. It is now tuned to the LHC multiplicity measurements at mid-rapidity. The physics included in HIJING does not produce flow.

4.3.2 AMPT

AMPT (A Multi-Phase Transport model) is an event generator, which includes both initial partonic and final hadronic scattering. It takes the hard mini jets and soft strings from HIJING to generate the initial conditions. It the uses Zhang's Parton Cascade (ZPC) to model the scattering among partons. Then the hadronisation process is simulated using either the Lund fragmentation model or a quark coalescence model. Finally, A Relativistic Transport model (ART) is used to treat hadronic scattering. By combining all of these models AMPT is able to describe RHIC data reasonably well.

With AMPT the user has the choice of either using the Lund string model or a quark coalescence model. In the MC generator world a string is a coloured connection between two

¹One of the possible MC model approaches to hadronisation.

²From PYTHIA 6.1 JETSET and PYTHIA was merged into PYTHIA.

coloured particles. In HIJING and the default AMPT setup, the energy of the so-called excited strings are not used in the partonic stage and only released in the hadronisation stage. This is how it is described in the Lund string fragmentation model. Another view of it is the quark coalescence model. In which all the excited strings that are not either part of a nucleus, or otherwise interacting, are converted into quarks and mesons at the partonic stage. This is known as string melting. For the default setup of AMPT, the Lund string fragmentation model is used at the hadronic stage to make hadrons from the excited strings. For the string melting setup, the excited strings are converted to quarks and mesons at the partonic stage. At the hadronic stage the left over quarks are then combined into either mesons or baryons [64].

The physics of AMPT contains flow. And the choice of either using or not using string melting has an impact on the flow. In particular the pseudorapidity dependence of the elliptic flow changes a lot between the two setups (see figure 4.5).

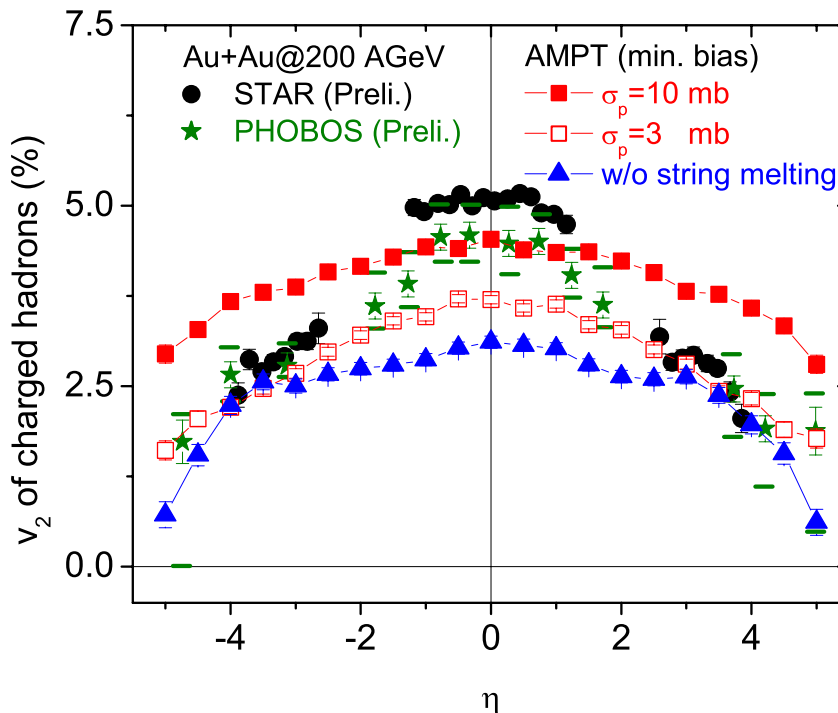


Figure 4.5: Elliptic flow in AMPT compared to RHIC data. Without string melting the flow drops to 0 around $\eta = 5$. With string melting and different settings for the in-medium parton-parton inelastic scattering cross section, σ_p , the model predicts flow out to very forward and backward directions [65].

4.3.3 GEANT3

GEometry ANd Tracking (GEANT) is a transport code developed at CERN. It is based on the EGS program developed at SLAC. It contains information about how particles interact with material. GEANT describes the particles as they are transported/propagated through matter. It utilizes a description of the geometry of a particle detector; both the physical size and what material the different parts are made of. When put together with an event generator e.g., HIJING or AMPT, GEANT tracks the particles as they move through the detector. GEANT then uses Monte Carlo methods when the particles are traversing detector material to estimate if and where new, secondary particles are created. When these secondary particles are created GEANT tracks them and stores all information on the new secondary particles [66]. Every time a particle hits a detector a track reference is saved. This track reference works in a similar way

as the Monte Carlo truth information does, and can be used to e.g. test how well a detector is at counting the particles that hit it.

4.3.4 Digitization

Digitization is used to simulate the detector response to the particles traversing it. For the FMD this means taking the integrated energy loss Δ_i of all particles that hit a silicon strip and convert it into ADC counts or so-called digits. To make the digits realistic random noise is added. The ADC count, c_i , for strip i is

$$c_i = p_i + x + g_i \Delta_i C \quad (4.1)$$

where p_i is a pedestal taken from actual pedestal runs, x is a random Gaussian distribution and g_i is the gain factor from actual gain calibration runs. C is a fixed conversion factor from gain calibrated signal to ADC counts and depends on the response of the VA1₃ pre-amplifier. By using many of the parameters from measurements done with the detector, the digits become as close as possible to the real ADC counts. At this point the MC data is stored in raw data files similar to those of real data and go through the same reconstruction as real data does [58].

4.4 Reconstruction

The reconstruction process takes the raw data and puts it into a more physics oriented format known as the Event Summary Data (ESD) format. Reconstruction is different for all the different detectors due to their different read-out formats and purposes. Below the reconstruction process for the FMD and SPD is described.

4.4.1 Reconstructing Bare Multiplicity with the FMD

The reconstruction process starts from digits, either from MC data or real ADC counts. If the pedestals have been subtracted the ADC counts are corrected for this by adding 3σ , where σ is the width of the pedestal in ADC values. If the pedestals have not been subtracted before by using the pedestal calibration values it can also be done in this step. Next the ADC count is converted into energy loss Δ . First the energy deposited, Δ'_i is calculated using

$$\Delta'_i = c'_i \frac{1}{g_i} \frac{1}{C} \quad (4.2)$$

where g_i is the gain of strip i and C is a common scale between ADC and energy. But since the particles traverse the FMD at different angles, they have a different path length through the detector. The path length through the detector can be calculated and used to correct the energy deposit, Δ_i , by

$$\Delta_i = \Delta'_i \cos \left[\tan^{-1} \left(\frac{r_i}{z_i - v_z} \right) \right] \quad (4.3)$$

where r_i is the radial distance from the beam to the strip, z_i is the z -coordinate of the strip and v_z is the z -coordinate of the primary vertex.

Finally the "multiplicity" is found by $N_{ch,i} = \Delta_i / \Delta_p$ where Δ_p is the most probable energy loss for a minimum ionizing particle. This information along with an η value is stored in the ESD file [58]. Currently the MIP peak, E_{MIP} , ends up at 0.8 in these units for real data and 0.6 for MC data. Particles hitting between two strips may leave a small energy signal in both strips, this is known as sharing, and a correction is needed for this before the data is ready for analysis. Similarly when there is a high occupancy, as in Pb+Pb collisions a second (and third) Landau distribution from two-(three-)particle hits is seen around 2(3) E_{mip} and there is an overlap region between the first and second (and third) Landau distribution. Both of the sharing and particle counting is done when then data is converted from ESD files to Analysis-Object Data (AOD) files. The process is described in Chapter 6.

4.4.2 Cluster Finding and Tracking with the SPD

The SPD reconstruction consists of two parts. First single particles are identified as clusters in each layer of the detector, secondly these are used for tracking.

In the SPD a single particle usually leaves a signal in several adjacent cells due to the fine resolution of the detector. It also leaves a signal in several time slots in the same cells, as the detector is read out very rapidly. All of these signals are merged into a cluster. If several particle signals overlap the signals are unfolded in the reconstruction. A comparison of cluster type distribution between experimental data and MC data is shown in figure 4.6.

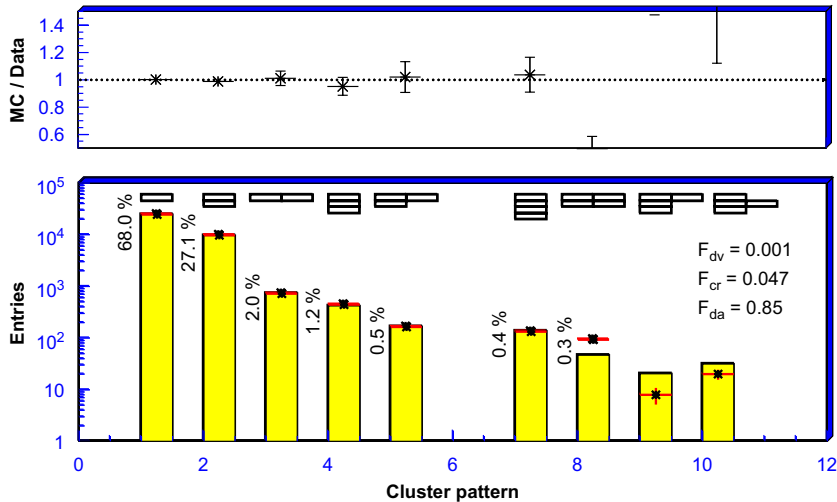


Figure 4.6: A comparison of cluster type distribution between experimental data and MC data with the SPD [67].

The tracking is divided into two methods. One is real tracking where the TPC is used to start the track reconstruction and an algorithm then propagates the TPC tracks to other detectors like the ITS, TOF and HMPID. What is used in this thesis is only information from the SPD. This means the tracks only have three points, one from the vertex and one from a cluster in each layer of the SPD. These are really called tracklets and not tracks. Tracklets do not contain any information about momentum or particle ID i.e., they only contain an η and a ϕ coordinate and a quality parameter $\Delta\phi$ which is defined by $\Delta\phi \equiv \phi_1 - \phi_2$, where ϕ_1 (ϕ_2) is the azimuthal angle between the primary vertex position and the cluster in the first (second) layer. [68]

The event vertex is found by drawing straight lines through clusters in each layer of the SPD. At the point where most of the lines intersect, the primary vertex is found. The procedure also define the tracklets from particles coming from the primary vertex. Using tracklets rather than just hits as in the FMD makes it possible to sort out secondary particles i.e., particles from resonance decays or particles created via interactions with detector material. Both the tracklets and clusters are saved in the ESD file. [68]

4.5 The Grid

The Grid is a computer network setup for analysis of LHC data. Though the setup varies between the experiments, and the data is not shared between experiments. The ALICE grid is called AliEn. The Grid has an enormous amount of computer power available, and is responsible for receiving the raw data and storing it. The ESD files are also produced centrally on the Grid. But users also have access to submit analysis jobs to the grid, although with limited quota. For the first 18 months of physics analysis in ALICE most user jobs were run on ESD files. But while ESD files are much smaller than raw data files, they are still quite big. So to save

resources, central productions of AOD files are made and is now the data format of choice for most analyses.

The analysis done with the FMD and by the FMD team is at the time of this writing not part of the official AOD productions, as final values of the cuts used are still being discussed. This means that for this analysis, the AOD files used were produced by the author from ESD files on the Grid. This gave the opportunity to try various cuts. A discussion on the setup used to create the final AOD files is found in Chapter 6.

Chapter 5

Method

The previous chapters have described the physics of heavy ion collisions and in particular flow and fluctuations. They have also described the LHC and the detectors of ALICE. This chapter presents a method to measure flow. In fact, it presents several. The way of measuring flow has changed a lot over the last 20 years, and today it is not unusual that a flow paper contains results from four or more different flow methods. These methods behave differently when they are subjected to non-flow or flow fluctuations. So while this thesis only presents two measurements in this respect, it is necessary to know something about the other common methods as well.

The first section presents the most intuitive way to measure flow, called the event-plane method. And though it is not used in this analysis it was the first flow method developed with flow coefficients as Fourier moments in mind, and is in many ways the basic method for flow analysis. The reason for not using it in this analysis is also explained. The next section is on a method called the Q-cumulants method. Finally a section is devoted to the other methods, not discussed in detail here. They are sorted into groups and classified by how they react to non-flow and fluctuations.

Originally flow analysis was done with tensors, and the flow observation was coupled to p_t or dN/dy distributions for different particles. The results from this approach were very model dependent, they were used both for the CERN SPS and BNL AGS. The idea of looking at anisotropies in the azimuthal particle spectrum had also been investigated, and indeed observations of anisotropies correlated with the reaction plane had been made. But it was not until 1996, where Voloshin and Zhang first proposed to decompose the azimuthal yield in Fourier moments that the modern approach to flow analysis was born [32]. The idea was simple and has been mentioned in chapter 2, but deserves repeating; the anisotropic dependence on the invariant yield of particles can be Fourier decomposed to:

$$\frac{d^3N}{dp_t^2 d\phi dy} = \frac{1}{2\pi} \frac{d^2N}{p_t dp_t dy} \left(1 + \sum_{n=1}^{\infty} 2v_n \cos[n(\phi - \Psi_R)] \right) \quad (5.1)$$

In principle using the Fourier moment picture, the flow is simply:

$$v_n = \langle \cos[n(\phi - \Psi_r)] \rangle \quad (5.2)$$

where Ψ_r is the reaction plane and the average is over all particles in all events.

5.1 The Event Plane Method

Unfortunately the reaction plane angle is not known experimentally. By 1998 the event plane method proposed by Voloshin and Zhang was well developed [69]. The basic idea is to first measure the event plane, Ψ_n . The event plane is the experimental version of the reaction plane,

and if there were no fluctuations and an unlimited number of particles the two would always coincide. But this is not the case. The event plane can be determined by

$$\Psi_n = \frac{1}{n} \tan^{-1} \left(\frac{\sum_i w_i \sin(n\phi_i)}{\sum_i w_i \cos(n\phi_i)} \right) \quad (5.3)$$

where n is the Fourier moment, the summation is over all particles in an event and w_i is a particle weight, like p_t or rapidity. Then the observed v_n follows trivially from equation 5.2 by replacing Ψ_r with Ψ_n .

To take care of the fact that the event plane does not exactly match the reaction plane, a correction factor known as the event plane resolution is applied. The event plane resolution is $\langle \cos[n(\Psi_n - \Psi_r)] \rangle$, which again introduces the unknown reaction plane angle. Fortunately this can be calculated for example, by using Bessel functions or by dividing the event into three sub-events, a , b and c . In which case it is the given by:

$$\langle \cos[n(\Psi_n^a - \Psi_r)] \rangle = \sqrt{\frac{\langle \cos[n(\Psi_n^a - \Psi_n^b)] \rangle \langle \cos[n(\Psi_n^a - \Psi_n^c)] \rangle}{\langle \cos[n(\Psi_n^b - \Psi_n^c)] \rangle}} \quad (5.4)$$

The n 'th moment then found as:

$$v_n = \frac{\langle \cos[n(\phi - \Psi_n)] \rangle}{\langle \cos[n(\Psi_n^a - \Psi_r)] \rangle} \quad (5.5)$$

With that it is in principle possible to measure any flow moment [69]. Originally it was believed that the event plane did not have to be measured for the same Fourier moment as the flow moment of interest. Not doing so added a few extra factors in the above equation for the event plane resolution, but other than that it was assumed there would be no problems. But with the discovery of the significance of higher v_3 and v_5 moments, and their couplings to flow fluctuations it is now necessary to be a bit more careful. In the case of even moments, there is still no problem as they are all correlated to the same event plane. But since the odd moments arise from fluctuations in the initial medium, the event plane found with these does not always (in fact rarely) align with those from even moments.

Often the event plane method is done with what is called an η -gap. This means that the different sub-events have a certain $\Delta\eta$ between them, and that the particles used for the v_n measurement comes from a different sub-event than the particles used to find the event plane it is being correlated to. Introducing such an η -gap can remove most if not all of the non-flow contributions to the measurement, since non-flow is known to be highly correlated in η .

The disadvantage of the event-plane method and the reason why it is not used for this thesis, is that when the flow measurement is only done differentially i.e., as a function of p_t or η , only the particles in the p_t - or η bin of interest is used for the flow. To make up for this the method requires a relatively large amount of statistics to be available. More modern flow methods allow for a reference measurement using a large sample of particles, and then relate the differential measurement to this. This kind of an approach is described in much more detail in the next section. While the event plane method does have some disadvantages, it should at some be implemented for the FMD due to its simplicity and ability to so easily remove non-flow.

5.2 Particle Cumulants

One of the widely used methods for measuring flow, and the method of choice for this thesis is the use of particle cumulants or multi-particle azimuthal correlations. The cumulants methods have two advantages; it is not required to know the event plane and it is expandable to multi-(more than two) particle correlations. Multi-particle correlations has the advantage that non-flow

does not affect them. They also behave differently under fluctuations, as shown below. Most experiments use the approach described by Borghini et al. using generating functions [70],[71], however a new approach has been developed in ALICE by Ante Bilandzic and others [54] and this is the approach used here.

While cumulant methods do not need the event plane, they need a different kind of reference, which is called reference flow. The approach is to make a flow measurement over a large part of phase space, and then use that as a reference for the differential flow measurement of interest in the analysis. In this case as a function of pseudorapidity. As mentioned above this has the advantage if making a flow measurement possible, even in a region of phase space where there are few particles.

In principle the correlation between any number of particles can be used. And it has recently been proposed to look at multi-particle correlations, with combinations of different particle correlations, in order to study the fluctuations measured with the odd moments [72]. For elliptic flow analysis it is customary to look at even number particle correlations. In practice only the two- and four-particle cumulants are used, but in principle one could also use six-particle cumulants or more. However, it is not believed that there is reason to do so, as the six-particle cumulant should give the same result as the four-particle cumulant, only requiring more statistics.

The cumulant method used here can be done with or without particle weights and with or without extra terms to compensate for a detector with non-uniform azimuthal coverage. Below the two- and four-particle cumulants are presented for a detector with non-uniform azimuthal coverage without particle weights, as that is the setup used in this thesis. First the reference flow for two- and four-particle cumulants is presented, and then the differential flow is presented. Finally there is a discussion on the calculation of statistical uncertainties.

5.2.1 Reference Flow

As mentioned above the reference flow is the flow measured over a large part of phase space. The flow does not have to be the same in that entire region of phase space. The two- and four-particle azimuthal correlation functions are defined as:

$$\langle 2 \rangle \equiv \left\langle e^{in(\phi_1 - \phi_2)} \right\rangle = \frac{1}{\binom{M}{2} 2!} \sum_{\substack{i,j=1 \\ (i \neq j)}}^M e^{in(\phi_i - \phi_j)} \quad (5.6)$$

$$\langle 4 \rangle \equiv \left\langle e^{in(\phi_1 + \phi_2 - \phi_3 - \phi_4)} \right\rangle = \frac{1}{\binom{M}{4} 4!} \sum_{\substack{i,j,k,l=1 \\ (i \neq j \neq k \neq l)}}^M e^{in(\phi_i + \phi_j - \phi_k - \phi_l)} \quad (5.7)$$

Where the sums are over all particles, and $\phi_{i,j,k,l}$ is the azimuthal angle of particle i, j, k, l . These are cumbersome calculations, in particular the four-particle cumulant requires four loops over all particles (i, j, k, l) , three of which are nested (j, k, l) . Doing this in a central heavy ion collision requires an enormous amount of computing power. By introducing Q-cumulants it can be done much easier. The Q-cumulant is defined as:

$$Q_n \equiv \sum_{i=1}^M e^{in\phi_i} \quad (5.8)$$

which is calculated with a single loop over all the particles.

Two-particle Reference Flow

As the sums in equation 5.6 are over the same particles, it follows trivially that the Q-cumulant can be related to this by:

$$Q_n Q_n^* = |Q_n|^2 = \sum_{i,j=1}^M e^{in(\phi_i - \phi_j)} = M + \sum_{\substack{i,j=1 \\ (i \neq j)}}^M e^{in(\phi_i - \phi_j)} \quad (5.9)$$

thus $\langle 2 \rangle$ can be calculated with a single loop over data where Q_n is calculated:

$$\langle 2 \rangle = \frac{|Q_n|^2 - M}{M(M-1)} \quad (5.10)$$

The next step is to average $\langle 2 \rangle$ over N events:

$$\langle \langle 2 \rangle \rangle \equiv \left\langle \left\langle e^{in(\phi_1 - \phi_2)} \right\rangle \right\rangle = \frac{\sum_{i=1}^N (W_{\langle 2 \rangle})_i \langle 2 \rangle_i}{\sum_{i=1}^N (W_{\langle 2 \rangle})_i} \quad (5.11)$$

where $W_{\langle 2 \rangle}$ is an event weight defined as

$$W_{\langle 2 \rangle} \equiv M(M-1) \quad (5.12)$$

The second order cumulant is then simply:

$$c_n\{2\} = \langle \langle 2 \rangle \rangle - \langle \langle \cos n\phi_1 \rangle \rangle^2 - \langle \langle \sin n\phi_1 \rangle \rangle^2 \quad (5.13)$$

where the last two terms are to counter bias from correlations due to non-uniform azimuthal coverage. They are defined as:

$$\langle \langle \cos n\phi_1 \rangle \rangle \equiv \frac{\sum_{i=1}^N (\Re[Q_n])_i}{\sum_{i=1}^N M_i} \quad (5.14)$$

and

$$\langle \langle \sin n\phi_1 \rangle \rangle \equiv \frac{\sum_{i=1}^N (\Im[Q_n])_i}{\sum_{i=1}^N M_i} \quad (5.15)$$

The n 'th flow moment then follows as [54]:

$$v_n\{2\} = \sqrt{c_n\{2\}} \quad (5.16)$$

Four-particle Reference Flow

The four-particle equations are in general much more complicated than the two-particles ones, but the principles are the same. The starting point is the same as before:

$$|Q_n|^4 = Q_n Q_n Q_n^* Q_n^* = \sum_{i,j,k,l=1}^M e^{in(\phi_i + \phi_j - \phi_k - \phi_l)} \quad (5.17)$$

the combinatorics in this case is a lot more complicated than before, and going from $\sum_{i,j,k,l=1}^M$ to $\sum_{i,j,k,l=1,(i \neq j \neq k \neq l)}^M$ is not trivial. Though it can be shown analytically that using the above

$$\begin{aligned} \langle 4 \rangle &= \frac{|Q_n|^4 + |Q_{2n}|^2 - 2 \cdot \Re [Q_{2n} Q_n^* Q_n^*]}{M(M-1)(M-2)(M-3)} \\ &- 2 \frac{2(M-2) \cdot |Q_n|^2 - M(M-3)}{M(M-1)(M-2)(M-3)} \end{aligned} \quad (5.18)$$

Averaged over N events this yields:

$$\langle \langle 4 \rangle \rangle \equiv \left\langle \left\langle e^{in(\phi_1 + \phi_2 - \phi_3 - \phi_4)} \right\rangle \right\rangle = \frac{\sum_{i=1}^N (W_{\langle 4 \rangle})_i \langle 4 \rangle_i}{\sum_{i=1}^N (W_{\langle 4 \rangle})_i} \quad (5.19)$$

where there is once again an event weight $W_{\langle 4 \rangle}$ defined as:

$$W_{\langle 4 \rangle} \equiv M(M-1)(M-2)(M-3) \quad (5.20)$$

The fourth order cumulant then follows as:

$$\begin{aligned} c_n \{4\} &= \langle \langle 4 \rangle \rangle - 2 \langle \langle 2 \rangle \rangle^2 - 4 \cdot \langle \langle \cos n\phi_1 \rangle \rangle \langle \langle \cos n(\phi_1 - \phi_2 - \phi_3) \rangle \rangle \\ &+ 4 \cdot \langle \langle \sin n\phi_1 \rangle \rangle \langle \langle \sin n(\phi_1 - \phi_2 - \phi_3) \rangle \rangle - \langle \langle \cos n(\phi_1 + \phi_2) \rangle \rangle^2 - \langle \langle \sin n(\phi_1 + \phi_2) \rangle \rangle^2 \\ &+ 4 \cdot \langle \langle \cos n(\phi_1 + \phi_2) \rangle \rangle [\langle \langle \cos n\phi_1 \rangle \rangle^2 - \langle \langle \sin n\phi_1 \rangle \rangle^2] \\ &+ 8 \cdot \langle \langle \cos n(\phi_1 - \phi_2) \rangle \rangle [\langle \langle \cos n\phi_1 \rangle \rangle^2 + \langle \langle \sin n\phi_1 \rangle \rangle^2] \\ &+ 8 \cdot \langle \langle \sin n(\phi_1 + \phi_2) \rangle \rangle \langle \langle \sin n\phi_1 \rangle \rangle \langle \langle \cos n\phi_1 \rangle \rangle - 6 \cdot [\langle \langle \cos n\phi_1 \rangle \rangle^2 + \langle \langle \sin n\phi_1 \rangle \rangle^2] \end{aligned} \quad (5.21)$$

where everything but the first two terms are to correct for bias from non-uniform azimuthal coverage. The new terms are defined as:

$$\langle \langle \cos n(\phi_1 + \phi_2) \rangle \rangle \equiv \frac{\sum_{i=1}^N (\Re [Q_n Q_n - Q_{2n}])_i}{\sum_{i=1}^N M_i (M_i - 1)} \quad (5.22)$$

$$\langle \langle \sin n(\phi_1 + \phi_2) \rangle \rangle \equiv \frac{\sum_{i=1}^N (\Im [Q_n Q_n - Q_{2n}])_i}{\sum_{i=1}^N M_i (M_i - 1)} \quad (5.23)$$

$$\langle \langle \cos n(\phi_1 - \phi_2) \rangle \rangle \equiv \frac{\sum_{i=1}^N (\Re [Q_n Q_n^* Q_n^* - Q_n Q_{2n}^*] - 2(M-1) \Re [Q_n^*])_i}{\sum_{i=1}^N M_i (M_i - 1) (M_i - 2)} \quad (5.24)$$

$$\langle \langle \sin n(\phi_1 - \phi_2) \rangle \rangle \equiv \frac{\sum_{i=1}^N (\Im [Q_n Q_n^* Q_n^* - Q_n Q_{2n}^*] - 2(M-1) \Im [Q_n^*])_i}{\sum_{i=1}^N M_i (M_i - 1) (M_i - 2)} \quad (5.25)$$

And finally the four-particle reference flow is found as [54]:

$$v_n\{4\} = \sqrt[4]{-c_n\{4\}} \quad (5.26)$$

5.2.2 Differential flow

The differential flow is calculated for several bins of the observable of interest, in this case the pseudorapidity. The differential flow calculations with Q-cumulants are a bit more complicated than those of the reference flow. For starters it is necessary to distinguish between particles that have been part of the reference flow calculation as well as differential flow calculation. First all of the particles used for the reference flow are marked as Reference Particles (RFPs), there is a total of M of these. Then each particle used for the differential flow is marked as a Particle of Interest (POI), in total there is m_p particles of interest in an event. It is possible to have an overlap between the reference particles and the particles of interest i.e., a particle can be marked as both POI and RFP. In general there are m_q of these particles in an event. The two- and four-particle correlations for differential flow (often called the reduced two- and four-particle correlations) are then:

$$\langle 2' \rangle \equiv \langle e^{in(\psi_1 - \phi_2)} \rangle = \frac{1}{m_p M - m_q} \sum_{i=1}^{m_p} \sum_{j=1}^M e^{in(\psi_i - \phi_j)} \quad (5.27)$$

$$\langle 4' \rangle \equiv \langle e^{in(\psi_1 + \phi_2 - \phi_3 - \phi_4)} \rangle = \frac{1}{(m_p M - 3m_q)(M-1)(M-2)} \sum_{i=1}^{m_p} \sum_{\substack{j,k,l=1 \\ (j \neq k \neq l)}}^M e^{in(\psi_i + \phi_j - \phi_k - \phi_l)} \quad (5.28)$$

where ψ_i denotes the azimuthal angle of the i 'th POI. These calculations can be made simpler by introducing the p - and q -vectors:

$$p_n \equiv \sum_{i=1}^{m_p} e^{in\psi_i} \quad (5.29)$$

$$q_n \equiv \sum_{i=1}^{m_q} e^{in\psi_i} \quad (5.30)$$

Two-particle Differential Flow

Using p - and q -vectors in can be shown[54] that equation 5.27 can be expressed as:

$$\langle 2' \rangle = \frac{p_n Q_n^* - m_q}{m_p M - m_q} \quad (5.31)$$

And as for the reference flow it can be averaged over N events to:

$$\langle \langle 2' \rangle \rangle = \frac{\sum_{i=1}^N (w_{\langle 2' \rangle})_i \langle 2' \rangle_i}{\sum_{i=1}^N (w_{\langle 2' \rangle})_i} \quad (5.32)$$

where the event weight $w_{\langle 2' \rangle}$ is defined as:

$$w_{\langle 2' \rangle} \equiv m_p M - m_q \quad (5.33)$$

The second order differential Q-cumulant is then:

$$d_n\{2\} = \langle \langle 2' \rangle \rangle - \langle \langle \cos n\psi_1 \rangle \rangle \langle \langle \cos n\phi_2 \rangle \rangle - \langle \langle \sin n\psi_1 \rangle \rangle \langle \langle \sin n\phi_2 \rangle \rangle \quad (5.34)$$

where the last two terms are again corrections for non-uniform acceptance. The new correction terms are defined as:

$$\langle\langle \cos n\psi_1 \rangle\rangle \equiv \frac{\sum_{i=1}^N (\Re[p_n])_i}{\sum_{i=1}^N (m_p)_i} \quad (5.35)$$

$$\langle\langle \sin n\psi_1 \rangle\rangle \equiv \frac{\sum_{i=1}^N (\Im[p_n])_i}{\sum_{i=1}^N (m_p)_i} \quad (5.36)$$

And finally the differential flow v'_n for using two-particle cumulants is [54]:

$$v'_n\{2\} = \frac{d_n\{2\}}{\sqrt{c_n\{2\}}} \quad (5.37)$$

Four-particle Differential Flow

The reduced four-particle correlations can be written in a similar, but much longer form as:

$$\begin{aligned} \langle 4' \rangle &= \left[p_n Q_n Q_n^* Q_n^* - q_{2n} Q_n^* Q_n^* - p_n Q_n Q_{2n}^* - 2 \cdot M p_n Q_n^* - 2 \cdot m_q |Q_n|^2 \right. \\ &\quad \left. + 7 \cdot q_n Q_n^* - Q_n q_n^* + q_{2n} Q_{2n}^* + 2 \cdot p_n Q_n^* + 2 \cdot m_q M - 6 \cdot m_q \right] \\ &\quad / \left[(m_p M - 3m_q)(M - 1)(M - 2) \right] \end{aligned} \quad (5.38)$$

This is averaged over N events to:

$$\langle\langle 4' \rangle\rangle = \frac{\sum_{i=1}^N (w_{\langle 4' \rangle})_i \langle 4' \rangle_i}{\sum_{i=1}^N (w_{\langle 4' \rangle})_i} \quad (5.39)$$

where the events weight is defined as:

$$w_{\langle 4' \rangle} \equiv (m_p M - 3m_q)(M - 1)(M - 2) \quad (5.40)$$

The fourth order differential Q-cumulant is then obtained as:

$$\begin{aligned}
d_n\{4\} &= \langle\langle 4' \rangle\rangle - 2 \cdot \langle\langle 2' \rangle\rangle \langle\langle 2 \rangle\rangle \\
&- \langle\langle \cos n\psi_1 \rangle\rangle \langle\langle \cos n(\phi_1 - \phi_2 - \phi_3) \rangle\rangle + \langle\langle \sin n\psi_1 \rangle\rangle \langle\langle \sin n(\phi_1 - \phi_2 - \phi_3) \rangle\rangle \\
&- \langle\langle \cos n\phi_1 \rangle\rangle \langle\langle \cos n(\psi_1 - \phi_2 - \phi_3) \rangle\rangle + \langle\langle \sin n\phi_1 \rangle\rangle \langle\langle \sin n(\psi_1 - \phi_2 - \phi_3) \rangle\rangle \\
&- 2 \cdot \langle\langle \cos n\phi_1 \rangle\rangle \langle\langle \cos n(\psi_1 + \phi_2 - \phi_3) \rangle\rangle - 2 \cdot \langle\langle \sin n\phi_1 \rangle\rangle \langle\langle \sin n(\psi_1 + \phi_2 - \phi_3) \rangle\rangle \\
&- \langle\langle \cos n(\psi_1 + \phi_2) \rangle\rangle \langle\langle \cos n(\phi_1 + \phi_2) \rangle\rangle - \langle\langle \sin n(\psi_1 + \phi_2) \rangle\rangle \langle\langle \sin n(\phi_1 + \phi_2) \rangle\rangle \\
&+ 2 \cdot \langle\langle \cos n(\phi_1 + \phi_2) \rangle\rangle [\langle\langle \cos n\psi_1 \rangle\rangle \langle\langle \cos n\phi_1 \rangle\rangle - \langle\langle \sin n\psi_1 \rangle\rangle \langle\langle \sin n\phi_1 \rangle\rangle] \\
&+ \langle\langle \sin n(\phi_1 + \phi_2) \rangle\rangle [\langle\langle \cos n\psi_1 \rangle\rangle \langle\langle \sin n\phi_1 \rangle\rangle + \langle\langle \sin n\psi_1 \rangle\rangle \langle\langle \cos n\phi_1 \rangle\rangle] \\
&+ 4 \cdot \langle\langle \cos n(\phi_1 - \phi_2) \rangle\rangle [\langle\langle \cos n\psi_1 \rangle\rangle \langle\langle \cos n\phi_1 \rangle\rangle + \langle\langle \sin n\psi_1 \rangle\rangle \langle\langle \sin n\phi_1 \rangle\rangle] \\
&+ 2 \cdot \langle\langle \cos n(\psi_1 + \phi_2) \rangle\rangle [\langle\langle \cos n\phi_1 \rangle\rangle^2 - \langle\langle \sin n\phi_1 \rangle\rangle^2] \\
&+ 4 \cdot \langle\langle \sin n(\psi_1 + \phi_2) \rangle\rangle \langle\langle \cos n\phi_1 \rangle\rangle \langle\langle \sin n\phi_1 \rangle\rangle \\
&+ 4 \cdot \langle\langle \cos n(\psi_1 - \phi_2) \rangle\rangle [\langle\langle \cos n\phi_1 \rangle\rangle^2 + \langle\langle \sin n\phi_1 \rangle\rangle^2] \\
&- 6 \cdot [\langle\langle \cos n\phi_1 \rangle\rangle^2 - \langle\langle \sin n\phi_1 \rangle\rangle^2] [\langle\langle \cos n\psi_1 \rangle\rangle \langle\langle \cos n\phi_1 \rangle\rangle - \langle\langle \sin n\psi_1 \rangle\rangle \langle\langle \sin n\phi_1 \rangle\rangle] \\
&- 12 \cdot \langle\langle \cos n\phi_1 \rangle\rangle \langle\langle \sin n\phi_1 \rangle\rangle [\langle\langle \sin n\psi_1 \rangle\rangle \langle\langle \cos n\phi_1 \rangle\rangle + \langle\langle \cos n\psi_1 \rangle\rangle \langle\langle \sin n\phi_1 \rangle\rangle] \quad (5.41)
\end{aligned}$$

where everything except the first line is to correct for non-uniform azimuthal acceptance. The new correction terms are defined as:

$$\langle\langle \cos n(\psi_1 + \phi_2) \rangle\rangle = \frac{\sum_{i=1}^N (\Re [p_n Q_n - q_{2n}])_i}{\sum_{i=1}^N (m_p M - m_q)_i} \quad (5.42)$$

$$\langle\langle \sin n(\psi_1 + \phi_2) \rangle\rangle = \frac{\sum_{i=1}^N (\Im [p_n Q_n - q_{2n}])_i}{\sum_{i=1}^N (m_p M - m_q)_i} \quad (5.43)$$

$$\langle\langle \cos n(\psi_1 + \phi_2 - \phi_3) \rangle\rangle = \frac{\sum_{i=1}^N (\Re [p_n (|Q_n|^2 - M)] - \Re [q_{2n} Q_n^* + m_q Q_n - 2q_n])_i}{\sum_{i=1}^N [(m_p M - 2m_q)(M - 1)]_i} \quad (5.44)$$

$$\langle\langle \sin n(\psi_1 + \phi_2 - \phi_3) \rangle\rangle = \frac{\sum_{i=1}^N (\Im [p_n (|Q_n|^2 - M)] - \Im [q_{2n} Q_n^* + m_q Q_n - 2q_n])_i}{\sum_{i=1}^N [(m_p M - 2m_q)(M - 1)]_i} \quad (5.45)$$

$$\langle\langle \cos n(\psi_1 - \phi_2 - \phi_3) \rangle\rangle = \frac{\sum_{i=1}^N (\Re [p_n Q_n^* Q_n^* - p_n Q_{2n}^*] - \Re [2m_q Q_n^* - 2q_n^*])_i}{\sum_{i=1}^N [(m_p M - 2m_q)(M - 1)]_i} \quad (5.46)$$

$$\langle\langle \sin n(\psi_1 - \phi_2 - \phi_3) \rangle\rangle = \frac{\sum_{i=1}^N (\Im [p_n Q_n^* Q_n^* - p_n Q_{2n}^*] - \Im [2m_q Q_n^* - 2q_n^*])_i}{\sum_{i=1}^N [(m_p M - 2m_q)(M - 1)]_i} \quad (5.47)$$

And the final result for the four-particle differential flow is then [54]:

$$v_n'\{4\} = -\frac{d_n\{4\}}{(-c_n\{4\})^{3/4}} \quad (5.48)$$

5.2.3 Discussion On Statistical Uncertainties

The paper referenced above does not contain any calculations of statistical uncertainties for the cumulants. The author of this work has been in contact with one of the authors of the paper, Ante Bilandzic, who has been kind enough to supply this author with some of the equations. At the time of this writing only the statistical uncertainty equations for the reference flow take into account non-uniform acceptance, but even without these extra terms the equations for the differential flow uncertainties are enormous. Furthermore, while analytically sound, the

equations do a poor job at estimating the statistical errors in the case of small flow values, as they are $\propto 1/v_n$. All of the equations can be found in Appendix A.

Another approach also suggested to the author by Ante Bilandzic is to divide the data sample into, say ten sub-samples, then calculate the flow in each of those and let the statistical uncertainty be the spread of the ten obtained values. The two approaches are compared in Section 6.3.

5.2.4 Discussion On Fluctuations and Non-flow

Above the multi-particle correlations estimate the averages of various orders of flow:

$$\langle\langle 2 \rangle\rangle = \langle v_n^2 \rangle \quad (5.49)$$

$$\langle\langle 4 \rangle\rangle = \langle v_n^4 \rangle \quad (5.50)$$

But the value of interest is $\langle v_n \rangle$. But since the particle cumulants find the quadrature of the flow, the flow estimates will be biased due to flow fluctuations, which are unavoidable. It can be shown that for $v_n\{2\}$ this bias is:

$$v_n\{2\} = \langle v_n \rangle + \frac{1}{2} \frac{\sigma_{v_n}^2}{\langle v_n \rangle} \quad (5.51)$$

where $\sigma_{v_n}^2$ is the variance of v_n . This means that flow fluctuations bias the two-particle cumulant method by enhancing the measured v_n . Similarly for $v_n\{4\}$:

$$v_n\{4\} = \langle v_n \rangle - \frac{1}{2} \frac{\sigma_{v_n}^2}{\langle v_n \rangle} \quad (5.52)$$

The last equation also holds for $v_n\{6\}$ and $v_n\{8\}$. So the higher order cumulants are all suppressed when there are fluctuations. Proof of the above equations is given in Appendix B. Please note that the calculations are for the reference flow. The author would like to thank Ante Bilandzic for making the calculation available during an email correspondence.

For the differential flow the situation is more complex. In the case where v and v' are independent the two-particle differential cumulant is systematically suppressed by:

$$v'_n\{2\} = \langle v'_n \rangle \left(1 - \frac{1}{2} \frac{\sigma_v^2}{\langle v_n \rangle} \right) \quad (5.53)$$

While in the case where v and v' are identical, or there is an overlap between the RFPs and POIs, it is systematically enhanced by:

$$v'_n\{2\} = \langle v'_n \rangle \left(1 + \frac{1}{2} \frac{\sigma_v^2}{\langle v_n \rangle} \right) \quad (5.54)$$

This means that care must be taken when choosing the reference flow, otherwise the two-particle cumulant may even be suppressed by fluctuations. At the time of this writing the derivations for $v_n\{4\}$ have not been done, but it is clear that it too may have non-trivial behaviour depending on the choice of reference flow. A derivation of the above can be found in Appendix C. The author would like to thank Ante Bilandzic for deriving these equations.

As explained in Section 2.6, non-flow is characterized by mostly being two back-to-back particles (e.g. from a resonance decay), which is highly correlated over a small range in η . When the differential flow is done in η bins it is difficult to avoid non-flow contributions to the above methods (as mentioned in the first section of this chapter it is possible with the event plane method). It can be shown[54] that $v_n\{2\}$ is affected by this non-flow, which enhances the measured value. But since non-flow is usually limited to being a strong correlation between

a small number of particles (two mostly) the higher order cumulants are unaffected. This means that $v_n\{4\}$ is unbiased by non-flow, and the same is of course true for $v_n\{6\}$ and $v_n\{8\}$. Mathematically the non-flow contribution to the two-particle methods can be shown to be [54]:

$$v_n\{2\} = \sqrt{\langle v_n \rangle^2 + \frac{1}{M}} \quad (5.55)$$

From this it is clear that the non-flow contribution is significant only in the most peripheral events where the multiplicity is low.

5.3 Other methods

A quick look at figure 2.9 will reveal a measurement marked $v_2\{q-dist\}$ and one marked $v_2\{LYZ\}$, and indeed there are more methods than these two, which are not described in detail in this thesis. This poses a problem if one experiment only uses one method, and the other experiments another method, since it makes comparisons rather difficult. The $v_2\{q-dist\}$ method is similar to that of azimuthal particle correlations discussed in section 2.3, and will in general give results similar to the multi-particle correlations [73].

Apart from the event plane method and particle cumulant method, the Lee-Yang Zeroes (LYZ) method is the most widely used method. It uses the same principle of generating functions as the original cumulants method, however rather than doing some fixed number of particle correlations, it uses correlation functions with all the particles in the phase space. Then by looking at the zeroes in the complex plane of the generating function (much like in the theory of phase transitions by Lee and Yang), it is possible to measure the flow. The method is similar to that of the particle cumulants as first a reference measurement over a large part of phase space is done, and then the measurement is done differentially. The results are similar to the multi-particle (more than two) cumulants method, in that they gain a negative bias to the flow measurement from fluctuations and they are unaffected by non-flow [74].

In general for all of the methods not described here, two-particle methods are biased by non-flow and enhanced by flow fluctuations. Multi-particle are unaffected by non-flow and suppressed by fluctuations. In the case of two-particle methods an η -gap is often introduced, also for the cumulants method described above. Although that is not done in this thesis. Depending on the size of the gap, it more or less effectively suppress non-flow. As a benchmark, an η -gap of two units in pseudorapidity or more is generally thought to suppress non-flow by as much as it is possible with η -gaps [43].

Chapter 6

Analysis

This chapter contains the main analysis done for this thesis i.e., an analysis of elliptic flow as a function of pseudorapidity, using the Forward Multiplicity Detector and Silicon Pixel Detector in ALICE on data from 2.76 TeV Pb+Pb collisions at the LHC. In particular the Monte Carlo studies and cuts done for the analysis are discussed here. The first part contains a toy Monte Carlo study. It is a toy MC as there is no physics involved, but it has played an important role in understanding the complexities of flow analysis for the author. It is a setup produced to make semi-realistic values of flow and send them through the analysis code in order to see what can be expected from more physics oriented input. The main code written for this analysis can be found in *AliRoot/PWG2/FORWARD/analysis2* tag v5-02-01-AN and is all the files containing the word "Flow", the main task being *AliForwardFlowTaskQC*.

In the second part of this chapter the cuts on the data as it is processed from ESD file format to AOD file format are discussed. Finally the optimal cuts are found and applied to the output of a full Monte Carlo simulation. The same cuts are applied to the real data, but the final results are not presented until Chapter 8 where a correction from the MC studies of this chapter is applied to the data.

6.1 Resolution effects

First a small study of how the limited resolution of detectors limit the accuracy of the flow measurement. Since some of the FMD rings only have 20 ϕ -segments the analysis is carried out with this ϕ -segmentation for all FMD rings and the SPD. This has an effect on the flow measurement, if not for elliptic flow then maybe for the higher orders of flow.

In the left panel of figure 6.1 a $dN/d\phi$ distribution filled with random numbers from a $1 + 0.2 \cdot \cos 2\phi$ distribution, simulating an elliptic flow of $v_2 = 0.1$ is shown. There are three histograms, one with 1000 ϕ -bins, one with 100 ϕ -bins and one with 20 ϕ -bins. A $\cos 2\phi$ -function is then fitted to the data. The fitted functions are drawn with a scaled down coefficient below the data points to show how similar they are. The legend also shows the fitted v_2 values. The fits to all three ϕ -segmentations find the correct value within the uncertainties, so apart from having a larger uncertainty there seems to be no problem in using 20 ϕ -segments for an elliptic flow analysis. The left panel of the figure shows higher order flow moments in 20 ϕ -bin histograms and corresponding fits. All of the distributions has an input value of $v_n = 0.1$, and for the second, third and fourth moment this value is found within the uncertainties. For the fifth and sixth moment the 20 ϕ -segments does not seem to give a good enough resolution and the obtained values are about 10 – 20% too low.

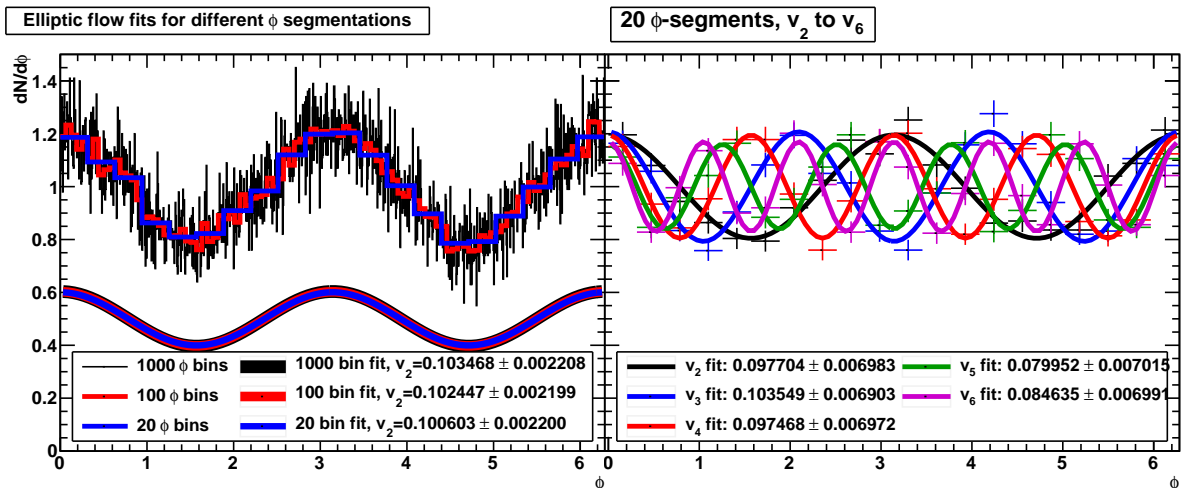


Figure 6.1: Left plot: $dN/d\phi$ distribution with an elliptic flow of $v_2 = 0.1$. The black histogram has 1000 ϕ -bins, the red has 100 and the blue has 20. A $\cos 2\phi$ function are fitted to each histogram, they are drawn scaled down by a factor 2 below the histograms. The colour indicate which histogram the function is fitted to. The legend also contains the fitted value of v_2 , and within the uncertainties it does not seem to matter which resolution is chosen. Right plot: $dN/d\phi$ for different flow moments, n , all have input value $v_n = 0.1$ and 20 ϕ -bins. The points are then fitted, and the obtained value are shown in the legend. For v_2 to v_4 the fits are in good agreement with the input, while v_5 and v_6 seem to suffer from the poor ϕ -resolution.

6.2 Toy Monte Carlo Studies

The toy MC model is set up to simulate events with flow. To make it as realistic as possible the x -axis has a range from -6 to 6 to make it resemble η , but in principle it could be any other observable. The axis is divided into 48 bins, so that each bin covers a range of 0.25 units. Each bin is filled with 100 particles, each with a random ϕ value taken from a function of the form:

$$f(\phi) = 1 + 2h(\eta) \cos 2(\phi - \Psi_{RP}) \quad (6.1)$$

where $h(\eta)$ can be any function representing an η -dependent flow. The ϕ -resolution is identical to the one used in the analysis of data i.e., 20 bins. The statistical uncertainties are estimated by dividing the sample into 10 sub-samples and taking the spread between those 10. A discussion on statistical error estimates is found in Section 6.3.

6.2.1 No Flow Fluctuations or Non-flow

Flat Distribution

First a simple test is done. A flat elliptic flow distribution is simulated in the same way as above, but for several η -bins. There are no fluctuations or non-flow. The result is seen in figure 6.2 The algorithm for both $v_n\{2\}$ and $v_n\{4\}$ does a good job of finding the input flow. Since there are no fluctuations or non-flow they also agree with each other within the statistical uncertainties as they should. In the left panel 20 ϕ -bins are used while 200 are used in the right panel, where the cumulants does a better job at finding the flow. Interestingly the cumulant method does seem to suffer a bit from the ϕ -segmentation, although theoretically it should be possible to determine the elliptic flow just fine with 20 ϕ segments as was shown above. It is not understood at this time why the cumulants method is more vulnerable to a lower ϕ -resolution. In these examples

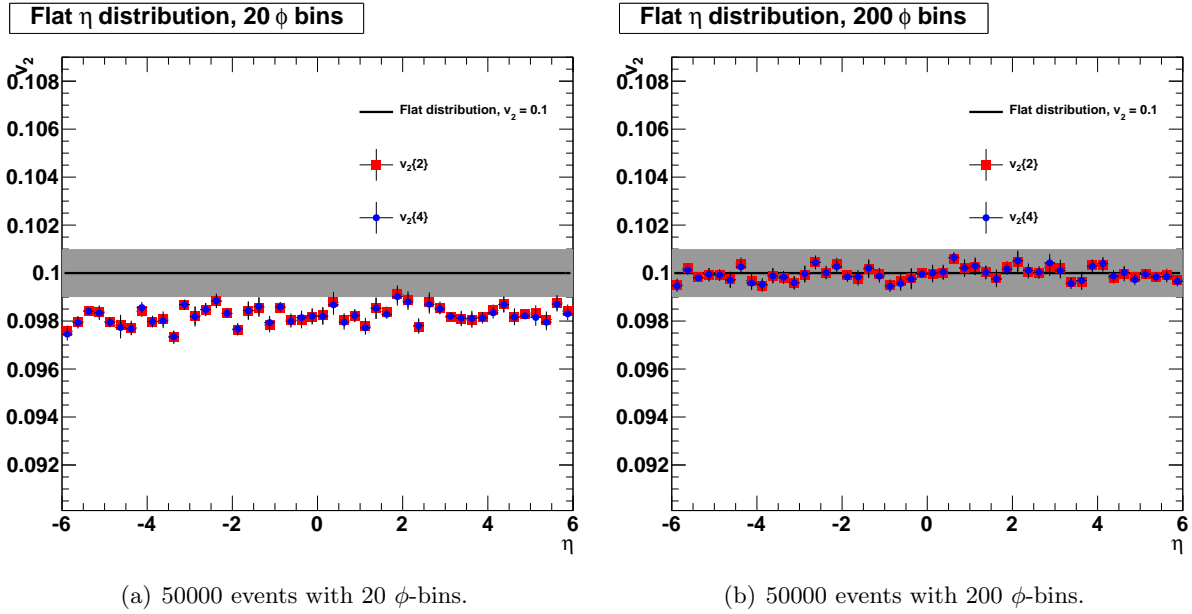


Figure 6.2: Cumulant calculations on 50000 events with different ϕ -segmentation. The input flow is elliptical and with a constant value of 0.1. The cumulants method suffer from the low ϕ -resolution and gives a flow measurement approximately 2% below the input value in the case of 20 ϕ -segments. The grey bands shows the statistical uncertainty in the input v_2 .

all the particle are used for the reference flow. But the results would have been identical if a specific part of phase space had been used instead of the entire phase space.

Gaussian Distribution

The next test is a Gaussian $v_2(\eta)$ distribution, done as before, but with a different amplitude on the $\cos 2\phi$ to simulate η -dependence. It is still with no fluctuations or non-flow. The results can be seen in figure 6.3. Again with 20 ϕ -bins on the left panel and 200 on the right. The results are identical to those of the flat distribution. This is best seen in the bottom part of the plots where $v_2\{QC\}/v_2\{input\}$ is shown to make the comparison to the flat distribution easier. This means the bias to the cumulants from the ϕ resolution does not depend on the magnitude of the flow, which is fortunate, as that makes it easier to correct for. Once again all particles are used for reference flow, and it would not make a difference to use a smaller part of phase space. For small η deviations are observed, they are due to the method having difficulties for very small values of v_2 .

Multiplicity Fluctuations

Now multiplicity fluctuations are added. The number of particles in each bin is a random number between 50 and 150 and is generated on an event-by-event basis i.e., with the same number of particles in each bin in a single event. That means the total multiplicity fluctuates between 2400 and 7200, thereby representing a very large centrality binning. It is done both for the flat distribution and the Gaussian. The result is shown in figure 6.4. It is seen that multiplicity fluctuations even of this order does not bias the result in any way. In fact the results are completely consistent with the previous plots. This is completely expected, as the flow is constant from event to event. And while different multiplicities give more weight to some events than others; as all events have the same flow it does not have an effect. A similar test

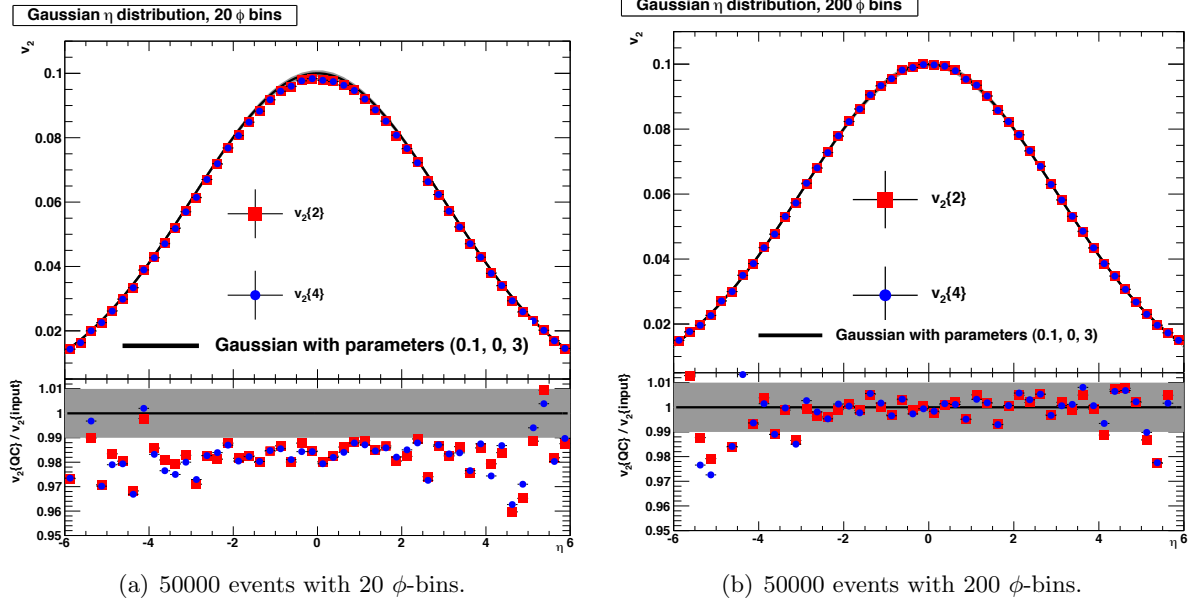


Figure 6.3: Cumulant calculations with different ϕ -segmentation for a Gaussian flow distribution. As for the flat distribution the cumulants with 20 ϕ -bins suffer from the low ϕ -resolution with about 2% too low a flow estimate (bottom plots). Though it appears to be uncorrelated with the magnitude of the flow, which is fortunate as it makes it easier to correct for. The grey bands shows the statistical uncertainty in the input v_2 .

has to be made with flow fluctuations included in order to estimate if multiplicity fluctuations have an effect. This is done at the end of this section.

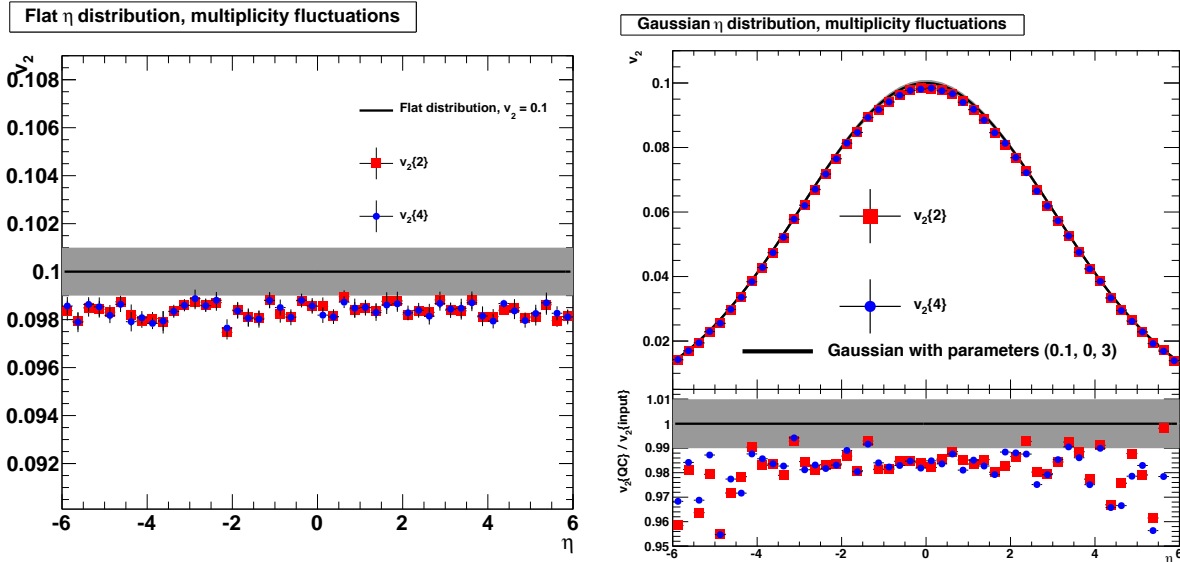
6.2.2 With Flow Fluctuations

In this section flow fluctuations are added. It is known from section 5.2.4 in the previous chapter that the two-particle cumulant is biased towards a higher v_2 and the four-particle is biased towards a lower v_2 in the case of fluctuations. So this is also a test of the algorithm, to see if it responds in the right way to fluctuations.

Simple Fluctuations

It turns out that dealing with flow fluctuations is an extremely difficult task. To visualize this, first two simple setups with flow fluctuations are made. Simple fluctuations means that σ_{v_2}/v_2 is constant over the entire distribution, i.e. there is no underlying extra pseudorapidity dependence embedded in the flow fluctuations. Again a flat distribution and a Gaussian distribution in η are used. The results can be seen in figure 6.5 and 6.6. In both plots the open squares represent an analysis done where all the particles are used for the reference flow calculation. The closed circles are the results of an analysis done with only the particles with $|\eta| > 3$ as reference flow, these particles are also indicated by the green area behind the plots. For the flat distribution the magnitude of the fluctuations is constant for all η -bins, while for the Gaussian the fluctuations follows the same Gaussian in magnitude as the flow does, thus keeping $\sigma_{v_2}/v_2 = \sigma_{v_2'}/v_2'$ i.e., the ratio is the same for the reference flow and all the differential flow bins.

The two-particle cumulant is enhanced and the four-particle is suppressed, as they should be. Remembering that there is only 20 ϕ -bins, which gives a 2% reduction it is also seen that the bias is of the same magnitude (around 5%) for both cumulants, also as expected. It is seen



(a) 50000 events with 20 ϕ -bins and a flat flow distribution. (b) 50000 events with 20 ϕ -bins and a Gaussian flow distribution.

Figure 6.4: In both of the above plots multiplicity fluctuations are added to the toy MC. The multiplicity in each bin varies between 50 and 150 from event to event, but is always the same for all bins in a single event. The total multiplicity is thus between 2400 and 7200. And while these are large multiplicity fluctuations, no effect were seen as the flow was the same in all events regardless of multiplicity. The grey bands shows the statistical uncertainty in the input v_2 .

directly from the flat distribution and by the comparison plot below the Gaussian that the choice of reference flow does not affect the measurement.

Independent Fluctuations

Next a flow independent η -dependence is added to the magnitude of the fluctuations. For independent fluctuations the magnitude of the fluctuations is uncorrelated with the magnitude of the elliptic flow i.e., $\sigma_{v_2}/v_2 \neq \sigma_{v_2'}/v_2'$. Essentially this means the shape of the elliptic flow vs. η is not always the same. The results are shown in figure 6.7 and 6.8. For the first figure the usual flat distribution is used with Gaussian dependent flow fluctuations. And the second figure is the usual Gaussian distribution but with a constant amount of fluctuations over the entire η -range. Again the open squares have all particles in the reference flow, and the filled circles have only particles in the range indicated by the green background.

Very surprisingly in both cases there is a huge difference between the flow measurements, with different reference flow. In certain areas for both distributions there is a negative bias, that pushes $v_2\{2\}$ down below the input flow. And for the Gaussian $v_2\{4\}$ is above the input flow in some places. This is new behaviour, it was initially observed in the analysis presented in Section 6.7 and not understood. These results helped to understand the observed behaviour and prompted the calculations in Appendix C to be done, and is now understood using those equations.

6.2.3 With Non-flow

In section 5.2.4 it is shown that only the two-particle cumulant should be affected by non-flow, which should enhance it. To test this the toy MC is setup such that there are no fluctuations,

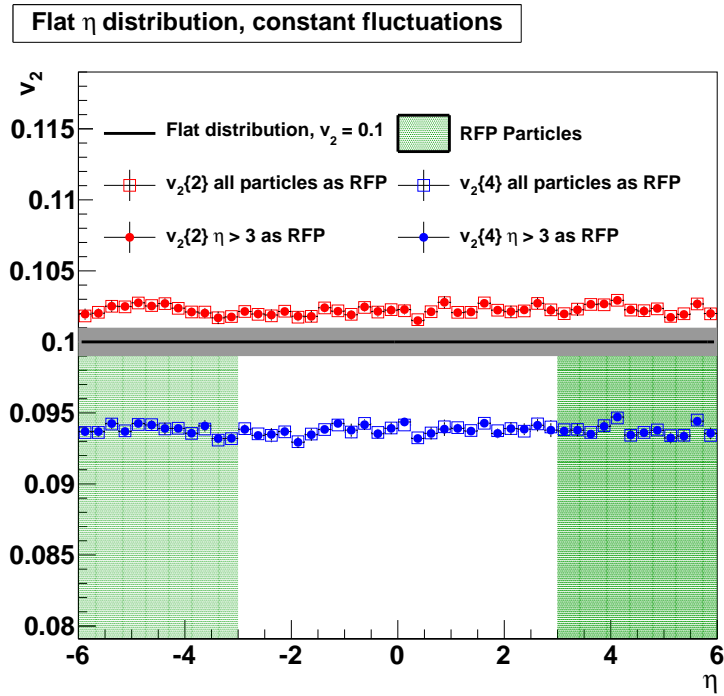


Figure 6.5: 50000 events with a flat $v_2(\eta)$. Flow fluctuations are added such that $\sigma_{v_2}/v_2 = \sigma_{v'_2}/v'_2$. As expected the two-particle result is enhanced and the four-particle result is suppressed. Two different reference flow regions are observed to yield identical results.

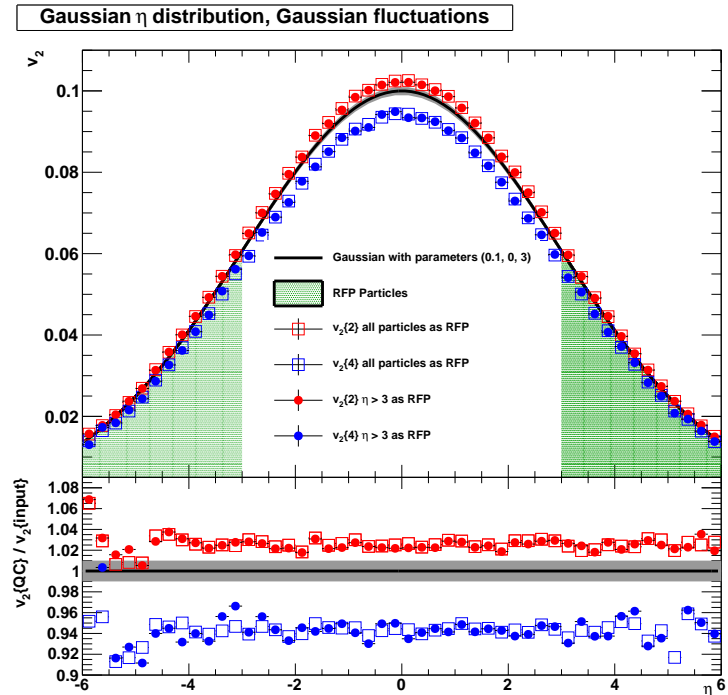


Figure 6.6: 50000 events with a Gaussian $v_2(\eta)$. Flow fluctuations are added such that $\sigma_{v_2}/v_2 = \sigma_{v'_2}/v'_2$. As expected the two-particle result is enhanced and the four-particle result is suppressed. Two different reference flow regions are observed to yield identical results.

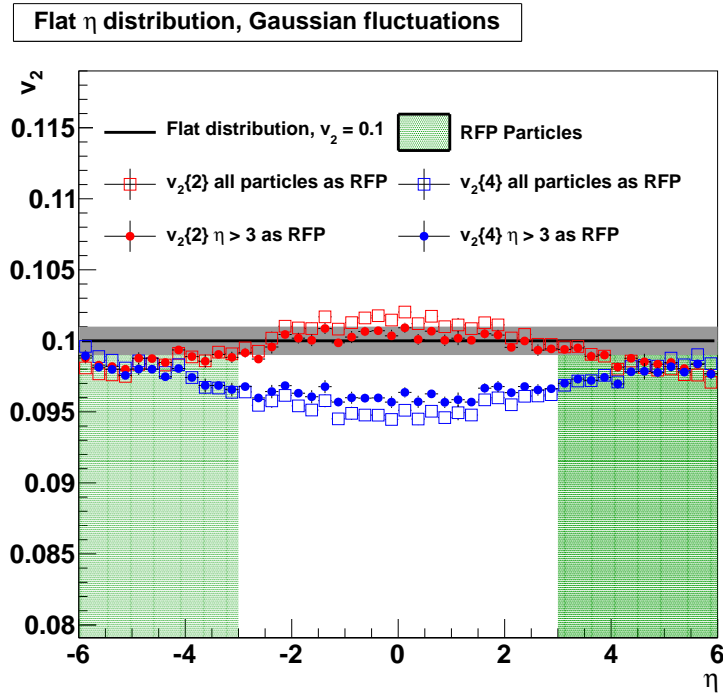


Figure 6.7: 50000 events with a flat $v_2(\eta)$. Flow fluctuations are added such that the magnitude follows a Gaussian. A more complicated behaviour is observed, which depends on the area chose for the reference flow. This behaviour was initially not understood, but can now be explained by equations 5.53 and 5.54.

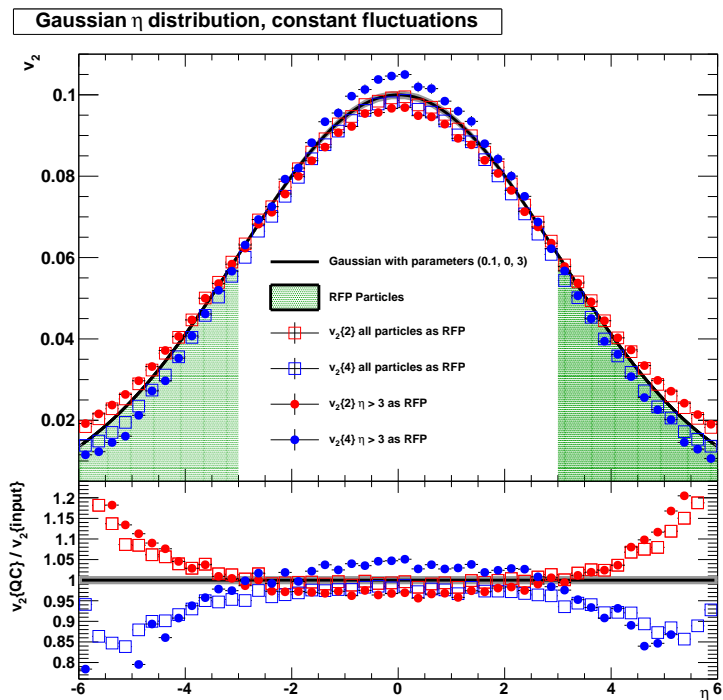


Figure 6.8: 50000 events with a Gaussian $v_2(\eta)$. Flow fluctuations are added such that the magnitude is constant even though the elliptic flow is not. A more complicated behaviour is observed, which depends on the area chose for the reference flow. This behaviour was initially not understood, but can now be explained by equations 5.53 and 5.54

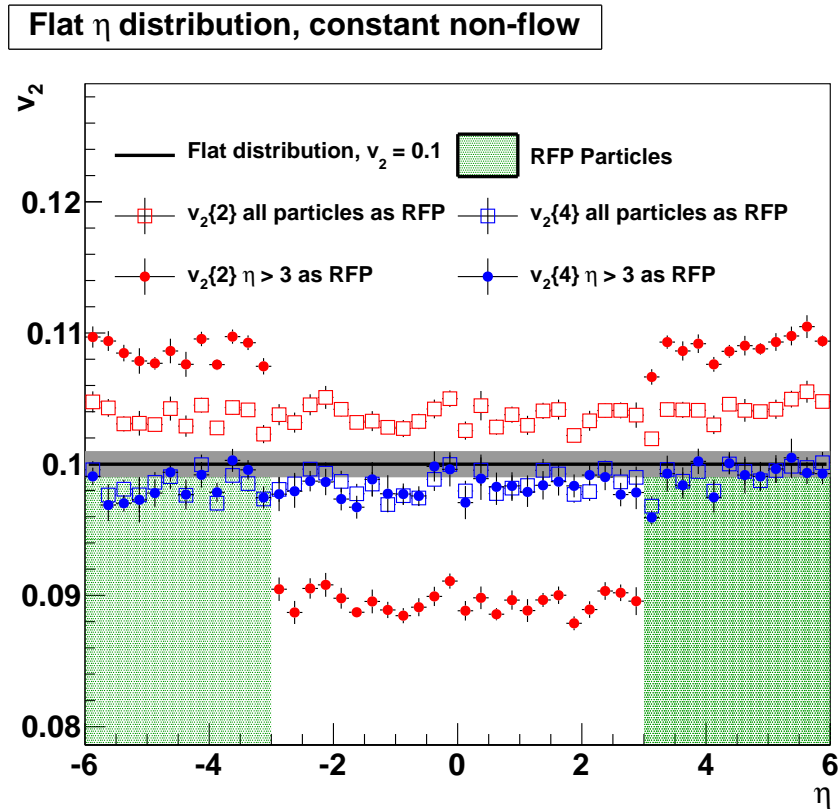


Figure 6.9: 100000 events with a flat $v_2(\eta)$ and non-flow added by counting each particle twice. Again a dependence of the area chosen for the reference flow is observed. The bias from choosing a limited reference area is well known, and is something one must be aware of in flow analysis.

only non-flow. The non-flow is simulated with the same setup as above, with no fluctuations, except instead of sampling 100 particles for each η -bin only 10 particles are sampled. The non-flow is added by counting all of the particles twice. The reason for the low multiplicity is that the non-flow contribution scales as $1/M$ for the two-particle cumulant, as can be seen in equation 5.55. To make up for the lower statistics with only 10 particles per bin twice as many events are simulated. Note that the four-particle method should be unaffected by any non-flow.

The result is seen in figure 6.9. The open squares are the result of an analysis where every particle is used for the reference flow. And the filled dots are the result of one where only particles with $|\eta| > 3$ is used. It is clearly seen that the four-particle method is completely unaffected by the non-flow. In the case where all the particles are used for reference flow there is a clear bias from non-flow, and the measurement is about 5% higher than without the non-flow as expected. The results are similar for the Gaussian η dependence. For the case where only part of the particles are used for the reference flow it is a bit more complicated. For $|\eta| > 3$ the enhancement due to non-flow is larger than for the analysis with the open points. This is because the number of particles used for the reference flow is only half as big, and because of the scaling due to non-flow the enhancement becomes larger. In the middle where $|\eta| < 3$ a suppression is observed. This is a well known effect from non-flow, where such a suppression happens if there is a large amount of non-flow in the RFPs, and the POIs are uncorrelated with the RFPs. So that is another thing to be mindful of, when choosing the reference flow area.

6.2.4 With Non-uniform Azimuthal Acceptance

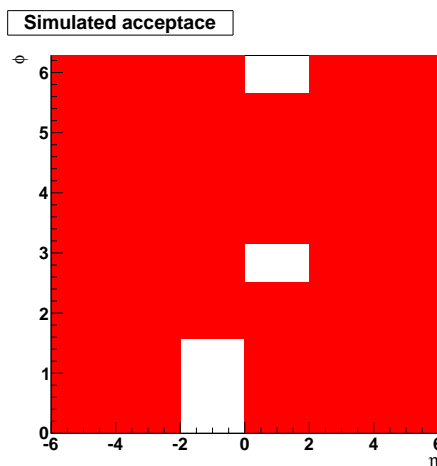
Finally a test of the terms in the cumulant equations correcting for a non-uniform acceptance is needed. The terms have been present in all the above analyses, but as the simulated coverage has been uniform they have been essentially zero in all the cases, and have thus not contributed to the flow measurement. They are now tested by simulating a non-uniform acceptance, which changes with η . The acceptance is seen in figure 6.10(a). The result is seen in figure 6.10(b), where it is done for the Gaussian distribution. The results are identical for the flat distribution. The reason for the change in acceptance versus η is to see that the equations also work in such cases. In one area 1/4 of the azimuthal angle is not covered, simulating a detector with a large hole. In the other area are two small holes each being 1/8 of the azimuthal angle, exactly π radians apart. From the figure it is clear that the equations work, but that some care is needed. In the case where all the particles are used for reference flow there is a very small bias in the $\eta \in [-2; 0]$ region, and a more noticeable one in the $[0; 2]$ region. These come from the fact that the acceptance changes in the phase space used for the reference flow. So while the algorithm does take care of non-uniform acceptance issues, it does have some limitations. So for the analysis the reference flow should be done in phase spaces with identical acceptance.

Added Multiplicity Fluctuations, Flow Fluctuations, Non-flow and Non-uniform Azimuthal Acceptance

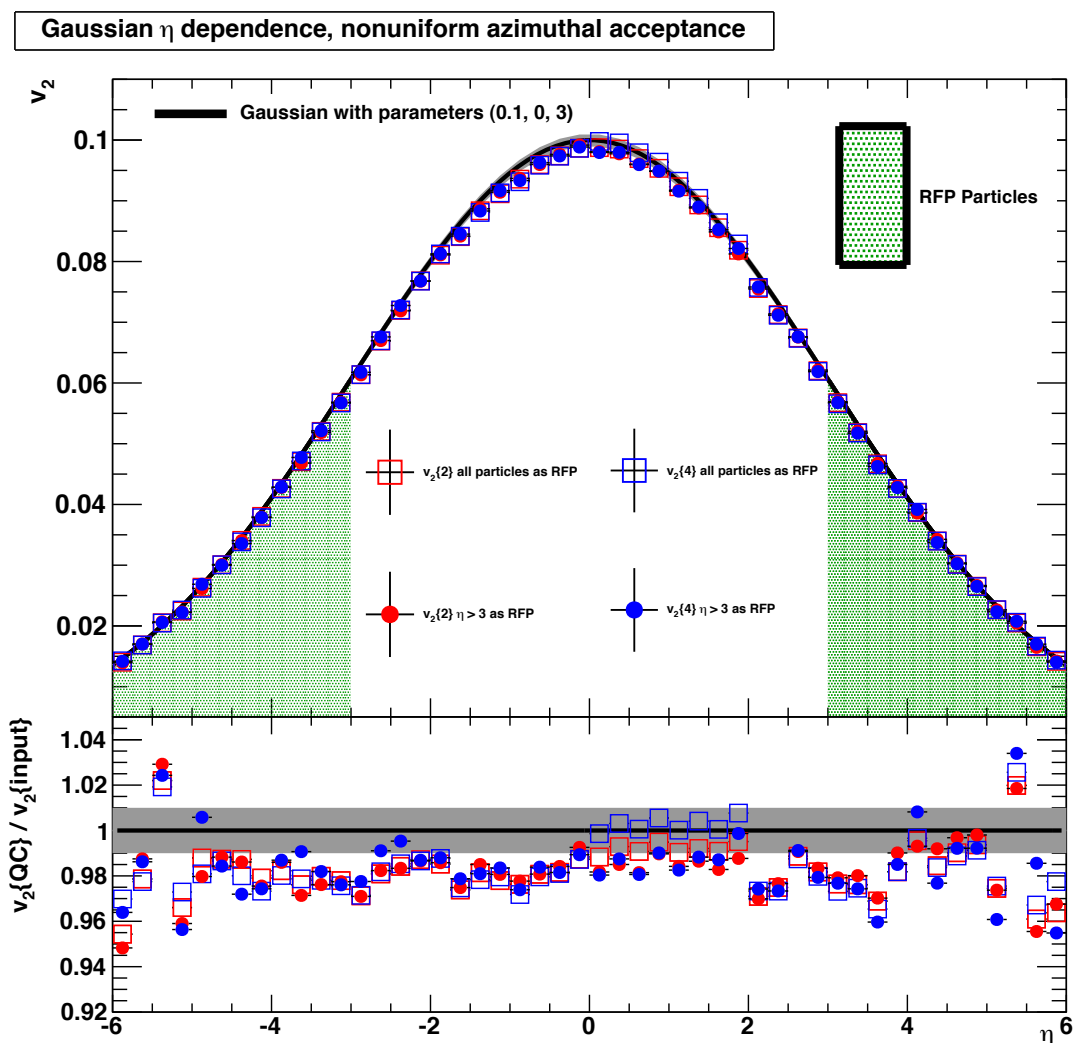
Finally it is time to put everything together and see that there is no interplay between the different complications, which adds a bias to the measurement. The multiplicity per bin fluctuates between 50 and 100. The flow fluctuations are of the simple kind, which follows the shape of the flow distribution. The non-flow is added by counting every particle twice, although the higher multiplicity used makes it much less noticeable. The acceptance is the same as above. The results are identical for the flat and Gaussian distributions, so only the Gaussian is shown (figure 6.11). It is clear that $v_2\{4\}$ only depends on the flow fluctuations, while $v_2\{2\}$ is also affected by the non-flow, this is seen most clearly in the forward and backward regions. As seen above the non-flow causes problems if the particles used for the reference flow are not chosen carefully.

6.3 Discussion On Statistical Uncertainty Calculations

The analytical equations for calculating the statistical errors in the two- and four-particle cumulant methods are presented in Appendix A. Another way to estimate the statistical errors is to divide the data into a number of smaller data sets, and then estimate the statistical uncertainty as σ/\sqrt{N} , where N is the total number of events. While the analytically derived equations naturally give the correct results, they do not take into account non-uniform acceptance. In figure 6.12 a comparison between the two approaches to find the statistical errors is presented. In figure 6.12(a) it is done for $v_2\{2\}$, and in figure 6.12(b) it is done for $v_2\{4\}$. The data is provided by the toy MC from the previous section with no fluctuations of any kind and no η dependence. 10000 events are created and analysed. As can be seen from the figure the two methods are in very good agreement. This suggests that for a detector with uniform acceptance both methods can be utilized, while in the case of non-uniform acceptance the method of dividing the data into sub-samples is preferred. Thus the method of choice for this thesis is to divide the data into ten samples, and get the statistical uncertainty from the spread of these samples, as it is shown in section 6.4.5 that the detectors used here does not have a uniform acceptance.



(a) Simulated azimuthal acceptance as a function of η .



(b) 50000 simulated events with the azimuthal coverage from figure (a).

Figure 6.10: From the bottom part of the plot it is seen that there is a small bias when all the particles are used for the reference flow. This is understood as an effect of changing azimuthal acceptance over the reference flow region, which should be avoided when possible. Although the effect is observed to be less than 2%, so it is not a large bias in any case.

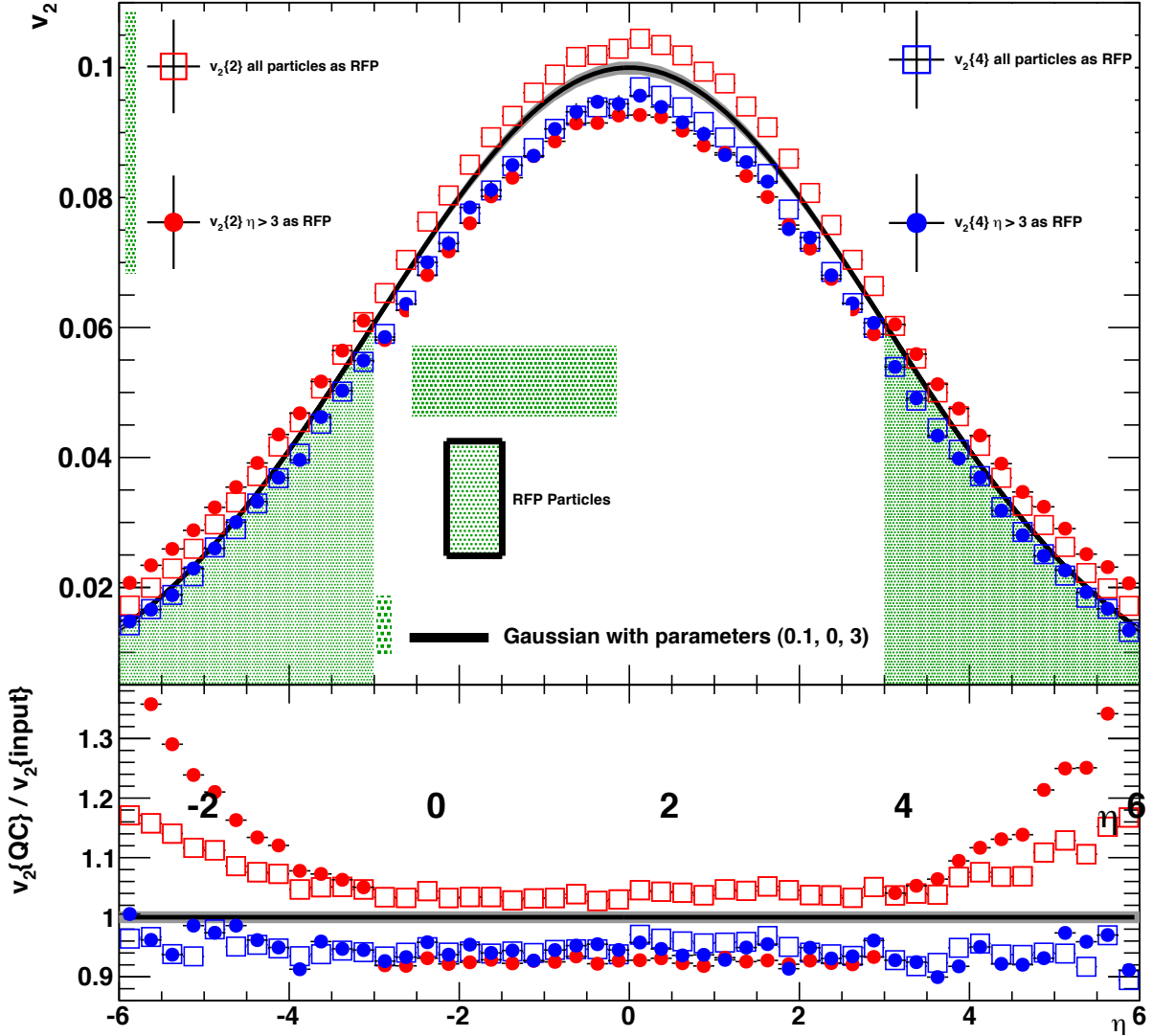


Figure 6.11: 50000 events with flow fluctuations, non-flow, multiplicity fluctuations and non-uniform azimuthal acceptance. The open points are a result of an analysis with all particles as part of the reference flow. A enhancement of $v_2\{2\}$ is observed due to the fluctuations and non-flow. A suppression of $v_2\{4\}$ is observed due to the fluctuations. And a small bias due to changing azimuthal coverage is observed. The same is observed for the filled points, where only particles with $\eta > 3$ are used for the reference flow. Except that the non-flow bias is seen as a suppression in the region that is not part of the reference flow.

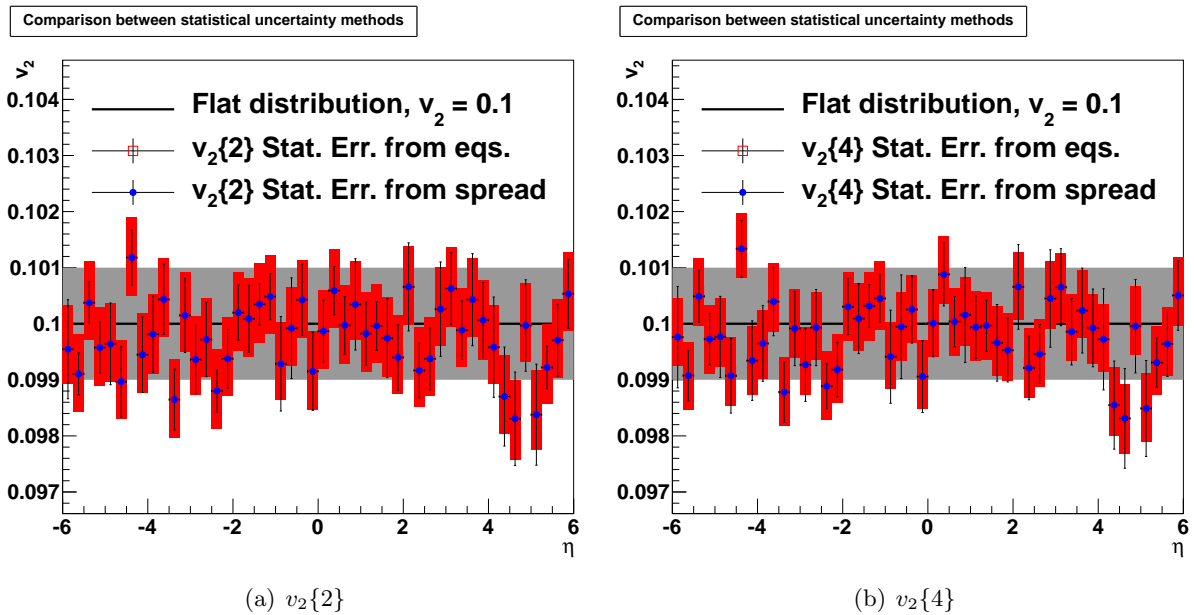


Figure 6.12: A comparison between the analytical equations for statistical uncertainties (red boxes) and a method where the data is divided into 10 sampled and the error is then estimated from the spread of these (black lines). A very good agreement between the two methods are observed both for the two- and four-particle cumulant methods. The grey band is the statistical uncertainty of the input flow.

6.4 Analysis Object Data

The data processing has been described up until the data is put into ESD files in chapter 3-4. But there is still a lot to be done before it can be used for flow analysis, this is done in the process taking the data from the ESD file format to the AOD file format. For the SPD data the path from ESD to AOD files is short, but for the FMD data there is a much longer analysis chain. Both are described below. All the tasks can be found in *AliRoot/PWG2/FORWARD/analysis2*.

6.4.1 The SPD: From Event Summary Data to Analysis Object Data

The path from ESD files to AOD files is short for SPD data. The task handling it for this analysis is the *AliCentralMultiplicityTask*. It takes the tracklets found with the method described in section 4.4.2 and unused clusters from the inner layer of the SPD and adds it to a $d^2N/d\eta d\phi$ -histogram for each event. That is essentially all that is done to the SPD data, though at this point it is still affected by a small amount of secondary particles and acceptance issues. How to tackle these is described below in the analysis chain for the FMD as the procedure to correct for these effects is identical for the two detectors.

6.4.2 The FMD: Sharing Correction With Hit Merging

So far it has been described how a charged particle traversing the FMD deposits a signal described by a Landau distribution, and that the output from the detector contains some leftover noise from electronic noise and thermal fluctuations. But there is in fact another effect embedded in the FMD signal. Even though the FMD is very thin ($\sim 300 \mu\text{m}$) it is possible for a particle to hit the detector at such an angle that it deposits a small signal in two neighbouring strips. This is illustrated in figure 6.13.

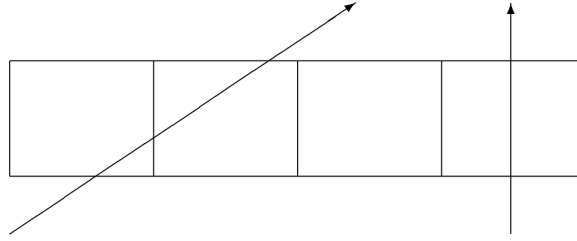


Figure 6.13: Drawing of two different ways a particle can traverse a FMD strip. The left one leads to a shared signal in two strips.

Another possibility is that the signal from one particle may leak into neighbouring strips, this is known as energy sharing or "cross talk", it is unknown if the FMD is affected by this. In any case the result would be identical to that of the sharing described above, and thus the correction for the two phenomena is identical. The sharing adds a plateau to the data between the pedestal remnant and the first MIP (Minimum Ionizing Particle) peak. It turns out from MC studies that due to backscattering a single particle may deposit a signal in as many as three adjoining strips [14].

The added plateau from sharing to the energy signal makes it difficult to say when the pedestal remnant stops and the actual signal begins, thus it is difficult to know what energy to make a cut at to prevent noise from getting into the signal. The problem is to set a cut, such that a particle is only counted once, even if it leaves a signal in more than one strip. To avoid all these problems a hit merging algorithm is used. The algorithm requires some external cuts to be set in order to work. Three thresholds, E_{low} , E_{high} and E_{hit} needs to be determined beforehand. All strips are looped over, when a strip has an energy deposit above E_{low} the next strips are checked for energy. If the strips have an energy deposit in the interval $[E_{low}; E_{high}]$ they are added together. In the end all strips with energy below E_{hit} are cut away. A flow chart of the algorithm is shown in figure 6.14. The cuts are determined by:

- Determination of E_{low} : This determines the lowest acceptable signal size that can be a shared signal. It is used to cut away what remains of the pedestal and is set roughly at three times the width of the noise, $E_{low} \propto 3\sigma_{noise}$. This turns out to be around 0.084 for the inner FMD rings and 0.12 for the outer rings in the units used in the ESD file. To stay completely clear from the pedestal the actual cuts are set at $E_{low} = 0.10$ for inner rings and $E_{low} = 0.15$ for outer rings [14]. This does not cut away too much of the shared signal, as a particle depositing so little in a strip is likely to have left a much larger deposit in a neighbouring strip, which counts as a particle by itself.
- Determination of E_{high} : This is the highest energy signal that may still be counted as part of a shared hit. It is determined using MC simulations where it is possible to track the deposited energy from a single particle directly, and from that determine the energy cut. The result of the analysis is shown in figure 6.15, from which the value of $0.7\Delta_p$ is obtained, where Δ_p is the energy at the peak. Linking this cut to the position of the peak allows the use of the MC result on the real data, even though the peaks are not in the same place in the two kinds of data, as is described in Chapter 4.
- Determination of E_{hit} : This is the minimum required energy for a deposit to count as a hit. After the sharing is done all strips with energy below this value is cut away. It is easy to see that it is limited by E_{high} such that $E_{hit} \leq E_{high}$. As E_{high} is cut right where the Landau starts it does not make sense to set E_{hit} any lower than that. So for this analysis $E_{hit} = 0.7\Delta_p$.

The result can be broken down to three cases:

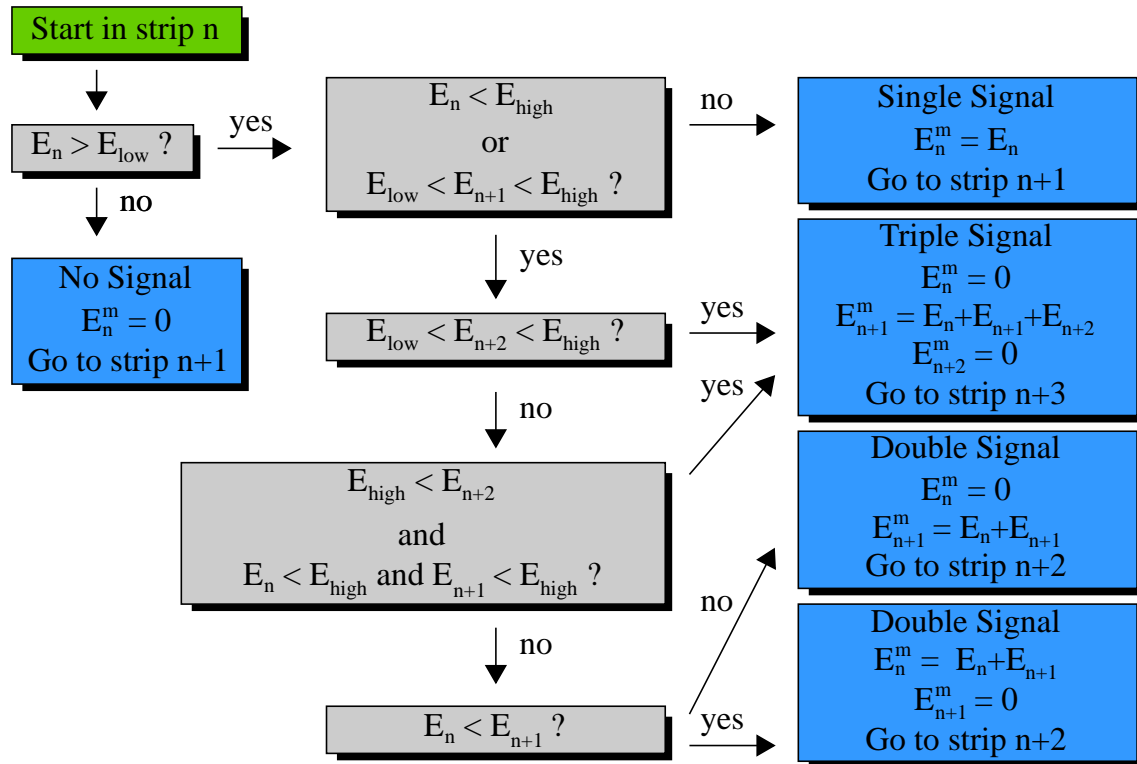
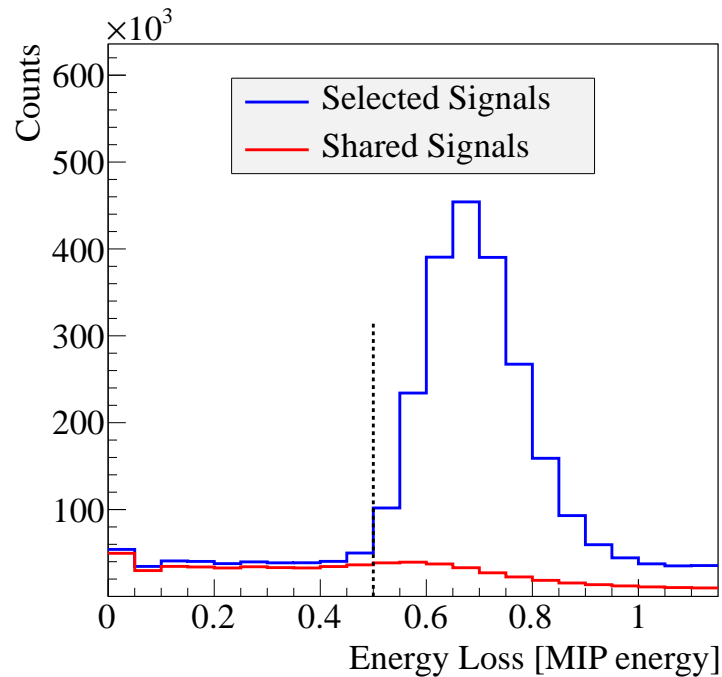


Figure 6.14: Flow chart of the sharing algorithm.

Figure 6.15: E_{hit} cut determination with MC data. The blue line is the energy distribution after the hit merging. The red line is signals from shared hits. The cut is set so the contamination from shared signals is minimal.

- There is a sharing signal across two neighbouring strips: The signals are added up and attributed to the strip with the highest initial signal. The other strip's signal is set to zero.
- There is a sharing signal across three neighbouring strips, and a maximum of one strip with a hit above E_{hit} : Regardless of which strip had the highest signal the three signals are added and attributed to the middle strip. The signal in the two others is set to zero.
- There is a sharing signal across three neighbouring strips, but two strips with hits above E_{hit} : The strip with energy below E_{hit} is added to the closest of the other two. Or in the case where it is the middle strip, to the neighbour strip with lowest energy.

Some of these cases are illustrated in figure 6.16. While some of the different multiplicity analysis done with the FMD is affected by a few % by these upper cuts, the flow analysis has turned out to be rather unaffected by these upper cuts. This can be attributed to the fact that the flow analysis looks more at particle multiplicity variations, than the absolute charged particle multiplicity.

As is shown below the sharing algorithm is quite efficient. But it does have some issues, which are discussed before the results are shown. Firstly there is a noise signal, which goes quite a long way into the Landau distribution. A small signal is unavoidable, but it turns out that it is actually quite a bit larger than expected. Figure 6.17 shows data from a run where there was no beam in the LHC, so everything in the plots is background noise. As the trigger in the run was completely random, the signal is likely also present during physics runs. It is seen that a significant part of this extends all the way where the Landau signal is for data.

Finally it is time to show the results of the sharing, compared to the distribution without sharing. This is done in figure 6.18 below. Keeping in mind the y -axis is logarithmic it is immediately obvious that the sharing is very efficient. The final distributions have variations of a few percent between the FMD rings, but on average there is 88% isolated hits, 10% once merged hits and only 2% twice merged hits.

6.4.3 The FMD: Particle Counting With Energy Distributions

There are two different approaches to particle counting with the FMD. One approach is to fit functions to the energy distributions and then use those to evaluate how much a particular energy deposit should count for. The other is to look at the overall occupancy (i.e. strips with hits) in an area and from that assume the particles follow Poisson distribution. In order to work on Pb+Pb data the energy fitting algorithm requires a centrality dependence, this is not yet implemented, so the method cannot be used for this analysis. However, it is still used to find the position of the MIP peak for the sharing algorithm, as the peak does not move with centrality. In this step the object handled in the analysis changes from being information for each strip (output from the sharing algorithm) to a single $d^2N/d\eta d\phi$ -histogram for the entire detector, which is also the format it is put into the AOD file in. At certain vertices there is an overlap in the coverage between the individual FMD rings, in those cases the average of the merged bins is saved. The histogram has 200 η -bins in the interval $[-4; 6]$ and 20 ϕ -bins. This means that the finer ϕ -segmentation of the outer rings is not really used. Eventually the analysis will be changed to take advantage of the 40 bins, but there are some analysis issues that need to be resolved first, and such is beyond the scope of this thesis to discuss.

Energy Distribution Fitting

As described in section 3.4.1 charged particles deposits energy according to a Landau distribution (actually it is a Landau distribution convoluted with a Gaussian distribution due to off shell

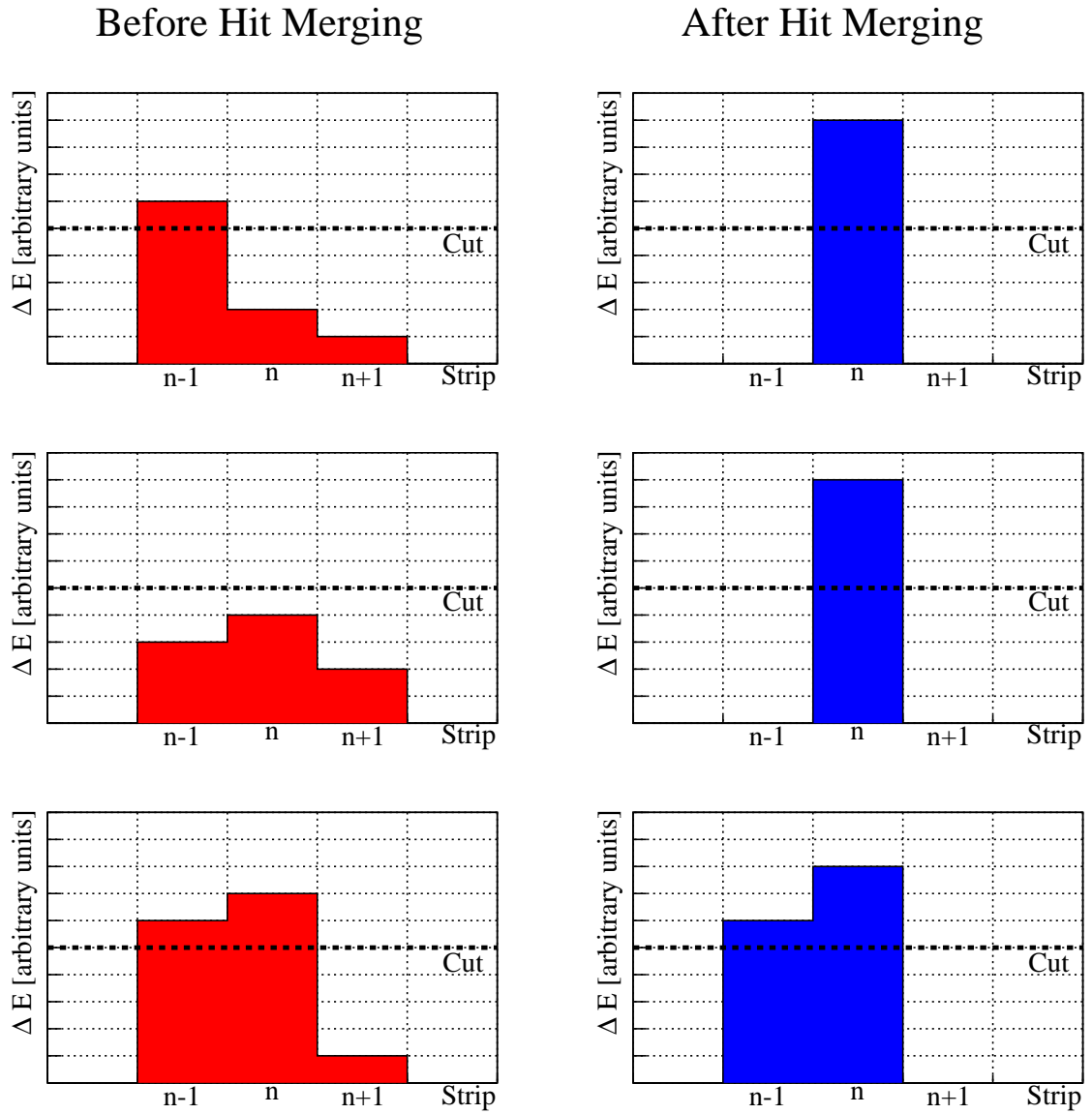


Figure 6.16: Different cases of sharing over three strips and how the algorithm handles it.

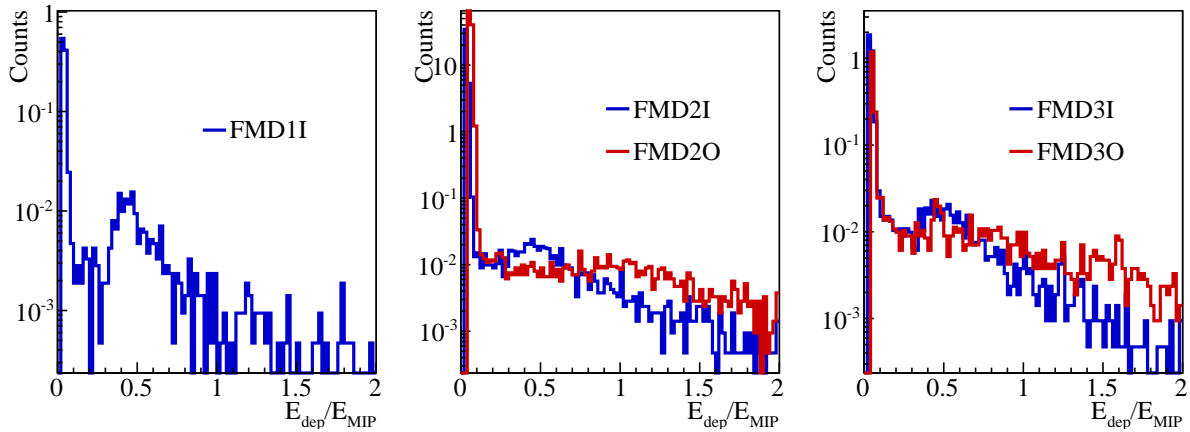


Figure 6.17: Signal from a run with no beam in the LHC. A large amount of background noise stretches all the way out under the primary signal. As the trigger in the run was completely random, it is likely that the signal is also present in physics runs. At the time of this writing the origin of the signal is not completely understood.

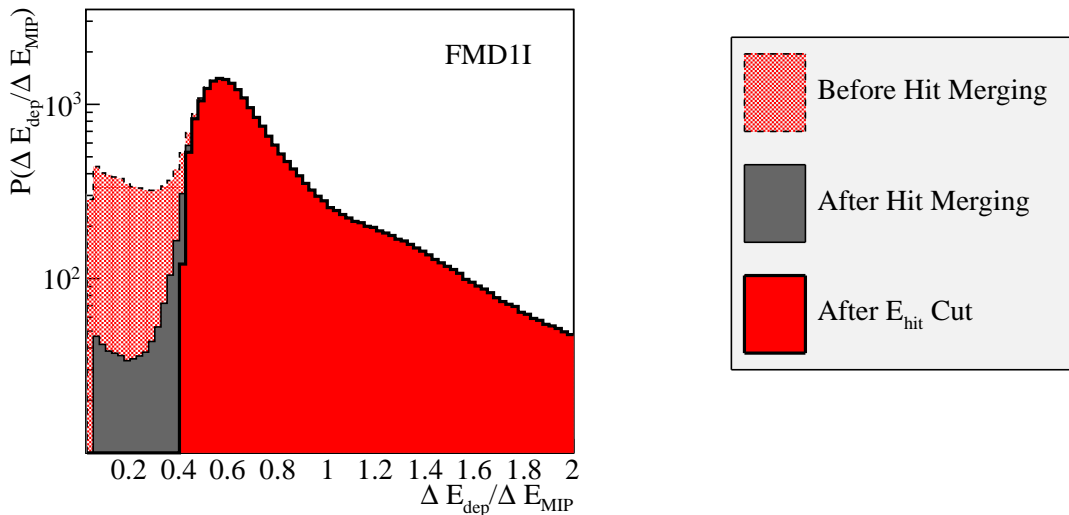


Figure 6.18: The energy distributions before and after hit merging. The coloured area indicates the area used after the E_{hit} cut-off.

excitations). The function describing the energy loss of up to N particles can be written as [75]:

$$F_N(x; C, \Delta_{mp}, \xi, \sigma, a) = C \sum_{i=1}^N a_i F(x; \Delta_{i,mp}, \xi_i, \sigma_i) \quad (6.2)$$

Where F is the convoluted Landau and Gaussian distributions. Even though F_N is made up of N convoluted functions it only has a few free parameters: The number of fitted particles, N , the standard deviation of the Gaussian, σ , a constant, the first peak of the Landau, $\Delta_{1,mp}$, the width of the first Landau, ξ_1 and the weight of the functions, a_i . Only the parameters of the first Landau are free, the rest are related to the first two via the following relations:

$$\Delta_{i,mp} = i\Delta_{1,mp} + \xi_1 i \ln i \quad (6.3)$$

$$\xi_i = i\xi_1 \quad (6.4)$$

$$\sigma_i = \sqrt{i}\sigma_1 \quad (6.5)$$

A derivation can be found in [75]. The algorithm fits up to $N_{max} = 5$ functions and the result is stored as a correction object for use during physics analysis. When a physics analysis is run the correction objects provide information about the parameters from the fits of up to five particles.

$$N_{ch} = \frac{\sum_n^{N_{max}} n F_n(E_{dep}, \Delta_{n,p}, \xi_n, \sigma_n)}{\sum_n^{N_{max}} F_n(E_{dep}, \Delta_{n,p}, \xi_n, \sigma_n)} \quad (6.6)$$

An example of the fits to energy deposited in FMD2 outer ring in minimum bias (all centralities) Pb+Pb collisions is seen in figure 6.19. It is seen that the fits for three or more particles describe the data very well, in general with about $0.5 < \chi^2/NDF < 3$. In order to really work on Pb+Pb data the correction object needs to have all the above information for different centrality bins, as the weight of the second and third Landau is larger for more central collisions due to the larger multiplicity. As mentioned above that is not yet implemented in the code. So the only thing used for this analysis from the fits is the position of the MIP peak.

The Poisson Method

In the Poisson method the FMD is divided into small regions. In one of these regions the true occupancy is defined as:

$$\mu = \langle N_{ch}/N_{channels} \rangle \quad (6.7)$$

and the measured occupancy as:

$$\mu_{meas} \equiv N_{ch}/N_{channels} \quad (6.8)$$

Assuming the charged particle multiplicity in such a region is distributed according to a Poisson distribution, the probability of $N_{ch} = n$ becomes:

$$P(n) = \frac{\mu^n e^{-\mu}}{n!} \quad (6.9)$$

Using this, and the fact that the measured occupancy is the probability of any number of hits the following equation is obtained:

$$\mu_{meas} = 1 - P(0) = 1 - e^{-\mu} \Rightarrow \mu = \ln(1 - \mu_{meas})^{-1} \quad (6.10)$$

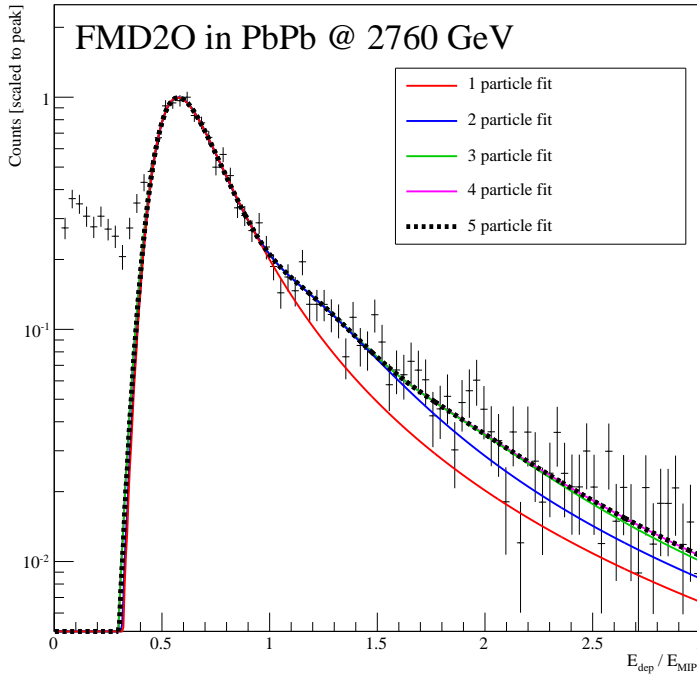


Figure 6.19: Energy distribution fitting with multiple Landaus (each convoluted with a Gaussian). For three or more particles the functions fit the data well. The data is minimum bias Pb+Pb data.

From this the mean number of particles in a strip becomes:

$$\begin{aligned}
 C(\mu) &= \frac{\sum_{n>0} nP(n)}{\sum_{n>0} P(n)} \\
 &= \frac{e^{-\mu}}{1 - e^{-\mu}} \mu \sum_{n>0} \frac{\mu^n}{n!} \\
 &= \frac{e^{-\mu}}{1 - e^{-\mu}} \mu e^{\mu} \\
 &= \frac{\mu}{1 - e^{-\mu}}
 \end{aligned} \tag{6.11}$$

μ can be calculated analytically, but for practical purposes it is calculated per event using equation 6.10 in the different regions in the FMD. This calculation μ_{meas} then goes into equation 6.11, and the multiplicity becomes:

$$N_{ch} = C(\mu_{meas}) \tag{6.12}$$

The implementation of the algorithm allows the user to choose the region in the FMD in (η, ϕ) -space. For the flow analysis presented here a single region covers 0.5 units in η and $\pi/10$ radians in ϕ . This corresponds to about 250 strips on average per region. Figure 6.20 shows how close $C(\mu_{meas})$ comes to $C(\mu)$ for different number of channels in a region. It is clear from the figure, that a higher number of strips would give a slightly more accurate result in the case of an occupancy of 95% or more. MC studies has shown for charged particle densities of $dN/d\eta|_{\eta=0} = 8000$ the occupancy in the FMD is 1 [57], and since it is about 1/5 of this number, the problems at high occupancy should not matter here. However, MC tests with different regions has shown that the regions mentioned here is optimal for flow analysis.

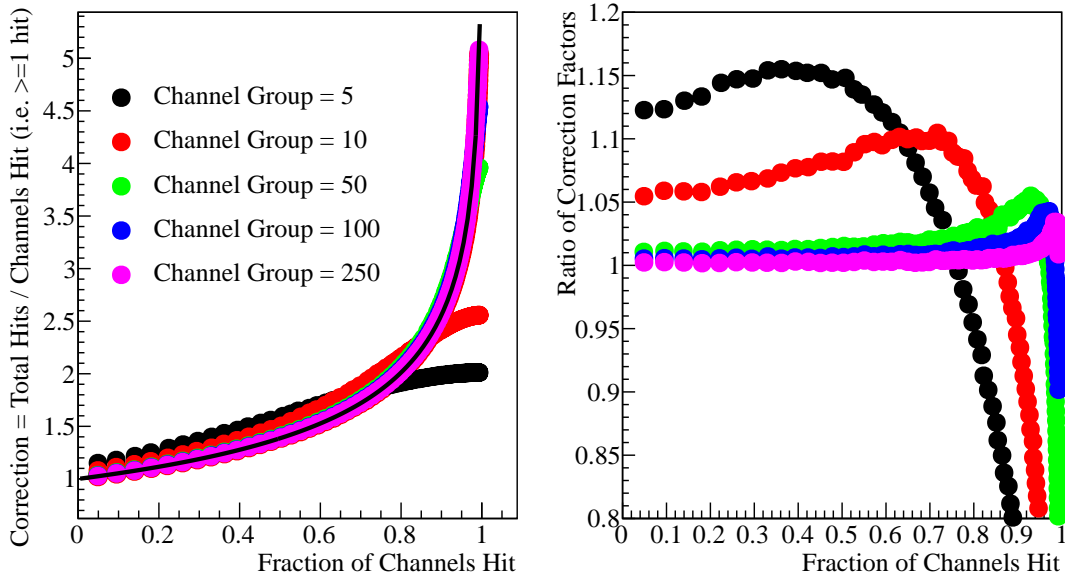


Figure 6.20: Poisson method correction for different numbers of channels in a group. In the left panel the analytical result is the black line, the coloured data points represent different numbers of channels in a group. In the right panel the ratios between the analytical result and the coloured points are shown. It is observed that for 250 channels in a group there is good agreement up to an occupancy of about 95%.

6.4.4 The FMD and SPD: Secondary Particles

As both tracklets and unused clusters are used from the SPD, and the FMD only provides hit information, particles that are not created in the collision or resonance decays are indistinguishable from particles created via interactions with detector or beam-pipe material. In the high-energy physics jargon the first type of particles are referred to as primary particles, while the latter is called secondary particles. The SPD and in particular the FMD are affected by a significant amount of secondary particles. Figure 6.21 shows the amount of secondary particles in the two detectors and their origin over the entire η -range. The plot is made with a Monte Carlo simulation of pp collisions using the GEANT3 transport code. The grey area in the plot shows the number of primary particles. It is seen that while the number of secondary particles hitting the SPD is only about 10% of the number of primary particles, the number goes up to as much as 200% in certain areas of the FMD. Most of these particles come from the support system of the Inner Tracking System and the FMD itself. In the most forward and backward regions the beam-pipe is the dominating contributor to secondary particle creation.

For particle multiplicity analysis this contamination with secondary particles is obviously a big issue. The analysis framework therefore contains correction objects made from MC simulations, which can be used to subtract event-by-event the average number of secondaries in a given (η, ϕ) -area from the measured number. The problem with this is that since the number of secondary particles in an event is not always the same, subtracting the average do not necessarily give the correct number on an event-by-event basis. Furthermore flow analysis is, as mentioned before, not dependent on the absolute number of particles, but rather relative variations in the number of particles. So if the material is simply an amplifier of the total number of particles, the flow analysis is unaffected. But if the material also scatters the particles in both the η and ϕ directions, it can change the flow signal. So it is necessary to study what happens with the direction of a particle when it interacts with the material (or the resulting particles after a

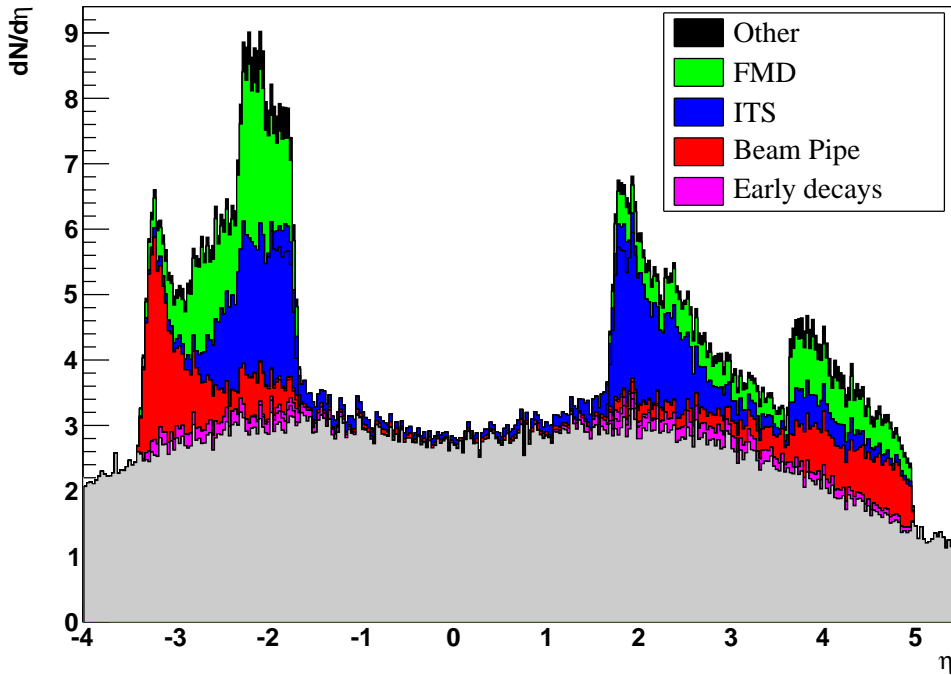


Figure 6.21: Proton collision MC data generated with PYTHIA and GEANT3. Gray area is primary particles in the FMD and SPD. Coloured areas are secondary particles hitting the FMD and SPD. It is seen that there are many more secondary particles in the FMD and that they are primarily from the FMD, ITS and beam pipe. In the legend "Other" refers to the TPC and other detectors.

collision with the material). This is done using a Monte Carlo event generator and transport code.

ϕ Blurring

Figure 6.22 shows the MC information of all secondary particles hitting the FMD or SPD. The true ϕ angle of the original (mother) particle is subtracted by the ϕ -angle as it is measured in the detector. A good fit is obtained with a function composed of a constant function and two Gaussians. The width of a strip in the FMD is shown as the two vertical bars to give an indication of how large the scattering angle is. The width of the Gaussian is not directly related to the azimuthal segmentation, as the same width is observed by only looking at the SPD. Finally a part of the particles seem to be completely randomly distributed, as seen by the constant function included in the fit. On average in the FMD 18% of the particles have a completely random azimuthal coordinate, while 40% is described by the wide Gaussian distribution. Finally 42% are part of the narrow Gaussian distribution. These numbers do change a little with pseudorapidity and azimuthal angle, but only with a few percent.

The wide Gaussian and flat background shows up in the measurement of the flow. To illustrate this figure 6.23 shows how such a blurring affects the measured elliptic flow component, v_2^{meas} . In the figure a clean flow signal is created from a $\cos(2\phi)$ function (green background). A blurred signal is then added by adding a random number of the distribution in figure 6.22 to the ϕ -coordinates of the clean signal. This is done twice for every particle that goes into the clean signal, thus simulating twice as many secondary particles as primary particles (yellow background). Finally the total signal is made by adding the clean and the blurred, simulating what is measured when there is both primary and secondary, blurred particles present (blue

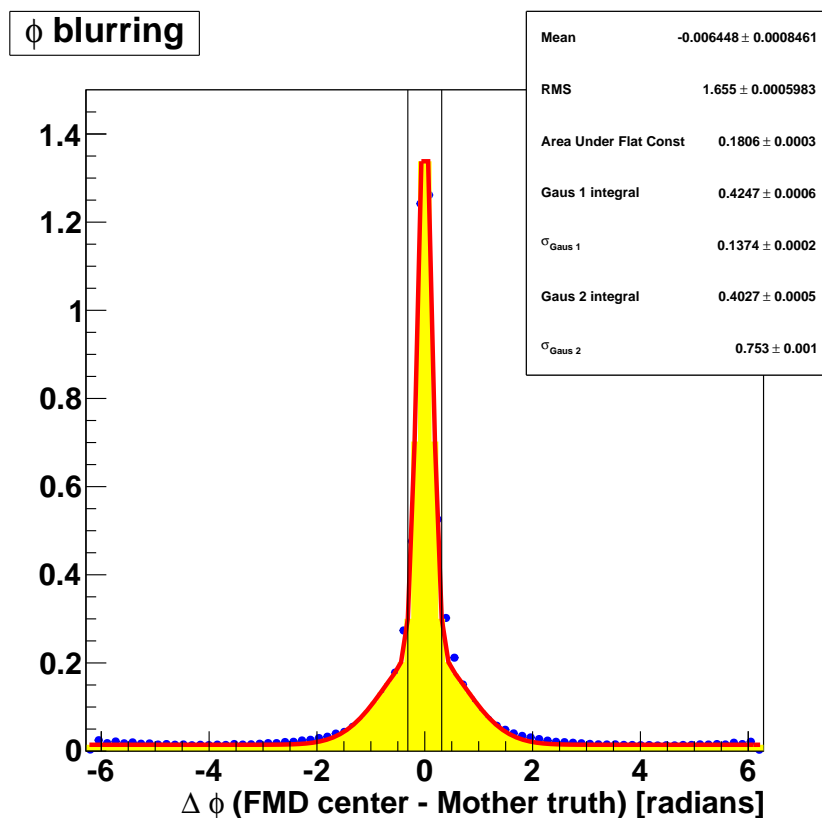


Figure 6.22: HIJING MC data with GEANT3 as transport code. The distribution shows the ϕ angle from where a secondary particle hit the FMD minus the ϕ angle of the mother particle. The distribution is normalized to 1. Two Gaussians and a constant function is fitted. The vertical lines indicate the ϕ -binning of the FMD, suggesting that the narrow Gaussian is a product of the limited resolution.

background).

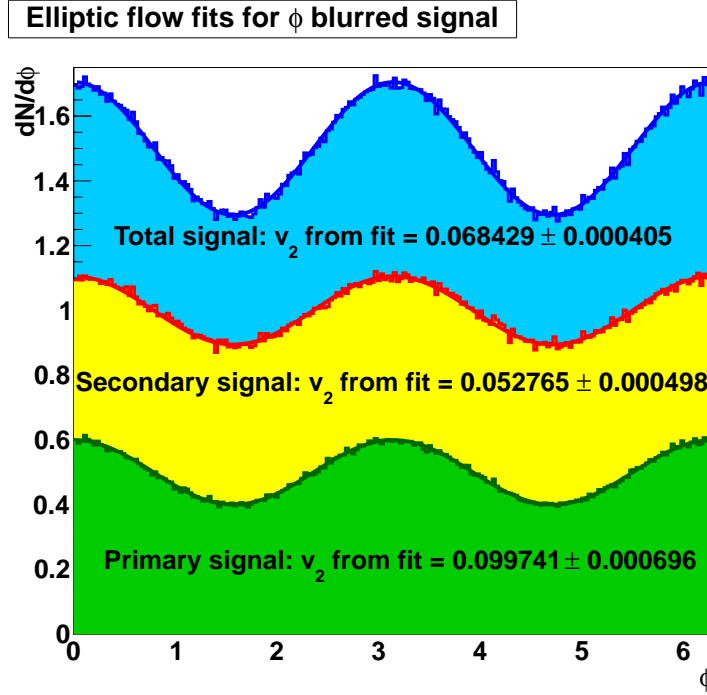


Figure 6.23: The effect of ϕ -blurring on a elliptic flow signal. The green distribution is a clean $\cos 2\phi$ distribution. In the yellow distribution each particle from the green distribution is blurred. This is done twice for every entry in the clean signal, to give the blurred signal twice the amount of particles of the green one. The blue is the sum of the green and the yellow, simulating both primary particles with a clean flow signal, and secondary particles with a blurred flow signal. Functions are fitted to each distribution to see how much the blurring affects the elliptic flow measurement.

The blurred signal shows almost a 50% loss of the original flow signal. As it turns out the measured signal can be written as:

$$v_2^{meas} = \left(\frac{N_{primary}}{N_{all}} \right) v_2^{true} + \left(\frac{N_{secondary}}{N_{all}} \right) v_2^{blurred} \quad (6.13)$$

where N_x represent the number of charged particle of type x in a given η -bin. Using this for the case of the FMD it is seen that v_2^{meas} is around 32% smaller than v_2^{true} i.e., the measurement gets a very significant bias from the large amount of secondary particles present. This means that while the correction for secondaries in the ESD-to-AOD framework does not matter for flow analysis, a correction for the suppression of the flow has to be made. The correction is made from a full MC simulation, and is discussed in the next two sections of this chapter. At this point it is worth noting two things; first the SPD is much less affected by the secondaries. Secondly, the only previous elliptic flow analysis over a wide pseudorapidity range, namely the one done by PHOBOS incorporated corrections of a similar size, due to the exact same problem [76]. By doing plotting figure 6.22 in η -bins, no pseudorapidity dependence is observed. So it is mainly the ratio between the number of primary and secondary particles that determine how much v_2^{meas} is reduced for the FMD. However, the scattering angle is very dependent on the momentum of the particle (high momentum particles scatter at smaller angles in general), and thus the underlying p_t spectrum and v_2 as a function of p_t plays an important role in the correction. Finally the scattering is also present in θ , thus having a non-trivial effect on the flow measurement as a function on η . This is made clear in Section 6.5.2.

6.4.5 The FMD and SPD: Acceptance Issues

While both the SPD and FMD were built with completely uniform azimuthal acceptance in mind this is not actually the case. In FMD1 a chip has seized functioning, causing a small hole in the azimuthal acceptance at the most forward rapidities. For the SPD the problem is more severe. Lack of cooling has rendered parts of the detector unable to perform a measurement. As such there is acceptance in the entire pseudorapidity range, but the azimuthal coverage is quite limited in some regions. A $d^2N/d\eta d\phi$ map of the coverage is shown in figure 6.24. Note that the holes shifts slightly at different vertices. In the figure it is seen that particularly for $\eta \in [0; 1.7]$ in the SPD there is a non-uniform azimuthal coverage.

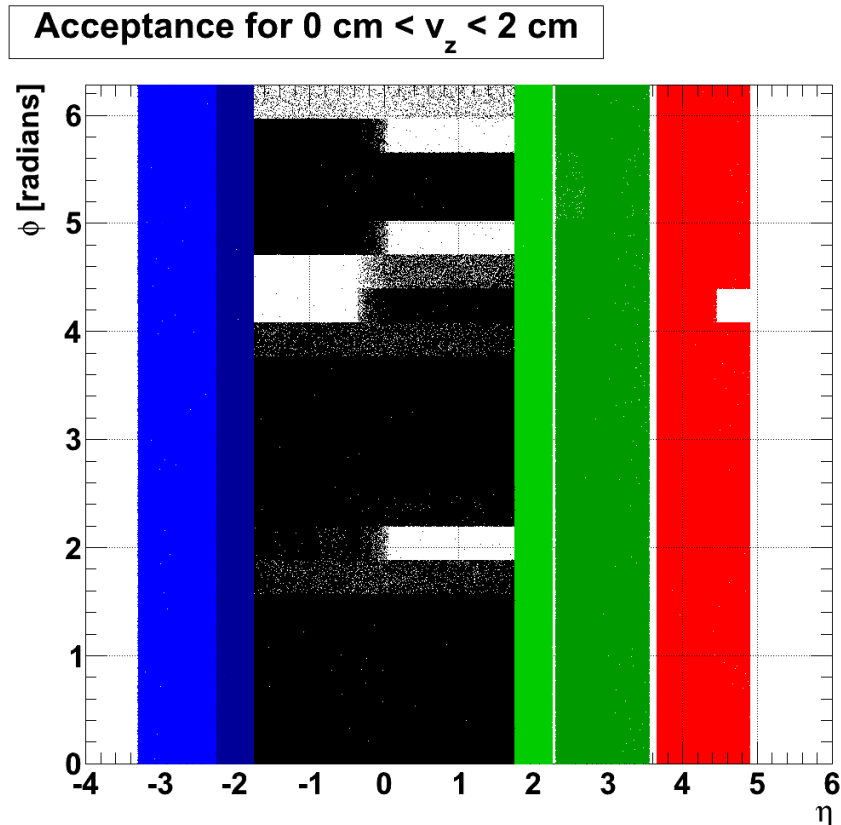


Figure 6.24: Azimuthal coverage in the SPD and the different rings in the FMD. For the FMD there is a non-uniform coverage for $\eta > 4.5$. For the SPD it is in the entire η range.

To correct for this the analysis framework incorporates a so-called acceptance correction. Once again it only concerns the total number of charged particles, which is irrelevant for flow analysis and is in place to be used in multiplicity analysis. Furthermore, as shown above the flow analysis utilized here contains equation to correct for lack of acceptance. There are two things to be mindful of though; As mentioned the holes in the acceptance shifts slightly at different vertices, thus it is necessary to do the analysis in vertex bins in order not to shift the acceptance from event to event in a given η -bin. Furthermore it has been shown above that even with acceptance terms, there is a small bias if the reference flow is not carefully chosen such that the acceptance does not shift over the phase space used. The azimuthal coverage at different vertex coordinates is shown in Appendix D.

There is also a small acceptance correction in place to correct for the holes in the corners between the FMD ring sectors, that is not used in this analysis either due to the correction terms in place in the method equations. And that concludes the data processing as it is put in

AOD files in two $d^2N/d\eta d\phi$ -histograms. One for the FMD and one for the SPD. Along with the histograms, vertex, trigger and centrality information.

6.5 Full Monte Carlo Simulations

6.5.1 Flow with an Afterburner

A full MC simulation is made with HIJING as the event generator and GEANT3 as the transport code. In between the two flow, is artificially added with the *AliGenAfterBurnerFlow* class. The class provides various parametrization of directed and elliptic flow, but the setup used here just adds a simple p_t dependence, no centrality dependence, and most importantly no η dependence. The analysis of both $v_2\{2\}$ and $v_2\{4\}$ is done on three levels; on MC truth information from HIJING and the afterburner, on the track references (see Section 4.3.3) provided by GEANT and finally on the simulated FMD and SPD data. This along with the fact that the η -distribution is flat allows for two important checks. First a comparison between the simulated detector data and the track references, which shows how well the data processing algorithms count the particles. Secondly a comparison between these and the MC truth information shows if indeed the secondaries lower the measured signal, as expected from the plots and equations above.

The result is seen in figure 6.25. The measurements with simulated data and track references agree very well. Furthermore a suppression on average of about 30% is observed in track references and data, which is in good agreement with the predicted 32% effect from ϕ -blurring in secondaries. In fact by comparing the amount of secondaries divided by primaries vs. η in figure 6.21 it is clearly seen that the measured signal goes down, as N_{sec}/N_{prim} goes up. For the SPD the agreement between track references and data is less convincing. The reconstruction used in the MC is the so-called pass 1, which the author has been made aware has some problems with the SPD tracklet algorithm. For a more realistic comparison of the SPD data see the AMPT MC below, which is the so-called pass 2 version of the reconstruction.

6.5.2 Flow with AMPT

As an official ALICE production on the Grid a test simulation using AMPT was made. There are a few bugs in the current AliRoot implementation of AMPT. While none of them are so serious as to render the data useless for this analysis, it did mean the production was stopped when the bugs were discovered, and because of that the statistics is limited. More importantly, and unfortunately for this analysis the "string melting" option was not turned on in the simulation. As mentioned in section 4.3.2 string melting has rather large implication on v_2 versus η , and with the option off the elliptic flow drops to 0 around $\eta = \pm 4$. This means the AMPT production cannot be used for MC correction on real data, though it does give a good indication on how η scattering affects the measurement when the flow has a pseudorapidity dependence.

The result of the analysis on the AMPT simulation is seen in figure 6.26. As before the simulated detector data and track references agree very well. However, the signal is less reduced away from mid-rapidity, than it was for the HIJING+Afterburner simulation. This is due to the η scattering. There are two opposing effects in the η scattering process:

- Particles originating at mid-rapidity (thus "carrying" a large flow signal) is scattered off in the forward or backward directions. Thereby increasing the flow signal at these rapidities where the particles in general "carry" a smaller flow signal due to the pseudorapidity dependence.
- Particles originating at forward or backward rapidities are scattered towards mid-rapidity. These particles lower the signal at mid-rapidity, as they were created at forward rapidities where the flow signal is lower.

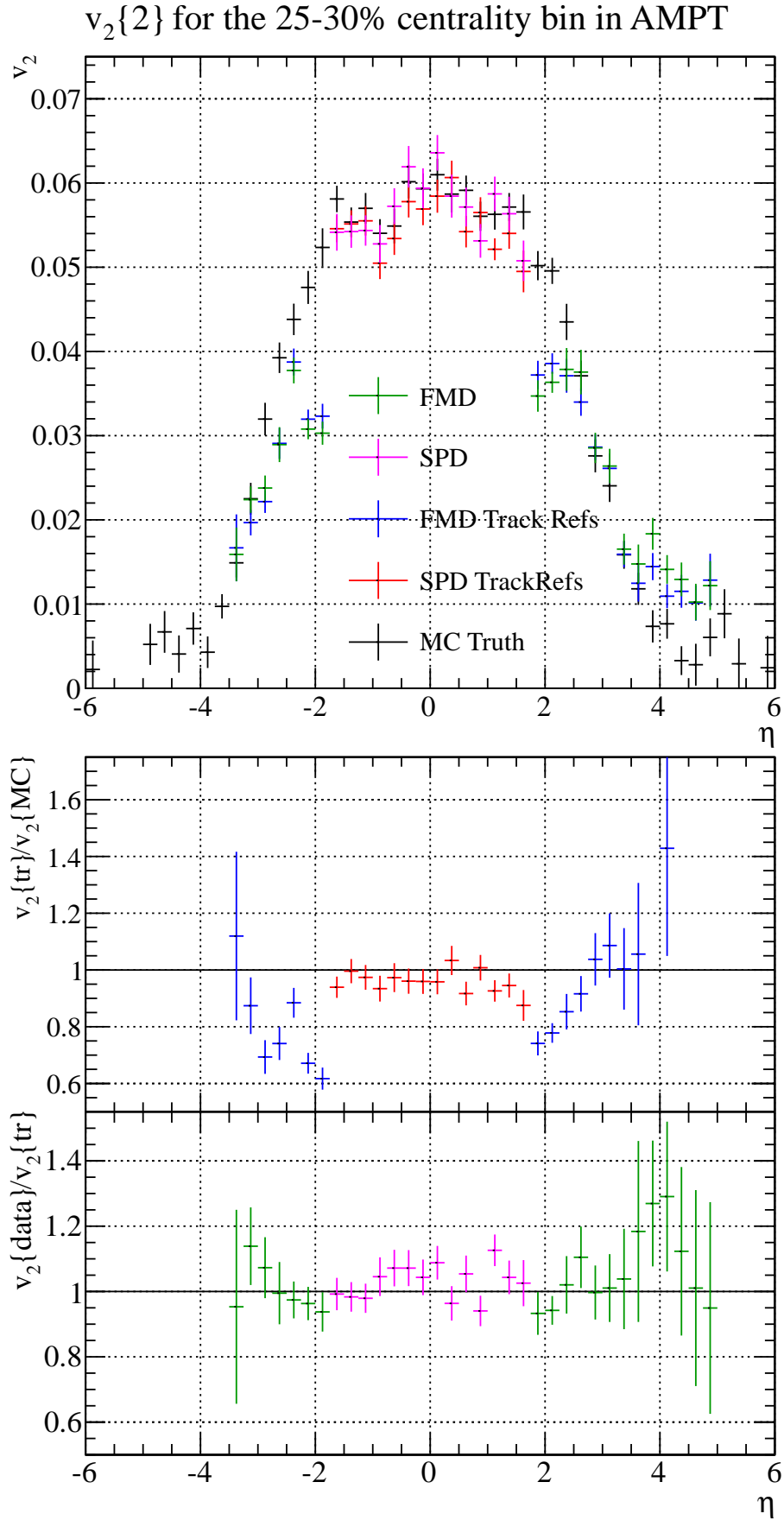


Figure 6.26: AMPT MC of Pb+Pb collisions at $\sqrt{s_{NN}} = 2.76$ TeV. Due to limited statistics only results for the two-particle cumulant method is shown. Other centralities yield similar results.

Of course the particles do not "carry" a flow signal, as flow is a collective phenomenon. But it is easier to understand the effect thinking of the individual particles as carrying a flow signal. Remembering that there are more particles at mid-rapidity than at high rapidities, it is clear that the first effect is the dominant one. Thus the overall result is a higher flow signal in the forward and backward directions. Whether this is very sensitive to the η -distribution or not is studied in chapter 7. The sensitivity to this is very important in determining the systematic uncertainties coming from the MC correction. For the SPD a better agreement between track references and data than with the afterburner is observed, indicating that the issues in the HIJING MC above are related to the tracklet algorithms issues in pass 1. There is also a good agreement between track references and data, which is a consequence of the very low amount of secondaries in the SPD. Only a very small reduction in the track reference signal is observed.

6.5.3 No Flow

One more thing can be obtained from the HIJING simulation. As mentioned physics in HIJING does not create flow, and as such the analysis should yield $v_2 = 0$ when run on the simulated data, except for a contribution to the two-particle cumulant from non-flow.

The result of this analysis is seen in figure 6.27 and 6.28. For v_2 vs. centrality it is observed that the two-particle cumulant is affected by non-flow at all centralities, which becomes significantly larger for peripheral events. Curiously the data and track references show a higher v_2 than the MC truth, which suggests that the secondary particles carries some non-flow. The points for the four-particle cumulant method generally has large errors and are scattered over a large v_2 range. This is understood as a consequence of there being no flow, and the method being unbiased by non-flow. In that case the reference flow becomes ≈ 0 , which causes problems for equation (5.48) where the denominator is ≈ 0 . As a consequence, in figure 6.28 only $v_2\{2\}$ is shown. In this case a structure is seen in the FMD data and track references. For $v_2\{4\}$ no clear structure is observed, which suggests it is non-flow. At the times of this writing it is not understood what the source of this non-flow is, but it might be related to non-flow in the secondary particles. The same structure is observed at all centralities, but it scales with centrality in a similar way as in figure 6.27. If it is non-flow from secondary particles it is likely correlated with structures in the detector geometry. It is obvious that if a particle collides with detector material and produce new particles, they will show up as non-flow in the detector. Since that is uncorrelated with the reaction plane in the collision, the effect should not be seen in cases where there is flow present. That is exactly what was observed in the AMPT MC, where the data and track references yielded a lower v_2 than the MC truth. So the data suggests it to be related to secondary particles and detector geometry. But unfortunately time constraints did not make it possible to study the effect further. But it is an important point to keep in mind for the real data analysis.

6.6 Track Reference Analysis

Making full Monte Carlo simulations requires a lot of computing time and flow analysis requires a lot of events. These two facts add up to more CPU power than has been available to this author. Because of this, in order to get enough statistics to make the necessary secondary correction only official ALICE MC production on the GRID are an option. Unfortunately these are limited to a lot of regular HIJING productions (with no flow afterburner) and the small AMPT production with no string melting described in the previous section. So the only option is HIJING.

As mentioned in section 4.3.1 the physics implemented in HIJING does not produce flow. Running the afterburner after the reconstruction is not doable, so it is not possible to add flow to the simulated FMD and SPD data. It was observed in the previous section that the simulated

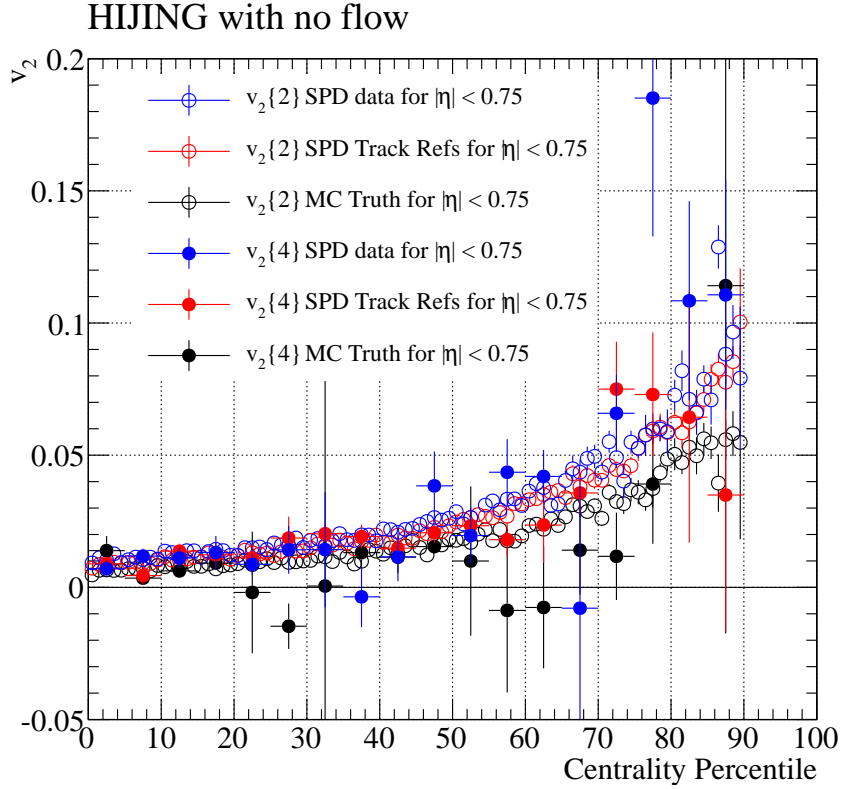


Figure 6.27: $v_2(\text{cent.})$ for a HIJING Pb+Pb simulation at $\sqrt{s_{NN}} = 2.76$ TeV. The two-particle cumulant (open points) is affected by the non-flow in the simulation. The four-particle method is having trouble because there is no flow present.

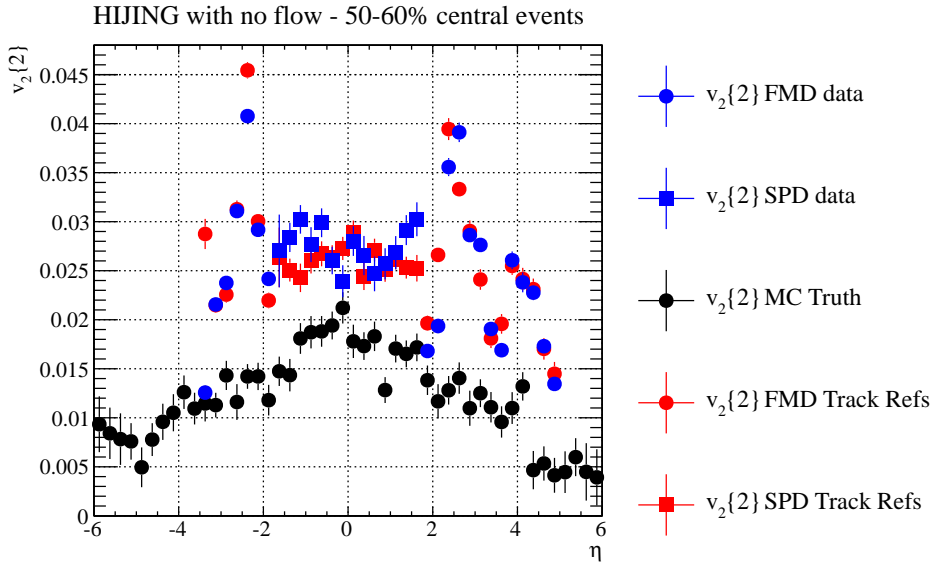


Figure 6.28: $v_2(\eta)$ for a HIJING Pb+Pb simulation at $\sqrt{s_{NN}} = 2.76$ TeV. The two-particle cumulant (open points) is affected by the non-flow in the simulation. For the track references and data, structures are observed which are not present in the MC truth analysis. This suggests they are from secondary particles, which both track references and data is affected by.

detector output and the track references agree reasonably well. And adding a flow signal to the track references is an easy task. In this way a correction object is made by adding a flow signal to the track references and the MC truth particles, and comparing the analysis results between the two. By varying the input flow it is also possible to estimate the systematic uncertainties using this method. Furthermore HIJING simulations with added and reduced material in the detectors are also available on the Grid. This makes it possible to estimate the systematic uncertainties coming from the geometrical description of ALICE, which produces the secondary particles. All of this is done in Chapter 7.

The flow signal is added by giving each particle a weight, $w(\eta, p_t, c)$ according to the pseudorapidity and transverse momentum of its mother particle i.e., not only pseudorapidity dependence, but also transverse momentum and centrality dependence is added. The η dependence is Gaussian. The p_t dependence is added because, as mentioned above the scattering angle is larger for smaller p_t , thus the underlying $v_2(p_t)$ is also important. The input p_t and centrality dependences uses the values measured by ALICE from [17] seen in figure 2.9 and 2.10. For the p_t the average of $v_2\{2\}$ and $v_2\{4\}$ from the 40 – 50% centrality bin is used. In both cases a linear extrapolation is used for values between the data points or outside the measured range. The result is shown for one of the centrality bins in figure 6.29. The correction factors are also obtained directly by dividing the true values with the track reference values, and are seen in the bottom plot on the figure. The truth analysis is done in 200 ϕ -bins, while the track reference analysis is done in only 20 ϕ -bins, thus the correction of $\sim 2\%$ due to the segmentation, observed in section 6.1 is also incorporated in the correction. On average the correction ends up being about 30% in the FMD and 5% in the SPD.

6.7 Analysis of Real Data

In this section the analysis is run on data from the 2010 LHC heavy ion run. For a complete list of the runs analysed see Appendix E. The analysis is done on the second pass of the reconstruction, meaning that the reconstruction code has been updated since the data was taken to optimize certain algorithms, like the one used for SPD tracklets. During the 2010 Pb+Pb run 30M events were recorded by ALICE. The runs chosen for this analysis contains about 18M of those events. The last 12M are spread over a large number of smaller runs, and time constraints prevented those from being analysed. Of these 18M events, 7.5M are used in this analysis. The 10.5M not analysed from those events either did not make it into the AOD files due to GRID inefficiencies, or were discarded due to the physics selection, centrality selection or vertex cuts applied for the analysis. As mentioned in section 6.4 there is non-uniform azimuthal acceptance in some parts of the SPD and FMD. In order for this not to move around too much due to different vertex z -coordinates, the analysis is done in vertex-bins in z and are then added together in the final step of the analysis. Originally it was planned to do it in 1 cm vertex bins, but when running the analysis in the full data set, the histograms came out empty. By changing it to 0.2 cm vertex bins the problem was solved, except for the four-particle cumulant method in the FMD. The problem is currently not understood, but the fact that the problem arise when there are many events in a vertex bin suggests a numerical problem. This also provides an automatic division of the data into sub-samples, so the statistical uncertainty can be estimated from the spread of those. This also solves another problem, as it was shown in section 6.3 that the preferred method to estimate statistical uncertainties in the case of a non-uniform acceptance is done by dividing the data into smaller samples. The amount of secondary particles in an η -bin also changes with the vertex, to avoid too large a bias from this effect only events with a vertex in the range $v_z \in [-5; 5]$ cm are chosen. The vertex distribution is shown in figure 6.30. Finally to make sure none of the cuts applied interfere with the centrality selection, i.e. that there is no specific centrality (or centralities) where more events are cut away a plot of the centrality distribution is shown in figure 6.31. The distribution is completely flat up to about

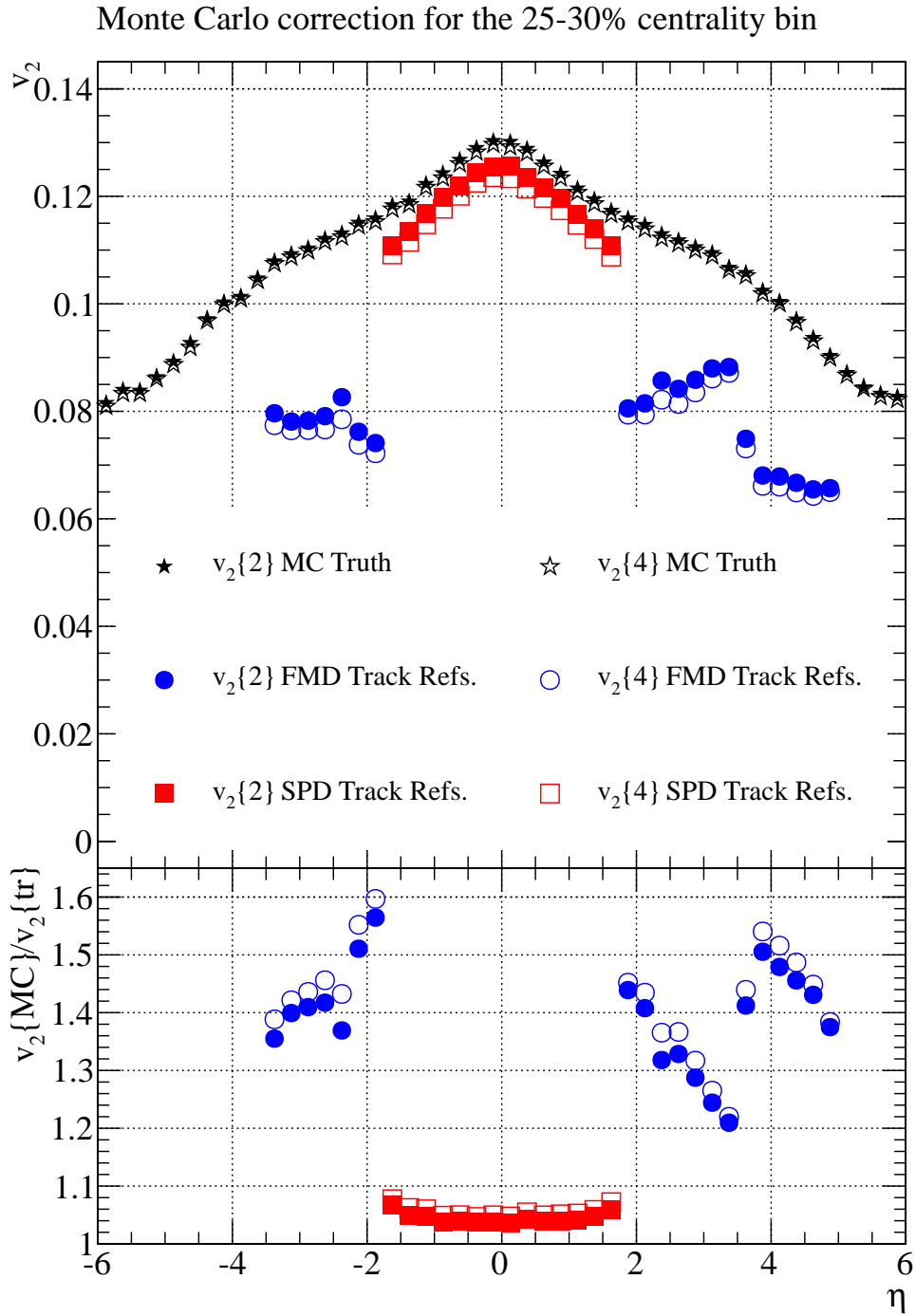


Figure 6.29: In the top plot $v_2(\eta)$ for the 25-30% centrality bin is shown for MC truth and track references is shown. With $v_2(p_t)$ as the average of the measured values for $v_2\{2\}$ and $v_2\{4\}$ in the 40-50% centrality bin. $v_2(\text{cent})$ is from the measured $v_2\{4\}$ values. An overall scaling with η follows a Gaussian. The non-Gaussian shape of the final $v_2(\eta)$ is due to changes in dN/dp_t with rapidity. The bottom plot is the correction applied to real data for this centrality bin.

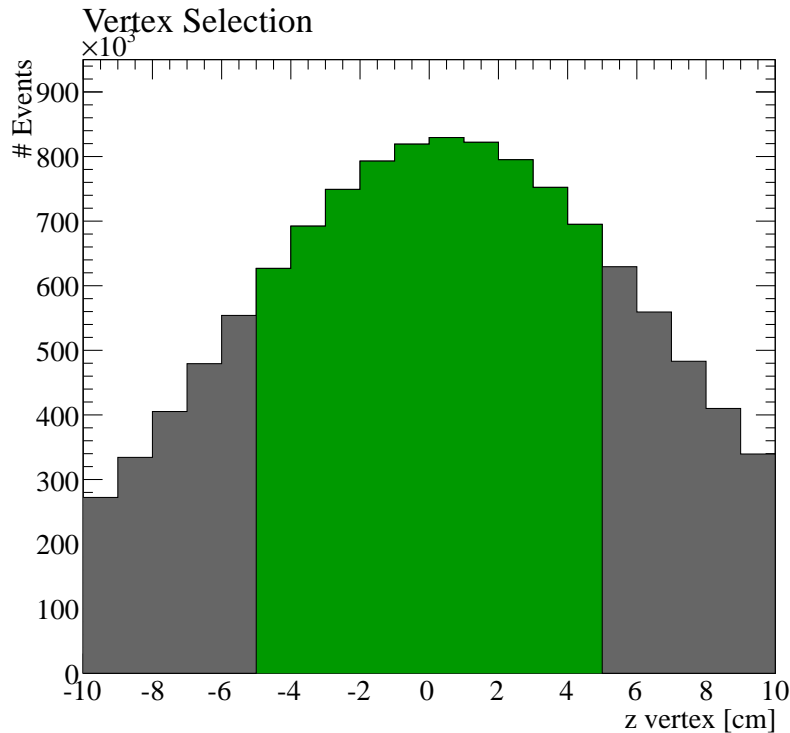


Figure 6.30: Vertex distribution in the selected events. The green area indicates the vertices used.

90% suggesting no bias in the event selection.

Section 6.2 showed that care is necessary when choosing the particles used for the reference flow, when there are fluctuations and non-flow present. In real data both are present, and it has never been studied how they change with pseudorapidity. To avoid a bias from non-flow the differential flow is always calculated with a reference flow from the same region. To avoid an unknown bias from fluctuations the reference flow cannot be over too wide an η -range. To find the optimal η -binning, the analysis is done first with only one reference bin. Then with two reference bins, then four, and so on until the result of the cumulants no longer changes. The reference flow should cover as many η -bins as possible without causing unwanted bias, in order to get the best differential result. In figure 6.32, first the entire pseudorapidity range is used to calculate one reference flow, which is then used on all particles. In the second case two reference flows are used, one using FMD data and the other using SPD data. They are then used in the differential flow measurements in the FMD and SPD respectively. As is seen there is a large difference in this case, which proves that the fluctuations do change with pseudorapidity in data. This is a new result, and the fluctuations should be studied in much more detail, but that is beyond the scope of this thesis. Furthermore the structures, in particular in the FMD data, due to the secondaries is also present in the data. They resembles the structures seen in the track reference analysis closely.

In figure 6.33 two more cases are shown. For the red points four η -bins are used for the reference flow: $|\eta| \in [3; 5]$, $|\eta| \in [1.75; 3]$, $\eta \in [-1.75; 0]$ and $\eta \in [0; 1.75]$. The binning is chosen such that the azimuthal coverage for the reference flow in the SPD does not change in a single reference bin. And such that FMD data is not used as reference for SPD data and SPD data is not used as reference for FMD data. For the blue points there are nine reference flow bins: $|\eta| \in [4; 5]$, $|\eta| \in [3; 4]$, $|\eta| \in [1.75; 3]$, $\eta \in [-1.75; -1]$, $\eta \in [-1; 0]$, $\eta \in [0; 1]$ and $\eta \in [1; 1.75]$. With these two binning the four-particle cumulant measurements agree in the SPD. The four-

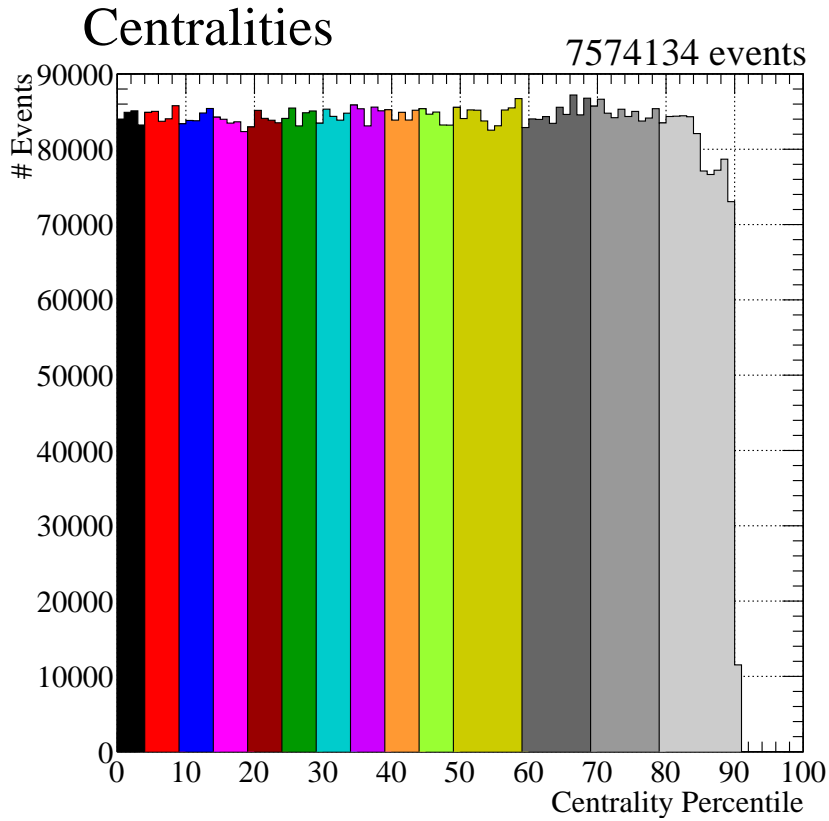


Figure 6.31: Centrality distribution from the events analysed. The coloured binning show the binning used.

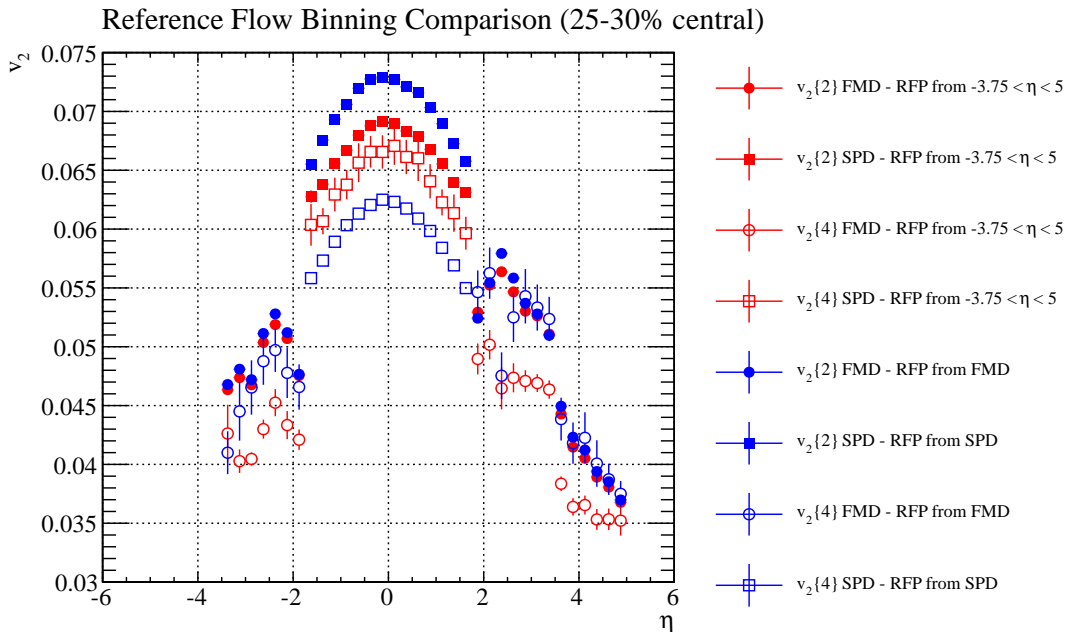


Figure 6.32: Analysis done on 7.5M events. Results from two different choices of reference flow binning is shown. In one (red point) all particles are used for a single reference flow measurement, used for the differential measurement in all bins. In the other (blue) there are two reference bins. One for the SPD and one for the FMD. A large discrepancy between the two is observed, which is due to changing fluctuation over the wide η range.

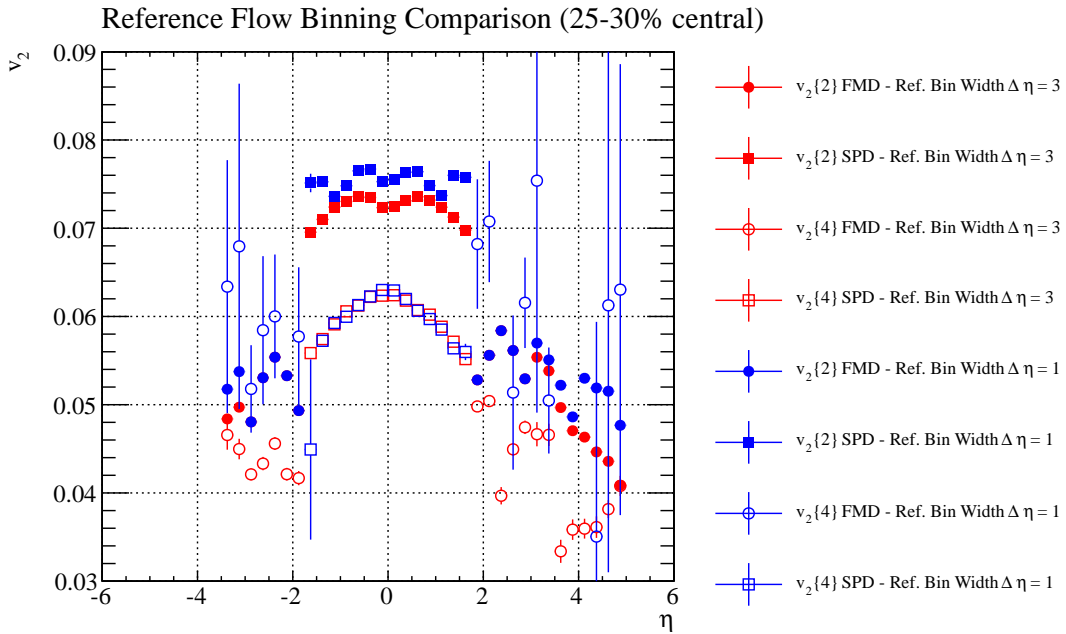


Figure 6.33: Analysis done on 7.5M events. Results from two different choices of reference flow binning is shown. In one (red points) four reference flow bins are used. In the other (blue) there are nine reference bins. A good agreement is observed for the four-particle cumulant method in the SPD, suggesting that the bias from fluctuations does not change in the chosen reference flow bins.

particle cumulant has problems in the FMD, so it cannot be used to estimate if the bias from fluctuations is under control with this binning. As mentioned the two-particle method is affected by non-flow, this is why the blue $v_2\{2\}$ points are slightly above the red ones. For the smaller reference flow binning the multiplicity in each bin is smaller, and the contribution from non-flow becomes larger. Due to the fact that the four-particle method agrees in the SPD, and that the two-particle method results are close enough to be explained by non-flow, the reference flow is done in bins of $|\eta| \in [3; 5]$, $|\eta| \in [1.75; 3]$, $\eta \in [-1.75; 0]$ and $\eta \in [0; 1.75]$ for the final analysis.

In figure 6.34 and 6.35 the results with the four η -bins for the reference flow is shown for more centralities. In order to get the final results the MC correction has to be applied, and the systematic errors estimated, this is done in the next two chapters.

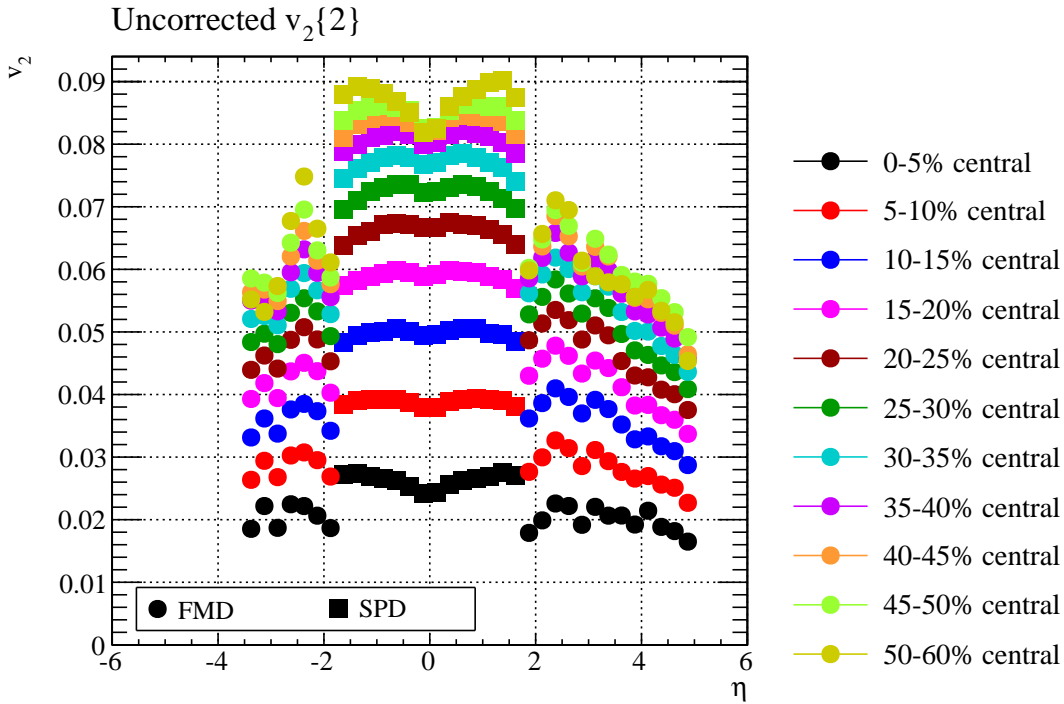


Figure 6.34: Analysis done on 7.5M events. These are the uncorrected results for the two-particle cumulant method at different centralities.

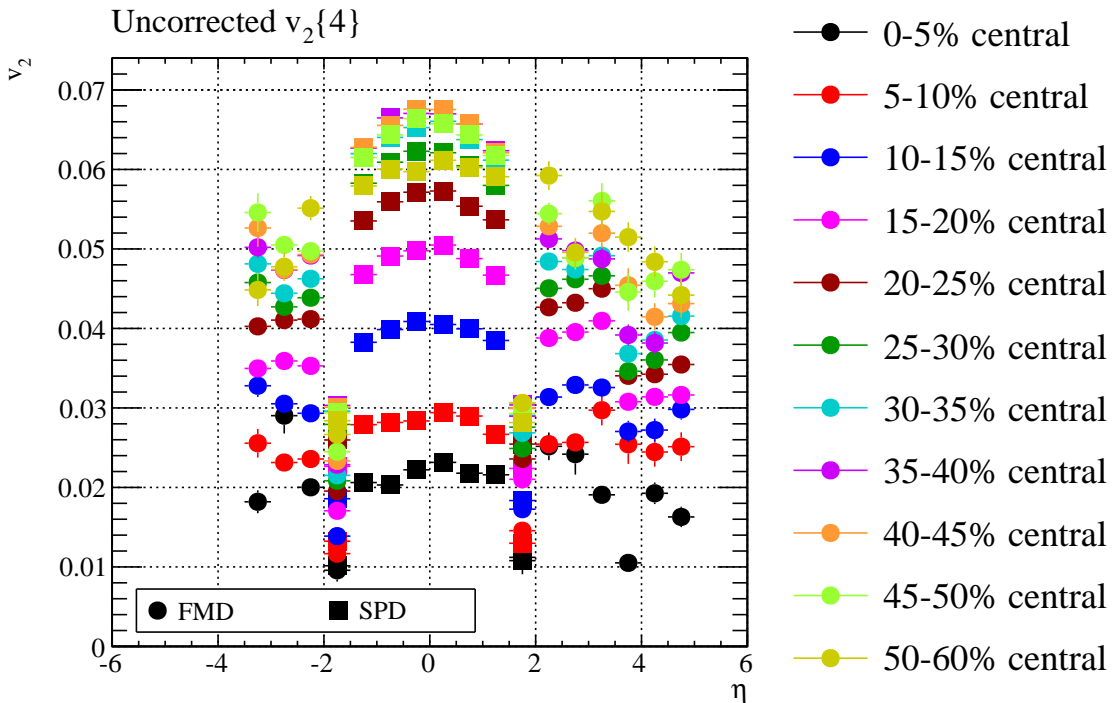


Figure 6.35: Analysis done on 7.5M events. These are the uncorrected results for the four-particle cumulant method at different centralities.

Chapter 7

Systematic Error Estimates

In this chapter the systematic errors are studied and calculated. The dominating error contribution is from the Monte Carlo correction applied to correct for the ϕ blurring using track references. Though other things, such as the particle counting method and sharing correction also factors in, albeit with much lower contributions. First plots of the systematic error studies are presented for each source. Then all the observed uncertainties are added together in a table, and the final systematic errors are estimated pseudorapidity intervals, both for overall systematic errors, point-to-point and the total systematic errors.

7.1 Error Contribution From Hit Merging and Particle Counting

In the previous chapter it was shown how the hit merging and particle counting algorithms work for the FMD. It was shown that there is some noise that is not removed before the particle counting is done. Furthermore the particle counting relies on the particle distribution following Poisson statistics. Both of the algorithms thus contribute to the systematic errors. There are two way to estimate the systematic errors from these algorithms. One is to vary the cuts for them, and see how much they change. But since this analysis is done by correcting SPD and FMD data with information from the track references, another approach is to estimate the systematics directly from the discrepancy between data and track references in the MC simulations presented in Section 6.5. Similarly for the SPD the track references do not get any clustering or tracklet algorithms applied. So while the particle counting is more simple, a systematic error may arise when correcting to track reference information. As mentioned in Section 6.5 the SPD tracklet algorithm is not optimized in the HIJING production with an afterburner, so that cannot be used for the SPD estimate. And since the AMPT production only contains flow for $\eta \in [-4; 4]$ that one cannot be used for the FMD. So the AMPT is used for the SPD estimate and the HIJING with afterburner is used for the FMD estimate. Figure 7.1 shows $v_2\{\text{data}\}/v_2\{\text{track references}\}$ for both detectors. The estimate is made only for the two-particle cumulant method, as the error is independent of method, and the four-particle cumulant has too large uncertainties due to limited statistics being available. This contributes to the overall systematic error.

7.2 Errors from the MC Correction

The MC correction contains an input elliptic flow, depending on pseudorapidity, transverse momentum and centrality. So each of these three variables contribute to the systematic error. Furthermore it is assumed that the correction factor does not depend on the elliptic flow of identified particles. But that assumption also needs testing. Finally the correction is mostly for ϕ blurring, and it was shown on the previous chapter that the correction is very dependent

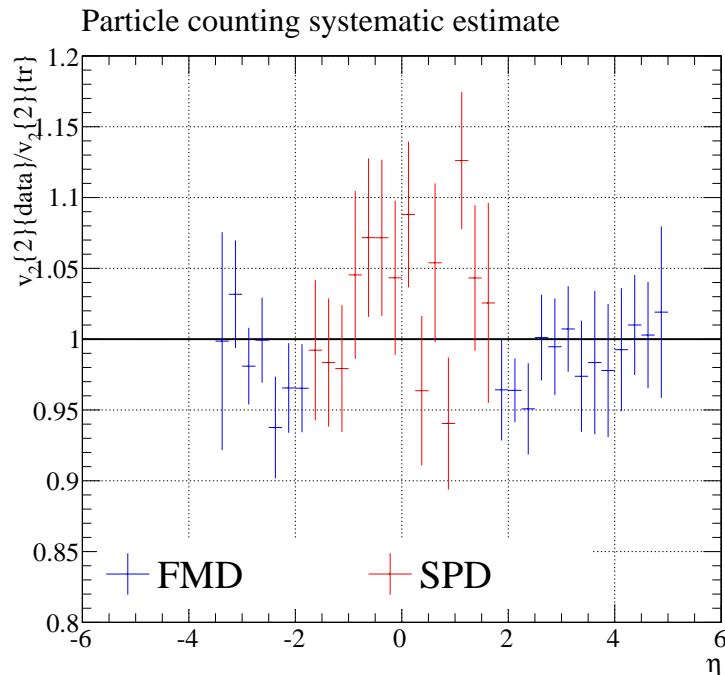


Figure 7.1: Difference between data and track reference measurements. The SPD points are from an AMPT simulation and the FMD points are from a HIJING with a flow afterburner.

on the N_{prim}/N_{sec} ratio. That ratio is essentially obtained from the geometrical description of the detector in the analysis framework. The geometrical description may not be perfect, and so what is called the material budget is also an important factor in the systematic errors from the MC correction. This contributes to the overall systematic error.

7.2.1 p_t Contribution

The input p_t distribution in the correction is the average of the values measured by ALICE for $v_2\{2\}$ and $v_2\{4\}$ in the 40 – 50% centrality bin. The real p_t distribution is known to be somewhere between these two, though exactly where is unknown due to the contribution from non-flow¹. Furthermore the p_t distribution may vary a little with η . In order to determine how sensitive the correction is to the input p_t dependence the input p_t is varied by only using the $v_2\{2\}$ measurement, and only using the $v_2\{4\}$ measurement. The results are shown in figure 7.2 and 7.3, where variations of up to 10% are observed. This contribution is to the point-to-point systematic error.

7.2.2 η Contribution

In the correction object, $v_2(\eta)$ is approximated by a Gaussian distribution. In order to test how sensitive the correction is to the shape of the distribution, two other Gaussian distributions are tested. One of the Gaussian distributions has smaller spread than the one used for the analysis, the other has a larger spread. The results are shown in figure 7.4 and 7.5. Particularly for the Gaussian with the small spread (termed narrow in the figure) a large sensitivity is observed. This is due to the fact that the flow is so small at the most forward rapidities, that the effects discussed in section 6.5.3 starts to dominate for the two-particle cumulant. Thus the systematic error estimate for the η sensitivity should either be estimated for both $v_2\{2\}$ and

¹The contribution from flow fluctuations is identical, but opposite for the two, and thus with known non-flow the fluctuations can also be determined.

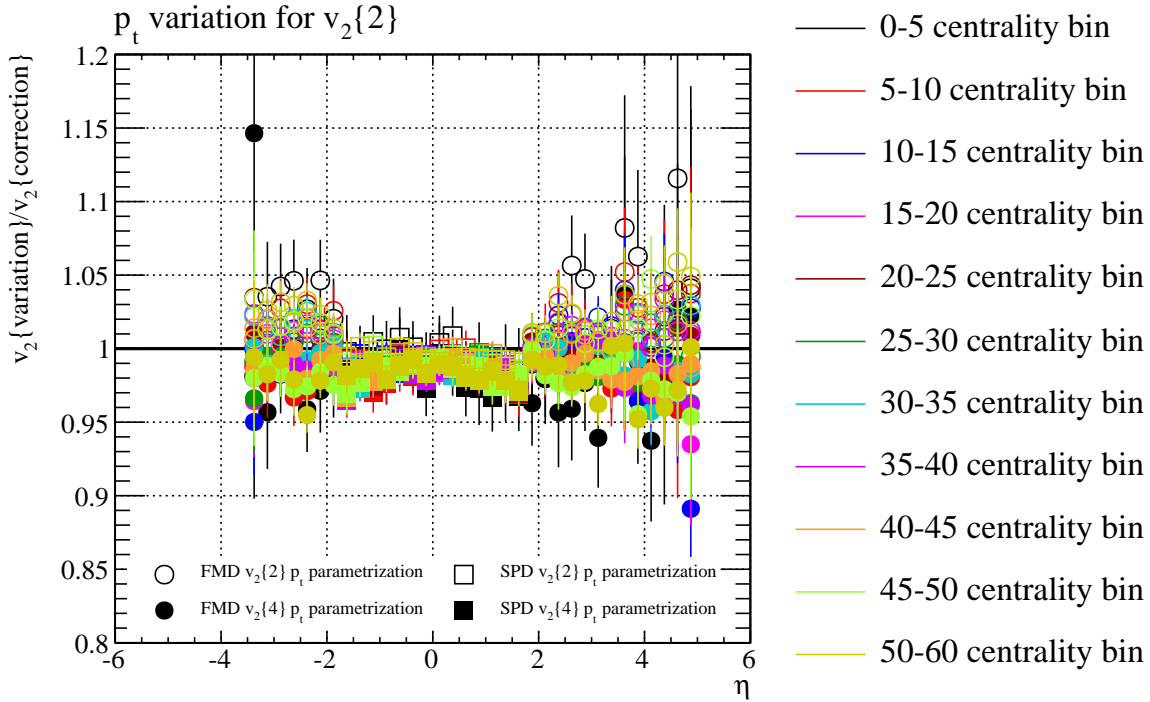


Figure 7.2: Variations in the MC correction for different input $v_2(p_t)$ distributions. Shown here is the $v_2\{2\}$ correction for the different centrality bins.

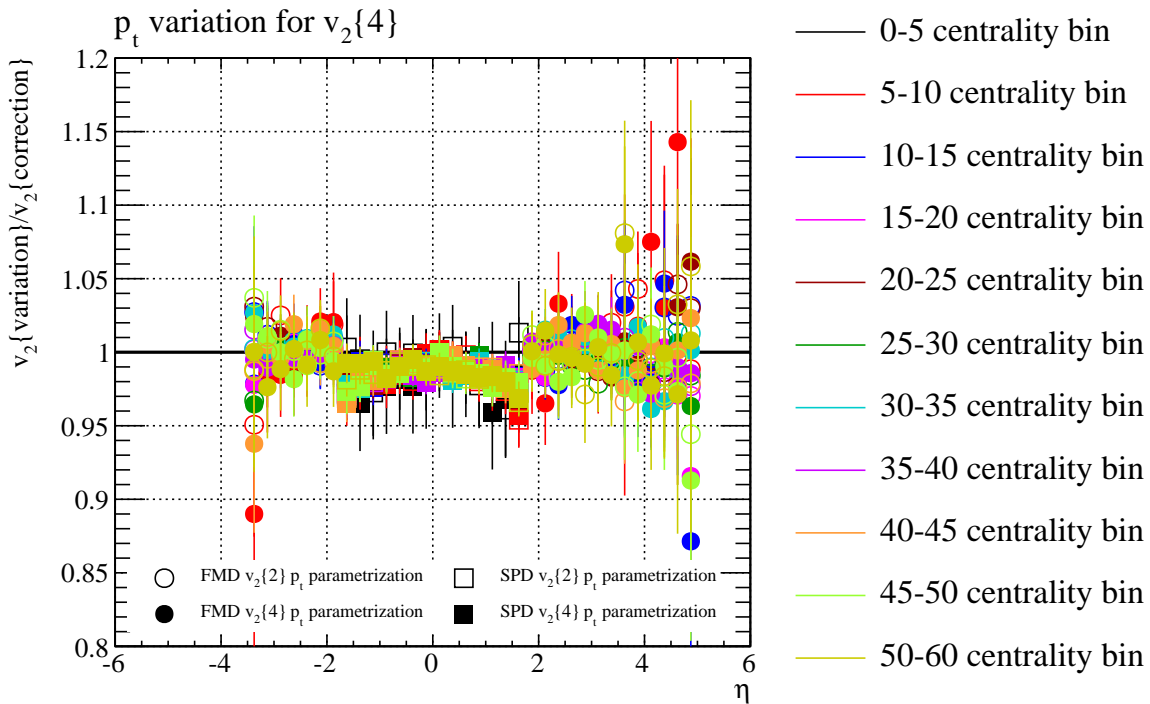


Figure 7.3: Variations in the MC correction for different input $v_2(p_t)$ distributions. Shown here is the $v_2\{4\}$ correction for the different centrality bins.

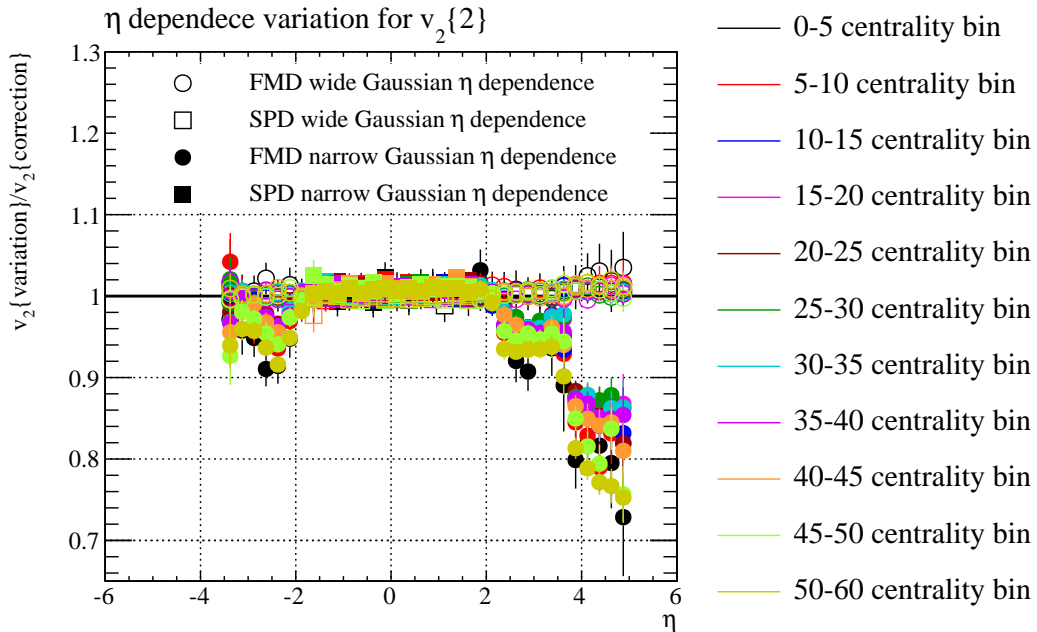


Figure 7.4: Variations in the MC correction for different input $v_2(\eta)$ distributions. Shown here is the $v_2\{2\}$ correction for the different centrality bins.

$v_2\{4\}$ from figure 7.5, or a new analysis with a slightly higher elliptic flow could be run. Due to time constraints the first solution is chosen. Note figure 7.4 supports the arguments made in section 6.5.3 about how the measurement of $v_2\{2\}$ in the FMD cannot be trusted for too small values of $v_2(\sim 0.01)$. The η -dependence is seen to contribute to the systematic error by as much as 15%. This contribution is to the point-to-point systematic error.

7.2.3 Centrality Contribution

The magnitude of the correction varies by more than 40% with centrality, but that does not factor directly into the systematic uncertainty. A very central collision is very rarely mistaken for a peripheral collision and vice versa. What does happen is that the centrality determination is off by maybe a percent. To estimate the error from this, the correction from one centrality bin is compared to the adjacent centrality bin in figure 7.6 and 7.7. In the figures a centrality bin is only compared to the more peripheral bin, but of course the error estimate goes both ways. The contribution is to the overall systematic error.

7.2.4 Particle ID Contribution

As mentioned the correction does not contain any PID dependence. But it is known that different species of particles has different elliptic flow. To test if this is important for the correction, pions are given 30% more flow than protons, which are given the standard amount of flow used in the correction. All other particles are given 30% less flow. The result is of course that the overall flow, and in particular the p_t dependence changes. Another test is made where all particles are given flow, as in the correction but with an extra factor of 1.207 to make it comparable to the setup with PID dependence. The result is shown in figure 7.8 and it appears that PID dependence is important, and will thus contribute further to the systematic error. The lack of PID dependence in the correction contribute to the systematic errors by up to 25%. This contribution is to the point-to-point systematic error.

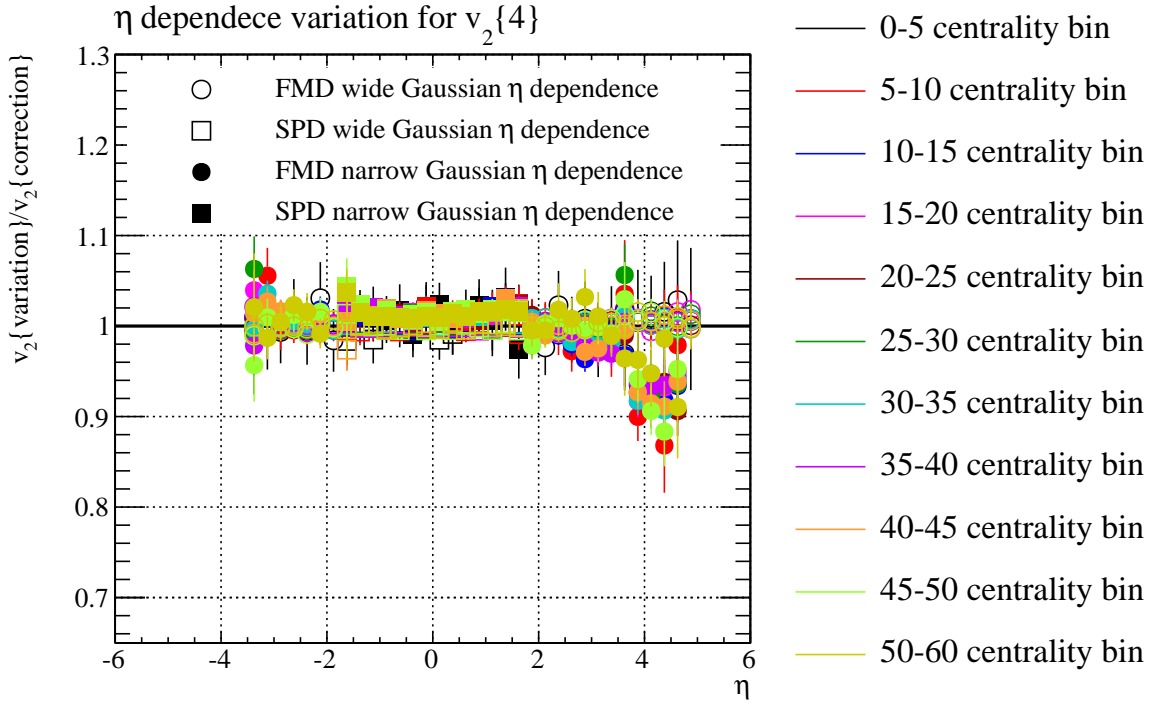


Figure 7.5: Variations in the MC correction for different input $v_2(\eta)$ distributions. Shown here is the $v_2\{2\}$ correction for the different centrality bins.

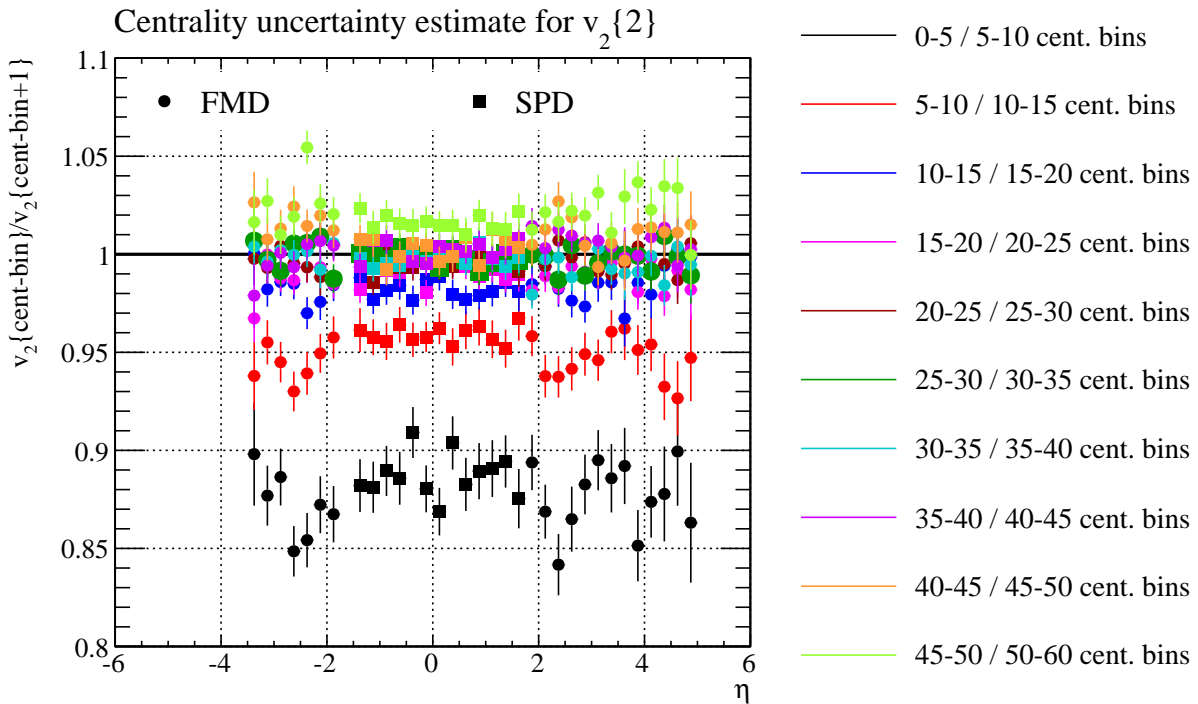


Figure 7.6: Systematic error estimate from centrality for $v_2\{2\}$. The estimate is made by comparing the correction in adjacent centrality bins.

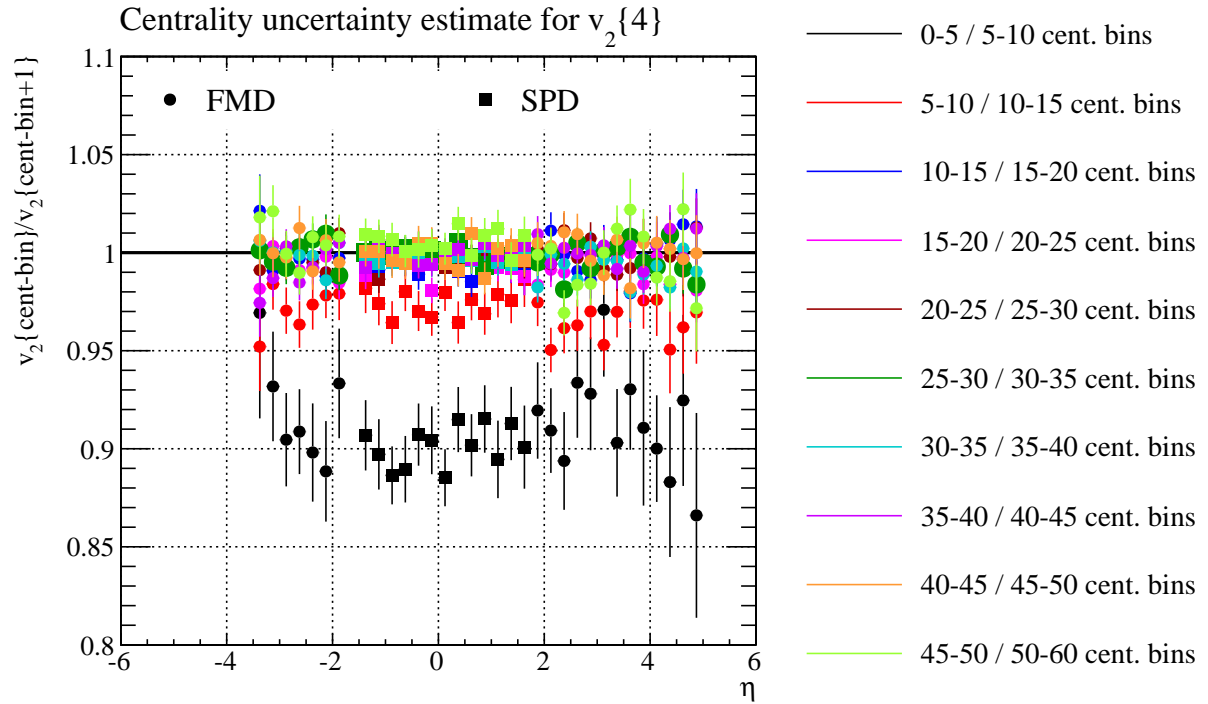


Figure 7.7: Systematic error estimate from centrality for $v_2\{4\}$. The estimate is made by comparing the correction in adjacent centrality bins.

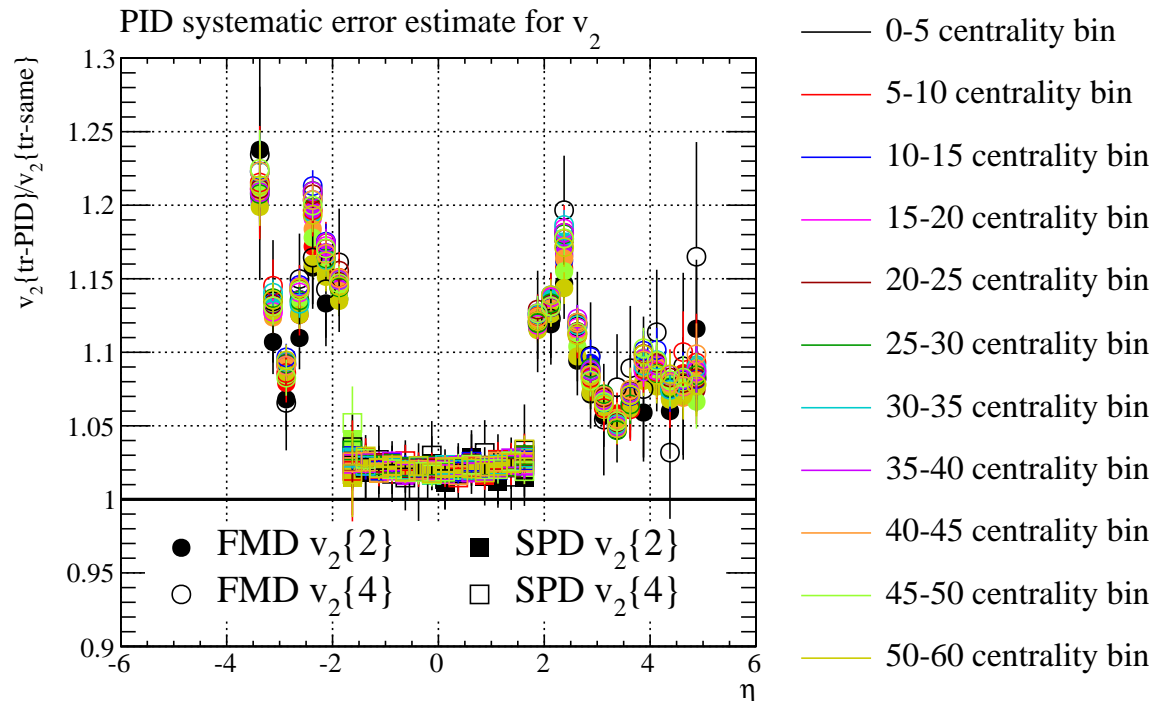


Figure 7.8: Systematic error estimate from centrality for the lack of PID dependent flow.

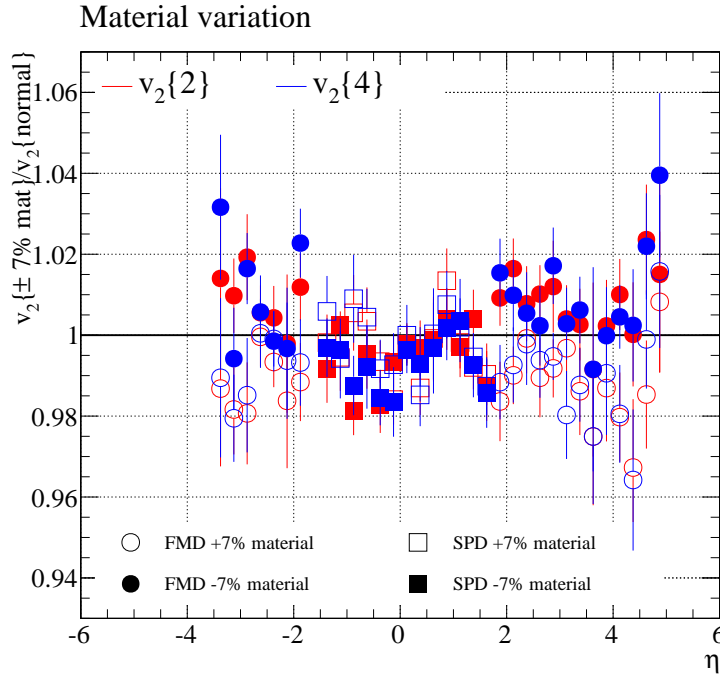


Figure 7.9: Systematic error estimate for the material description. The open points are from a MC with 7% less material. The filled points are from a MC with 7% added material. Both are compared to a MC with the normal amount of material.

7.2.5 Material Budget

The systematic error from the material budget is estimated in a different way. The flow is still added at the track reference level, but full MC simulations with more and less material are needed. These have been made as central production on the ALICE Grid, although only with about 30k events. One production has a 7% decrease in material, the other has a 7% increase in material. A comparison between these two and the production used for the correction object is seen in figure 7.9. An uncertainty in the material budget of 7% is not unrealistic, so the contribution to the systematic error is found directly from the plot. The variations are observed to contribute by less than 6% over the entire η -range, and contributes to the overall systematic error.

7.3 Final Error Estimate

While the sharing, Poisson and material budget contributions are all independent enough to be added in quadrature, it could be argued that the η , centrality, PID, and p_t errors are correlated such that extra care should be taken. However, at this point it is not clear how that should be done, so of the above systematic errors are added in quadrature. In table 7.1 and 7.2 the systematic error contribution from each source is added up, and the total is calculated for $v_2\{2\}$ and $v_2\{4\}$. In general the systematic error is only computed in η intervals, though in certain cases it is also done for specific centralities. All of the systematics could be made a lot smaller by doing the analysis on a larger sample of MC data, as it is seen from the figures that the statistical error bars dominate the contributions. Unfortunately time constraints and limited available statistics has not made that possible. The final errors end up being as large as 35% in some cases. A number that could be made a lot smaller with some more time. It should be possible to get the systematic error in the FMD below 20% and below 10% in the SPD.

Source	Centrality	$[-3.75; -1.75]$	$[-1.75; 1.75]$	$[1.75; 3.75]$	$[3.75; 5]$
Sharing and Poisson	All	10%	15%	8%	8%
p_t dependence	All	10%	6%	9%	17%
η dependence	All	11%	4%	9%	19%
Centrality uncertainty	0-10%	17%	14%	17%	17%
	10-15%	8%	6%	7%	9%
	15-60%	4%	3%	4%	3%
PID	All	25%	5%	20%	15%
Material	All	4%	3%	4%	5%
Point-to-point	All%	29%	8.8%	24%	30%
	0-10%	20%	21%	19%	19%
	10-15%	13%	16%	11%	12%
Overall	15-60%	11%	16%	9.7%	9.1%
	0-10%	35%	23%	31%	35%
	10-15%	32%	19%	26%	32%
Total	15-60%	31%	18%	26%	31%

 Table 7.1: Systematic errors for $v_2\{2\}$.

Source	Centrality	$[-3.75; -1.75]$	$[-1.75; 1.75]$	$[1.75; 3.75]$	$[3.75; 5]$
Sharing and Poisson	All	10%	15%	8%	8%
p_t dependence	All	10%	8%	10%	17%
η dependence	All	11%	4%	9%	19%
Centrality uncertainty	0-10%	14%	13%	13%	18%
	10-15%	7%	5%	6%	7%
	15-60%	3%	2%	3%	5%
PID	All	25%	5%	20%	15%
Material	All	5%	3%	4%	6%
Point-to-point	All%	29%	10%	24%	30%
	0-10%	18%	20%	16%	21%
	10-15%	13%	16%	11%	12%
Overall	15-60%	12%	15%	9.4%	11%
	0-10%	34%	23%	29%	36%
	10-15%	32%	19%	26%	32%
Total	15-60%	31%	19%	26%	32%

 Table 7.2: Systematic errors for $v_2\{4\}$.

Chapter 8

Results

In this chapter the Monte Carlo correction is applied to the data and the final results are presented. As mentioned in Chapter 2 there are already preliminary results from ATLAS and CMS for $\eta \in [-2.5; 2.5]$, and all three experiments have published data on the centrality dependence. The results shown here should of course agree with these measurements, keeping in mind that all of those have a p_t cut, while the results presented here does not.

8.1 Applying the Monte Carlo Correction

The Monte Carlo correction obtained in section 6.6 are applied to the results presented in section 6.7. The results are shown in figure 8.1 and 8.2 for different centrality bins, note that the systematic errors are not shown. For centralities larger than 60% the flow becomes very large, and the results no longer look realistic, this problem is not understood, but as it resembles the structures observed in Section 6.5.3 it is likely related to the secondary particles. For the two-particle cumulant there is a structure around $\eta \approx 0$. In fact it is at $\eta = 0$ that the measurement is correct. A small enhancement is observed in the rest of the SPD, it is understood as a consequence of the azimuthal coverage changing for the reference flow for some of the vertices (see Appendix D), which causes a bias. It can be removed by making the choice of reference flow binning depend on the vertex z -coordinate, but currently the analysis code does not support that. Furthermore a structure is observed around $|\eta| \approx 3$, which is less well understood. However, the $dN/d\eta$ analysis shows some structures in the same place (see figure 1.7), which suggests it may be related to some problems in the geometrical description of the experiment. For the 10% most central events the distribution appears flat over the entire range. For the more peripheral events a small pseudorapidity dependence is observed, which becomes more pronounced for $\eta > 4$. Due to numerical problems with the code the four-particle cumulant does not give good results for the FMD, but the SPD results looks consistent for the 50% most central events. The problems with the FMD are not completely understood at this time. Figure 8.3 shows the forward-backward symmetry, and it seems that within the error bars there is forward-backward symmetry, which suggests that the correction does a reasonable job correction for ϕ blurring from secondaries. Using the results from the two-particle cumulant it is possible to compare to the RHIC top energy of $\sqrt{s_{NN}} = 200$ GeV, this is done in figure 8.4. It is clear from the figure that the shape of $v_2(\eta)$ has changed, and that the elliptic flow is generally higher. In fact up to 100% higher in the most forward regions.

A centrality dependence is also obtained and is presented in figure 8.5, where the systematic errors are shown for $|\eta| < 0.75$. In figure 8.6 and 8.7 it is shown in $|\eta|$ bins without systematic errors. For $v_2\{2\}$ the centrality dependence is very similar for for all η . Interestingly when integrated over more η bins $v_2\{4\}$ gives reasonable results, which compares well to the $v_2\{2\}$ results. It is not understood why this is the case.

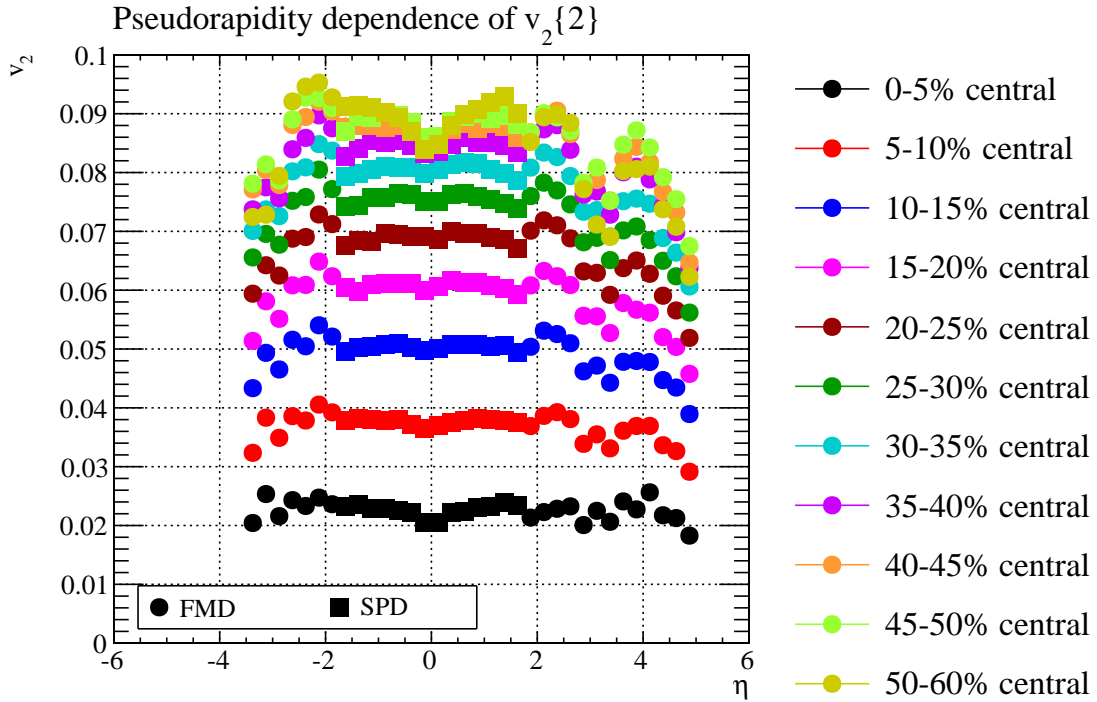


Figure 8.1: The results of the two-particle cumulant after the MC correction is applied for the 60% most central events. The shape with the dip at $\eta = 0$ for the SPD is an acceptance effect from shifting azimuthal coverage at some vertices. The structures around $|\eta| = 3$ are less well understood. Systematic errors are not shown.

8.2 Comparing to Published LHC Data

The pseudorapidity dependence results from CMS were done for particles in the p_t range 0.3 to 3 GeV. By using a MC correction for the difference in p_t range, the results above are compared to the CMS results. It is presented in figure 8.8 and 8.9. At mid-rapidity a very good agreement is observed for all centralities. Away from mid-rapidity the agreement is less good, but as described above it is understood that there is a bias from changing azimuthal coverage at different vertices. The systematic errors are not shown, but it is clear that with systematic errors of up to more than 35% the results are in agreement within the errors.

Similarly the ATLAS analysis was done in the p_t range 0.5 to 0.7 GeV and applying a correction for this yields a bad agreement. The input $v_2(p_t)$ dependence is from a measurement over a wide p_t range. It is possible that it does not give a good description of such a limited p_t range as is shown here. This could also be a pointer to how the correction might be improved.

The published ALICE results for elliptic flow vs. centrality are made using the TPC, and has a p_t cut from 0.2 to 5.0 GeV. There should naturally also be an agreement between these results and the results from this analysis using the SPD in the same η -range, particularly because this is the measurement used for the input parametrization of $v_2(p_t)$ and $v_2(\text{cent})$. The comparison is shown in figure 8.11 and a very good agreement is observed. From this it is also seen that the systematic errors are very likely overestimated, at least at mid-rapidity, as the two distributions agree to within a few percent.

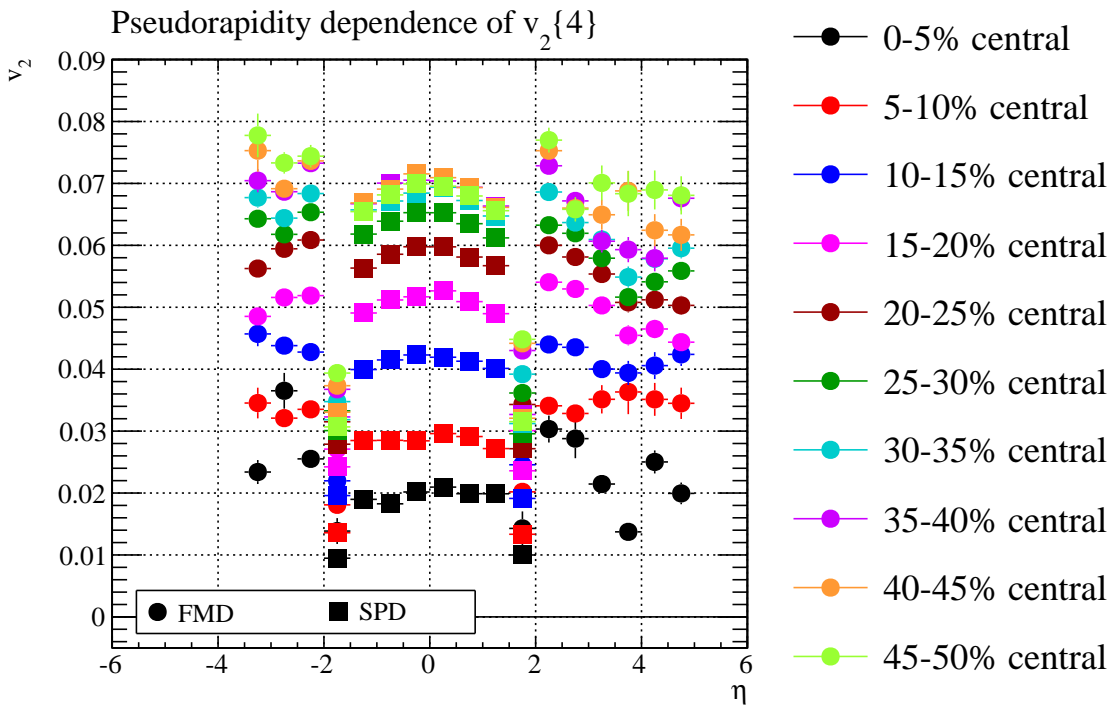


Figure 8.2: The results of the four-particle cumulant after the MC correction is applied for the 50% most central events. The small asymmetry in the SPD points is an acceptance effect from shifting azimuthal coverage at some vertices. Due to problems with the code, which are not completely understood, the FMD points do not give consistent results. Systematic errors are not shown.

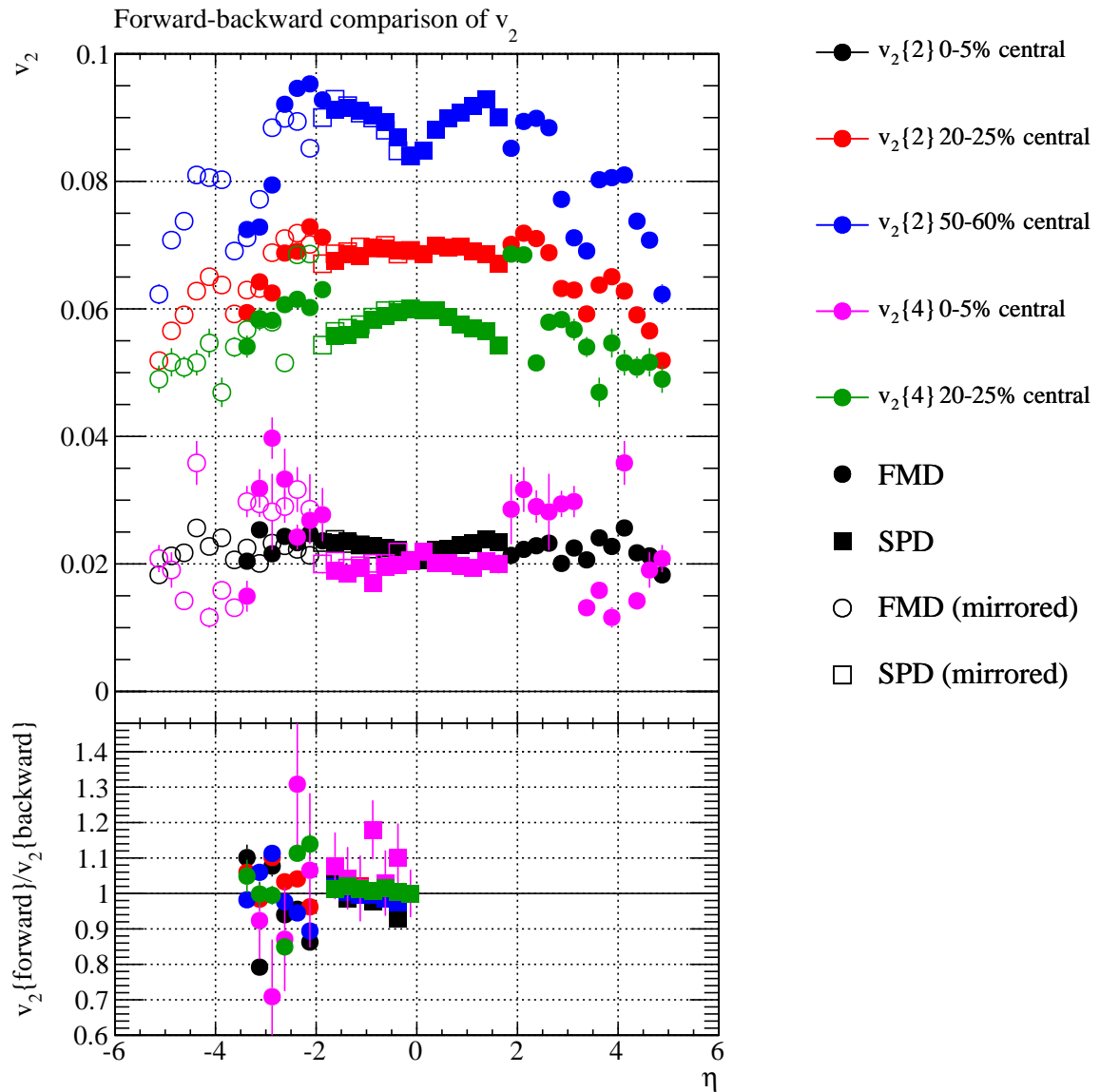


Figure 8.3: A look at the forward-backward symmetry. Within the errors a very good agreement is observed, which suggests that the MC correction applied does account for the ϕ blurring. Systematic errors are not shown.

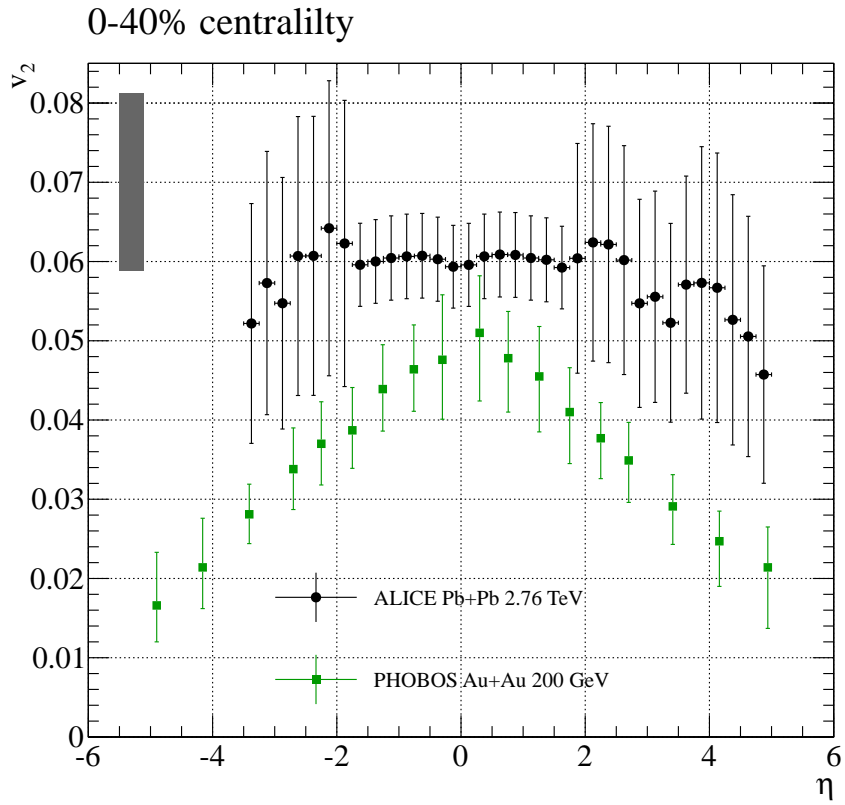


Figure 8.4: A comparison of the $v_2\{2\}$ results for the 0-40% centrality class to RHIC data from Au+Au at $\sqrt{s_{NN}} = 200$ GeV[46]. The error bars are from the point-to-point systematic errors. The gray band is the overall systematic error.

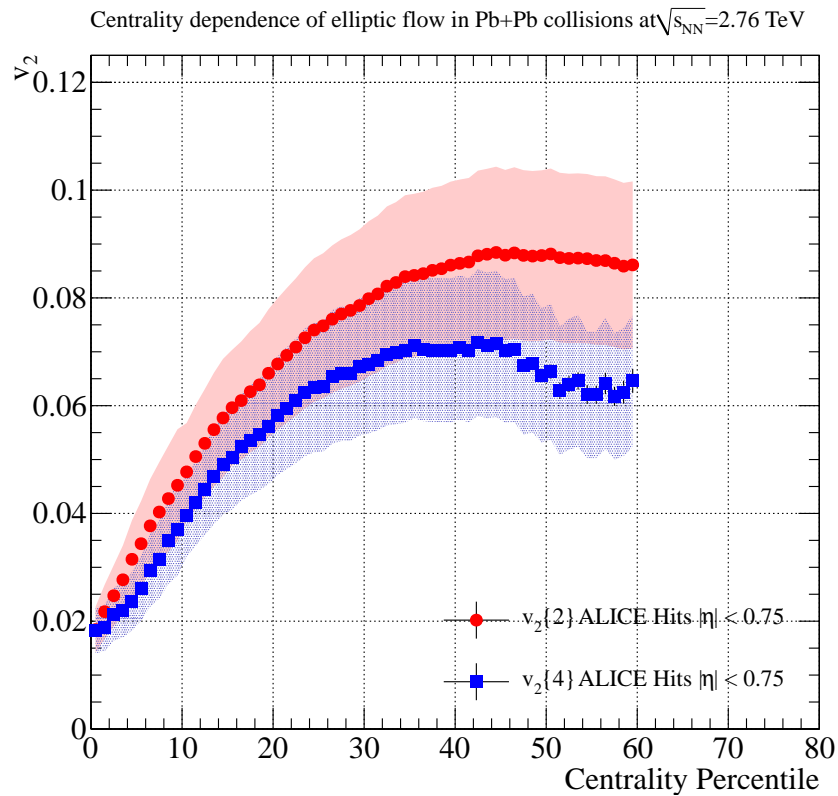


Figure 8.5: Centrality dependence for $|\eta| < 0.75$ with systematic errors bars.

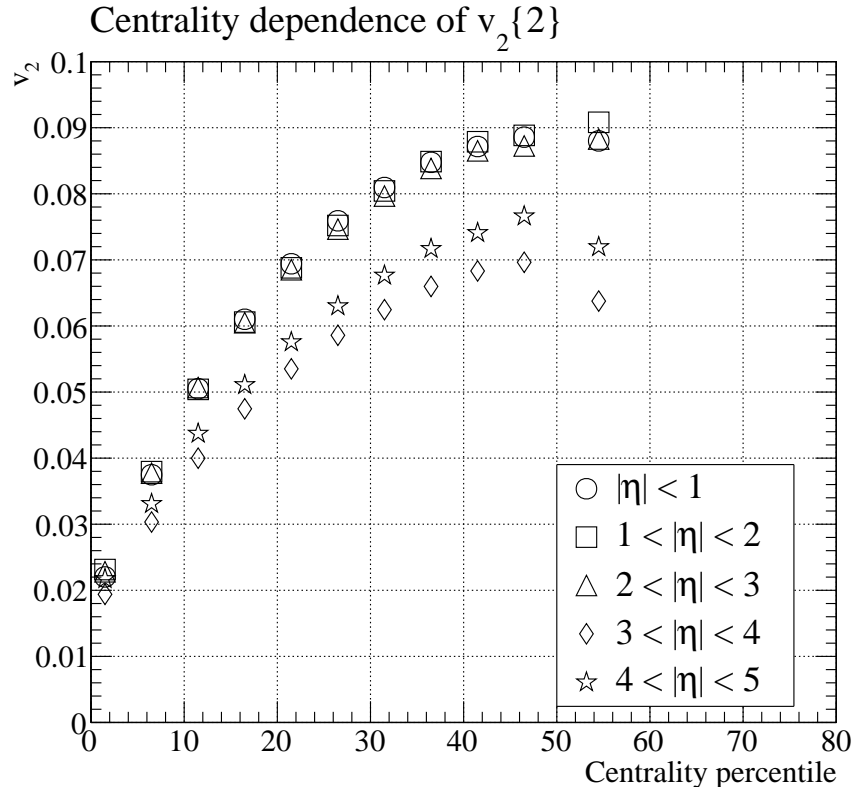


Figure 8.6: $v_2\{2\}$ vs. centrality for different η -ranges. The dependence is similar for all the measure η .

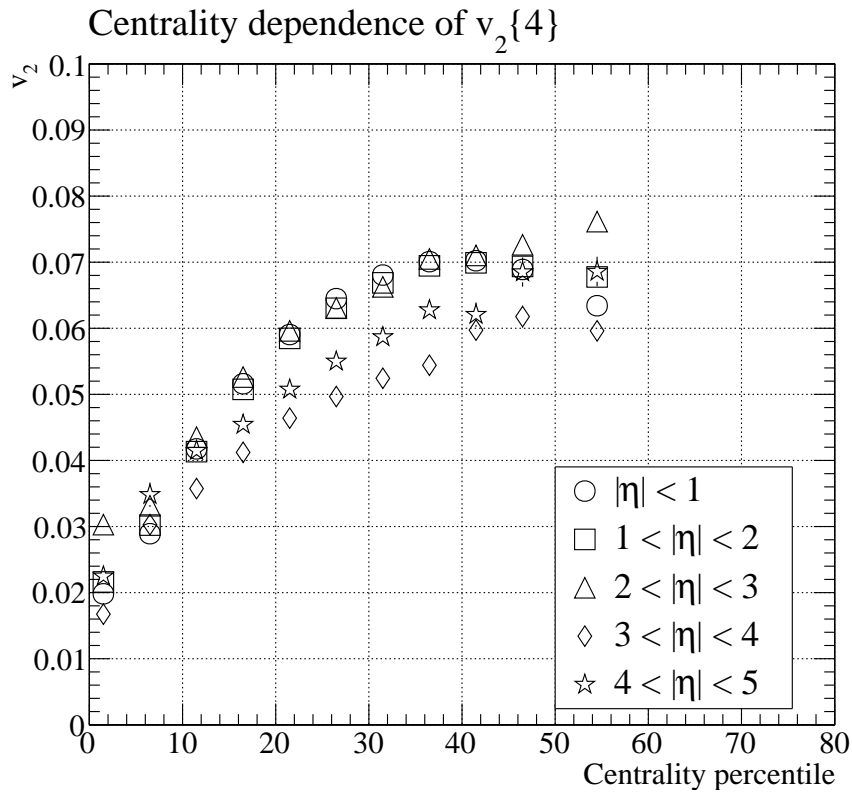


Figure 8.7: $v_2\{4\}$ vs. centrality for different η -ranges. Interestingly the results appear consistent, when integrated over several η -bins. The dependence is similar for all the measure η .

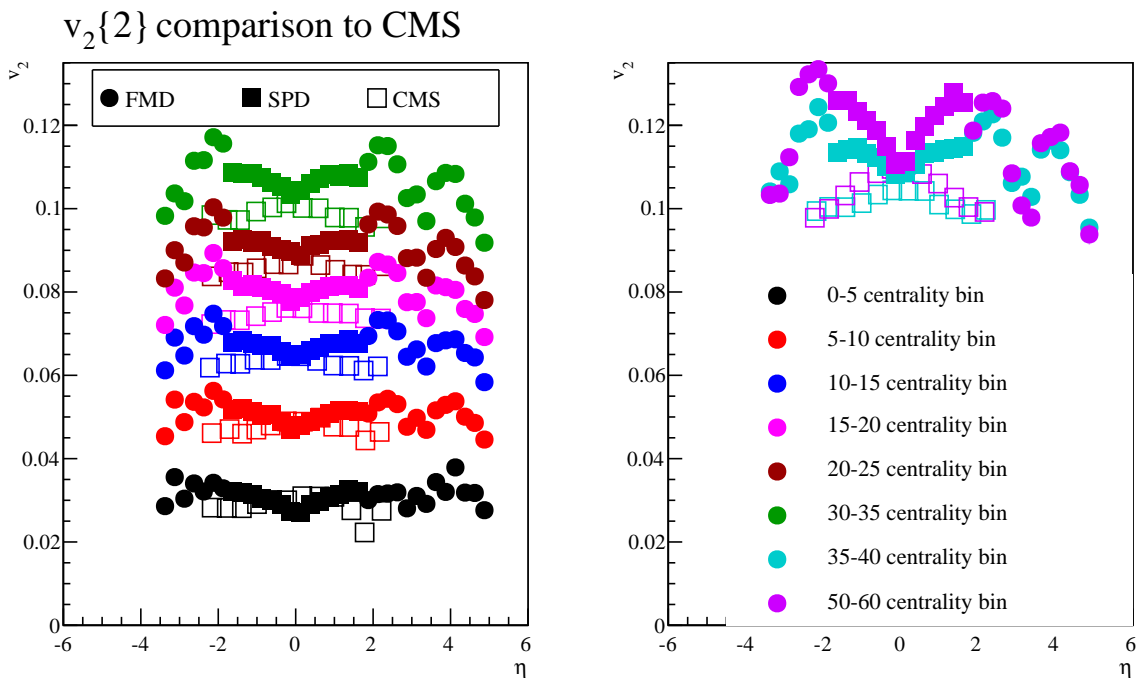


Figure 8.8: Comparison to CMS results for $v_2\{2\}$. A good agreement is observed at mid-rapidity. At the more forward rapidities the agreement is less convincing. Systematic errors are not shown

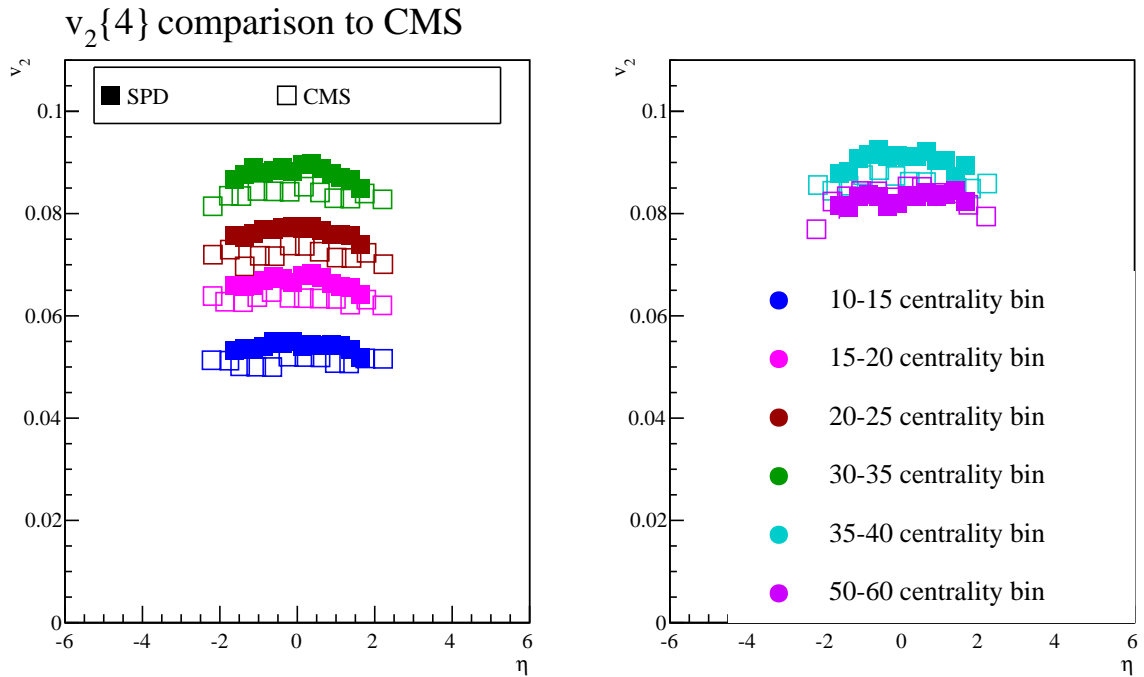


Figure 8.9: Comparison to CMS results for $v_2\{4\}$. Only SPD results are shown. A good agreement is observed. Systematic errors are not shown.

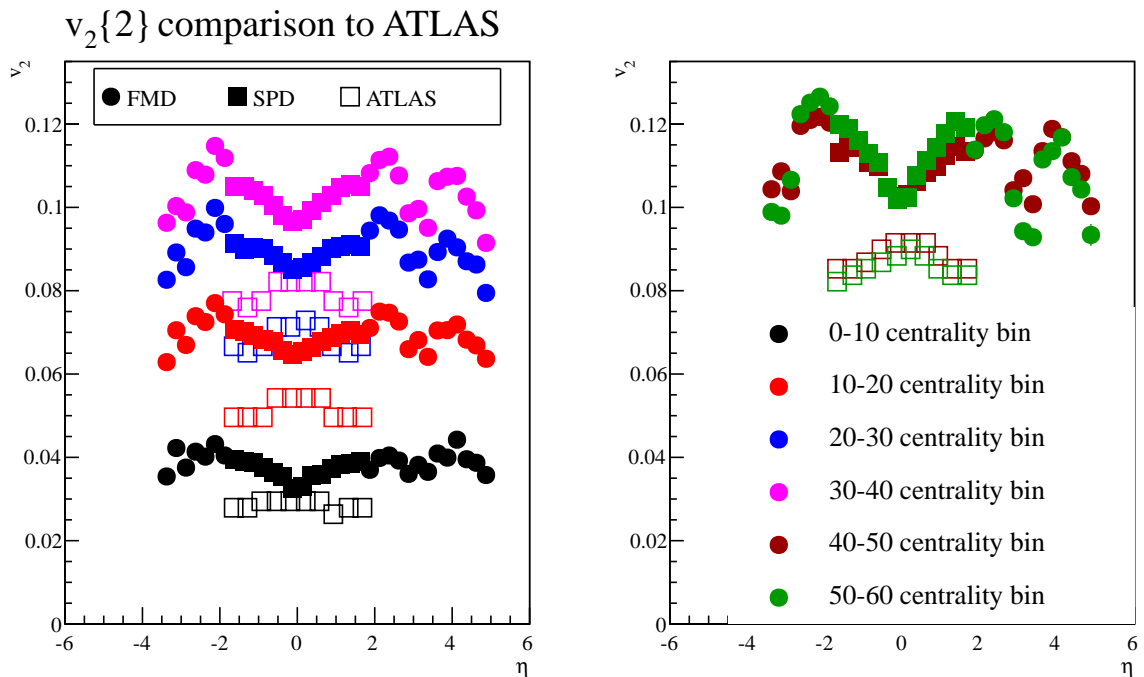


Figure 8.10: Comparison to ATLAS results for $v_2\{2\}$, the ATLAS points are from the event-plane method. A bad agreement is observed. This could be an indication that the correction does not work on such a small p_t interval as was used by ATLAS, which is $0.5 < p_t < 0.7$ GeV. Systematic errors are not shown.

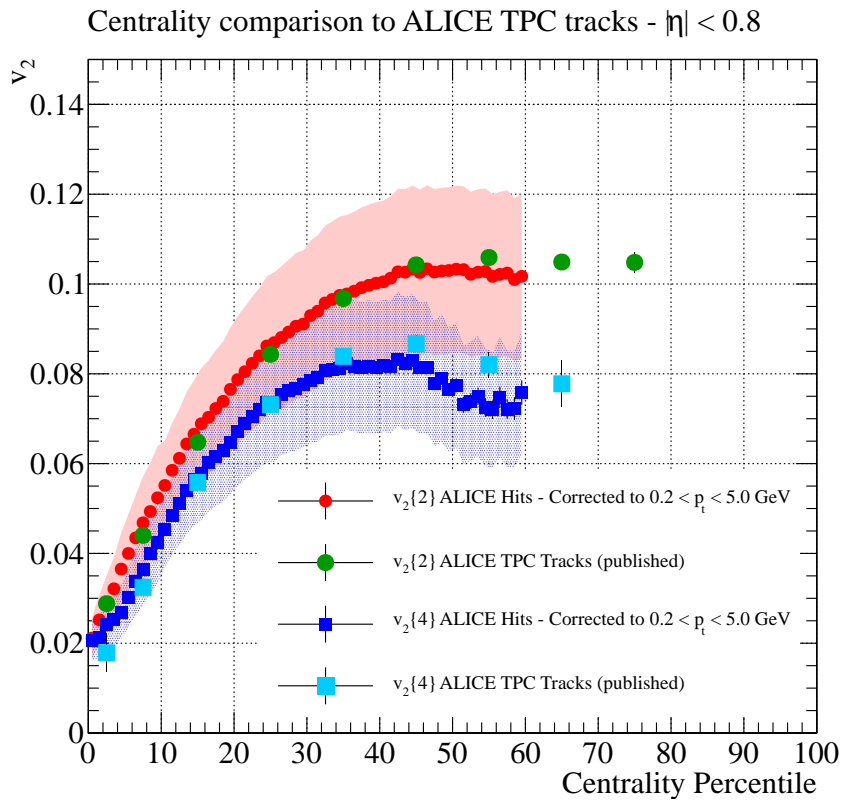


Figure 8.11: Comparison to the centrality dependence measured by ALICE using TPC tracks. A very good agreement is observed for both methods. The error band represents the systematic errors.

8.3 Comparing to Previous Experiments

To compare with a number of previous experiments there is the integrated flow measurement, which is done for the $\sqrt{s_{NN}}$ plot. The results are integrated over all p_t , and as that is also the way this analysis is done, no extra correction is needed. It is done in the 20 – 30% centrality class and in the pseudorapidity range -0.8 to 0.8. The plot is shown in figure 8.12 and once again a very good agreement with the published ALICE result is observed.

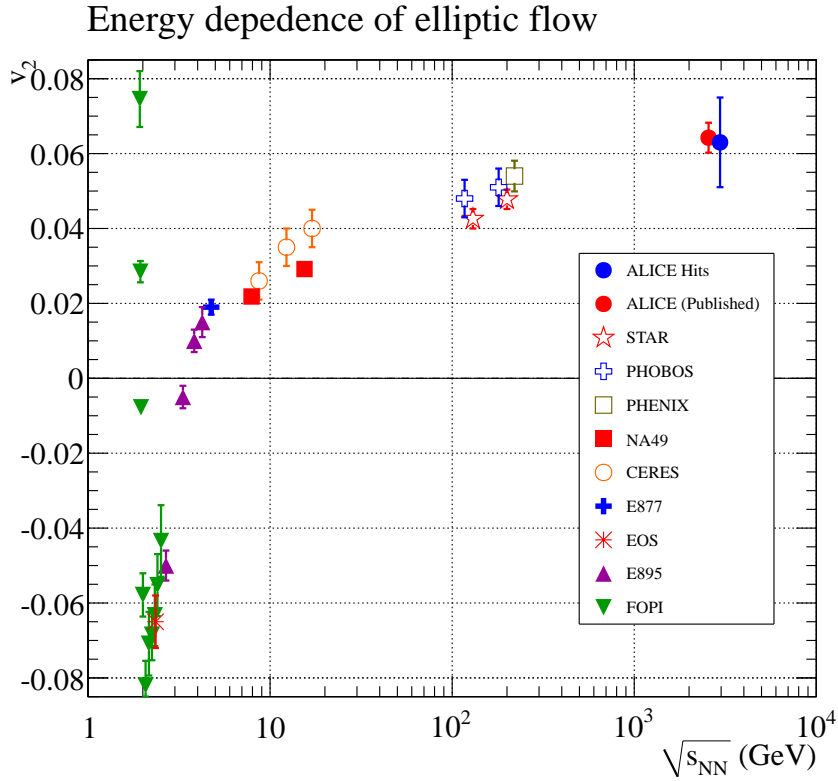


Figure 8.12: Elliptic flow as a function of $\sqrt{s_{NN}}$. The points are from the 20-30% centrality bin, with $|\eta| < 0.8$, integrated over all p_t . The point from this analysis is from the $v_2\{4\}$ analysis. A good agreement with the published result is observed.

PHOBOS and STAR are the only experiments to have previously measured v_2 vs. η over a wide pseudorapidity range, they did it for the 0 – 40% most central events. It was done with Au nuclei at four different energies and with Cu nuclei at two different energies, and thus covers a relatively large energy range. This is now expanded with the current results. A plot of v_2 vs. η with all the PHOBOS data and the results from this analysis for $v_2\{2\}$ for the 0 – 40% most central events is shown in figure 8.13. Most interestingly it appears that the slope of the η dependence at forward and backward rapidities is the same for all energies.

PHOBOS also published a result showing the $\sqrt{s_{NN}}$ dependence in different $|\eta|$ -bins. The results from this analysis makes it possible to expand the plot by an order of magnitude. The result is shown in figure 8.14. Logarithmic fits show that for the $|\eta| < 3$ plots, are consistent with the flattening of the distribution seen at the LHC energy. For the $3 < \eta < 4.5$ fit the logarithmic scaling with energy is still observed, but it does not appear to follow the same trend as the other rapidity intervals.

PHOBOS showed that in the rest frame of one of the colliding nuclei the pseudorapidity dependence of elliptic flow does not depend on energy. This is done by plotting for the data in figure 8.13 as a function of $\eta - y_{beam}$. In the case of the Pb+Pb collisions at $\sqrt{s_{NN}} = 2.76$

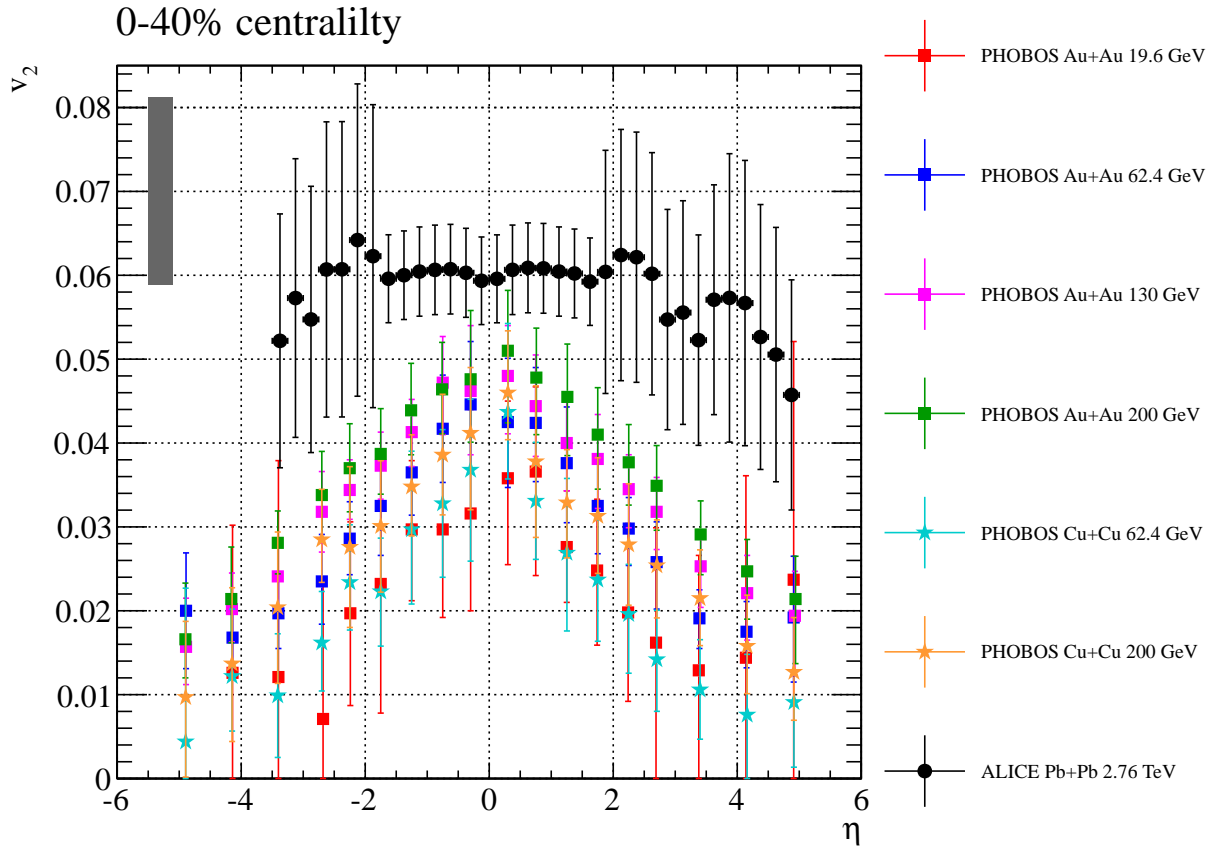


Figure 8.13: Elliptic flow vs. pseudorapidity over a wide energy range[46],[47]. Interestingly it appears that the slope of the η dependence at forward and backward rapidities is the same for all energies. The error bars are the point-to-point systematic errors. The gray band is the overall systematic error.

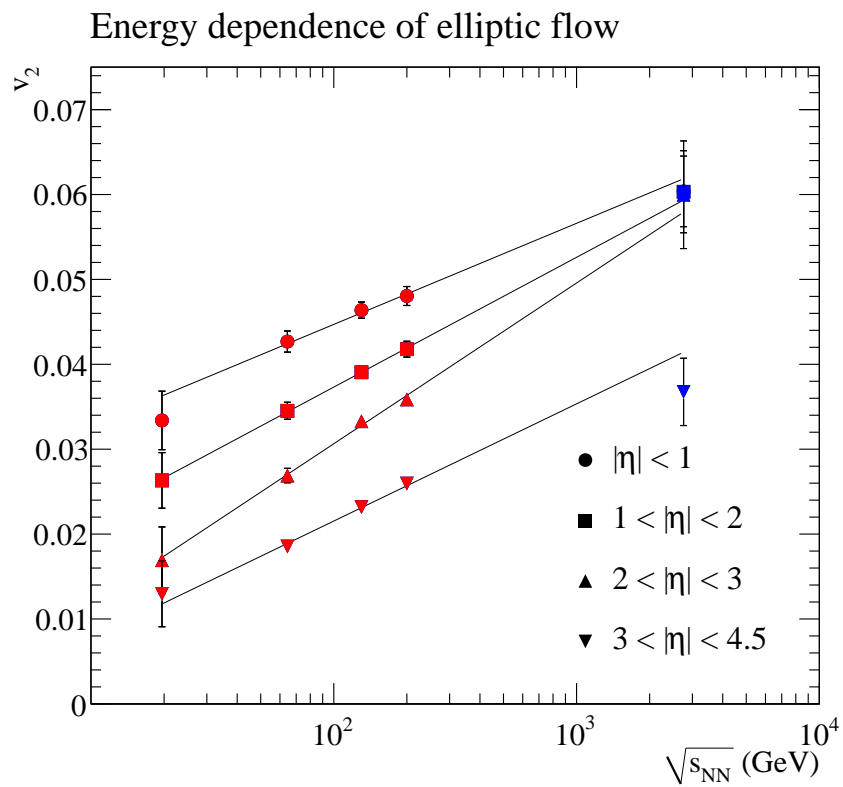


Figure 8.14: Elliptic flow as a function of $\sqrt{s_{NN}}$ for different η -intervals. The logarithmic scaling observed at lower energies appears to continue to LHC energies. Red points are PHOBOS[46], blue points are ALICE.

8.3 Comparing to Previous Experiments

TeV, $y_{beam} \approx \cosh\left(-1 \frac{\sqrt{s_{NN}}}{2m_p}\right) = 7.99$. In Au+Au collisions in the RHIC energy range the 0-40% central events correspond to an average number of participants of $\langle N_{part} \rangle = 201$ to 211. For Pb+Pb collisions at the LHC energy the average number of participants in that centrality class is $\langle N_{part} \rangle = 233$. Since elliptic flow scales with the number of participants, a small correction is added so that for the PHOBOS data points $\eta - y_{beam}$ is really $\eta - y_{beam} - \langle N_{part}^{LHC} \rangle / \langle N_{part}^{RHIC} \rangle$. The result is shown in figure 8.15. Interestingly it seems that the scaling of elliptic flow with pseudorapidity, as seen from the rest frame of one of the colliding nuclei, is similar over an energy range of two orders of magnitude.

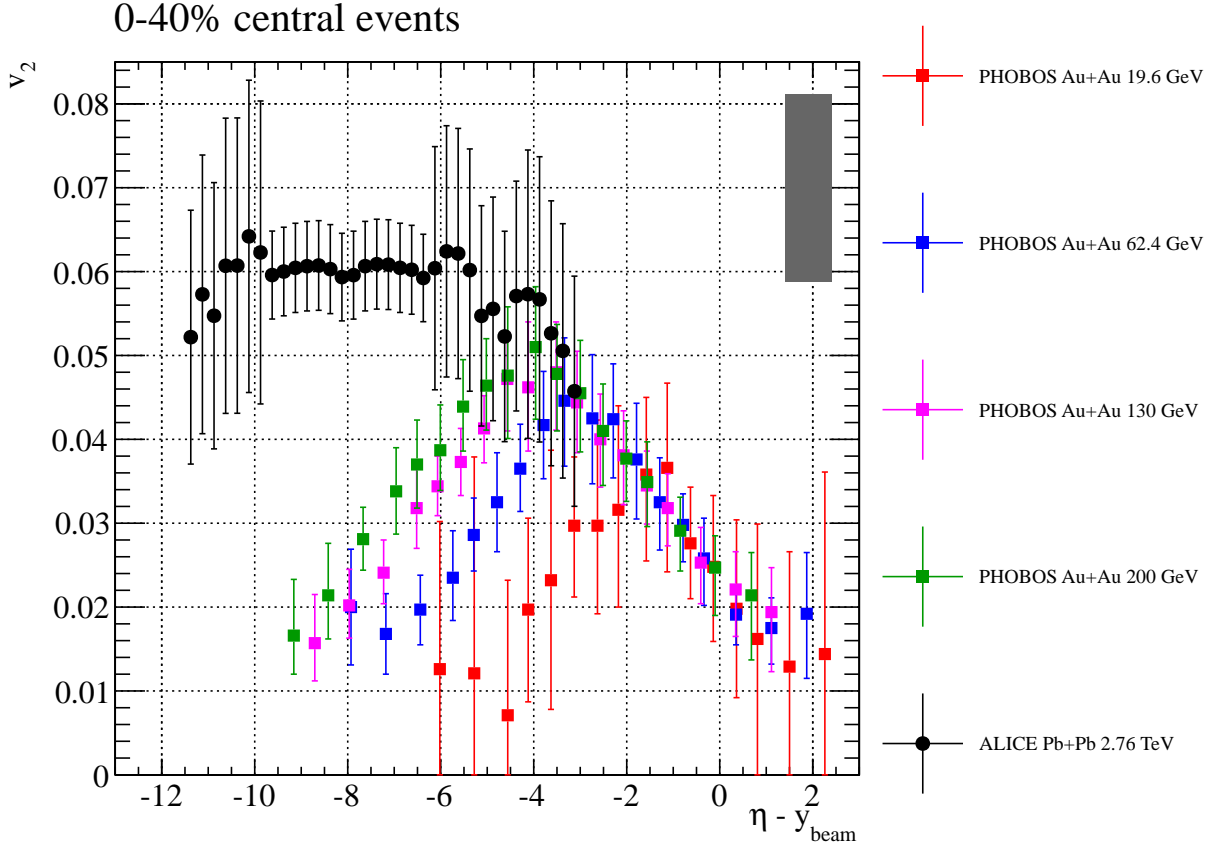


Figure 8.15: Elliptic flow vs. $\eta - y_{beam}$ [46]. It is seen that in the rest frame of one of the colliding nuclei, the pseudorapidity dependence of v_2 does not change over two orders of magnitude in energy. The error bars are the point-to-point systematic errors. The gray band is the overall systematic error.

Chapter 9

Conclusion

In this thesis data from Pb+Pb collisions at $\sqrt{s_{NN}} = 2.76$ has been analysed, using the Forward Multiplicity Detector and Silicon Pixel Detector in ALICE at the LHC. The analysis has looked at the elliptic flow component, v_2 over a very wide pseudorapidity range, $-3.75 < \eta < 5$, which doubles the range of previous measurements at this energy.

By looking at the two detectors in more detail it was found that, particularly for the FMD, secondary particles created in interactions with detector material after the collision, suppress the flow signal by an average of 30%. This meant that a Monte Carlo correction had to be applied to the data. This MC correction caused some problems, since the available MC statistics with flow was very limited. The problem was solved by adding flow artificially to track references from the MC. However, it turned out that the correction is very sensitive to the other variables v_2 depend on. This coupled with limited time caused the systematic error estimate to be very large in the results presented. Up to as much as 36%. It was estimated that with some more time and more studies the systematic errors can be reduced by about 50% compared to the ones presented here.

The method used to calculate the flow was a new method to calculate multi-particle cumulants, developed by people in the ALICE FLOW group. It was a refinement of a widely used method, and results should be directly comparable between the new and old cumulants method. The method works by first doing a reference measurement, over a wide area of phase space, and then doing a differential measurement in e.g., p_t or η in a smaller part of phase space. When applying the method over a wide pseudorapidity range it was found that the measured values would change a quite a lot with different reference phase spaces. At first this was not understood, but by doing studies on a toy MC model, it was found that if the flow fluctuations had a non-trivial pseudorapidity dependence, it would cause a bias to the differential measurement. To prevent this uncontrolled bias from entering the results, different reference measurements were done, until the optimal region was found.

Since the FMD and SPD does not have a uniform azimuthal acceptance over their entire pseudorapidity range, a choice was made to estimate statistical uncertainties by dividing the data into several sub-samples and estimate the error from those, rather than using the analytically derived equations, as they did not take non-uniform acceptance into account. It was shown that the two methods give very similar results.

When running the analysis on the full 7.5M events analysed in this thesis, it was found that the analysis no longer produces any results. The problem was solved for the two-particle cumulant method and for the SPD in the four-particle method, by dividing the data into 50 sub-samples rather than the originally planned 10. This suggests the problem to be numerical in nature, but that it is still under investigation.

Finally results were presented for the two-particle cumulant method over the entire pseudorapidity range, and for the four-particle method for $-1.75 < \eta < 1.75$. It was found that a bias remained for the SPD from the azimuthal coverage changing with different vertex z -coordinate.

Further more some structures were observed around $|\eta| = 3$ in the FMD. These structures are also present in the $dN/d\eta$ measurement with the FMD, which suggests it to be due to poorly understood detector geometry in that area. The results showed a change in shape for $v_2(\eta)$ as compared to at RHIC energies. At RHIC the distribution showed a peak at mid-rapidity, while at the LHC the distribution appears flat out to about $|\eta| = 4$ for the most central events. This also means that the elliptic flow value is doubled at $|\eta| = 4$ as compared to the RHIC top energy. It was found that the measurement presented here is in reasonable agreement with both the ALICE and CMS measurements, which were also done over a large p_t range. The agreement with the much smaller p_t range used by ATLAS was not good. It was observed that the logarithmic scaling with $\sqrt{s_{NN}}$ observed over several η -ranges at RHIC continues at the LHC energy. Furthermore it was shown that as seen in the rest frame of one of the colliding nuclei, $v_2(\eta - y_{beam})$ does not depend on the centre of mass energy over more than two orders of magnitude (19.4 GeV to 2.76 TeV).

The analysis presented here is a work in progress, albeit one that is close to being finished. First of all the problems still present in the four-particle cumulant measurement with the FMD, when running over a large amount of data needs to be resolved. The analysis code also needs to take into account shifting coverage at different vertices, in order to remove the bias in the SPD. Then more studies need to be done on the MC correction. And in particular a large MC production with flow in from the beginning (AMPT or an afterburner) is needed in order to reduce some of the statistical uncertainties contributing to the systematic errors of the final measurement. With this it should be possible to get the systematic errors down to less than 20% over the entire FMD and less than 10% for the SPD. The apparent non-flow observed for centralities larger than 60% needs to be understood, and the measured range preferably extended out to 80%.

After that it would be natural to extend the analysis to at least also do v_3 and v_4 , and maybe more if at all possible with the available ϕ -resolution in the FMD. The analysis code is already able to calculate these moments, but studies of the suppression of the signal due to secondaries need to be done for these higher moments also.

Finally, with the discovery that the flow fluctuations change with pseudorapidity in a non-trivial way suggests that a study should be done in flow fluctuations over a wide pseudorapidity range. Flow fluctuations has previously not been studied much, and as far as the author is aware, it has never been done over a wide pseudorapidity range. That should really be done.

With the discovery of ridge-like components in the two-particle azimuthal correlation analysis in high multiplicity pp collisions at $\sqrt{s} = 7$ TeV by CMS, it is only natural to consider flow in these pp collisions. At the moment the methods utilised in A+A collisions are not able to measure flow in pp collisions, due to the low multiplicity and a very large amount of non-flow. Thus the analysis presented here is not directly applicable on pp data. But currently many are trying to develop methods to measure flow in high multiplicity pp collisions. It is definitely an interesting area, and if significant flow is found in these pp collisions it will be very big news.

Bibliography

- [1] I. Arsene et al., “Quark Gluon Plasma an Color Glass Condensate at RHIC? The perspective from the BRAHMS experiment,” *Nucl. Phys.*, vol. A757, pp. 1–27, 2005.
- [2] K. Nakamura et al., “2011 Review of Particle Physics,” *Journal of Physics*, vol. G37, pp. 075021, 2010.
- [3] B.R. Martin and G. Shaw, *Particle Physics*, Wiley, 2nd edition, 2005.
- [4] Gunnar S. Bali, “QCD forces and heavy quark bound states,” *Phys. Rept.*, vol. 343, pp. 1–136, 2001.
- [5] Gordon Baym, “RHIC: From dreams to beams in two decades,” *Nucl.Phys.*, vol. A698, pp. XXIII–XXXII, 2002.
- [6] T. Hatsuda K. Yagi and Y. Miake, *Quark-Gluon Plasma*, Cambridge University Press, 1st edition, 2005.
- [7] The DOE/NSF Nuclear Science Advisory Committee, “The Frontiers of Nuclear Science, A Long Range Plan,” 2008, arXiv:0809.3137 [nucl-ex].
- [8] A. Andronic et al., “Excitation function of elliptic flow in Au+Au collisions and the nuclear matter equation of state,” *Phys.Lett.*, vol. B612, pp. 173–180, 2005.
- [9] Michael L. Miller, Klaus Reygers, Stephen J. Sanders, and Peter Steinberg, “Glauber modeling in high energy nuclear collisions,” *Ann. Rev. Nucl. Part. Sci.*, vol. 57, pp. 205–243, 2007.
- [10] B. Alver, M. Baker, C. Loizides, and P. Steinberg, “The PHOBOS Glauber Monte Carlo,” 2008, arXiv:0805.4411 [nucl-ex].
- [11] K. Aamodt et al., “Charged-particle multiplicity density at mid-rapidity in central Pb-Pb collisions at $\sqrt{s_{NN}} = 2.76$ TeV,” *Phys.Rev.Lett.*, vol. 105, pp. 252301, 2010.
- [12] H. H. Dalsgaard, “The Forward Multiplicity Detector for ALICE,” M.S. thesis, University of Copenhagen, 2007.
- [13] Alberica Toia for the ALICE Collaboration, “Bulk Properties of Pb-Pb collisions at $\sqrt{s_{NN}} = 2.76$ TeV measured by ALICE,” 2011, Presented at Quark Matter 2011, Annecy, France.
- [14] H. H. Dalsgaard, Ph.D. thesis, University of Copenhagen, 2011.
- [15] Alberica Toia for the ALICE Collaboration, “Bulk Properties of Pb-Pb collisions at $\sqrt{s_{NN}} = 2.76$ TeV measured by ALICE,” 2011, arXiv:1107.1973 [nucl-ex].
- [16] I.G. Bearden et al., “Pseudorapidity distributions of charged particles from Au+Au collisions at the maximum RHIC energy,” *Phys.Rev.Lett.*, vol. 88, pp. 202301, 2002.

-
- [17] K Aamodt et al., “Elliptic flow of charged particles in Pb-Pb collisions at 2.76 TeV,” *Phys.Rev.Lett.*, vol. 105, pp. 252302, 2010.
- [18] Jacek Otwinowski for the ALICE Collaboration, “Charged particle production at large transverse momentum in PbPb collisions at $\sqrt{s_{NN}} = 2.76$ TeV measured with ALICE at the LHC.,” 2011, Presented at Quark Matter 2011, Annecy, France.
- [19] Michele Floris for the ALICE Collaboration, “Production of identified particles in pp and PbPb collisions at LHC energies with the ALICE detector,” 2011, Presented at Quark Matter 2011, Annecy, France.
- [20] S. S. Adler et al., “High- p_T charged hadron suppression in $Au + Au$ collisions at $\sqrt{s_{NN}} = 200$ GeV,” *Phys. Rev. C*, vol. 69, no. 3, pp. 034910, Mar 2004.
- [21] K. Aamodt et al., “Suppression of Charged Particle Production at Large Transverse Momentum in Central Pb–Pb Collisions at $\sqrt{s_{NN}} = 2.76$ TeV,” *Phys.Lett.*, vol. B696, pp. 30–39, 2011.
- [22] S. S. Adler et al., “Absence of Suppression in Particle Production at Large Transverse Momentum in $\sqrt{s_{NN}} = 200$ GeV $d + Au$ Collisions,” *Phys. Rev. Lett.*, vol. 91, no. 7, pp. 072303, Aug 2003.
- [23] S. S. Adler et al., “Centrality Dependence of Direct Photon Production in $\sqrt{s_{NN}} = 200$ GeV $Au + Au$ Collisions,” *Phys. Rev. Lett.*, vol. 94, no. 23, pp. 232301, Jun 2005.
- [24] M. Gyulassy, P. Levai, and I. Vitev, “Reaction operator approach to nonabelian energy loss,” *Nucl.Phys.*, vol. B594, pp. 371–419, 2001, nucl-th/0006010.
- [25] T. Matsui and H. Satz, “J/psi Suppression by Quark-Gluon Plasma Formation,” *Phys.Lett.*, vol. B178, pp. 416, 1986.
- [26] Yen-Jie Lee, “Nuclear modification factors from the CMS experiment,” 2011, arXiv:1107.2131 [hep-ex].
- [27] J. Adams et al., “Experimental and theoretical challenges in the search for the quark-gluon plasma: The STAR Collaboration’s critical assessment of the evidence from RHIC collisions,” *Nuclear Physics A*, vol. 757, no. 1-2, pp. 102 – 183, First Three Years of Operation of RHIC.
- [28] Georges Aad et al., “Observation of a Centrality-Dependent Dijet Asymmetry in Lead-Lead Collisions at $\sqrt{s_{NN}} = 2.76$ TeV with the ATLAS Detector at the LHC,” *Phys.Rev.Lett.*, vol. 105, pp. 252303, 2010.
- [29] B. Alver and G. Roland, “Collision geometry fluctuations and triangular flow in heavy-ion collisions,” *Phys.Rev.*, vol. C81, pp. 054905, 2010.
- [30] J.D. Bjorken, “Highly Relativistic Nucleus-Nucleus Collisions: The Central Rapidity Region,” *Phys.Rev.*, vol. D27, pp. 140–151, 1983.
- [31] Jean-Yves Ollitrault, “Anisotropy as a signature of transverse collective flow,” *Phys.Rev.*, vol. D46, pp. 229–245, 1992.
- [32] S. Voloshin and Y. Zhang, “Flow study in relativistic nuclear collisions by Fourier expansion of Azimuthal particle distributions,” *Z. Phys.*, vol. C70, pp. 665–672, 1996.
- [33] E. Kreyszig, *Advanced Engineering Mathematics*, Wiley, 8th edition, 1999.

- [34] John Adams et al., “Azimuthal anisotropy at RHIC: The first and fourth harmonics,” *Phys. Rev. Lett.*, vol. 92, pp. 062301, 2004.
- [35] “Measurement of higher-order harmonic flow in Pb+Pb collisions at center-of-mass energy = 2.76 TeV,” Tech. Rep., CERN, Geneva, June 2011, CMS-PAS-HIN-11-005.
- [36] Derek Teaney and Li Yan, “Triangularity and Dipole Asymmetry in Heavy Ion Collisions,” 2010, arXiv:1010.1876 [nucl-th].
- [37] Fernando G. Gardim, Frederique Grassi, Yojiro Hama, Matthew Luzum, and Jean-Yves Ollitrault, “Directed flow at mid-rapidity in event-by-event hydrodynamics,” 2011, arXiv:1103.4605 [nucl-th].
- [38] K. Aamodt et al., “Harmonic decomposition of two particle angular correlations in Pb-Pb collisions at $\sqrt{s_{NN}} = 2.76$ TeV,” 2011, In preparation.
- [39] A. Adare et al., “Dihadron azimuthal correlations in Au+Au collisions at $\sqrt{s_{NN}=200}$ GeV,” *Phys. Rev. C*, vol. 78, no. 1, pp. 014901, Jul 2008.
- [40] Vardan Khachatryan et al., “Observation of Long-Range Near-Side Angular Correlations in Proton-Proton Collisions at the LHC,” *JHEP*, vol. 1009, pp. 091, 2010.
- [41] B.I. Abelev et al., “Long range rapidity correlations and jet production in high energy nuclear collisions,” *Phys.Rev.*, vol. C80, pp. 064912, 2009.
- [42] A. Adare et al., “Measurements of Higher-Order Flow Harmonics in Au+Au Collisions at $\sqrt{s_{NN}} = 200$ GeV,” 2011, arXiv:1105.3928 [nucl-ex].
- [43] “Measurement of elliptic flow and higher-order flow coefficients with the ATLAS detector in $\sqrt{s_{NN}}=2.76$ TeV Pb+Pb collisions,” Tech. Rep. ATLAS-CONF-2011-074, CERN, Geneva, May 2011.
- [44] K. Aamodt et al., “Higher harmonic anisotropic flow measurements of charged particles in Pb-Pb collisions at $\sqrt{s_{NN}} = 2.76$ TeV,” *Phys.Rev.Lett.*, vol. 107, pp. 032301, 2011.
- [45] A. Taranenko, “PHENIX studies of the scaling properties of elliptic flow at RHIC,” *J.Phys.G*, vol. G34, pp. S1069–1072, 2007.
- [46] B. B. Back et al., “Energy dependence of elliptic flow over a large pseudorapidity range in Au + Au collisions at RHIC,” *Phys. Rev. Lett.*, vol. 94, pp. 122303, 2005.
- [47] B. Alver et al., “System size, energy, pseudorapidity, and centrality dependence of elliptic flow,” *Phys.Rev.Lett.*, vol. 98, pp. 242302, 2007.
- [48] B. B. Back et al., “Centrality and pseudorapidity dependence of elliptic flow for charged hadrons in Au + Au collisions at $\sqrt{s_{NN}} = 200$ GeV,” *Phys. Rev.*, vol. C72, pp. 051901, 2005.
- [49] B.I. Abelev et al., “Centrality dependence of charged hadron and strange hadron elliptic flow from $\sqrt{s_{NN}} = 200$ GeV Au + Au collisions,” *Phys.Rev.*, vol. C77, pp. 054901, 2008.
- [50] M. Csanad, T. Csorgo, R. A. Lacey, and B. Lorstad, “Universal scaling of the elliptic flow at RHIC,” 2006, arXiv:nucl-th/0605044.
- [51] Tetsufumi Hirano, “Is early thermalization achieved only near mid-rapidity at RHIC?,” *Phys.Rev.*, vol. C65, pp. 011901, 2002.

-
- [52] Wit Busza, “Trends in multiparticle production and some ‘predictions’ for pp and PbPb collisions at LHC,” *J.Phys.G*, vol. G35, pp. 044040, 2008.
- [53] Mike Miller and Raimond Snellings, “Eccentricity fluctuations and its possible effect on elliptic flow measurements,” 2003, arXiv:nucl-ex/0321008.
- [54] Ante Bilandzic, Raimond Snellings, and Sergei Voloshin, “Flow analysis with cumulants: Direct calculations,” *Phys.Rev.*, vol. C83, pp. 044913, 2011.
- [55] Nicolas Borghini, Phuong Mai Dinh, and Jean-Yves Ollitrault, “Are flow measurements at SPS reliable?,” *Phys.Rev.*, vol. C62, pp. 034902, 2000.
- [56] Jean-Yves Ollitrault, Arthur M. Poskanzer, and Sergei A. Voloshin, “Effect of flow fluctuations and nonflow on elliptic flow methods,” *Phys. Rev.*, vol. C80, pp. 014904, 2009.
- [57] K. Aamodt et al., “The ALICE experiment at the CERN LHC,” *JINST*, vol. 3, pp. S08002, 2008.
- [58] C. H. Christensen, *ALICE Forward Multiplicity Detector: From Design to Installation*, Ph.D. thesis, University of Copenhagen, 2007.
- [59] F. Osmic, *The ALICE Silicon Pixel Detector System*, Ph.D. thesis, Technical University of Vienna, 2005.
- [60] Torbjorn Sjostrand, Stephen Mrenna, and Peter Z. Skands, “PYTHIA 6.4 Physics and Manual,” *JHEP*, vol. 0605, pp. 026, 2006.
- [61] Hans-Uno Bengtsson and Torbjorn Sjostrand, “The Lund Monte Carlo for Hadronic Processes: Pythia Version 4.8,” *Comput.Phys.Commun.*, vol. 46, pp. 43, 1987.
- [62] Torbjorn Sjostrand, “The Lund Monte Carlo for Jet Fragmentation and e+ e- Physics: Jetset Version 6.2,” *Comput.Phys.Commun.*, vol. 39, pp. 347–407, 1986.
- [63] Miklos Gyulassy and Xin-Nian Wang, “HIJING 1.0: A Monte Carlo program for parton and particle production in high-energy hadronic and nuclear collisions,” *Comput. Phys. Commun.*, vol. 83, pp. 307, 1994.
- [64] Zi-Wei Lin, Che Ming Ko, Bao-An Li, Bin Zhang, and Subrata Pal, “A Multi-phase transport model for relativistic heavy ion collisions,” *Phys.Rev.*, vol. C72, pp. 064901, 2005.
- [65] Lie-Wen Chen, Vincenzo Greco, Che Ming Ko, and Peter F. Kolb, “Pseudorapidity dependence of anisotropic flows in relativistic heavy-ion collisions,” *Phys. Lett.*, vol. B605, pp. 95–100, 2005.
- [66] Rene Brun, Federico Carminati, and Simone Giani, “GEANT Detector Description and Simulation Tool,” 1994, CERN Program Library Long Writeup.
- [67] R. Santoro, “Status of the ALICE silicon pixel detector,” *Nucl.Instrum.Meth.*, vol. A581, pp. 330–334, 2007.
- [68] J. F. Grosse-Oetringhaus, *Measurement of the Charged-Particle Multiplicity in Proton-Proton Collisions with the ALICE Detetor*, Ph.D. thesis, University of Munster, 2009.
- [69] Arthur M. Poskanzer and S. A. Voloshin, “Methods for analyzing anisotropic flow in relativistic nuclear collisions,” *Phys. Rev.*, vol. C58, pp. 1671–1678, 1998.

- [70] Nicolas Borghini, Phuong Mai Dinh, and Jean-Yves Ollitrault, “Flow analysis from multi-particle azimuthal correlations,” *Phys. Rev.*, vol. C64, pp. 054901, 2001.
- [71] Nicolas Borghini, Phuong Mai Dinh, and Jean-Yves Ollitrault, “Flow analysis from cumulants: A practical guide,” 2001, arXiv:nucl-ex/0110016.
- [72] Rajeev S. Bhalerao, Matthew Luzum, and Jean-Yves Ollitrault, “Determining initial-state fluctuations from flow measurements in heavy-ion collisions,” 2011, arXiv:1104.4740 [nucl-th].
- [73] John Adams et al., “Azimuthal anisotropy and correlations at large transverse momenta in p+p and Au+Au collisions at $\sqrt{s_{NN}} = 200$ GeV,” *Phys.Rev.Lett.*, vol. 93, pp. 252301, 2004.
- [74] R. S. Bhalerao, N. Borghini, and J. Y. Ollitrault, “Analysis of anisotropic flow with Lee-Yang zeroes,” *Nucl. Phys.*, vol. A727, pp. 373–426, 2003.
- [75] J. Movchet S. Hancock, F. James et al., “Energy Loss And Energy Stragglng Of Protons And Pions In The Momentum Range 0.7 GeV/c To 115 GeV/c,” *Phys. Rev.*, vol. A28, pp. 615, 1983, <http://cdsweb.cern.ch/record/145395/files/PhysRevA.28.615.pdf>.
- [76] B. B. Back et al., “Pseudorapidity and centrality dependence of the collective flow of charged particles in Au + Au collisions at $\sqrt{s_{NN}} = 130$ GeV,” *Phys. Rev. Lett.*, vol. 89, pp. 222301, 2002.
- [77] A. Bilandzic, Ph.D. thesis, Nikhef, Amsterdam, 2011.

Appendix A

Statistical Uncertainties

The analytical results of the two- and four-particle cumulants is presented here. For an analytical derivation, see [77]. Note that these equations do not contain terms to correct for non-azimuthal acceptance.

First two general results are needed:

$$s_x^2 \equiv \left[\frac{\sum_{i=1}^N (w_x)_i (x_i - \langle x \rangle)^2}{\sum_{i=1}^N (w_x)_i} \right] \times \left[\frac{1}{1 - \frac{\sum_{i=1}^N (w_x)_i^2}{[\sum_{i=1}^N (w_x)_i]^2}} \right] \quad (\text{A.1})$$

and

$$\langle x \rangle \equiv \frac{\sum_{i=1}^N (w_x)_i x_i}{\sum_{i=1}^N (w_x)_i} \quad (\text{A.2})$$

where in both cases x_i is the measured random observable x in event i , and $(w_x)_i$ is the observables weight. These two equations are used to estimate $s_{\langle n \rangle}$ and $\langle n \rangle$ directly from data, where n can be 2, 4, 2' or 4'.

A.1 Two-particle Reference Flow

The two-particle reference flow is

$$\langle v_n \{2\} \rangle \pm s_{\langle v_n \{2\} \rangle} \quad (\text{A.3})$$

where

$$s_{\langle v_n \{2\} \rangle} = \frac{1}{2\sqrt{\langle \langle 2 \rangle \rangle}} \frac{\sqrt{\sum_{i=1}^N (w_{\langle 2 \rangle})_i^2}}{\sum_{i=1}^N (w_{\langle 2 \rangle})_i} s_{\langle 2 \rangle}^2 \quad (\text{A.4})$$

A.2 Four-particle Reference Flow

The four-particle reference flow is

$$\langle v_n \{4\} \rangle \pm s_{\langle v_n \{4\} \rangle} \quad (\text{A.5})$$

where

$$s_{\langle v_n \{4\} \rangle}^2 = \frac{1}{[2 \cdot \langle \langle 2 \rangle \rangle^2 - \langle \langle 4 \rangle \rangle]^{3/2}} \times \left[\langle \langle 2 \rangle \rangle^2 \frac{\sum_{i=1}^N (w_{\langle 2 \rangle})_i^2}{[\sum_{i=1}^N (w_{\langle 2 \rangle})_i]^2} s_{\langle 2 \rangle}^2 + \frac{1}{16} \frac{\sum_{i=1}^N (w_{\langle 4 \rangle})_i^2}{[\sum_{i=1}^N (w_{\langle 4 \rangle})_i]^2} s_{\langle 4 \rangle}^2 - \frac{1}{2} \langle \langle 2 \rangle \rangle \frac{\sum_{i=1}^N (w_{\langle 2 \rangle})_i (w_{\langle 4 \rangle})_i}{\sum_{i=1}^N (w_{\langle 2 \rangle})_i \sum_{j=1}^N (w_{\langle 4 \rangle})_j} \text{Cov}(\langle 2 \rangle, \langle 4 \rangle) \right] \quad (\text{A.6})$$

A.3 Two-particle Differential Flow

The two-particle differential flow is

$$\langle v'_n \{2\} \rangle \pm s_{\langle v'_n \{2\} \rangle} \quad (\text{A.7})$$

where

$$\begin{aligned} s_{\langle v'_n \{2\} \rangle}^2 &= \frac{1}{4 \cdot \langle \langle 2 \rangle \rangle^3} \times \left[\langle \langle 2' \rangle \rangle^2 \frac{\sum_{i=1}^N (w_{\langle 2 \rangle})_i^2}{\left[\sum_{i=1}^N (w_{\langle 2 \rangle})_i \right]^2} s_{\langle 2 \rangle}^2 \right. \\ &+ 4 \cdot \langle \langle 2 \rangle \rangle^2 \frac{\sum_{i=1}^N (w_{\langle 2' \rangle})_i^2}{\left[\sum_{i=1}^N (w_{\langle 2' \rangle})_i \right]^2} s_{\langle 2' \rangle}^2 - 4 \cdot \langle \langle 2 \rangle \rangle \langle \langle 2' \rangle \rangle \\ &\left. \times \frac{\sum_{i=1}^N (w_{\langle 2 \rangle})_i (w_{\langle 2' \rangle})_i}{\sum_{i=1}^N (w_{\langle 2 \rangle})_i \sum_{j=1}^N (w_{\langle 2' \rangle})_j} \text{Cov}(\langle 2 \rangle, \langle 2' \rangle) \right] \quad (\text{A.8}) \end{aligned}$$

A.4 Four-particle Differential Flow

And finally the four-particle differential flow is

$$\langle v'_n \{4\} \rangle \pm s_{\langle v'_n \{4\} \rangle} \quad (\text{A.9})$$

where

$$\begin{aligned} s_{\langle v'_n \{4\} \rangle}^2 &= \frac{1}{[2 \cdot \langle \langle 2 \rangle \rangle^2 - \langle \langle 4 \rangle \rangle]^{\frac{7}{2}}} \times \\ &\left\{ [2 \cdot \langle \langle 2 \rangle \rangle^2 \langle \langle 2' \rangle \rangle - 3 \cdot \langle \langle 2 \rangle \rangle \langle \langle 4' \rangle \rangle + 2 \cdot \langle \langle 4 \rangle \rangle \langle \langle 2' \rangle \rangle]^2 \right. \\ &\times \frac{\sum_{i=1}^N (w_{\langle 2 \rangle})_i^2}{\left[\sum_{i=1}^N (w_{\langle 2 \rangle})_i \right]^2} s_{\langle 2 \rangle}^2 \\ &+ \frac{9}{16} \cdot [2 \cdot \langle \langle 2 \rangle \rangle \langle \langle 2' \rangle \rangle - \langle \langle 4' \rangle \rangle]^2 \frac{\sum_{i=1}^N (w_{\langle 4 \rangle})_i^2}{\left[\sum_{i=1}^N (w_{\langle 4 \rangle})_i \right]^2} s_{\langle 4 \rangle}^2 \\ &+ 4 \cdot \langle \langle 2 \rangle \rangle^2 [2 \cdot \langle \langle 2 \rangle \rangle^2 - \langle \langle 4 \rangle \rangle]^2 \frac{\sum_{i=1}^N (w_{\langle 2' \rangle})_i^2}{\left[\sum_{i=1}^N (w_{\langle 2' \rangle})_i \right]^2} s_{\langle 2' \rangle}^2 \\ &+ [2 \cdot \langle \langle 2 \rangle \rangle^2 - \langle \langle 4 \rangle \rangle]^2 \frac{\sum_{i=1}^N (w_{\langle 4' \rangle})_i^2}{\left[\sum_{i=1}^N (w_{\langle 4' \rangle})_i \right]^2} s_{\langle 4' \rangle}^2 \\ &- \frac{3}{2} \cdot [2 \cdot \langle \langle 2 \rangle \rangle \langle \langle 2' \rangle \rangle - \langle \langle 4' \rangle \rangle] \\ &\left. \times [2 \cdot \langle \langle 2 \rangle \rangle^2 \langle \langle 2' \rangle \rangle - 3 \cdot \langle \langle 2 \rangle \rangle \langle \langle 4' \rangle \rangle + 2 \cdot \langle \langle 4 \rangle \rangle \langle \langle 2' \rangle \rangle] \right\} \end{aligned}$$

$$\begin{aligned}
 & \times \frac{\sum_{i=1}^N (w_{\langle 2 \rangle})_i (w_{\langle 4 \rangle})_i}{\sum_{i=1}^N (w_{\langle 2 \rangle})_i \sum_{j=1}^N (w_{\langle 4 \rangle})_j} \text{Cov}(\langle 2 \rangle, \langle 4 \rangle) \\
 & - 4 \cdot \langle \langle 2 \rangle \rangle [2 \cdot \langle \langle 2 \rangle \rangle^2 - \langle \langle 4 \rangle \rangle] \\
 & \times [2 \cdot \langle \langle 2 \rangle \rangle^2 \langle \langle 2' \rangle \rangle - 3 \cdot \langle \langle 2 \rangle \rangle \langle \langle 4' \rangle \rangle + 2 \cdot \langle \langle 4 \rangle \rangle \langle \langle 2' \rangle \rangle] \\
 & \times \frac{\sum_{i=1}^N (w_{\langle 2 \rangle})_i (w_{\langle 2' \rangle})_i}{\sum_{i=1}^N (w_{\langle 2 \rangle})_i \sum_{j=1}^N (w_{\langle 2' \rangle})_j} \text{Cov}(\langle 2 \rangle, \langle 2' \rangle) \\
 & + 2 \cdot [2 \cdot \langle \langle 2 \rangle \rangle^2 - \langle \langle 4 \rangle \rangle] \\
 & \times [2 \cdot \langle \langle 2 \rangle \rangle^2 \langle \langle 2' \rangle \rangle - 3 \cdot \langle \langle 2 \rangle \rangle \langle \langle 4' \rangle \rangle + 2 \cdot \langle \langle 4 \rangle \rangle \langle \langle 2' \rangle \rangle] \\
 & \times \frac{\sum_{i=1}^N (w_{\langle 2 \rangle})_i (w_{\langle 4' \rangle})_i}{\sum_{i=1}^N (w_{\langle 2 \rangle})_i \sum_{j=1}^N (w_{\langle 4' \rangle})_j} \text{Cov}(\langle 2 \rangle, \langle 4' \rangle) \\
 & + 3 \cdot \langle \langle 2 \rangle \rangle [2 \cdot \langle \langle 2 \rangle \rangle^2 - \langle \langle 4 \rangle \rangle] [2 \cdot \langle \langle 2 \rangle \rangle \langle \langle 2' \rangle \rangle - \langle \langle 4' \rangle \rangle] \\
 & \times \frac{\sum_{i=1}^N (w_{\langle 4 \rangle})_i (w_{\langle 2' \rangle})_i}{\sum_{i=1}^N (w_{\langle 4 \rangle})_i \sum_{j=1}^N (w_{\langle 2' \rangle})_j} \text{Cov}(\langle 4 \rangle, \langle 2' \rangle) \\
 & - \frac{3}{2} \cdot [2 \cdot \langle \langle 2 \rangle \rangle^2 - \langle \langle 4 \rangle \rangle] [2 \cdot \langle \langle 2 \rangle \rangle \langle \langle 2' \rangle \rangle - \langle \langle 4' \rangle \rangle] \\
 & \times \frac{\sum_{i=1}^N (w_{\langle 4 \rangle})_i (w_{\langle 4' \rangle})_i}{\sum_{i=1}^N (w_{\langle 4 \rangle})_i \sum_{j=1}^N (w_{\langle 4' \rangle})_j} \text{Cov}(\langle 4 \rangle, \langle 4' \rangle) \\
 & - 4 \cdot \langle \langle 2 \rangle \rangle [2 \cdot \langle \langle 2 \rangle \rangle^2 - \langle \langle 4 \rangle \rangle]^2 \\
 & \times \left. \frac{\sum_{i=1}^N (w_{\langle 2' \rangle})_i (w_{\langle 4' \rangle})_i}{\sum_{i=1}^N (w_{\langle 2' \rangle})_i \sum_{j=1}^N (w_{\langle 4' \rangle})_j} \text{Cov}(\langle 2' \rangle, \langle 4' \rangle) \right\} \tag{A.10}
 \end{aligned}$$

Appendix B

Flow Fluctuations

In chapter 5 the resulting bias from fluctuations on the two- and four-particle cumulants were presented. This appendix presents the mathematical derivation of equations 5.51-5.52. The following is adapted from [77]

First consider a random observable x sampled from some probability density function $f(x)$. The mean of x is denoted by μ_x and the variance of x is denoted by $\sigma_x^2 = V[x]$. The mean and the variance can be calculated by:

$$\mu_x = E[x] = \int_{-\infty}^{\infty} xf(x)dx \quad (\text{B.1})$$

$$\sigma_x^2 = V[x] = E[(x - E[x])^2] = \int_{-\infty}^{\infty} (x - \mu_x)^2 f(x)dx \quad (\text{B.2})$$

where $E[x]$ is the expectation value of x . A function of x , $h(x)$, can be Taylor expanded around the mean, μ_x up to second order as:

$$h(x) = h(\mu_x) + (x - \mu_x)h'(\mu_x) + \frac{(x - \mu_x)^2}{2!}h''(\mu_x) \quad (\text{B.3})$$

For the cumulants the expectation value of $h(x)$, $E[h(x)] = \langle h(x) \rangle$, is needed. It follows from (B.3) that:

$$\begin{aligned} \langle h(x) \rangle \equiv E[h(x)] &= h(\mu_x) + (E[x] - \mu_x)h'(\mu_x) + \frac{1}{2}E[(x - \mu_x)^2]h''(\mu_x) \\ &= h(\mu_x) + (\mu_x - \mu_x)h'(\mu_x) + \frac{\sigma_x^2}{2}h''(\mu_x) \\ &= h(\mu_x) + \frac{\sigma_x^2}{2}h''(\mu_x) \end{aligned} \quad (\text{B.4})$$

The sample mean $\langle x \rangle$ of a random variable is used as an unbiased estimator for the mean μ_x in the subsequent sections. And for convenience the subscript n has been dropped on the flow moments i.e., v_n is written as v .

B.1 $v\{2\}$

Using the above equation the flow bias is calculated for the two-particle cumulant. From the definition:

$$v\{2\} = \sqrt{\langle v^2 \rangle} \quad (\text{B.5})$$

Plugging this in to (B.4) as $h(x) = v^2$ yields:

$$\langle v^2 \rangle = \langle v \rangle^2 + \sigma_v^2 \quad (\text{B.6})$$

which can be inserted into (B.5) to obtain:

$$\begin{aligned}
 v\{2\} &= (\langle v \rangle^2 \sigma_v^2)^{1/2} \\
 &= \langle v \rangle \left(1 + \frac{\sigma_v^2}{\langle v \rangle^2} \right)^{1/2} \\
 &\approx \langle v \rangle \left(1 + \frac{1}{2} \frac{\sigma_v^2}{\langle v \rangle^2} \right)
 \end{aligned} \tag{B.7}$$

where for the approximation it is assumed that

$$\sigma_v \ll \langle v \rangle \tag{B.8}$$

Finally equation 5.51 is obtained:

$$v\{2\} = \langle v \rangle + \frac{1}{2} \frac{\sigma_v^2}{\langle v \rangle} \tag{B.9}$$

where it is seen that the two-particle cumulant is enhanced by fluctuations.

B.2 $v\{4\}$

From the definition of the four-particle cumulant it is seen that:

$$v\{4\} = (-\langle v^4 \rangle + 2\langle v^2 \rangle^2)^{1/4} \tag{B.10}$$

Using (B.3) with $h(x) = v^4$ yields

$$\langle v^4 \rangle = \langle v \rangle^4 + 6\sigma_v^2 \langle v \rangle^2 \tag{B.11}$$

where only up to second order terms in σ_v is kept. Inserting this into (B.10):

$$\begin{aligned}
 v\{4\} &= \left[-\langle v \rangle^4 - 6\sigma_v^2 \langle v \rangle^2 + 2(\langle v \rangle^2 + \sigma_v^2)^2 \right]^{1/4} \\
 &= \left[\langle v \rangle^4 - 2\sigma_v^2 \langle v \rangle^2 + \mathcal{O}(\sigma_v^4) \right]^{1/4} \\
 &= \langle v \rangle \left(1 - 2 \frac{\sigma_v^2}{\langle v \rangle^2} \right)^{1/4} \\
 &\approx \langle v \rangle \left(1 - \frac{1}{2} \frac{\sigma_v^2}{\langle v \rangle^2} \right)
 \end{aligned} \tag{B.12}$$

where the same approximation as before was used for the last step. Finally equation 5.52 is obtained:

$$v\{4\} = \langle v \rangle - \frac{1}{2} \frac{\sigma_v^2}{\langle v \rangle} \tag{B.13}$$

where the suppression of the four-particle cumulant from fluctuations is seen.

Appendix C

Differential Flow Fluctuations

In chapter 5 equations 5.53-5.54 showed the bias to the differential two-particle cumulant from flow fluctuations. The mathematical derivations are presented below. They follow the approach and notation from appendix B. It is adapted from [77]

Directly from the definition of the two-particle cumulant:

$$\begin{aligned} v'\{2\} &= \frac{\langle v'v \rangle}{\langle v^2 \rangle} \\ &= \frac{\langle v'v \rangle}{\langle v \rangle + \frac{1}{2} \frac{\sigma_v^2}{\langle v \rangle}} \\ &= \frac{\langle v'v \rangle}{\langle v \rangle} \left(1 - \frac{1}{2} \frac{\sigma_v^2}{\langle v \rangle^2} \right) \end{aligned} \tag{C.1}$$

The problem here is to determine $\langle v'v \rangle$. In general it depends on how the reference flow is chosen with respect to the differential flow. Below three cases are calculated:

C.1 v' and v are independent

This is the case where there is no overlap between the RFPs and the POIs. In this case $\langle v'v \rangle \approx \langle v' \rangle \langle v \rangle$ and the result trivially becomes:

$$v'\{2\} \approx \langle v' \rangle \left(1 - \frac{1}{2} \frac{\sigma_v^2}{\langle v \rangle^2} \right) \tag{C.2}$$

and now a suppression in the two-particle cumulant is observed as a bias from fluctuations.

C.2 v' and v are identical

In this case the choice of RFPs and POIs does not matter, as $v = v'$ and $\sigma_v^2 = \sigma_{v'}^2$. Equation (C.1) can then be written as

$$\begin{aligned}
v'\{2\} &= \frac{\langle v'^2 \rangle}{\langle v' \rangle} \left(1 - \frac{1}{2} \frac{\sigma_{v'}^2}{\langle v' \rangle^2} \right) \\
&= \frac{\sigma_{v'}^2 + \langle v' \rangle^2}{\langle v' \rangle} \left(1 - \frac{1}{2} \frac{\sigma_{v'}^2}{\langle v' \rangle^2} \right) \\
&= \langle v' \rangle \left(1 + \frac{\sigma_{v'}^2}{\langle v' \rangle^2} \right) \left(1 - \frac{1}{2} \frac{\sigma_{v'}^2}{\langle v' \rangle^2} \right) \\
&\approx \langle v' \rangle \left(1 + \frac{\sigma_{v'}^2}{\langle v' \rangle^2} - \frac{1}{2} \frac{\sigma_{v'}^2}{\langle v' \rangle^2} \right) \\
&= \langle v' \rangle \left(1 + \frac{1}{2} \frac{\sigma_{v'}^2}{\langle v' \rangle^2} \right) \\
&= \langle v' \rangle \left(1 + \frac{1}{2} \frac{\sigma_v^2}{\langle v \rangle^2} \right)
\end{aligned} \tag{C.3}$$

and in this case the differential flow is seen to be systematically enhanced by the fluctuations.

C.3 v' and v are dependent

This is the case where there is an overlap between RFPs and POIs, but where v' is not necessarily the same as v . Then

$$v = \langle v' \rangle = \frac{\sum_b^{N_{bins}} v'_b}{N_{bins}} \tag{C.4}$$

where for simplicity unit weights in the average is assumed. Using (B.1) and (B.2) the expectation value E and variance V of the mean $\langle x \rangle$ is

$$\begin{aligned}
E[\langle x \rangle] &= \mu \\
V[\langle x \rangle] &= \frac{\sigma^2}{N}
\end{aligned} \tag{C.5}$$

where N is the size of the data sample. For the differential and reference flow this means:

$$\begin{aligned}
\langle v \rangle &= \langle v' \rangle \\
\sigma_v^2 &= \frac{\sigma_{v'}^2}{N_{bins}}
\end{aligned} \tag{C.6}$$

where $\langle v' \rangle$ is the mean of all the differential bins, not to be confused with the mean differential flow in a single bin, $\langle v'_b \rangle$. For bin b and event i :

$$\begin{aligned}
v'_{b,i} \cdot v_i &= v'_{b,i} \cdot \frac{\sum_k v'_{k,i}}{N_{bins}} \\
&= v'_{b,i} \cdot \frac{v'_{b,i} + \sum_{k \neq b} v'_{k,i}}{N_{bins}} \\
&= \frac{1}{N_{bins}} \left((v'_{b,i})^2 + \sum_{k \neq b} v'_{k,i} v'_{b,i} \right)
\end{aligned} \tag{C.7}$$

which gives the event average

$$\begin{aligned}
 \langle v'_b v \rangle &= \frac{1}{N_{bins}} \left(\langle v_b'^2 \rangle + \sum_{k \neq b} \langle v'_k v'_b \rangle \right) \\
 &= \frac{1}{N_{bins}} \left(\langle v_b'^2 \rangle + \sum_{k \neq b} \langle v'_k \rangle \langle v'_b \rangle \right) \\
 &= \frac{1}{N_{bins}} \left(\langle v_b'^2 \rangle + (N_{bins} - 1) \langle v'_b \rangle^2 \right) \\
 &= \frac{1}{N_{bins}} \left(\sigma_{v'_b}^2 + \langle v'_b \rangle^2 + N_{bins} \langle v'_b \rangle^2 - \langle v'_b \rangle^2 \right) \\
 &= \frac{\sigma_{v'_b}^2}{N_{bins}} + \langle v'_b \rangle^2 \\
 &= \sigma_v^2 + \langle v'_b \rangle^2 \tag{C.8}
 \end{aligned}$$

Inserting this and (C.6) into (C.1) yields

$$\begin{aligned}
 v'\{2\} &\approx \frac{\langle v'_b v \rangle}{\langle v \rangle} \left(1 - \frac{1}{2} \frac{\sigma_v^2}{\langle v \rangle^2} \right) \\
 &= \frac{\sigma_{v'}^2 + \langle v'_b \rangle^2}{\langle v' \rangle} \left(1 - \frac{1}{2} \frac{\sigma_v^2}{\langle v \rangle^2} \right) \\
 &\approx \langle v'_b \rangle \left(1 + \frac{1}{2} \frac{\sigma_v^2}{\langle v \rangle^2} \right) \tag{C.9}
 \end{aligned}$$

from which it is seen that the differential two-particle flow is enhanced by the reference flow.

Appendix D

Azimuthal Coverage for Different Vertex Bins

Azimuthal acceptance plots for the FMD and SPD for different vertex bins.

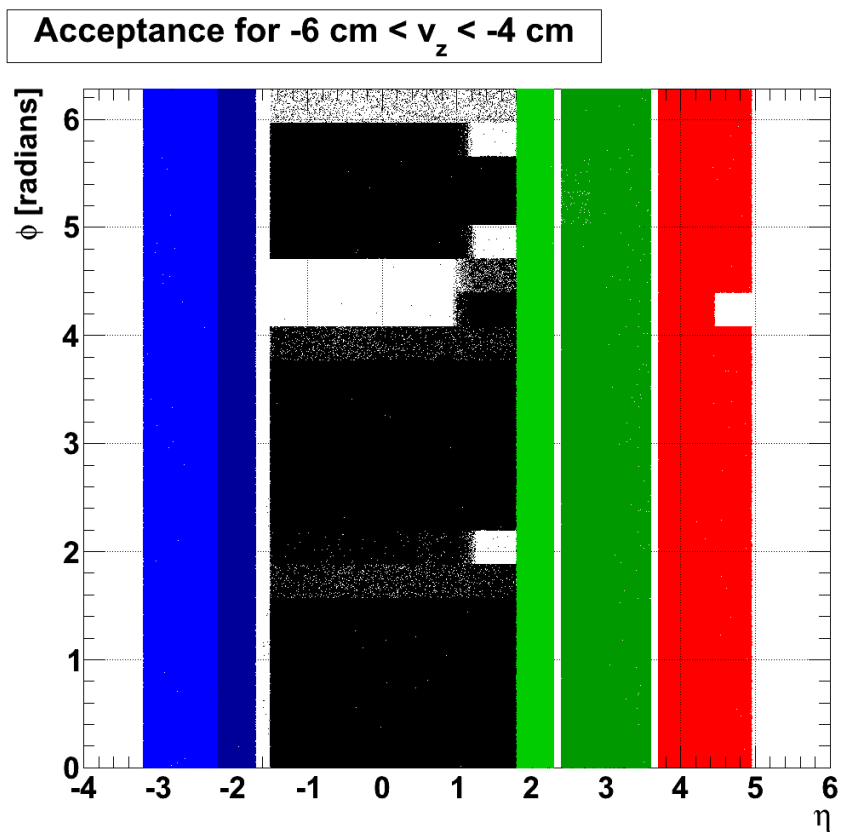
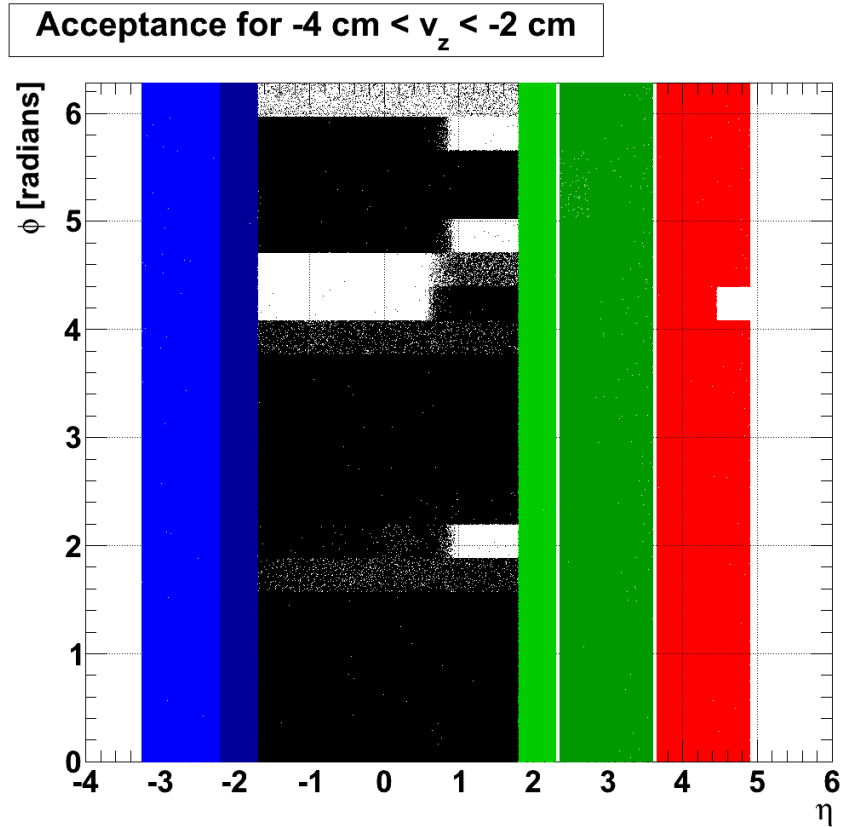
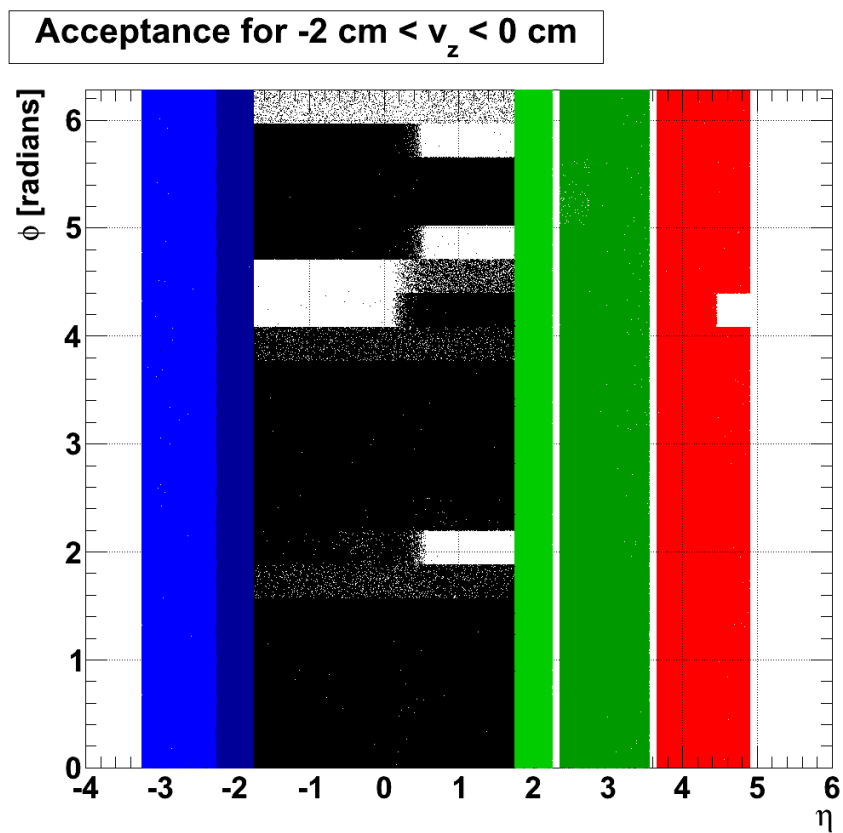


Figure D.1: Azimuthal acceptance for $-6 \text{ cm} < v_z < -4 \text{ cm}$

Figure D.2: Azimuthal acceptance for $-4 \text{ cm} < v_z < -2 \text{ cm}$ Figure D.3: Azimuthal acceptance for $-2 \text{ cm} < v_z < 0 \text{ cm}$

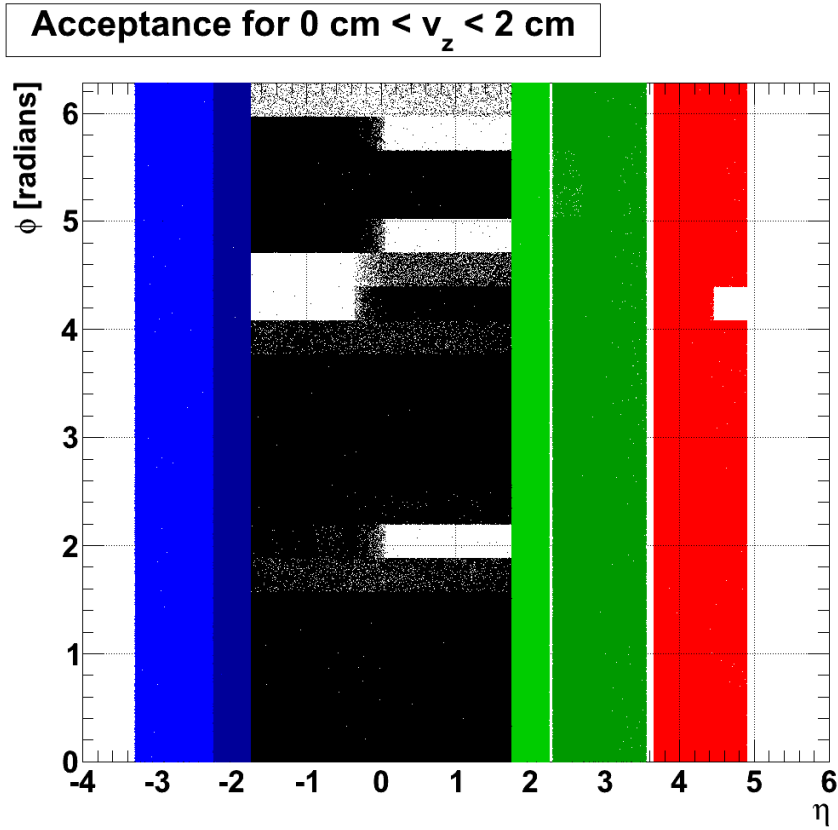


Figure D.4: Azimuthal acceptance for $0 \text{ cm} < v_z < 2 \text{ cm}$

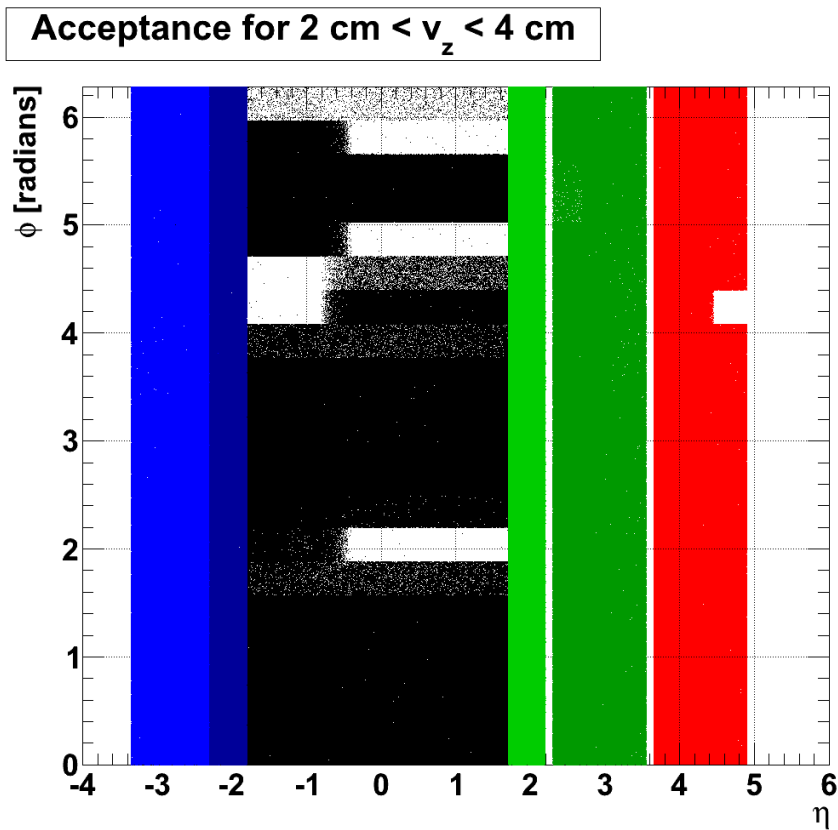
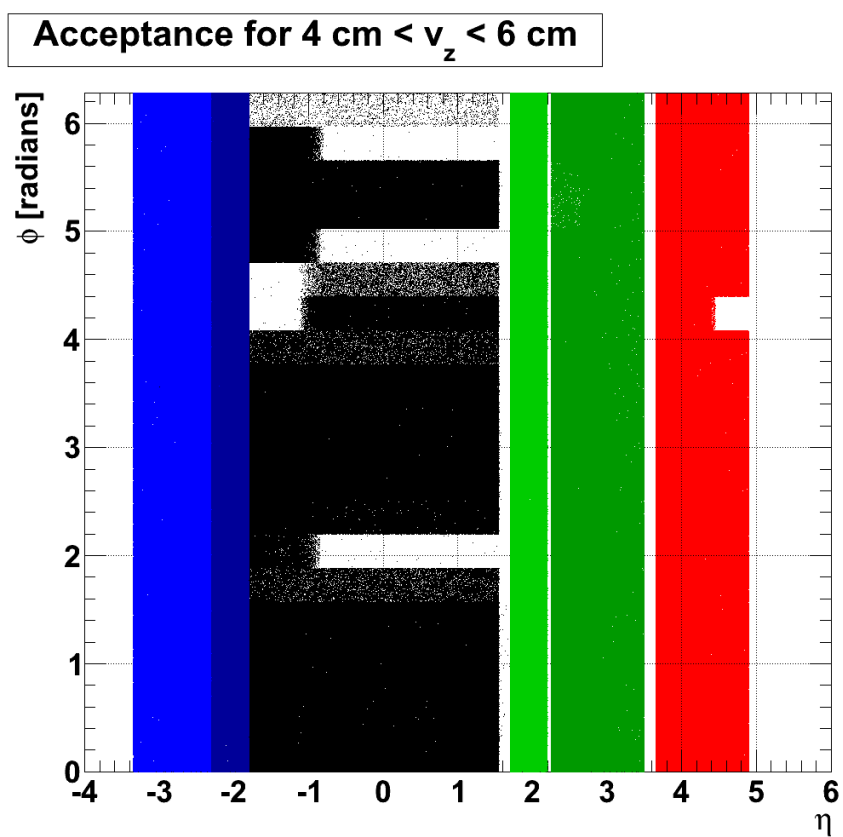


Figure D.5: Azimuthal acceptance for $2 \text{ cm} < v_z < 4 \text{ cm}$

Figure D.6: Azimuthal acceptance for $4 \text{ cm} < v_z < 6 \text{ cm}$

Appendix E

Run Number List

The run numbers seen in the table, from the 2010 LHC Pb+Pb period (LHC10h in ALICE terms) were, the ones used for the analysis in this thesis. Even though more than 18 M events were in those runs, only 7.5 M was accepted by the physics selection, centrality determination and vertex cuts applied for the analysis.

Run number	Triggers	Magnetic field
137231	141,019	-/-
137366	205,645	-/-
137431	189,477	-/-
137549	302,613	-/-
137595	232,976	-/-
137722	406,022	-/-
137748	833,891	-/-
137844	976,399	-/-
138125	767,377	-/-
138126	707,513	-/-
138192	396,270	-/-
138225	272,916	-/-
138275	1,620,331	-/-
138359	327,172	+/+
138364	689,060	+/+
138396	513,422	+/+
138442	584,718	+/+
138534	1,525,880	+/+
138578	310,480	+/+
138653	430,196	+/+
138795	1,814,915	+/+
138836	406,551	+/+
139038	415,551	+/+
139107	519,252	+/+
139110	1,422,017	+/+
139173	312,626	+/+
139437	474,726	+/+
139465	610,237	+/+
139466	323,493	+/+
139467	303,150	+/+
139507	312,631	+/+